

Università di Brescia

DOTTORATO DI RICERCA IN
INGEGNERIA CIVILE, AMBIENTALE, DELLA COOPERAZIONE INTERNAZIONALE E DI MATEMATICA - DICACIM

Settore Scientifico Disciplinare: ICAR/09-Tecnica delle Costruzioni

Recupero di Edifici Storici e Contemporanei

XXXVIII CICLO

Structural Assessment of Existing Deteriorated Girders and Advanced Strengthening Strategies: Analytical, Experimental and Numerical Approaches

DOTTORANDO:
Anna Bontempi

SUPERVISOR:
Chiar.mo Prof. Fausto Minelli

CO-SUPERVISOR:
Ing. Nico Di Stefano, PhD

SYNOPSIS

This doctoral research focuses on the assessment and strengthening of deteriorated girders, with particular emphasis on full-scale structural members subjected to natural corrosion and tested at the end of their service life. The work combines analytical development, experimental investigation, and supportive numerical interpretation within a coherent mechanics-based framework.

A first contribution consists in the development of an analytical formulation for predicting the shear strength of corroded reinforced concrete beams within the framework of *fib* Model Code 2020. Corrosion-induced degradation mechanisms are explicitly incorporated into the model, allowing a rational estimation of residual capacity during the assessment phase.

A central part of the research is devoted to full-scale experimental testing on naturally deteriorated girders removed from service at the end of their life. These investigations provide rare evidence on structural behavior under realistic boundary conditions and establish a reliable basis for evaluating both residual capacity and the effectiveness of intervention strategies.

Particular emphasis is placed on the design, application, and experimental validation of strengthening interventions on real degraded members. Ultra-high-performance fiber-reinforced concrete (UHPFRC) overlays and hybrid CFRP–FRM systems were implemented at full scale and assessed under monotonic loading. The results demonstrate that properly designed strengthening solutions can not only restore but significantly enhance structural performance, while maintaining compatibility with the existing degraded substrate. The study highlights the role of interface behavior, load redistribution mechanisms, and interaction between original reinforcement and new materials in achieving effective service-life extension.

Nonlinear finite element analyses were employed to interpret the observed behavior and to explore stress redistribution in degraded and strengthened configurations. In addition, a complementary stochastic investigation was conducted to examine the influence of material and corrosion variability on structural response.

Overall, the thesis contributes to a mechanics-based and experimentally validated approach for the assessment and service-life extension of aging girders, with primary emphasis on real-scale evidence and practical applicability in infrastructure management.

ACKNOWLEDGMENTS

I would like to express my sincere gratitude to Prof. Fausto Minelli for giving me the opportunity to undertake this doctoral journey and for his constant guidance throughout these years. His scientific rigor, support, and trust have been fundamental to the development and completion of this thesis.

I am deeply grateful to my co-supervisor, Eng. Nico Di Stefano, for his continuous advice, technical support, and valuable discussions, which greatly contributed to the progress of this research.

I would like to express my sincere appreciation to the Municipality of Brescia for donating the historical girders investigated in this thesis. This contribution made it possible to conduct experimental research on a full-scale naturally deteriorated structural element, representing a rare and valuable opportunity.

I would also like to acknowledge MAPEI for providing the materials used in this work and for their technical support during the experimental phases.

My sincere thanks go to CMM Rizzi and Sofia Costruzioni for their essential assistance in the handling and movement of the structural elements tested in this research.

I would like to thank my colleagues Paolo, Elisa, Ivan, Luca, Alessandra, Matteo, Giulia, Dechen, Mesfin, Giovanni and Francesca for sharing this academic journey.

I am deeply grateful to my family for their constant encouragement and unwavering presence.

I would also like to thank my boyfriend Luca for his patience, understanding, and steady presence throughout this journey.

Finally, a special thanks goes to my dearest friend Giulia, for believing in me more than I often believe in myself. Her confidence and support have been a constant source of strength.

CONTENTS

CONTENTS **1**

1. INTRODUCTION **5**

1.1 Background and Research Motivation 5

1.2 Research and Objectives 6

1.3 Structure of the Thesis 7

2. AN ENHANCED ANALYTICAL MODEL FOR PREDICTING SHEAR STRENGTH IN REINFORCED CONCRETE BEAMS WITH CORRODED REINFORCEMENT **9**

2.1 *INTRODUCTION* 11

2.2 DEVELOPMENT OF THE ANALYTICAL MODEL 14

2.3 MODEL Application - WORKED EXAMPLE 27

2.4 MODEL VALIDATION 30

2.5 Corrosion Definition 32

2.5.1. RODRIGUEZ ET AL. (1997) *32*

2.5.2. ZHAO AND JIN (2012) *33*

2.5.3. WANG ET AL. (2011) *33*

2.5.4. ALASKAR (2013) *34*

2.5.5. XUE ET AL. (2013) *34*

2.5.6. XUE ET AL. (2014) *35*

2.5.7. EL-SAYED ET AL. (2016) *35*

2.5.8. HAN ET AL. (2019) *36*

2.5.9. LU ET AL. (2019) *36*

2.5.10. DI STEFANO (2022) *36*

2.6 Results of the Validation 37

2.7 COMPARISONS between formulations 49

2.7.1. Model Code 2020 ..... *50*

2.7.2. Rossi and Spinella (2023) *53*
2.7.3. Juarez et al. (2011) *54*
2.7.4. Xu et al. (2017) *55*
2.7.5. Lu et al. (2018) *55*
2.7.6. Cladera (2021) *56*
2.8 Results 56
2.9 CONCLUDING REMARKS 59
2.10 ACKNOWLEDGMENTS 62
2.11 NOTATION 62
2.12 REFERENCES 65
2.13 LIST OF TABLES 70
2.14 LIST OF FIGURES 70

3 EXPERIMENTAL AND NUMERICAL STUDY ON SHEAR-CRITICAL PRESTRESSED GIRDERS STRENGTHENED WITH HIGH PERFORMANCE FIBRE REINFORCED CONCRETE 71

3.1. INTRODUCTION 71
3.2. EXPERIMENTAL PROGRAMME 73
3.2.1. Specimens' location and geometry *73*
3.2.2. Strengthening technique *76*
3.2.3. Experimental tests and results *80*
3.3. FINITE ELEMENT MODELS 95
3.3.1. Model Geometry and Discretization *95*
3.3.2. Boundary conditions and loading phases *99*
3.3.3. Constitutive lows *100*
3.3.4. Diagnostic and Materials Properties *101*
3.3.5. Numerical Results *107*
3.4. CONCLUSIONS 118
3.5. REFERENCES 119
3.6. LIST OF TABLES 121

3.7. LIST OF FIGURES 121

4. EXTENDING THE SERVICE LIFE OF HISTORICAL BRIDGES: EXPERIMENTAL EVALUATION OF A CFRP–FRM RETROFIT SYSTEM 123

4.1. INTRODUCTION 124

4.2. EXPERIMENTAL PROGRAM 126

4.2.1. Structural element and original condition 126
4.2.2. Existing materials 127
4.2.3. Strengthening Materials 128
4.2.3.1. 10 cubes (dimensions 150 × 150 × 150 mm) 129
4.2.3.2. 6 notched beams (dimensions 150 × 150 × 600 mm) 131
4.2.3.3. 12 prismsmatic specimens (dimensions 40 × 40 × 160 mm) 134
4.2.3.4. Elastic Modulus 136
4.2.3.5. CFRP bars diameter 12 mm 138
4.2.4. Strengthening procedure 140
4.2.5. Test setup and instrumentation 144

4.3. EXPERIMENTAL RESULTS 148

4.4. ANALYTICAL MOMENT-CURVATURE DIAGRAM 156

4.5. CONCLUDING REMARKS 159

4.6. NOTATION 160

4.7. REFERENCES 162

4.8. LIST OF TABLES 165

4.9. LIST OF FIGURES 166

5. STOCHASTIC MODELLING OF ADVANCED STRENGTHENING STRATEGIES ON EXISTING DETERIORATED GIRDERS 168

5.1. *INTRODUCTION* 169

5.2. EXPERIMENTAL PROGRAMS AND RESULTS 170

5.2.1. Historical girder strengthened with a CFRP–FRM retrofit system 170
5.2.2. 60 years PRC girders strengthened with UHPFRC 172

5.3. DETERMINISTIC ANALYSES ... 173
5.3.1. Constitutive Models ... 173
5.3.2. Historical RC Girder ... 175
5.3.3. 60 Years PRC Girders ... 178
5.4. STOCHASTIC ANALYSES ... 181
5.4.1. Stochastic Modelling Strategy ... 181
5.4.2. Corrosion-Only Stochastic analysis ... 182
5.4.3. Materials-Only Stochastic analysis ... 187
5.4.4. Full Stochastic material + corrosion analysis ... 188
5.4.5. Monte Carlo Implementation and Convergence ... 188
5.5. NUMERICAL RESULTS AND DISCUSSION ... 190
5.6. LABORATORY BEAMS WITH ACCELERATED CORROSION ... 195
5.6.1. Experimental Program ... 196
5.6.2. Deterministic Modelling ... 198
5.6.3. Stochastic Scenarios ... 199
5.6.4. Results and Discussion ... 201
5.7. GLOBAL DISCUSSION ... 207
5.8. CONCLUDING REMARKS ... 208
5.9. REFERENCES ... 210
5.10. LIST OF TABLES ... 213
5.11. LIST OF FIGURES ... 213
6 CONCLUSIONS AND RECOMMENDATIONS FOR FUTURE WORK ... 215
6.1 Conclusions ... 215
6.2 Recommendations for future research ... 216

1. INTRODUCTION

1.1 Background and Research Motivation

The assessment and rehabilitation of aging reinforced concrete (RC) and prestressed reinforced concrete (PRC) bridges represent a major engineering challenge in contemporary infrastructure management. A significant amount of the existing bridge stock was constructed during the first half of the twentieth century and in the post-war period, and many of these structures are currently operating beyond their nominal design service life. In several cases, they have been subjected to decades of environmental exposure, increasing traffic demands, and evolving safety requirements that were not anticipated at the time of design.

Among deterioration mechanisms, reinforcement corrosion is widely recognized as the most critical and pervasive cause of structural degradation. Corrosion leads to reduction of steel cross-section, cracking and spalling of the concrete cover, degradation of bond between steel and concrete, and progressive loss of stiffness and load-bearing capacity. In prestressed members, corrosion of tendons may further induce prestress losses or, in extreme cases, brittle rupture. As a consequence, reliable evaluation of residual structural capacity becomes essential for rational decision-making regarding maintenance, strengthening, or replacement.

Within this framework, several research gaps can be identified.

There is limited experimental evidence on full-scale structural members affected by long-term natural corrosion. Opportunities to perform destructive testing on real bridge components removed from service are rare, and most available knowledge derives from small-scale laboratory specimens or artificially accelerated corrosion processes. While such studies provide valuable insights, they cannot fully reproduce the complex and non-uniform degradation patterns that develop over decades of natural exposure. Experimental investigations on real-scale members at the end of their service life are therefore essential to better understand actual residual capacity and governing failure mechanisms under realistic boundary conditions.

There is also a lack of analytical models explicitly incorporating corrosion effects within advanced mechanical frameworks. Many existing formulations are derived from models originally calibrated for undamaged elements and subsequently modified through empirical reduction factors. A more consistent approach requires integrating corrosion-induced degradation (such as steel cross-section loss, deterioration of transverse reinforcement, and reduction of effective concrete width due to cover damage) directly into mechanically based formulations. Such analytical tools are particularly relevant in the assessment phase, where quantification of the

residual capacity of degraded beams must rely on physically grounded assumptions rather than purely empirical adjustments.
Furthermore, there is a clear need for experimental validation of innovative strengthening systems applied to real bridge components. Advanced materials such as ultra-high-performance fibre-reinforced concrete (UHPFRC) and fibre-reinforced polymer (FRP) systems offer promising mechanical and durability properties. However, their structural effectiveness depends on interaction with aged and degraded substrates, interface performance, compatibility between materials, and the governing failure mechanisms of the strengthened system. Full-scale applications on naturally deteriorated members provide crucial evidence regarding their structural contribution and practical feasibility.
Finally, insufficient integration of probabilistic approaches into the nonlinear assessment of deteriorated and strengthened structures remains an open issue. Deterministic nonlinear analyses, even when based on refined constitutive models, do not inherently account for the variability associated with material properties and degradation processes. Although the primary focus of this research is on mechanical assessment and full-scale validation, a complementary stochastic numerical investigation has been conducted to evaluate the predictive capability of nonlinear models in the presence of degradation and strengthening. This aspect is addressed in a supportive and interpretative manner, with the objective of improving understanding rather than emphasizing purely numerical outcomes.
Within this context, the present doctoral research concentrates on the assessment of full-scale bridge girders subjected to long-term natural degradation and tested at the end of their service life. Particular attention is devoted to the formulation of analytical tools capable of estimating residual structural capacity and to the experimental evaluation of strengthening interventions applied to these elements. Numerical analyses are employed as an additional instrument to interpret structural behaviour and to support the assessment framework, while maintaining primary emphasis on real-scale experimentation and mechanically based formulations.

1.2 Research and Objectives

The overarching aim of this thesis is the contribution to a rational, mechanics-based framework for the assessment and strengthening of deteriorated reinforced and prestressed concrete bridge girders.
Within this general aim, the research focuses on:

- the development of an analytical formulation for predicting the shear strength of corroded reinforced concrete beams within the framework of *fib*

Model Code 2020, with explicit incorporation of corrosion-induced degradation mechanisms;

- the experimental evaluation of the structural response of full-scale bridge girders affected by long-term natural corrosion and tested at the end of their service life;
- the investigation of strengthening interventions based on UHPFRC overlays and hybrid CFRP–FRM systems applied to real structural components, with emphasis on structural effectiveness and interaction with degraded substrates;
- the numerical reproduction and mechanical interpretation of the observed experimental behaviour through nonlinear finite element analyses based on advanced constitutive models;
- the complementary exploration of the influence of material and corrosion variability on structural response through a stochastic nonlinear assessment framework.

Through the integration of analytical development, full-scale experimentation, strengthening applications, and numerical interpretation, the thesis aims at providing a coherent contribution to the assessment and service-life extension of aging bridge infrastructure.

1.3 Structure of the Thesis

The thesis is organized into four main research chapters, each addressing a complementary aspect of the assessment and strengthening of deteriorated reinforced and prestressed concrete bridge girders.

Following this introduction, in Chapter 2 an analytical model is developed for predicting the shear strength of reinforced concrete beams affected by corrosion. The formulation is based on the Level IIb approach of *fib* Model Code 2020 and explicitly incorporates corrosion-induced degradation mechanisms, including reduction of longitudinal reinforcement area, degradation of stirrup yield strength, and reduction of effective concrete width due to cover cracking and spalling. The proposed model is validated against a database of 108 experimental tests and is critically compared with existing formulations from the literature, demonstrating a balanced compromise between accuracy and conservativeness.

In Chapter 3, the structural behaviour of three full-scale prestressed concrete girders removed from service after approximately 60 years is experimentally and numerically investigated. The beams are strengthened using ultra-high-performance

fibre-reinforced concrete (UHPFRC) web overlays. The experimental results show a significant increase in shear resistance, improved crack control, and a transition from brittle shear failure to a more ductile flexural-dominated response. Nonlinear finite element analyses performed with VecTor2 provide a good representation of the observed structural behaviour.

In Chapter 4, the strengthening of a historical reinforced concrete girder that remained in service for nearly 90 years is examined. A hybrid retrofit system consisting of CFRP bars embedded in a fibre-reinforced mortar (FRM) overlay is experimentally evaluated under four-point bending. The strengthened configuration exhibits an increase in ultimate load of approximately 33% while maintaining satisfactory global ductility due to the interaction between existing steel reinforcement and CFRP bars. An analytical moment–curvature model is developed and compared with experimental results, showing good predictive capability.

In Chapter 5, a stochastic nonlinear finite element framework is introduced to quantify the influence of uncertainty on the structural response of deteriorated and strengthened girders. Monte Carlo simulations are conducted considering different variability scenarios, including corrosion-only uncertainty, material-property variability, and combined effects. The results highlight that the deterministic nonlinear analyses do not represent the mean structural response of nonlinear systems and tend to underestimate ultimate capacity. It is also shown that variability in mechanical properties governs response dispersion more significantly than corrosion-rate uncertainty when the mean penetration level is preserved.

Chapter 6 presents the main conclusion of the research.

2 AN ENHANCED ANALYTICAL MODEL FOR PREDICTING SHEAR STRENGTH IN REINFORCED CONCRETE BEAMS WITH CORRODED REINFORCEMENT

ABSTRACT

This work presents an analytical model to predict the shear strength of RC beams affected by corrosion within the Level IIb framework of *fib* Model Code 2020. Corrosion is accounted for by (i) reducing the area of longitudinal reinforcement, (ii) degrading the yield strength of stirrups a and (iii) reducing the effective concrete width due to cover cracking and spalling. The model is solved iteratively by explicitly considering the average longitudinal strain state and the contributions of both concrete and transverse reinforcement to shear transfer. A curated database of 108 tests (76% corroded) on slender beams is compiled to validate the model and benchmark it against established formulations (MC2020 approach IIa, Rossi and Spinella, Cladera, Juarez, Xu, and Lu). Overall, the proposed method attains a mean analytical-to-experimental ratio of 1.02 with a coefficient of variation of 25%. The dispersion increases with high corrosion level and in small-scale specimens, while full-scale tests, though fewer, are captured satisfactorily. Compared to the reference formulations, the present approach yields a balanced trade-off between accuracy and conservativeness and is therefore well suited for structural assessment. Scope and limitations are discussed, and guidance is provided for practical application and future extensions to members under axial load and prestress.

Keywords: shear strength; corrosion; reinforced concrete; analytical model; *fib* Model Code; degraded structures; structural assessment.

2.1 INTRODUCTION

Corrosion is one of the most critical deterioration mechanisms affecting reinforced and prestressed concrete (RC and PRC) girders, particularly due to prolonged exposure to aggressive environmental conditions. As infrastructure systems age, reliable assessment of structural degradation becomes essential to inform decisions related to maintenance, strengthening or decommissioning of bridges and similar structures (Belletti et al., 2020a). Among the various structural responses impacted by corrosion, shear capacity remains particularly vulnerable and difficult to predict with precision.

Shear is a brittle failure mode that can lead to sudden and catastrophic collapse. It is therefore crucial to accurately evaluate the residual shear strength of deteriorated elements, especially in safety-critical applications. Corrosion typically initiates at the most exposed reinforcement components (namely, the stirrups) making them especially susceptible. Moreover, small-diameter bars, often employed for shear reinforcement, have been shown to be particularly sensitive to corrosion effects (Imperatore et al., 2017).

The degradation of shear capacity in corroded RC elements arises from several interrelated factors: reduction in the cross-sectional area of stirrups (Cairns et al., 2005; Apostolopoulos, 2009), cracking and spalling of the concrete cover (Higgins et al., 2010; Pedeferri, 2018), deterioration of the bond between longitudinal reinforcement and concrete (Coronelli and Gambarova 2004; Lin et al., 2017), loss of

aggregate interlock (Belletti et al., 2020b), and diminished confinement effects due to stirrup deterioration. These mechanisms contribute collectively to a reduction in structural integrity and complicate the formulation of reliable predictive models.

Only a few experimental studies have investigated the structural response of reinforced concrete (RC) beams with corroded stirrups and/or longitudinal reinforcement (Rossi and Spinella, 2023). Some authors collected in databases the tests presented in the aforementioned papers and applied different formulations for the shear strength calculation (Cladera 2021; Lu et al. 2018). Some databases were later revised to clarify key aspects needed for a correct application of the formulations (Rossi and Spinella, 2022).

Various approaches have been proposed in the literature to estimate the residual shear strength of corroded beams. Many are derived from design provisions of standards such as the ACI 318-19 Building Code (2014), including the model by Juarez et al. (2011). Additional, empirical formulations have been developed, for example, by Xu et al. (2017) and Lu (2018), while Cladera (2021) proposed a more mechanistic approach based on the Compression Chord Capacity Model. Rossi and Spinella (2023) proposed a formulation based on the Simplified Modified Compression Field Theory (SMCFT) (Bentz et al. 2006), which requires an iterative procedure. Subsequently, they developed a simplified and more practical version, which provides results fully comparable to those obtained with the original formulation.

The *fib* Model Code for Concrete Structures 2020 (*fib*, 2023) (hereafter referred to as MC2020) represents the most refined model for calculating the shear strength of reinforced concrete elements. For uncorroded beams, it provides three possible approaches: I, IIa, IIb. Furthermore, within the MC2020 document, a specific formulation is also proposed for evaluating the shear resistance of corroded members with shear reinforcement, based on the Level IIa (plasticity-based) approach.

In this study, a new analytical method is proposed to estimate the residual shear strength of RC beams affected by corrosion. The formulation builds upon the *fib* MC2020, specifically adopting the Level IIb approximation for shear strength evaluation. In fact, in the authors' opinion, Level IIb model (based on the SMCFT) is the most suitable in presence of little or no shear reinforcement as it accounts for both concrete and steel contribution. In fact, several existing structures, such as bridges, were originally constructed with a low amount of shear reinforcement, as evidenced by many inspection reports. Moreover, the exposure conditions often lead to a further reduction in the cross-sectional area of the stirrups due to corrosion.

The model, starting from the MC2020 formulation, explicitly incorporates corrosion-related degradation of both concrete and steel components, while neglecting the reduction of bond between concrete and steel reinforcement. Further studies are required to properly consider this phenomenon. In paragraph 5, the main differences and similarities between the MC2020 approach and the proposed analytical model are discussed.

A significant number of papers were analyzed and data for the formulation applications were extracted, starting from the aforementioned existing databases and implementing the number of considered tests.

Finally, results are critically compared with selected formulations from the literature through validation against a comprehensive experimental database.

2.2 DEVELOPMENT OF THE ANALYTICAL MODEL

Several analytical models have been proposed in the literature to estimate the shear strength of corroded RC beams. However, a widely accepted, standardized formulation that accounts for corrosion effects in a comprehensive manner is still lacking.

Most available models are relatively simplified to facilitate their use in engineering practice, but this often compromises their ability to accurately reproduce experimental results, especially in the presence of material degradation.

To achieve more realistic predictions, it is necessary to separate and explicitly model the contributions of concrete and steel reinforcement to shear strength. Simplified code-based formulations, such as those in Eurocode 2 (2004), typically fail to capture this complexity and are therefore of limited usefulness in the structural assessment of deteriorated members. When corrosion is introduced, the predictive performance of such models tends to deteriorate further due to the additional uncertainty and variability introduced by degradation phenomena.

The formulation here proposed is based on the *fib* MC2020, specifically adopting the Level IIb approximation for shear strength evaluation.

Within MC2020, approach IIb was adopted so as to retain the concrete contribution to shear; the stirrup contribution is evaluated with a corrosion-degraded yield stress, while the original stirrup area is kept in the truss mechanism.

First, Level IIb approach herein considered for the assessment of existing members in shear, requires the state of strain to be taken into account. Consider the beam with a generic cross-section shown in Figure 2-1. The average state of strain (ε_x) is conventionally calculated by the MC2020 at the mid-depth of the effective shear depth or core layer being considered, as in Equation 1.

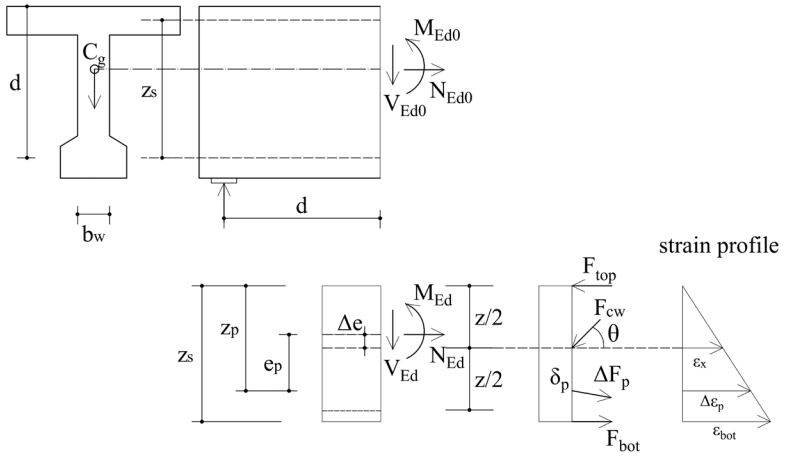


Figure 2-1: Schematic representation of ε_x (fib MC2020)

$$\varepsilon_x = \frac{1}{2 \cdot E_s \cdot A_{L,corr}} \cdot \left(\frac{M_E}{z_v} + \frac{V_E}{2}\cot\theta\right) < \frac{\varepsilon_y}{2} \quad \text{Equation 1}$$

where:

- E_s is the Young's modulus of the steel;
- $A_{L,corr}$ is the cross section of the tensile reinforcements considering corrosion, defined below;
- M_E and V_E are the acting bending moment and shear actions (they shall be taken as positive quantities);
- z_v is the effective shear depth. It is assumed that $z_v = 0.9 \cdot d$, where d is the effective depth.

This strain is a function of the bending moment and shear force acting on the critical section, as well as the stiffness and cross-sectional area of the tensile reinforcement. In the presence of corrosion, the cross-sectional area is reduced proportionally to the measured mass loss, thereby increasing ε_x and potentially triggering early yielding. The imposed strain limit in Equation 1 reflects the dominant failure mechanism: if the steel yields, the beam is assumed to fail in flexure rather than in shear. The shear resistance is hence governed by the limitation on the resistant bending moment. It should be noted that the effect of corrosion on the yielding strain is not explicitly considered in the right-hand side of Equation 1. In this formulation, corrosion of the longitudinal reinforcing bars is represented only as a reduction in the cross-sectional area, while the yield stress, and consequently the yield strain, are assumed to remain equal to those of uncorroded bars. As a result, the average strain ε_x, which is inversely proportional to the corroded area, reaches the yield condition more rapidly in corroded elements. This leads to an earlier onset of yielding and, consequently, a

lower shear resistance. Such an approach was found to provide results that are more consistent with the experimental failure modes than when the yield strain is explicitly introduced into the equation.

Conversely, for the shear reinforcement, the equation proposed by Imperatore et al. was adopted to calculate the yield stress. This formulation was developed to be used with the original, uncorroded cross-sectional area of the stirrups. In conclusion, two distinct approaches were employed to account for corrosion in the longitudinal reinforcement and in the stirrups: corrosion in the longitudinal reinforcement is considered through the reduction of the reinforcement cross-sectional area, whereas for the stirrups, it is accounted for by reducing the yield stress. To reflect this behaviour, an iterative process is adopted, in which the yielding condition is checked and strain-limited shear resistance is updated so that when ε_x is higher than $\frac{\varepsilon_y}{2}$, it is assumed that yielding has occurred, so that:

$$\varepsilon_x = \frac{\varepsilon_y}{2} \qquad \text{Equation 2}$$

Note that the axial force is not included at this stage, so the model is not suitable for prestressed beams or in any case of combined shear and axial force. These cases will be further studied in the future.

Furthermore, in Equation 1, it should be noted that, to facilitate the application of the formulas, the horizontal component of the shear force (which would be equal to $V_{Eh} = \frac{V_E}{2} \cdot \cot\vartheta$, where ϑ is angle of inclination of the compressive stress field, as

defined below) is taken, as a first approximation (according to the MC2020), equal to the shear force. It is therefore assumed, only in this equation, that $\cot\vartheta = 2$. Note that the inclination of the compressive stress field ϑ will be discussed in more details in the determination of the V_s term in the following (Equation 12).

While the actions reported by MC2020 are meant to be in their design values, $M_E$and V_E herein derive from experimental tests and, therefore, they do not include any load amplification factor. In the same way, materials properties are taken in their mean (experimentally measured) values.

Furthermore, as the model is used for strength prediction purposes, $M_E$and V_E are not known a priori.

M_E is calculated in the most critical shear section, which, by convention, is taken at a distance from the load point (in the direction of the support) equal to d, for a beam in simple support subjected to concentrated loads. Consequently, the bending moment is defined in Equation 3, where a is the shear span length.

$$M_E = V_E \cdot (a - d) \qquad \text{Equation 3}$$

It is, therefore, necessary to iterate until V_E does correspond to the resistance shear (hereinafter referred to as V_{AN}).

The corrosion ratios are defined according to Cladera et al. (2021). Accordingly, the average corrosion along the length of the reinforcement bars is expressed as a mass loss ratio, whereas the maximum corrosion ratio refers to a local sectional value. In

the present study, only the average corrosion ratio is considered in the analyses, corresponding to the first definition described above.

Corrosion of the longitudinal reinforcement is considered in Equation 4 by modifying the original area A_s and determining $A_{s,corr}$.

$$A_{L,corr} = A_L \cdot \left(1 - m_{corr,L}\right) \quad \text{Equation 4}$$

where:

$A_{L,corr}$ is the reduced cross section of longitudinal rebars;

A_L is the original (uncorroded) cross section of the tensile reinforcement;

$m_{corr,L}$ is the average mass loss ratio related to the longitudinal rebars.

The stirrups average yield strength must take into account the effect of corrosion. The estimation of $f_{yw,corr}$ in the presence of corrosion was therefore obtained with the Equation 5 (Imperatore et al., 2017).

$$f_{yw,corr} \geq f_{yw} \cdot \left(1 - \alpha_w \cdot m_{corr,w}\,[\%]\right) \quad \text{Equation 5}$$

where f_{yw} is the initial yield stress of the stirrups without corrosion, and $m_{corr,w}$ is expressed here in percentage. $m_{corr,w}$ is the average area reduction of the stirrups. Note that using the average stirrup cross-section yielded the most accurate shear strength predictions across the experimental validation dataset. This choice was made to account for the probabilistic distribution of the mechanical properties. Such an approach is applicable when there is redundancy among the reinforcing bars involved in the resisting mechanism, as in the tests considered in the present study. In fact, the critical shear crack always intercepts more than one stirrup, and each

stirrup consists of two legs. Conversely, adopting the maximum sectional corrosion value would only be reasonable in the case of a single-leg stirrup intercepting the critical shear crack.

The stresses are calculated based on the initial area of the steel (not corroded). This aspect makes Imperatore et al.'s formulation easily applicable also in practice.

Equation 5 was obtained from a sample of corroded bars with a diameter of 8 mm, assuming uniform corrosion.

The value of α_w in Equation 5 is defined in Table 2-1, based on Imperatore et al. (2017).

Table 2-1: Coefficient α_w employed as a function of the stirrups' diameters

Φ_w **[mm]**	**N of specimens**	**% of specimens**	α_w
6	73	68%	0.01642
8	23	21%	0.01642
10-14	12	11%	0.01435
TOT	108	100%	

Alternatively, in the presence of pronounced pitting corrosion, different values of the coefficient α_w could be adopted to reflect a more localized degradation mechanism. However, this option was not implemented in the present study, as such corrosion patterns were not consistently identifiable or quantifiable within the considered experimental database.

Moreover, note that Equation 5 does not apply to corrosion percentages above 60.9%. However, corrosion values of this type are difficult to observe in real cases.

In summary, the formulation considers corrosion contribution in the stirrups by reducing the yield stress as in Equation 5, where the reduction depends on the mean percentage of lost mass ($m_{corr,w}$); while for the longitudinal reinforcements, corrosion is considered in terms of reduced area (Equation 4) and the reduction depends on the mean percentage of lost mass ($m_{corr,L}$).

The shear strength (V_{AN}) is obtained through the following equation:

$$V_{AN} = V_C + V_S \leq V_{R,max} \qquad \text{Equation 6}$$

In which V_C and V_S are the contribution of the concrete and the stirrups on the shear strength, respectively. $V_{R,max}$ is the maximum shear strength related to crushing of concrete carrying the compression field.

V_C is calculated as Equation 7.

$$V_C = k_v \cdot \sqrt{f_c} \cdot b_{corr} \cdot z_v \qquad \text{Equation 7}$$

where k_v is a coefficient that depends on ε_x and is calculated in Equation 8.

$$k_v = \frac{0.4}{1 + 1500 \cdot \varepsilon_x} \qquad \text{Equation 8}$$

b_{corr} is defined considering the effect of concrete cover cracks due to the corrosive products. In particular, this effect was considered by reducing the initial base b (undamaged) thanks to the formulation proposed by Higgins et al. (2010) and widely used in literature. This formulation is reported in Equation 9 and Equation 10.

$$b_{corr} = b - 2(c_n + \phi_w) + \frac{s_w}{5.5} \qquad \text{Equation 9}$$

$$if\ s_w \leq 5.5 c_n$$

$$b_{corr} = b - \frac{5.5}{s_w}(c_n + \phi_w)^2 \qquad \text{Equation 10}$$

$$if\ s_w > 5.5c_n$$

where c_n is the clear concrete cover, $\phi_w$is the initial stirrup rebar diameter, and s_w is the stirrup spacing.

Higgins et al. suggest using the previous equations when stirrups exhibit 10% average cross-section loss or more and when, based on field observations, concrete cover is damaged. If not, so for example in the non-corroded control beams or in cases of low corrosion percentage, b_{corr} is equal to b.

Equation 9 and Equation 10 derive from experimental and field observations on the spalling of the concrete cover in girders. An example of spalling damage is illustrated in Figure 2-2. The figure on the right indicates that for widely spaced stirrups there is non-overlapping spall damage. As the stirrup spacing becomes tighter (Figure 2-2a), spall wedges begin to interact and the entire cover area may spall (Higgins et al., 2010). Based on observed spall patterns for experimental beams and field observed damage, the angle of discrete spalls was taken as approximately 20°, originating at the intersection of the concrete core and the rebar cross-section. As the stirrup spacing becomes small, the effective concrete width approaches the core width.

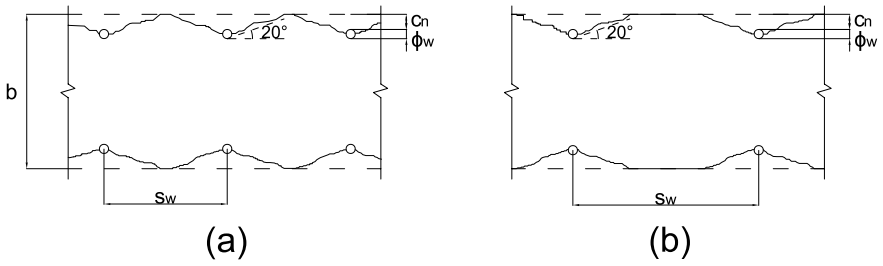


Figure 2-2: Schematic plan view of concrete spalling in a beam web due to corrosion for two different stirrup spacings. Adapted from Higgins and Farrow (2010)

The contribution of stirrups V_S is calculated as Equation 11.

$$V_S = \frac{A_w}{s_w} \cdot z_v \cdot f_{yw,corr} \cdot (\cot\theta + \cot\alpha) \sin\alpha \qquad \text{Equation 11}$$

where A_w is the initial stirrups cross section (area of the single vertical arm multiplied by the number of arms), α is the stirrups inclination to the vertical direction, θ is the inclination of the compressive stress field with respect to the longitudinal axis of the beam and is defined in Equation 12.

$$\theta = 29° + 7000 \cdot \varepsilon_x \qquad \text{Equation 12}$$

Equation 12 derives from the SMCFT.

In Equation 11 the contribution of the corrosion for the stirrups is considered only in the reduction of $f_{yw,corr}$, calculated according to Equation 5. For that reason, the initial area of the stirrups A_w is considered, as corrosion is already taken into account in the constitutive law.

Finally, the maximum shear strength related to crushing of concrete carrying the compression field, $V_{R,max}$, is defined in Equation 13.

$$V_{R,max} = k_\varepsilon \cdot f_c \cdot b_{corr} \cdot z_v \frac{\cot\theta + \cot\alpha}{1 + \cot^2\theta} \qquad \text{Equation 13}$$

where:

$$k_\varepsilon = \frac{1}{1.2 + 60 \cdot \varepsilon_1} \qquad \text{Equation 14}$$

and

$$\varepsilon_1 = \varepsilon_x + (\varepsilon_x + 0.001) \cdot \cot^2\theta \qquad \text{Equation 15}$$

In the present study, the maximum shear resistance associated with crushing of the concrete compression field, $V_{R,max}$, was consistently found to be significantly higher than the shear resistance obtained from the sum of the concrete and stirrup contributions. For this reason, this limitation does not govern any of the specimens included in the database and is therefore not explicitly represented in the flow chart of the proposed procedure. Nevertheless, the verification in Equation 6 should always be performed in practical applications, as it may become critical in members with high performance concrete.

Note that approximation level IIb is applicable only for elements where the percentage of stirrups (ρ_w) is greater than the minimum, defined in Equation 16.

$$\rho_w \geq 0.08 \cdot \frac{\sqrt{f_c}}{f_{yw}} \qquad \text{Equation 16}$$

where f_c and f_{yw} are, respectively, the concrete cylinder compressive strength and the stirrup yield strength, both taken in MPa, and considered, again, in their mean values.

In addition, one should note that the proposed model does not account for reductions in the effective depth d, and consequently z_v, due to corrosion-induced damage in the compressive zone. Indeed, spalling often occurs only at the tensile lower zone of a beam. If, on the other hand, the beam shows an extensive loss of concrete cover even at the compressed zone, it is suggested not to consider this concrete cover in the calculation of d. Figure 2-3 summarizes the solution technique adopted providing the complete flow chart.

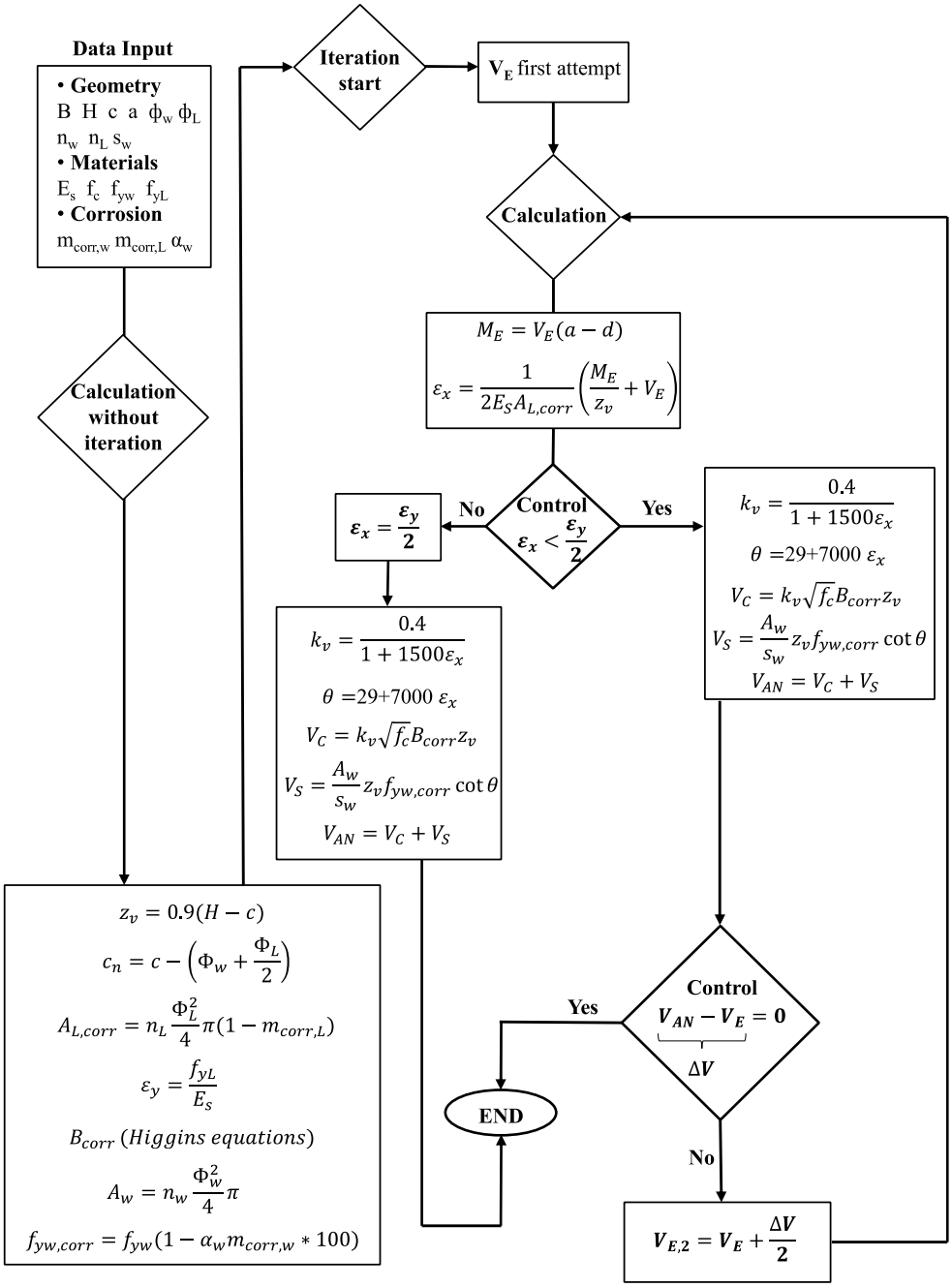


Figure 2-3: Flow chart of the proposed method.

2.3 MODEL Application - WORKED EXAMPLE

A worked example is herein illustrated concerning specimen BS15_2A tested by Di Stefano (2022). The main specimen details are summarized in the brief description below.

The specimen's section dimensions were 200 mm (b) × 500 mm (h) with a concrete cover of about 40 mm. The shear span (a) was 1.15 m. The concrete compressive cylindrical strength was 35 MPa; the yield stress of stirrups and longitudinal rebars were 524 MPa and 516 MPa respectively. Stirrups' diameter was 6 mm and the spacing 330 mm; for longitudinal reinforcement three 20 mm rebars were employed. Corrosion interested only stirrups, and the percentage of mass loss was experimentally measured as 16.6%. The uncorroded reference specimens exhibited an experimental ultimate shear resistance of approximately 162 kN.

Calculation

Beginning with the input data, the first step involves calculating the parameters that do not require iteration. Specifically, the effective shear depth and the effective concrete cover are computed as follows:

$$z_v = 0.9(H - c) = 0.9(500\ mm - 40\ mm) = 414\ mm$$

$$c_n = c - \left(\Phi_w + \frac{\Phi_L}{2}\right) = 40\ mm - \left(6\ mm + \frac{20\ mm}{2}\right) = 24\ mm$$

Since corrosion did not affect the longitudinal reinforcement in this case (i.e., $m_{corr,L} = 0$), the reduced steel area remains equal to the original value:

$$A_{L,corr} = n_L \frac{\Phi_L^2}{4}\pi\left(1 - m_{corr,L}\right) = 3\frac{(20\ mm)^2}{4}\pi(1-0) = 942.5\ mm^2$$

The yield strain of the longitudinal reinforcement is calculated as:

$$\varepsilon_y = \frac{f_{yL}}{E_s} = \frac{516\ MPa}{210000\ MPa} = 2.46\ 10^{-3}$$

For the stirrups, the yield stress is reduced to account for corrosion. Given α_w= 0.016417, the corroded yield stress becomes:

$$f_{yw,corr} = f_{yw}\left(1 - \alpha_w m_{corr,w} * 100\right) = 524\ MPa(1 - 0.016417 \cdot 0.166 \cdot 100)$$

$$= 381 MPa$$

Next, the width of the effective section is reduced using Higgins' formulation. First, verify whether the stirrup spacing exceeds the limit defined by $5.5 \cdot c_n$:

$$s_w > 5.5 \cdot c_n$$

$$330\ mm > 5.5 \cdot 24\ mm = 132\ mm$$

Since the condition is satisfied, the reduced effective width is calculated as:

$$b_{corr} = b - \frac{5.5}{s_w}(c_n + \phi_w)^2 = 200\ mm - \frac{5.5}{330\ mm}(24\ mm + 6\ mm)^2 = 185\ mm$$

Note that Higgins' equations are applicable only when the stirrup corrosion rate $m_{corr,w}$ exceeds 10%. Otherwise, the original section width b should be used.

Iterative Calculation Procedure

The iterative process begins by selecting an initial trial value for the shear force V_E, e.g., 100 kN. All dependent parameters are then computed as a function of this value, starting with the bending moment M_E and the average strain ε_x:

$$M_E = V_E(a - d) = 100\ kN(1.15\ m - 0.46\ m) = 69\ kNm$$

$$\varepsilon_x = \frac{1}{2E_S A_{L,corr}}\left(\frac{M_E}{z_v} + V_E\right) = \frac{1}{2 \cdot 210000\ MPa \cdot 942.5\ mm^2}\left(\frac{69\ kNm}{0.414\ m} + 100kN\right)$$

$$= 0.6737\ 10^{-3}$$

The value of ε_x must be lower than $\frac{\varepsilon_y}{2}$, in this case:

$$0.6737\ 10^{-3} < \frac{2.46\ 10^{-3}}{2} = 1.23\ 10^{-3}$$

If $\varepsilon_x > \frac{\varepsilon_y}{2}$, the strain is assumed as $\frac{\varepsilon_y}{2}$ and the shear strength V_{AN} is immediately defined.

With ε_x known, the shear parameters are computed:

$$k_v = \frac{0.4}{1 + 1500\varepsilon_x} = \frac{0.4}{1 + 1500 \cdot 0.000673672} = 0.19895$$

$$\theta = 29 + 7000\ \varepsilon_x = 29 + 7000 \cdot 0.000673672 = 33.7°$$

$$V_C = k_v\sqrt{f_c} b_{corr} z_v = 0.19895 \cdot \sqrt{35MPa} \cdot 185\ mm \cdot 414\ mm = 90.1\ kN$$

$$V_S = \frac{A_w}{s_w} z_v f_{yw,corr} \cot\theta = \frac{56.5\ mm^2}{330\ mm} \cdot 414\ mm \cdot 381\ MPa \cdot \cot 33.7° = 40.5\ kN$$

$$V_{AN} = V_C + V_S = 90.1\ kN + 40.5\ kN = 130.7\ kN$$

This value is compared to the trial shear force V_E. Since $V_{AN} \neq V_E$, a new estimate is made using:

$V_{E,2} = V_{E,1} + \frac{\Delta V}{2}$ where $\Delta V = V_{AN} - V_E$.

$$V_{E,2} = 100\ kN + \frac{(130.7 - 100)}{2} = 115.35\ kN$$

Final Result

The iterative procedure is repeated until the computed shear strength V_{AN} converges with V_E. The final value of the analytical shear strength is:

$V_{AN} = 120.7\ kN$

The corresponding experimental value is $V_{EXP} = 118.0\ kN$, resulting in a quite satisfactory analytical-to-experimental ratio of:

V_{AN}/V_{EXP}=1.02

2.4 MODEL VALIDATION

The proposed analytical model was applied to a curated database of experimental tests on RC beams with corroded reinforcement, primarily subjected to accelerated corrosion procedures. The dataset includes five full-scale specimens tested in Brescia and extensively described in Di Stefano (2022), along with additional data extracted from a comprehensive literature review covering over 300 corroded beam specimens. To ensure the applicability of the model, developed within the framework of the *fib* MC2020 and primarily aimed at predicting shear strength, specific filtering criteria were applied. In particular, tests involving flexural failure or beams with a shear span-to-effective depth ratio (a/d) less than 2.5 were excluded. This decision is based on the fact that the formulation assumes the activation of the "beam mechanism," which is unlikely to develop in deep beams or in members governed by strut-and-tie behaviour, typically observed for a/d < 2.5.

Additionally, although longitudinal reinforcement ratios (ρ_L) greater than 2.5% are uncommon in real structural elements, this threshold was not enforced during the selection process. Applying such a limit would have significantly reduced the size of

the dataset. As a result, 38% of the specimens included in the final database exhibit ρ_L values exceeding 2.5%. However, a sensitivity analysis confirmed that this simplification does not substantially influence the overall conclusions.

Despite most of the available tests involving small-scale specimens, these were retained in the analysis as long as they satisfied the other inclusion criteria. Full-scale experimental data on corroded RC beams remain scarce, making small-scale testing a practical necessity in the current research landscape.

Based on the above filtering criteria, the following constraints were applied:

- Shear failure as the dominant failure mode
- Shear span-to-depth ratio $a/d > 2.5$
- (Optional) Longitudinal reinforcement ratio $\rho_L < 2.5\%$ (not enforced)

After applying these conditions, the final database comprises 108 specimens drawn from ten key studies (Alaskar 2013; Di Stefano 2022; El-Sayed, Hussain, and Shuraim 2016; Han et al. 2019; Lu et al. 2019; Rodriguez, Ortega, and Casal 1997; Wang and Liu 2004; Xue, Seki, and Chen 2013; Xue, Seki, and Song 2014; Zhao and Jin 2012). These selected cases offer a representative cross-section of shear behaviour in beams with varying degrees and patterns of corrosion.

2.5 Corrosion Definition

For each study examined, the details concerning the corrosion ratio are presented below, with explicit reference to the values reported in the source publication and those employed in the present analytical formulation.

2.5.1.RODRIGUEZ ET AL. (1997)

Corrosion is herein estimated from the given parameter "attack penetration" x. Note that, in the paper, attack penetration is given both as an average value through gravimetric method and as a maximum value through geometric measurements. For the calculation, the average value of corrosion was considered, calculated as follows (Equation 17).

$$1 - \left(\frac{\phi_w - 2x}{\phi_w}\right)^2 \qquad \text{Equation 17}$$

The hypothesis for corrosion distribution in the section was therefore the one in Figure 2-4a (Biondini and Vergani, 2012).

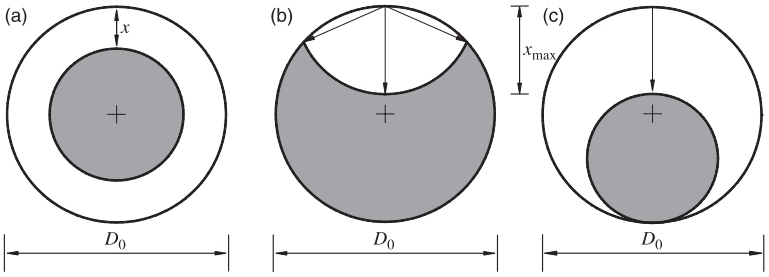


Figure 2-4: Corrosion distribution along the considered section (Biondini and Vergani, 2012)

2.5.2. ZHAO AND JIN (2012)

The original article is in Chinese language, so the data were extrapolated from the previous database of Cladera et al. (2021). In the paper, the section loss ratio is given, so the weight loss ratio was obtained dividing the first for the constant value 1.36, due to Equation 18 employed in Cladera et al. (2021), simplification of Lu e al. (2018).

$$\eta_{sn} = 1.36\eta_{wt} \qquad \text{Equation 18}$$

Where:

η_{sn} is the section loss ratio

η_{wt} is the weight loss ratio

2.5.3. WANG ET AL. (2011)

The authors reported average weight and maximum cross section loss of the longitudinal rebars and the stirrups. They divide the longitudinal reinforcement in 3 specimens called Lc1, Lc2 and Lcm, then the average value was calculated. For the

stirrups they show the value of three different stirrups, then again, the average value among all the stirrups.

For the calculations, the average value of mass loss ratio calculated among the three specimens was employed for the longitudinal reinforcement, while for stirrups the value of mass loss ratio of the broken stirrup was taken into account.

2.5.4. ALASKAR (2013)

15 beams were tested in the paper. However, 3 of them were strengthened before the load test, so only 12 beams are considered in the database. The beams are subdivided into four typologies (A, B, C, D): for typologies A, B and C four stirrups are corroded, while 8 in type D.

For the calculations, the average value of the mass loss ratio of the stirrups of each beam was calculated and provided.

2.5.5. XUE ET AL. (2013)

Corrosion is induced just in the longitudinal rebars. In the paper, both the average mass loss ratio (PAM) and the maximum local mass loss (PMM) are provided. During the calculations the first aforementioned value was employed for all the tested beams.

2.5.6. XUE ET AL. (2014)

In this case corrosion was induced just in stirrups and the evaluation of the corrosion levels is presented in using two typologies of index: the average mass loss ratio (PAM) and the maximum local mass loss (PMM), estimated from the differences between the yield stress of the original stirrups and the corroded ones, using Equation 19.

$$PMM = \frac{f_y - f_{y,corr}}{f_y} \qquad \text{Equation 19}$$

In the calculation the PAM value was employed, to provide a better coherence between the experimental data. In fact, in all the article the calculation method of the mass loss ratio is the same and it is performed accordingly to the ASTM standard (ASTM-C876-09), while the calculation of the maximum local corrosion ratio is calculated in widely different ways.

2.5.7. EL-SAYED ET AL. (2016)

The mass loss for each beam was determined based on the average mass loss ratio of the shear reinforcement in the failure region.

2.5.8.HAN ET AL. (2019)

Only longitudinal reinforcement was corroded, and the results are presented in terms of average mass loss ratio among the two longitudinal rebars. Corrosion values are all lower than 10%.

2.5.9.LU ET AL. (2019)

The minimum diameter of each segment was measured, and then its cross-sectional loss was calculated using the minimum remaining diameter and uncorroded bars' diameter. Since there may be some differences in the corrosion levels of reinforcement bars in different regions in the same RC beam, the average value of the localized minimum remaining areas of all the reinforcement bar segments from stirrups or longitudinal bars were used to represent the corrosion degree of the RC beam, namely, the average cross-sectional loss ratio.

For the calculations, those values were divided by 1.36 to obtain the average mass loss ratio, according to Equation 18.

2.5.10. DI STEFANO (2022)

The average mass loss ratio for stirrups and, just in one case for longitudinal rebars and was evaluated according to ASTM standard. For each test, two stirrups were corroded and the mean value of mass loss ratio was calculated on the four vertical arms. Finally, the mass loss of the longitudinal rebars was assessed based on three

representative specimens, each corresponding to a distinct rebar position within the cross-section.

2.6 Results of the Validation

About the whole database, control specimens, i.e., beams without corrosion, were also included for benchmarking purposes. Of the entire database, 76% of the specimens were corroded. Within this subset:

- 29% exhibited corrosion in both longitudinal and transverse reinforcement, a condition that closely resembles field-exposed structures;
- 40% exhibited corrosion only in the stirrups, which is consistent with the fact that corrosion generally initiates in the outermost elements;
- 7% exhibited corrosion only in the longitudinal reinforcement, a scenario less commonly encountered in practice.

A summary of the key geometric and material parameters of the final dataset is presented in Table 2-2, including their minimum and maximum values across the database.

	Minimum value	**Maximum value**
$\boldsymbol{f_c}$ **[MPa]**	21	56
$\boldsymbol{\rho_L}$**[%]**	1	4
$\boldsymbol{\rho_w}$ **[%]**	0.1	0.6

$\boldsymbol{a/d}$	2.5	4.57
d **[mm]**	149	460
$\boldsymbol{m_{corr,w}}$ **[%]**	0.4	44.2
$\boldsymbol{m_{corr,L}}$ **[%]**	1.1	26.2

Table 2-2: Database Characterisation.

While the values of key parameters such as f_c, ρ_w and a/d align well with the objectives of this study, it is important to acknowledge that the small dimensions of many specimens are not fully representative of real-world structural elements. In fact, the largest effective depth d in the database is 460 mm, corresponding to the full-scale tests conducted by Di Stefano et al. (2022). Excluding this case, the maximum effective depth in the remaining specimens is approximately 325 mm. Given that corrosion is a critical concern in exposed infrastructure such as bridge girders, it is essential to expand future datasets with additional full-scale specimens.

The results of the model application to the 108 selected experimental specimens are presented in Tables 3 through 6. These tables report only the material properties and geometric characteristics necessary for the implementation of the proposed analytical formulation. For additional test-specific information, the reader is referred to the original publications.

In Tables 3 to 6, the first columns list the source authors and the identifiers of each specimen. The subsequent parameters are defined as follows:

- a/d: shear span-to-effective depth ratio;
- ρ_L: longitudinal reinforcement ratio, uncorrected for corrosion;
- Φ_w: stirrup diameter, which aligns with the calibration of the degradation coefficient α_w, based on 8 mm bars;
- ρ_w: transverse reinforcement ratio, uncorrected for corrosion;
- f_c: cylindrical compressive strength of concrete;

Additional variables reported include:

- b_{corr} : width of the section reduced due to corrosion;
- z_v : effective shear depth;
- $A_{L,corr}$: area of longitudinal reinforcement corrected for corrosion;
- ε_x: average longitudinal strain;
- $\frac{\varepsilon_y}{2}$: critical strain limit, equal to half the yield strain.

The strain limit was reached in only three specimens, identifiable in the tables where $\varepsilon_x = \frac{\varepsilon_y}{2}$. In all other cases (97% of the dataset), the predicted failure mode remained consistent with the experimentally observed shear failure. In only three cases did the model predict a flexural-type failure, resulting in shear strength governed by bending moment capacity.

Other model parameters such as k_v, V_C, θ, $f_{yw,corr}$, V_S, are computed as described in Section 2. The experimentally measured shear capacity is reported as V_{EXP}, and the final columns provide the analytically predicted values V_{AN} and the ratio V_{AN}/V_{EXP}.

It should be noted that the maximum concrete shear strength due to compression field crushing, $V_{R,max}$, is not reported in these tables, as this value was consistently greater than V_{AN} for all specimens.

Finally, the bottom rows of Table 2-6 present summary statistics for each group of specimens, including the mean value of $\frac{V_{AN}}{V_{EXP}}$, the standard deviation, and the coefficient of variation (CoV). These statistics are reported both for the full dataset and for the subset of corroded specimens.

Authors	Specimen Name	a/d	ρ_L	φ_w [mm]	ρ_w	f_c [MPa]	$m_{corr,w}$ [%]	$m_{corr,L}$ [%]	B_{corr} [cm]	z_t [cm]	$A_{L,corr}$ [mm^2]	ε_s	$\varepsilon_y/2$	$\rho_{w,min}$ [%]	k_v	V_C [kN]	ϑ [°]	$f_{yw,corr}$ [MPa]	V_S [kN]	V_{AN} [kN]	V_{EXP} [kN]	V_{ANI}/V_{EXP}
Rodriguez et al. 1997	123	4,57	1,7%	6	0,2%	35	24,3%	11,3%	13,8	15,8	401	0,00131	0,00146	0,076%	0,135	17,4	38,2	376	25,1	42,4	37	1,14
Rodriguez et al.	124	4,57	1,7%	6	0,2%	35	30,0%	13,2%	13,8	15,8	393	0,00125	0,00146	0,076%	0,139	17,9	37,7	318	21,5	39,5	28	1,41
Rodriguez et al.	125	4,57	1,7%	6	0,2%	35	32,2%	12,9%	13,8	15,8	394	0,00121	0,00146	0,076%	0,142	18,3	37,5	295	20,2	38,4	31	1,22
Rodriguez et al.	131	4,57	1,7%	6	0,2%	52	0,0%	0,0%	15,0	15,8	452	0,00146	0,00146	0,092%	0,125	21,3	39,2	626	40,2	61,5	50	1,23
Rodriguez et al.	132	4,57	1,7%	6	0,2%	52	0,0%	0,0%	15,0	15,8	452	0,00146	0,00146	0,092%	0,125	21,3	39,2	626	40,2	61,5	53	1,16
Rodriguez et al.	134	4,57	1,7%	6	0,2%	37	21,4%	10,4%	13,8	15,8	405	0,00136	0,00146	0,078%	0,132	17,5	38,5	406	26,8	44,2	35	1,28
Rodriguez et al.	133	4,57	1,7%	6	0,2%	37	22,6%	11,3%	13,8	15,8	401	0,00135	0,00146	0,078%	0,132	17,5	38,4	394	26,0	43,6	35	1,26
Rodriguez et al.	136	4,57	1,7%	6	0,2%	37	30,6%	12,9%	13,8	15,8	394	0,00125	0,00146	0,078%	0,139	18,5	37,7	312	21,1	39,6	29	1,36
Rodriguez et al.	135	4,57	1,7%	6	0,2%	37	32,2%	12,6%	13,8	15,8	395	0,00122	0,00146	0,078%	0,141	18,7	37,5	295	20,1	38,8	34	1,15
Rodriguez et al.	215	4,57	1,7%	6	0,2%	35	23,1%	12,0%	13,8	15,8	398	0,00134	0,00146	0,076%	0,133	17,2	38,4	388	25,7	42,9	39	1,11
Rodriguez et al.	216	4,57	1,7%	6	0,2%	35	27,2%	10,1%	13,8	15,8	407	0,00126	0,00146	0,076%	0,138	17,8	37,8	347	23,4	41,2	36	1,14
Rodriguez et al.	213	4,57	1,7%	6	0,2%	35	31,7%	13,8%	13,8	15,8	390	0,00123	0,00146	0,076%	0,141	18,1	37,6	301	20,4	38,6	27	1,45
Rodriguez et al.	214	4,57	1,7%	6	0,2%	35	37,6%	16,9%	13,8	15,8	376	0,00117	0,00146	0,076%	0,145	18,7	37,2	240	16,6	35,3	29	1,23
Rodriguez et al.	315	4,57	1,7%	6	0,4%	37	37,6%	16,3%	12,7	15,8	379	0,00146	0,00146	0,078%	0,125	15,3	39,2	240	30,8	46,0	28	1,66
																					Mean	1,27
																					St. Dev.	0,15
																					CoV	12%
Zhao et al. 2009	1-0	3,10	2,8%	6	0,3%	21	0,0%	0,0%	15,0	13,5	628	0,00060	0,00092	0,110%	0,210	19,5	33,2	332	25,8	45,3	40	1,13
Zhao et al.	1-1	3,10	2,8%	6	0,3%	21	0,4%	0,0%	15,0	13,5	628	0,00060	0,00092	0,110%	0,211	19,5	33,2	330	25,6	45,2	40	1,13
Zhao et al.	1-2	3,10	2,8%	6	0,3%	21	1,3%	0,0%	15,0	13,5	628	0,00060	0,00092	0,110%	0,211	19,6	33,2	325	25,3	44,9	40	1,12
Zhao et al.	1-3	3,10	2,8%	6	0,3%	21	1,8%	0,0%	15,0	13,5	628	0,00059	0,00092	0,110%	0,212	19,6	33,2	322	25,1	44,7	48	0,93
Zhao et al.	1-4	3,10	2,8%	6	0,3%	21	2,4%	0,0%	15,0	13,5	628	0,00059	0,00092	0,110%	0,212	19,7	33,1	319	24,9	44,5	50	0,89
Zhao et al.	1-5	3,10	2,8%	6	0,3%	21	2,9%	0,0%	15,0	13,5	628	0,00059	0,00092	0,110%	0,212	19,7	33,1	316	24,6	44,4	46	0,96
Zhao et al.	2-0	3,10	2,8%	6	0,4%	21	0,0%	0,0%	15,0	13,5	628	0,00073	0,00092	0,110%	0,191	17,7	34,1	332	37,4	55,1	48	1,15
Zhao et al.	2-1	3,10	2,8%	6	0,4%	21	0,3%	0,0%	15,0	13,5	628	0,00073	0,00092	0,110%	0,191	17,7	34,1	330	37,2	55,0	42	1,31
Zhao et al.	2-2	3,10	2,8%	6	0,4%	21	0,5%	0,0%	15,0	13,5	628	0,00073	0,00092	0,110%	0,191	17,7	34,1	329	37,1	54,9	40	1,37
Zhao et al.	2-3	3,10	2,8%	6	0,4%	21	1,6%	0,0%	15,0	13,5	628	0,00072	0,00092	0,110%	0,192	17,8	34,0	323	36,5	54,3	44	1,23
Zhao et al.	2-4	3,10	2,8%	6	0,4%	21	2,6%	0,0%	15,0	13,5	628	0,00072	0,00092	0,110%	0,193	17,9	34,0	318	36,0	53,9	42	1,28
Zhao et al.	2-5	3,10	2,8%	6	0,4%	21	3,6%	0,0%	15,0	13,5	628	0,00071	0,00092	0,110%	0,194	18,0	34,0	312	35,4	53,4	52	1,03
Zhao et al.	3-0	3,10	2,8%	8	0,4%	21	0,0%	0,0%	15,0	13,5	628	0,00080	0,00092	0,110%	0,182	16,9	34,6	332	43,5	60,4	36	1,68
Zhao et al.	3-1	3,10	2,8%	8	0,4%	21	0,6%	0,0%	15,0	13,5	628	0,00080	0,00092	0,110%	0,182	16,9	34,6	329	43,2	60,1	38	1,58
Zhao et al.	3-2	3,10	2,8%	8	0,4%	21	1,5%	0,0%	15,0	13,5	628	0,00079	0,00092	0,110%	0,183	17,0	34,5	325	42,7	59,7	48	1,24
Zhao et al.	3-3	3,10	2,8%	8	0,4%	21	2,8%	0,0%	15,0	13,5	628	0,00078	0,00092	0,110%	0,184	17,1	34,5	319	42,0	59,0	40	1,48
Zhao et al.	3-4	3,10	2,8%	8	0,4%	21	2,8%	0,0%	15,0	13,5	628	0,00078	0,00092	0,110%	0,184	17,1	34,5	319	42,0	59,0	46	1,28
Zhao et al.	3-5	3,10	2,8%	8	0,4%	21	2,8%	0,0%	15,0	13,5	628	0,00078	0,00092	0,110%	0,184	17,1	34,5	319	42,0	59,0	46	1,28
																					Mean	1,23
																					St. Dev.	0,21
																					CoV	17%

Table 2-3 - Pt. (1 of 4): Application of the method to 108 samples.

Authors	Specimen Name	a/d	ρ_L	ϕ_w [mm]	ρ_w	f_c [MPa]	$m_{corr,w}$ [%]	$m_{corr,l}$ [%]	B_{corr} [cm]	z_r [cm]	$A_{L,corr}$ [mm^2]	ε_x	$\varepsilon_y/2$	$\rho_{w,min}$ [%]	K_v	V_C [kN]	ϑ [°]	$f_{yw,corr}$ [MPa]	V_S [kN]	V_{AN} [kN]	V_{EXP} [kN]	V_{AN}/V_{EXP}
Wang et al. 2011	BC3.0	3.00	2.4%	6	0.2%	46	0.0%	0.0%	16.1	14.0	603	0.00073	0.00088	0.123%	0.191	29.1	34.1	442	25.7	54.8	61	0.90
Wang et al.	B3.0-300-10	3.00	2.5%	6	0.2%	32	24.9%	5.7%	14.8	13.9	569	0.00057	0.00086	0.102%	0.215	24.8	33.0	261	15.7	40.5	57	0.71
Wang et al.	B3.0-300-25	3.00	2.5%	6	0.2%	38	35.9%	24.8%	14.7	13.9	454	0.00064	0.00086	0.112%	0.203	25.6	33.5	181	10.7	36.3	58	0.62
Wang et al.	B3.0-450-0	3.00	2.6%	6	0.2%	40	0.0%	0.0%	15.4	13.4	603	0.00068	0.00087	0.114%	0.198	25.8	33.8	442	25.0	50.9	59	0.86
Wang et al.	B3.0-450-10	3.00	2.6%	6	0.2%	37	26.2%	9.5%	13.9	13.4	546	0.00058	0.00086	0.110%	0.215	24.4	33.0	252	14.7	39.1	58	0.68
Wang et al.	B3.0-450-25	3.00	2.5%	6	0.2%	39	38.9%	26.2%	15.1	13.6	445	0.00064	0.00086	0.113%	0.204	26.1	33.5	160	9.3	35.4	58	0.61
																				Mean		0.73
																				St. Dev.		0.12
																				CoV		17%
Alaskar 2013	10M-0%-UR	3.07	4.0%	11	0.5%	38	0.0%	0.0%	20.0	26.9	2402	0.00075	0.00120	0.123%	0.189	62.6	34.2	400	158.6	221.2	225	0.98
Alaskar	10M-7.5%-UR	3.07	4.0%	11	0.5%	44	9.9%	0.0%	20.0	26.9	2402	0.00070	0.00120	0.133%	0.195	69.7	33.9	343	137.8	207.4	206	1.01
Alaskar	10M-15%-UR	3.07	4.0%	11	0.5%	44	15.6%	0.0%	16.4	26.9	2402	0.00063	0.00120	0.133%	0.206	60.1	33.4	310	126.9	187.0	193	0.97
Alaskar	D12-0%-UR	3.08	4.0%	13	0.6%	38	0.0%	0.0%	20.0	26.8	2402	0.00083	0.00120	0.130%	0.179	58.9	34.8	380	185.4	244.3	206	1.19
Alaskar	D12-7.5%-UR	3.08	4.0%	13	0.6%	44	8.0%	0.0%	20.0	26.8	2402	0.00078	0.00120	0.140%	0.184	65.3	34.5	336	166.0	231.3	238	0.97
Alaskar	D12-15%-UR	3.08	4.0%	13	0.6%	44	15.0%	0.0%	16.1	26.8	2402	0.00070	0.00120	0.140%	0.195	55.8	33.9	298	150.6	206.4	185	1.12
Alaskar	D6-0%-UR	3.02	4.0%	6	0.2%	38	0.0%	0.0%	20.0	27.3	2402	0.00044	0.00120	0.130%	0.241	81.0	32.1	380	52.4	133.5	127	1.06
Alaskar	D6-7.5%-UR	3.02	4.0%	6	0.2%	44	1.2%	0.0%	20.0	27.3	2402	0.00046	0.00120	0.140%	0.238	86.2	32.2	373	51.2	137.4	165	0.83
Alaskar	D6-15%-UR	3.02	4.0%	6	0.2%	44	3.7%	0.0%	20.0	27.3	2402	0.00045	0.00120	0.140%	0.239	86.6	32.1	357	49.2	135.8	153	0.89
Alaskar	D6-0%-UR-100	3.02	4.0%	6	0.3%	38	0.0%	0.0%	20.0	27.3	2402	0.00057	0.00120	0.130%	0.215	72.4	33.0	380	101.2	173.6	168	1.04
Alaskar	D6-7.5%-UR-100	3.02	4.0%	6	0.3%	44	1.0%	0.0%	20.0	27.3	2402	0.00058	0.00120	0.140%	0.213	77.3	33.1	374	99.3	176.6	191	0.92
Alaskar	D6-15%-UR-100	3.02	4.0%	6	0.3%	44	2.9%	0.0%	20.0	27.3	2402	0.00058	0.00120	0.140%	0.214	77.8	33.0	362	96.3	174.1	226	0.77
																				Mean		0.98
																				St. Dev.		0.12
																				CoV		12%
Xue et al. 2013	B(2.6)-ms	2.64	2.2%	6	0.4%	33	0.0%	0.0%	12.0	19.8	574	0.00082	0.00177	0.153%	0.179	24.5	34.8	300	42.7	67.1	74	0.91
Xue et al.	B(2.6)-m1s	2.64	2.2%	6	0.4%	35	0.0%	3.1%	12.0	19.8	556	0.00085	0.00177	0.158%	0.176	24.7	35.0	300	42.4	67.1	77	0.87
Xue et al.	B(2.6)-m2s	2.64	2.2%	6	0.4%	36	0.0%	18.4%	12.0	19.8	468	0.00097	0.00177	0.160%	0.163	23.2	35.8	300	41.1	64.4	82	0.78
Xue et al.	B(3.2)-ms	3.18	2.2%	6	0.4%	35	0.0%	0.0%	12.0	19.8	574	0.00096	0.00177	0.158%	0.164	23.1	35.7	300	41.2	64.3	71	0.91
Xue et al.	B(3.2)-m1s	3.18	2.2%	6	0.4%	35	0.0%	5.0%	12.0	19.8	545	0.00099	0.00177	0.158%	0.160	22.5	36.0	300	40.8	63.4	71	0.90
Xue et al.	B(3.2)-m2s	3.18	2.2%	6	0.4%	33	0.0%	6.0%	12.0	19.8	540	0.00100	0.00177	0.154%	0.160	22.0	36.0	300	40.8	62.8	72	0.88
																				Mean		0.87
																				St. Dev.		0.04
																				CoV		5%

Table 2-4 - Pt. (2 of 4): Application of the method to 108 samples.

Authors	Specimen Name	a/d	ρ_L	φ_w [mm]	ρ_w	f_c [MPa]	$m_{corr,w}$ [%]	$m_{corr,L}$ [%]	B_{corr} [cm]	z_v [cm]	$A_{L,corr}$ [mm^2]	ε_x	$\varepsilon_y/2$	$\rho_{w,min}$ [%]	K_v	V_C [kN]	ϑ [°]	$f_{yw,corr}$ [MPa]	V_S [kN]	V_{AN} [kN]	V_{EXP} [kN]	V_{AN}/V_{EXP}
Xue et al. 2014	B(39)-s0	2,64	2,2%	6	0,4%	33	0,0%	0,0%	12,0	19,8	574	0,00080	0,00177	0,153%	0,182	24,8	34,6	300	40,6	65,4	74	0,88
Xue et al.	B(39)-s1	2,64	2,2%	6	0,4%	34	5,6%	0,0%	12,0	19,8	574	0,00077	0,00177	0,156%	0,185	25,8	34,4	272	37,1	62,9	72	0,87
Xue et al.	B(39)-s2	2,64	2,2%	6	0,4%	34	8,3%	0,0%	12,0	19,8	574	0,00075	0,00177	0,155%	0,188	26,0	34,3	259	35,5	61,4	74	0,83
Xue et al.	B(39)-s3	2,64	2,2%	6	0,4%	35	14,0%	0,0%	11,5	19,8	574	0,00071	0,00177	0,157%	0,194	25,9	34,0	231	32,0	57,9	69	0,83
Xue et al.	B(39)-s4	2,64	2,2%	6	0,4%	35	16,3%	0,0%	11,5	19,8	574	0,00070	0,00177	0,158%	0,195	26,4	33,9	220	30,5	56,9	70	0,81
Xue et al.	B(39)-s5	2,64	2,2%	6	0,4%	35	19,3%	0,0%	11,5	19,8	574	0,00068	0,00177	0,158%	0,198	26,7	33,8	205	28,6	55,3	69	0,80
Xue et al.	B(39)-sa	2,64	2,2%	6	0,4%	33	0,0%	0,0%	12,0	19,8	574	0,00080	0,00177	0,153%	0,182	24,8	34,6	300	40,6	65,4	70	0,93
Xue et al.	B(39)-sb	2,64	2,2%	6	0,4%	33	0,0%	0,0%	12,0	19,8	574	0,00080	0,00177	0,153%	0,182	24,8	34,6	300	40,6	65,4	63	1,04
Xue et al.	B(52)-s0	2,64	2,2%	6	0,5%	33	0,0%	0,0%	12,0	19,8	574	0,00092	0,00177	0,153%	0,168	22,9	35,5	300	52,4	75,3	84	0,90
Xue et al.	B(52)-s1	2,64	2,2%	6	0,5%	35	5,5%	0,0%	12,0	19,8	574	0,00089	0,00177	0,158%	0,172	24,1	35,2	273	48,1	72,2	88	0,82
Xue et al.	B(52)-s2	2,64	2,2%	6	0,5%	35	9,1%	0,0%	12,0	19,8	574	0,00086	0,00177	0,157%	0,175	24,5	35,0	255	45,3	69,8	81	0,87
Xue et al.	B(52)-s3	2,64	2,2%	6	0,5%	34	13,4%	0,0%	11,3	19,8	574	0,00081	0,00177	0,155%	0,181	23,6	34,7	234	42,1	65,8	72	0,91
Xue et al.	B(52)-s4	2,64	2,2%	6	0,5%	35	0,0%	0,0%	12,0	19,8	574	0,00093	0,00177	0,158%	0,167	23,5	35,5	300	52,3	75,8	56	1,35
																					Mean	0,91
																					St. Dev.	0,15
																					CoV	16%

Authors	Specimen Name	a/d	ρ_L	φ_w [mm]	ρ_w	f_c [MPa]	$m_{corr,w}$ [%]	$m_{corr,L}$ [%]	B_{corr} [cm]	z_v [cm]	$A_{L,corr}$ [mm^2]	ε_x	$\varepsilon_y/2$	$\rho_{w,min}$ [%]	K_v	V_C [kN]	ϑ [°]	$f_{yw,corr}$ [MPa]	V_S [kN]	V_{AN} [kN]	V_{EXP} [kN]	V_{AN}/V_{EXP}
El-Sayed et al. 2016	B0-200	2,77	3,0%	8	0,3%	35	0,0%	0,0%	20,0	29,3	1963	0,00067	0,00120	0,096%	0,199	69,0	33,7	495	109,1	178,1	142	1,25
El-Sayed et al.	B10-200	2,77	3,0%	8	0,3%	35	7,2%	0,0%	20,0	29,3	1963	0,00064	0,00120	0,095%	0,204	70,6	33,5	444	98,7	169,3	157	1,08
El-Sayed et al.	B20-200	2,77	3,0%	8	0,3%	41	17,0%	0,0%	19,6	29,3	1963	0,00061	0,00120	0,103%	0,210	76,5	33,2	374	84,0	160,5	136	1,18
El-Sayed et al.	B0-150	2,77	3,0%	8	0,3%	28	0,0%	0,0%	20,0	29,3	1963	0,00076	0,00120	0,086%	0,187	58,4	34,3	495	142,2	200,6	166	1,21
El-Sayed et al.	B10-150	2,77	3,0%	8	0,3%	35	10,3%	0,0%	19,4	29,3	1963	0,00071	0,00120	0,095%	0,194	64,8	34,0	422	122,8	187,6	166	1,13
El-Sayed et al.	B20-150	2,77	3,0%	8	0,3%	41	16,8%	0,0%	19,4	29,3	1963	0,00069	0,00120	0,103%	0,197	71,6	33,8	376	110,0	181,7	173	1,05
El-Sayed et al.	B0-100	2,77	3,0%	8	0,5%	37	0,0%	0,0%	20,0	29,3	1963	0,00098	0,00120	0,098%	0,162	57,6	35,8	495	201,5	259,1	194	1,34
El-Sayed et al.	B10-100	2,77	3,0%	8	0,5%	44	9,0%	0,0%	20,0	29,3	1963	0,00092	0,00120	0,108%	0,168	65,5	35,4	431	178,1	243,6	204	1,19
El-Sayed et al.	B20-100	2,77	3,0%	8	0,5%	44	18,0%	0,0%	19,1	29,3	1963	0,00083	0,00120	0,107%	0,178	66,0	34,8	367	155,1	221,1	173	1,28
																					Mean	1,19
																					St. Dev.	0,09
																					CoV	8%

Authors	Specimen Name	a/d	ρ_L	φ_w [mm]	ρ_w	f_c [MPa]	$m_{corr,w}$ [%]	$m_{corr,L}$ [%]	B_{corr} [cm]	z_v [cm]	$A_{L,corr}$ [mm^2]	ε_x	$\varepsilon_y/2$	$\rho_{w,min}$ [%]	K_v	V_C [kN]	ϑ [°]	$f_{yw,corr}$ [MPa]	V_S [kN]	V_{AN} [kN]	V_{EXP} [kN]	V_{AN}/V_{EXP}
Han et al. 2019	TS-0	2,86	2,3%	10	0,5%	56	0,0%	0,0%	17,0	18,9	839	0,00124	0,00159	0,112%	0,140	33,7	37,7	534	102,5	136,2	119	1,14
Han et al.	TS-3	2,86	2,3%	10	0,5%	56	0,0%	1,1%	17,0	18,9	829	0,00125	0,00159	0,112%	0,139	33,5	37,8	534	102,3	135,8	141	0,96
Han et al.	TS-8	2,86	2,3%	10	0,5%	56	0,0%	4,1%	17,0	18,9	804	0,00128	0,00159	0,112%	0,137	33,0	38,0	534	101,6	134,6	106	1,27
Han et al.	TH-0	2,86	2,3%	10	0,5%	56	0,0%	0,0%	17,0	18,9	839	0,00124	0,00159	0,112%	0,140	33,7	37,7	534	102,5	136,2	99	1,38
Han et al.	TH-3	2,86	2,3%	10	0,5%	56	0,0%	1,6%	17,0	18,9	825	0,00126	0,00159	0,112%	0,139	33,4	37,8	534	102,2	135,6	118	1,15
Han et al.	TH-8	2,86	2,3%	10	0,5%	56	0,0%	4,6%	17,0	18,9	800	0,00129	0,00159	0,112%	0,137	32,9	38,0	534	101,4	134,4	114	1,18
																					Mean	1,18
																					St. Dev.	0,14
																					CoV	12%

Table 2-5 - Pt. (3 of 4): Application of the method to 108 samples.

Authors	Specimen Name	a/d	ρ_L	φ_w [mm]	ρ_w	f_c [MPa]	$m_{corr,w}$ [%]	$m_{corr,l}$ [%]	B_{corr} [cm]	z_r [cm]	$A_{L,corr}$ [mm^2]	ε_x	$\varepsilon_y/2$	$\rho_{w,min}$ [%]	K_ν	V_C [kN]	ϑ [°]	$f_{yw,corr}$ [MPa]	V_S [kN]	V_{AN} [kN]	V_{EXP} [kN]	V_{Ad}/V_{EXP}
Lu et al. 2019	A-2	2,50	2,1%	6	0,1%	34	5,6%	1,3%	20,0	24,3	1125	0,00055	0,00098	0,137%	0,219	62,0	32,9	308	32,8	94,7	138	0,69
Lu et al.	A-3	3,00	2,1%	8	0,2%	34	34,2%	12,1%	19,2	24,3	1002	0,00065	0,00098	0,125%	0,202	54,9	33,6	190	28,0	82,8	120	0,69
Lu et al.	A-4	3,50	2,1%	8	0,3%	34	32,6%	11,5%	19,0	24,3	1010	0,00078	0,00098	0,125%	0,184	49,6	34,5	199	35,4	84,9	110	0,77
Lu et al.	A-6	2,50	2,1%	6	0,1%	34	0,0%	0,0%	20,0	24,3	1140	0,00061	0,00098	0,102%	0,208	58,9	33,3	458	47,9	106,9	139	0,77
Lu et al.	A-7	3,00	2,1%	8	0,2%	34	44,2%	16,7%	19,2	24,3	950	0,00065	0,00098	0,108%	0,202	55,0	33,6	159	23,3	78,3	115	0,68
Lu et al.	A-10	2,50	2,1%	6	0,1%	34	12,9%	3,2%	19,0	24,3	1104	0,00058	0,00098	0,098%	0,215	57,7	33,0	375	39,6	97,3	112	0,87
Lu et al.	A-11	3,00	2,1%	8	0,2%	34	28,5%	9,3%	19,2	24,3	1034	0,00074	0,00098	0,089%	0,190	51,6	34,2	310	44,7	96,3	94	1,03
Lu et al.	A-12	3,50	2,1%	8	0,3%	34	30,0%	9,9%	19,0	24,3	1027	0,00088	0,00098	0,089%	0,172	46,2	35,2	298	51,7	98,0	121	0,81
Lu et al.	B-2	2,50	2,1%	6	0,1%	42	9,8%	2,4%	20,0	24,3	1114	0,00057	0,00098	0,152%	0,215	67,4	33,0	285	30,1	97,5	120	0,81
Lu et al.	B-3	3,00	2,1%	8	0,2%	42	22,4%	7,6%	19,2	24,3	1053	0,00071	0,00098	0,138%	0,193	58,2	34,0	253	36,7	94,8	126	0,75
Lu et al.	B-6	2,50	2,1%	6	0,1%	42	37,8%	10,4%	19,0	24,3	1022	0,00054	0,00098	0,113%	0,221	65,8	32,8	174	18,5	84,3	134	0,63
Lu et al.	B-7	3,00	2,1%	8	0,2%	42	32,4%	11,6%	19,2	24,3	1008	0,00072	0,00098	0,119%	0,193	57,9	34,0	232	33,5	91,5	116	0,79
Lu et al.	B-10	2,50	2,1%	6	0,1%	42	29,9%	7,8%	19,0	24,3	1052	0,00056	0,00098	0,108%	0,217	64,6	32,9	242	25,7	90,3	156	0,58
Lu et al.	B-11	3,00	2,1%	8	0,2%	42	23,8%	7,7%	19,2	24,3	1052	0,00078	0,00098	0,098%	0,184	55,3	34,5	345	49,1	104,4	110	0,95
																					Mean	0,77
																					St. Dev.	0,12
																					CoV	16%
Di Stefano et al. 2022	Control_A	2,50	1,0%	6	0,1%	35	0,0%	0,0%	20,0	41,4	942	0,00091	0,00123	0,090%	0,169	82,8	35,4	524	52,4	135,2	162	0,83
Di Stefano et al.	BS15_1A	2,50	1,0%	6	0,1%	35	24,4%	0,0%	18,5	41,4	942	0,00078	0,00123	0,090%	0,184	83,5	34,5	314	32,5	115,9	136	0,85
Di Stefano et al.	BS15_2A	2,50	1,0%	6	0,1%	35	16,6%	0,0%	18,5	41,4	942	0,00081	0,00123	0,090%	0,180	81,6	34,7	381	39,1	120,7	118	1,02
Di Stefano et al.	BS25_3A	2,50	1,0%	6	0,1%	35	39,1%	0,0%	18,5	41,4	942	0,00072	0,00123	0,090%	0,192	87,1	34,0	188	19,7	106,9	161	0,66
Di Stefano et al.	BLS15_4A	2,50	1,0%	6	0,1%	35	24,1%	4,7%	18,5	41,4	898	0,00081	0,00123	0,090%	0,181	81,9	34,7	317	32,5	114,4	100	1,14
Di Stefano et al.	Control_B	2,50	1,0%	6	0,1%	35	0,0%	0,0%	20,0	41,4	942	0,00091	0,00123	0,090%	0,169	82,8	35,4	524	52,4	135,2	128	1,06
Di Stefano et al.	BS15_1B	2,50	1,0%	6	0,1%	35	18,4%	0,0%	18,5	41,4	942	0,00081	0,00123	0,090%	0,181	82,1	34,6	366	37,6	119,6	109	1,10
Di Stefano et al.	BS15_2B	2,50	1,0%	6	0,1%	35	16,6%	0,0%	18,5	41,4	942	0,00081	0,00123	0,090%	0,180	81,6	34,7	381	39,1	120,7	181	0,67
Di Stefano et al.	BS25_3B	2,50	1,0%	6	0,1%	35	32,5%	0,0%	18,5	41,4	942	0,00075	0,00123	0,090%	0,189	85,5	34,2	244	25,5	110,9	171	0,65
Di Stefano et al.	BLS15_4B	2,50	1,0%	6	0,1%	35	17,1%	4,7%	18,5	41,4	898	0,00084	0,00123	0,090%	0,177	80,3	34,9	377	38,4	118,6	130	0,91
																					Mean	0,89
																					St. Dev.	0,19
																					CoV	21%
Only Corroded Specimens																					**Mean**	**1,00**
																					Standard Deviation	**0,25**
																					CoV	**25%**
All Specimens																					**Mean**	**1,02**
																					Standard Deviation	**0,24**
																					CoV	**23%**
Control Specimens																					**Mean**	**1,09**
																					Standard Deviation	**0,21**
																					CoV	**19%**

Table 2-6 - Pt. (4 of 4): Application of the method to 108 samples.

The performance of the proposed analytical model was evaluated using a database of 108 experimental tests on reinforced concrete beams, including both corroded and uncorroded specimens. For corroded beams, the mean ratio between the analytically predicted shear strength (V_{AN}) and the experimentally measured value (V_{EXP}) was approximately 1.00, with a standard deviation of 0.25 and a coefficient of variation (CoV) of 25%. In comparison, the CoV for the control (uncorroded) beams was lower, at approximately 19%, indicating an expected increase in variability when corrosion is introduced (see last rows of Table 2-6 and Table 2-8).

The highest $\frac{V_{AN}}{V_{EXP}}$ ratio, 1.27, was observed in specimens reported by Rodriguez et al. (1997), likely due to discrepancies in the estimation of corrosion levels, as abovementioned. Conversely, the lowest ratio of 0.75 was found in two studies (Lu et al., 2019; Wang and Liu, 2004), both involving small-scale specimens. This suggests that model reliability may be reduced when applied to beams with limited cross-sectional dimensions, such as those with 200×300 mm or 150×190 mm sections.

Table 2-7 summarizes the maximum and minimum values of the $\frac{V_{AN}}{V_{EXP}}$ ratio, standard deviation, and CoV across all studies in the database.

	Mean V_{AN}/V_{EXP}		Dev. St.		CoV	
MAX	1.27	Rodriguez et al. (1997)	0.21	Zhao and Jin (2012)	21%	Di Stefano et al. (2022)
MIN	0.75	Wang et al. (2004)	0.04	Xue et al. (2013)	5%	Xue et al. (2013)

Table 2-7: Maximum and minimum values of mean V_{AN}/V_{EXP}, St. Dev. and CoV.

Figure 2-5 illustrates the comparison between analytically calculated and experimental shear strengths for all specimens. A general alignment is observed, though deviations are more pronounced in cases of advanced corrosion or non-representative geometries.

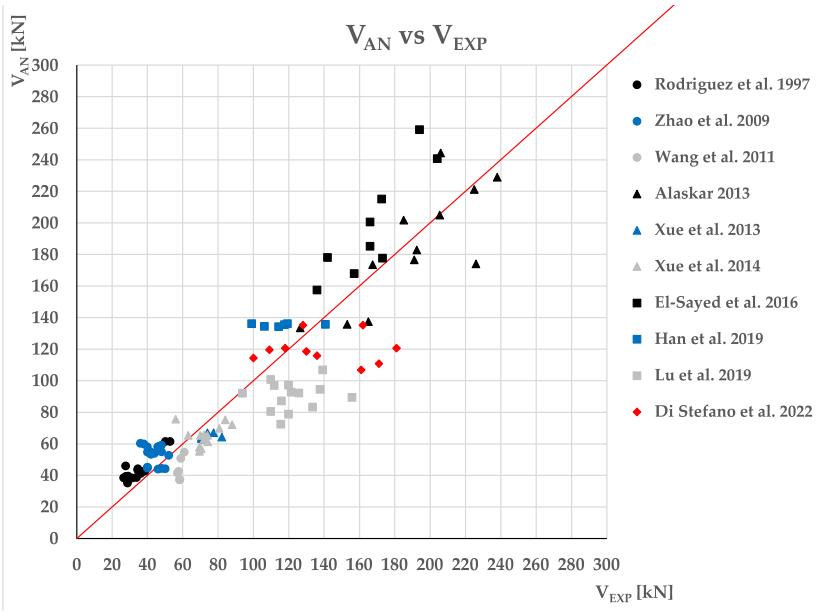


Figure 2-5: Analytical prediction vs. experimental shear strength.

Figure 2-6 and Figure 2-7 provide insights into the influence of reinforcement corrosion on model performance. In more detail, Figure 2-6 plots the $\frac{V_{AN}}{V_{EXP}}$ ratio against the average corrosion level of the stirrups. Control samples (with zero

stirrup corrosion) are excluded for clarity. It is evident that the spread of data increases with the corrosion rate, reflecting growing uncertainty. Figure 2-7 shows the same ratio as a function of the average corrosion rate in longitudinal reinforcement. Data points on the vertical axis correspond to specimens where longitudinal bars were uncorroded. A wider dispersion is again observed at higher corrosion levels.

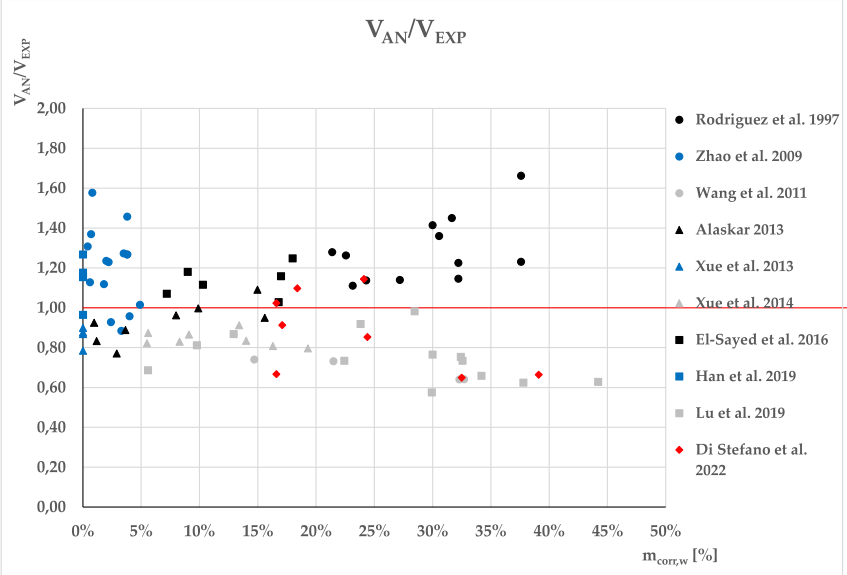


Figure 2-6: Analytical predictions vs stirrups mean corrosion rate.

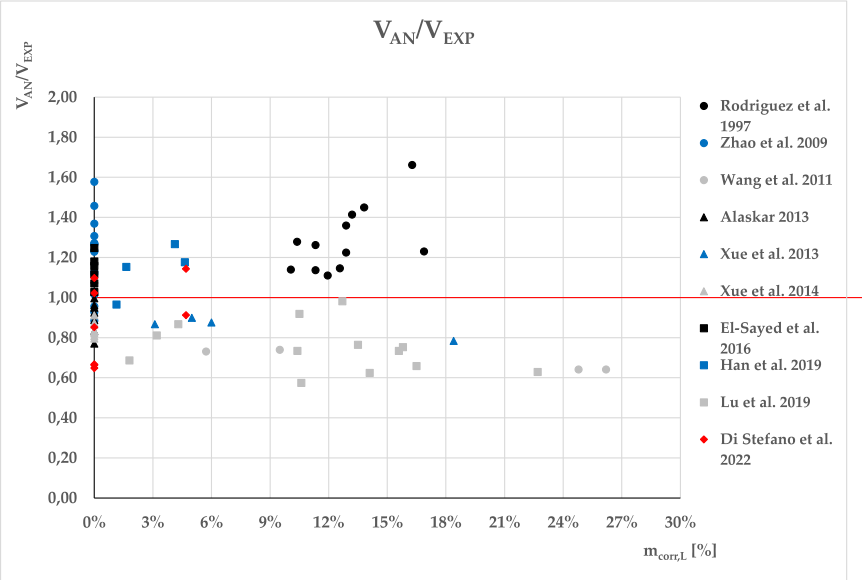


Figure 2-7: Analytical predictions vs longitudinal reinforcement mean corrosion rate.

While the overall mean of the V_{AN}/V_{EXP} ratio approaches unity, significant variability is observed across different studies. Four datasets (Rodriguez et al., 1997; Zhao et al., 2012; Han et al., 2019; El-Sayed et al., 2016) exhibit mean ratios between 1.18 and 1.27, suggesting potential overestimation by the model. In contrast, six studies (Wang and Liu, 2004; Alaskar, 2013; Xue et al., 2013 and 2014; Lu et al., 2019; Di Stefano, 2022) yielded mean ratios below 1.0, ranging from 0.75 to 0.97, indicating conservative results.

This spread is reflected in the relatively high CoV values across the database. The best-performing dataset, in terms of accuracy, was reported by Alaskar (2013) with a

mean ratio of 0.97 and CoV of 12%. The lowest CoV (5%) was observed in the study by Xue et al. (2013), with a corresponding mean value of 0.87.

Furthermore, when the model is applied exclusively to uncorroded specimens, it still shows notable variability, with an average ratio of 1.09 and a CoV of 19%. This baseline variability, independent of corrosion, suggests that shear behaviour itself inherently exhibits dispersion, even under ideal conditions, and that the model reflects this intrinsic variability.

Additionally, the limited scale of most test specimens may contribute to deviations. The experimental database predominantly includes small-scale beams that do not fully reflect the behaviour of real-world structural elements, including bridge girders, for which the MC2020 methodology is best suited. As such, the addition of more full-scale test data is strongly recommended to further validate and calibrate the model under realistic conditions.

2.7 COMPARISONS between formulations

To further assess the robustness and predictive capacity of the proposed model, a comparative analysis was conducted against the *fib* MC2020, which represents the most refined model for calculating the shear strength of reinforced concrete elements available, and four existing formulations available in the literature. While these alternative methods do not incorporate the same restrictive assumptions as the proposed model, they were nonetheless applied to the same experimental database

to ensure consistency in benchmarking. As a result, all five models, including the one presented herein, were evaluated against the same set of 108 test specimens. Detailed descriptions of the selected comparison methods can be found in the original references cited earlier.

In addition to benchmarking accuracy, the application of each method also served as a means of verifying the reliability of the database, through cross-validation with the data used by the respective authors.

2.7.1.Model Code 2020

The *fib* MC2020 represents the most refined model for calculating the shear strength of reinforced concrete elements. For uncorroded beams, it provides three possible approaches, among which Level IIb is adopted in the proposed model, modifying some parameters to account for the effects of corrosion. However, within the MC2020 document, a specific formulation is also proposed for evaluating the shear strength of corroded members with shear reinforcement, based on the Level IIa approach. While approach IIa is a plasticity-based model, approach IIb is derived from the SMCFT. Furthermore, the Level IIa approach neglects the concrete contribution to the shear strength, whereas the Level IIb approach accounts for it. Some differences are introduced in the parameters used to account for the effects of corrosion:

- The MC2020 accounts for the effect of corrosion on the stirrups' contribution by reducing their cross-sectional area, whereas in the proposed model, the

initial uncorroded area is used and the yield stress is reduced according to Imperatore et al. (2017);

- Likewise the approach adopted in the MC2020, the evaluation of the strain ε_x is performed by reducing the area of the longitudinal reinforcement, which is generally subjected to lower corrosion levels;
- The MC2020 introduces a deteriorated depth, z_{det}, reducing the concrete area of the compression stress field to account for cracking and concrete cover spalling, thereby decreasing the maximum shear strength $V_{Rd,max}$. In this study, the authors assumed this term to be undamaged, since the calculated $V_{Rd,max,det}$ was significantly higher than the analytically determined resistance for the members included in the database;
- The MC2020 also recommends considering a reduced effective width, b, as a consequence of corrosion, but does not provide a specific method for its evaluation. In the proposed model, the expression by Higgins is used to determine the corroded width $b_{w,eff}$. For consistency in the analysis of the results, these formulations were also applied when implementing the MC2020 to the considered database. However, even in this case, the effect was negligible, since $b_{w,det}$ appears only in the expression of $V_{Rd,max,det;}$
- In the MC2020, a coefficient k_{bond} is introduced in the determination of ε_x , set equal to 1 for uncorroded beams and to 0.75 for beams with corrosion of the longitudinal reinforcement lower than 5%, while no value is specified for

higher corrosion levels. The authors chose not to include this coefficient, since the influence of bond deterioration on shear capacity is still a matter of considerable debate. For low corrosion levels of the longitudinal reinforcement, confinement effects may even enhance the bond conditions. Conversely, at high corrosion levels, debonding can modify the failure mechanism, shifting it from a beam-like to an arch-like behaviour. In intermediate scenarios, corrosion could be quite detrimental on shear strength. Further studies are required to incorporate the effects of bond deterioration into the proposed formulation.

Applying the MC2020 model to the database resulted in a mean analytical-to-experimental shear strength ratio V_{AN}/V_{EXP} of 1.03 and a CoV equal to 43%. The CoV value is significantly higher than that obtained with all the other formulations, which explicitly consider both the concrete and stirrup contributions to shear strength. In addition, Coronelli (2025) concludes that, in certain cases, Level IIa appears to be overly conservative, and that the contribution of the concrete should be considered. Figure 2-8 shows the comparison between the two formulations' results, while Table 2-8 reports the mean values, standard deviation and CoV of the ratio V_{AN}/V_{EXP} for the two models, for both all specimens and for only corroded ones. The exclusion of non-corroded control specimens had no significant impact on the overall mean, standard deviation, or CoV, as highlighted in the table.

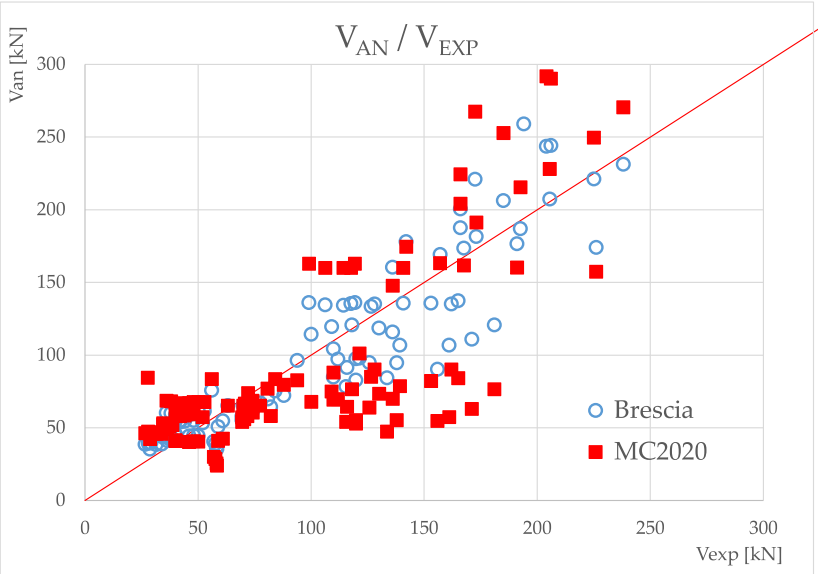


Figure 2-8: Comparison between Analytical prediction and experimental shear strength of the proposed model and the MC2020 corrosion model.

Table 2-8: Comparison of the values of the proposed model and the Model Code 2020 for Corroded specimens, Control Specimens and All Specimens.

	Corroded Specimens		**All Specimens**		**Control Specimens**	
	Proposed Model V_{AN}/V_{EXP}	**MC2020 V_{AN}/V_{EXP}**	**Proposed Model V_{AN}/V_{EXP}**	**MC2020 V_{AN}/V_{EXP}**	**Proposed Model V_{AN}/V_{EXP}**	**MC2020 V_{AN}/V_{EXP}**
Mean	**1.00**	**1.00**	**1.02**	**1.03**	**1.09**	**1.10**
St. Dev.	**0.25**	**0.47**	**0.24**	**0.44**	**0.21**	**0.35**
CoV	**25%**	**47%**	**23%**	**43%**	**19%**	**32%**

2.7.2.Rossi and Spinella (2023)

The model proposed by Rossi and Spinella is based on an iterative procedure that employs the full set of equations of the SMCFT. Its validation was carried out on a

dataset comprising 72 experimental tests, which is therefore smaller than the dataset used in the present study. In Table 2-9 the results are compared only for corroded specimens, the only ones studied by Rossi and Spinella.

The results show a satisfactory V_{AN}/V_{EXP} ratio; however, the corresponding CoV is higher than that of the newly proposed model: the value is about 28% instead of 25%.

Table 2-9: Comparison between the proposed formulation, Model Code 2020 and Rossi&Spinella (2023)

	Corroded Specimens		
	Proposed Model V_{AN}/V_{EXP}	**MC V_{AN}/V_{EXP}**	**R&S V_{AN}/V_{EXP}**
Mean	**1.00**	**1.00**	**1.02**
St. Dev.	**0.25**	**0.47**	**0.29**
CoV	**25%**	**47%**	**28%**

2.7.3.Juarez et al. (2011)

The model proposed by Juarez et al. is developed within the framework of ACI standards and it is a closed form solution, accounting for both the contribution of stirrups and concrete in the calculation of the shear strength. The formulation yielded a mean analytical-to-experimental shear strength ratio V_{AN}/V_{EXP} of 0.90. The corresponding standard deviation was 0.22, with a coefficient of variation (CoV) of 24%. These results indicate a generally conservative prediction for the current dataset. As observed with the proposed model, the relatively high CoV reflects the inherent variability of both shear behaviour and corrosion-related degradation.

2.7.4.Xu et al. (2017)

Xu et al. formulation is a closed form empirical formulation, accounting for corrosion though coefficient α_x and β (see.Table 2-10 for more details). Again, the contribution of concrete is taken into account in the shear strength calculation.

The analytical model proposed by Xu et al. produced a mean V_{AN}/V_{EXP} ratio of 0.90 as well, but with improved consistency. The standard deviation was approximately 0.17, resulting in a CoV of 19%, which is slightly lower than that of Juarez et al. This suggests a moderately better strength in predictions across the database.

2.7.5.Lu et al. (2018)

Lu formulation is an empirical formulation, that can be applied to both slender and non-slender beams. However in the present study, only the first hypothesis was considered. This is a closed form formulation, taking into account the contribution of stirrups and concrete.

The method introduced by Lu et al. (2018) generated the highest mean ratio among all evaluated models, with V_{AN}/V_{EXP}=1.45. Although the CoV remained comparable at 19%, the elevated mean value suggests that the method significantly overestimates the shear capacity of the tested specimens. This lack of conservatism limits its applicability for safety-focused structural assessments.

2.7.6. Cladera (2021)

The approach by Cladera et al. is based on the Compression Chord Capacity Model and is a closed form solution, considering both the contribution of stirrups and concrete in the shear strength calculation. There is also a calculation method for non-slender beams which is not reported in the present paper.

The formulation resulted in a mean V_{AN}/V_{EXP} ratio of 1.13. The corresponding standard deviation was 0.28, with a CoV of 25%. While the formulation performs better than Lu's in terms of conservatism, it still tends to overestimate shear capacity when compared to experimental outcomes.

2.8 Results

Table 2-10 presents a summary of the key statistical indicators (mean, standard deviation, and CoV) for all five models applied to the 108-specimen database. Notably, the CoV across all formulations remains close to 20%, which underscores the influence of two highly variable phenomena: shear failure and corrosion-induced degradation. When these factors are combined, the predictive uncertainty of any model naturally increases.

Furthermore, Rossi and Spinella (2023) also reports, as final results of the analytical formulation, a mean value of about 1.02 and a CoV of 28%.

Figure 2-9 shows the comparison of the V_{AN}/V_{EXP} diagrams for the different formulations studied.

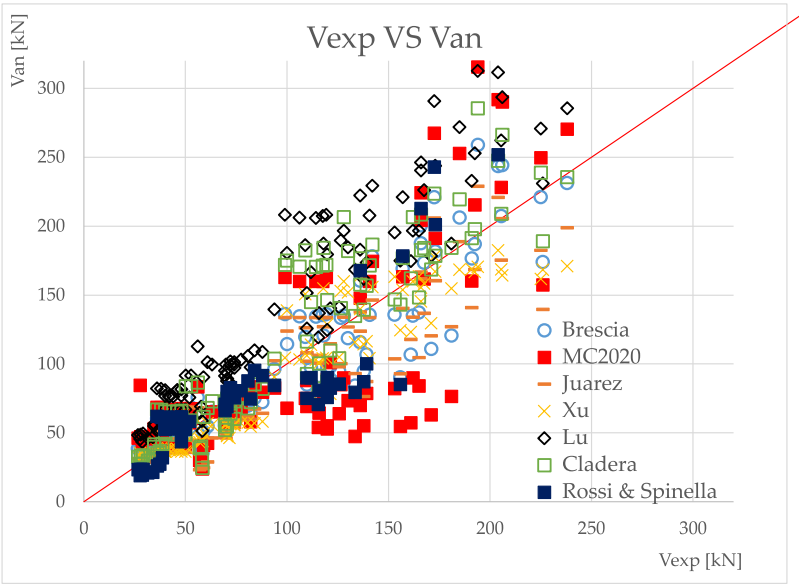


Figure 2-9: Comparison of the analytical prediction and experimental shear strength diagram for all formulations.

Formulation	Equations	V_{AN}/V_{EXP}	St. Dev.	CoV
Proposed Model	See Paragraph 2- Analytical model	1.00	0.25	25%
Model Code 2020 (2023)	$V_{Rds,det} = z\cot\theta\frac{A_{sw,det}f_{ywd}}{s} < V_{Rd,det,max}$ $V_{Rd,det,max} = k_{c,det}\frac{f_{ck}}{\gamma_c}b_{w,det}z_{det}\sin\theta\cos\theta$ $k_{c,det} = k_{\varepsilon,det}\eta_{fc,det}$ $k_{\varepsilon,det} = \frac{1}{1{,}2 + 55\varepsilon_{1,det}} \le 0{,}65$ $\eta_{fc,det} = \left(\frac{30}{f_{ck,det}}\right)^{\frac{1}{3}} \le 1{,}0$ $\varepsilon_{1,det} = \varepsilon_{x,det} + (\varepsilon_{x,det} + 0.002)\cot^2\theta$ $\theta_{min} = \theta = 20° + 4000\varepsilon_x$ $\varepsilon_{x,det} = \frac{1}{2E_sA_{s,det}}\frac{1}{k_{bond}}\left\{\frac{M_{Ed}}{z} + V_{Ed}\right\}$	1.00	0.44	43%
Juarez (2011)	$V_{AN} = V_S + V_C$ $V_S = \frac{A_{w,corr}}{s_w}f_{wy}d$ $V_C = 0.17\sqrt{f_c}bd$	0.90	0.22	24%
Xu (2017)	$V_{AN} = V_S + V_C$ $\alpha_X = 1 - 1.077\cdot m_{corr,w}$ $V_S = \alpha_X(0.25 + 0.4\frac{a}{d})f_{wy}\frac{A_w}{s_w}d$ $\beta = \begin{cases} 1 & m_{corr,w} \le m_{corr,w,cr} \\ \left(\frac{m_{corr,w}}{m_{corr,w,cr}}\right)^{0.069\frac{a}{d}-0.43} & m_{corr,w} > m_{corr,w,cr} \end{cases}$ $V_C = \beta\left(\frac{0.08}{a/d - 0.3} + \frac{100\rho_L(1-m_{corr,L})}{a/d\,f_c}\right)$	0.90	0.17	19%
Lu (2018)	$V_{AN} = \phi V_C + V_S$ $\phi = \begin{cases} 0.008e^{\left(-0.122\frac{a}{d}\right)} - 0.003m_{corr,w} + 1.01 & \frac{a}{d} < 2.5 \\ 0.1e^{\left(-0.122\frac{a}{d}\right)} - 0.003m_{corr,w} + 1.38 & \frac{a}{d} \ge 2.5 \end{cases}$ $V_C = MAX\left(0.2\sqrt[3]{100f_c\rho_L(1-m_{corr,L})}\sqrt{10^3/d}\left(0.75 + 1.4d/a\right)bd; \frac{0.24\sqrt[3]{f_c^2}\left(1+\sqrt{\rho_L(1-m_{corr,L})}\right)\left(1+3.33\,r/d\right)bd}{1+\left(\frac{a}{d}\right)^2}\right)$	1.45	0.27	19%

	$V_S = f_{wy}\frac{A_{w,corr}}{s_w}d$			
Cladera (2021)	$V_{AN} = V_C + V_S$ $\xi = \frac{2}{\sqrt{1+\frac{d}{200}}}\left(\frac{d}{a}\right)^{0.2} < 0.45$ $\frac{x}{d} = 0.75\sqrt[3]{n_L\rho_L(1-m_{corr,L})}$ $cot\theta = \frac{0.85}{1-\frac{x}{d}} \leq 2.5$ $V_C = 0.3\xi\frac{x}{d}f_c^{2/3}bd$ $V_S = 1.4\frac{A_{w,corr}}{s_w}f_{wy}d\left(1-\frac{x}{d}\right)cot\theta$	1.13	0.28	25%

Table 2-10: Comparison between the mean value, standard deviation and CoV of the V_{AN}/V_{EXP} ratio for the different formulations.

2.9 CONCLUDING REMARKS

This study has presented a novel analytical method for evaluating the shear strength of RC beams affected by corrosion, developed within the framework of the Level IIb approximation of the *fib* MC2020, considering both stirrup and concrete contributions. The proposed formulation accounts for the effects of corrosion through:

- reduction of the cross-sectional area of longitudinal reinforcement;
- degradation of the yield strength of stirrups;
- reduction in effective concrete width due to cover cracking and spalling.

The model was validated against an extensive database of 108 experimental tests, 76% of which involved beams with corroded reinforcement. The analytical-to-experimental shear strength ratio achieved a mean value of 1.00 with a coefficient of

variation (CoV) of 25%, demonstrating the robustness of the method even under conditions of high variability associated with shear and corrosion mechanisms.

Based on the results and analyses, the following key conclusions can be drawn:

- The proposed model, based on the SMCFT, represents a rigorous extension of the *fib* MC2020 framework and exhibits strong predictive accuracy across a wide range of test scenarios.
- In 97% of the specimens, the predicted failure mode was consistent with the experimental observations, reinforcing the model's reliability in simulating real structural behaviour.
- Compared with other analytical formulation, such as the Model Code 2020 approach IIa for corroded elements and Rossi and Spinella formulation, the proposed model provides improved prediction capacity in terms of mean value of V_{AN}/V_{EXP} and yields the lowest CoV.
- Compared with existing empirical and semi-empirical formulations, the model offers a balanced approach between accuracy and conservatism, making it suitable for assessment purposes.
- The relatively high CoV is expected, given the inherent uncertainties in both corrosion development and shear failure. Nevertheless, the model consistently captures the primary trends in the experimental data, especially in configurations representative of field conditions. It is also worth noting that the control specimens (without corrosion) exhibited a CoV of 19%, a

value that can reasonably be expected to increase when corrosion effects are introduced. Finally, all the examined formulations yielded comparable CoV values, ranging from 19% to 25%, with the notable exception of MC2020, which exhibited a substantially higher CoV of 43%

- Most of the specimens analyzed were small-scale beams, limiting direct extrapolation to full-scale applications such as bridge girders. Notably, the experiments conducted by Di Stefano (2022) are among the few available full-scale corrosion tests. Future research should prioritize expanding the dataset with additional full-scale tests.
- The current formulation does not account for bond deterioration between concrete and corroded reinforcement; further studies are required to address this aspect.
- The formulation does not address prestressed concrete elements or cases involving combined shear and axial loads. Future developments should extend the model to incorporate axial effects and prestressing loss, alongside appropriate formulations to estimate corrosion-induced degradation in prestressing strands.
- The current database mainly comprises specimens exposed to artificially accelerated corrosion (impressed current); expanding it to include full-scale members with naturally occurring corrosion would improve representativeness.

In conclusion, the proposed model provides a robust and practical analytical tool for evaluating the shear strength of corroded RC beams. It lays the groundwork for improved reliability in condition assessment and maintenance strategies for aging infrastructure affected by corrosion.

2.10 ACKNOWLEDGMENTS

The Authors would like to thank The Road Administration Service of Provincia di Brescia, Italy, and its technical team (Arch. Pierpaola Archini, Eng. Enrica Savoldi, Eng. Stefano Vitalini and Eng. Luisa Zavanella), for the financial support provided to this research.

2.11 NOTATION

a	shear span
A_L	cross section of the uncorroded tensile reinforcements
$A_{L,corr}$	cross section of the tensile reinforcements considering corrosion
A_w	cross section of the uncorroded stirrups
$A_{w,corr}$	cross section of the stirrups considering corrosion
b	uncorroded section width
b_{corr}	section width reduced by corrosion
c	total concrete cover
c_n	clear concrete cover

d effective depth

E_s Young's Modulus of the rebars steel

f_c concrete cylindrical compressive resistance

f_{yL} tensile rebars yield stress

f_{yw} stirrups initial yield stress

$f_{yw,corr}$ corroded stirrups yield stress

H section heigth

k_v coefficient that depends on ε_x

$m_{corr,L}$ mean percentage of mass loss of the longitudinal tensile reinforcement

$m_{corr,w}$ mean percentage of mass loss of stirrups

$m_{corr,w,cr}$ critical value of $m_{corr,w}$

n_L number of tensile rebars

n_w number of stirrups arms

M_E acting bending moment

r load plate dimensions in Lu formulation

s_w stirrups spacing

V_{AN} shear strength calculated with analytical formulation

V_C concrete contribution to shear strength

V_E acting shear action

V_{EXP} experimental value of shear strength

$V_{R,max}$ maximum shear strength related to crushing of concrete carrying the compression field

V_S stirrups contribution to shear strength

z_v effective shear depth equal to 0.9d, where d is the effective depth

α inclination of stirrups with respect to the vertical direction

α_w correlation coefficient between yielding strain and stress in corroded stirrups

α_X numerical coefficient in Xu formulation

β numerical coefficient in Xu formulation

ε_x effective state of strain at the mid-depth of the effective shear depth

ε_y yielding strain of longitudinal tensile reinforcement

ϕ numerical coefficient in Lu formulation

ϕ_L longitudinal tensile reinforcement diameter

ϕ_w stirrups diameter

ρ_L percentage of longitudinal tensile reinforcement in the uncorroded section

ρ_w percentage of stirrups in the uncorroded section

θ inclination of the strut with respect to the beam axis direction

ξ coefficient in Cladera formulation

2.12 REFERENCES

[1] Belletti B, Damoni C, Hendriks MAX, de Boer A. Assessment of shear capacity of existing reinforced concrete slab-strip bridges. Eng Struct. 2020a;205:110078. https://doi.org/10.1016/j.engstruct.2019.110078

[2] Imperatore S, Rinaldi Z, Drago C. Degradation relationships for the mechanical properties of corroded steel rebars. Constr Build Mater. 2017;148:219–230. https://doi.org/10.1016/j.conbuildmat.2017.05.066

[3] Apostolopoulos CA. Mechanical behavior of corroded reinforcing steel bars S500s tempcore under low cycle fatigue. Constr Build Mater. 2009;23(3):1447–1456. https://doi.org/10.1016/j.conbuildmat.2008.08.008

[4] Higgins C, Farrow W. Tests of reinforced concrete beams with corrosion-damaged stirrups. ACI Struct J. 2010;107(4):408–417. https://doi.org/10.14359/51663895

[5] Pedeferri P. Corrosion of Reinforced Concrete Structures. Springer; 2018.

[6] Coronelli D, Gambarova PG. Structural assessment of corroded reinforced concrete beams: Modeling guidelines. J Struct Eng. 2004;130(8):1214–1224. https://doi.org/10.1061/(ASCE)0733-9445(2004)130:8(1214)

[7] Lin H, Zhao Y, Ozbolt J. Bond strength evaluation of corroded steel bars via the surface crack width induced by reinforcement corrosion. Eng Struct. 2017;152:506–522. https://doi.org/10.1016/j.engstruct.2017.09.027

[8] Belletti B, Damoni C, Hendriks MAX, de Boer A. Shear capacity of RC members without transverse reinforcement: Interaction between critical shear crack and aggregate interlock. Eng Struct. 2020b;205:110078.

[9] Rossi PP, Spinella N. Shear strength of RC beams with corroded stirrups: Experimental investigation and analytical modeling. Eng Struct. 2023;284:115951. https://doi.org/10.1016/j.engstruct.2023.115951

[10] Cladera A, Mari AR, Bairán JM, Oller E, Ribas C. Shear strength of corroded reinforced concrete beams: Experimental database and simplified mechanical model. Eng Struct. 2021;247:113163. https://doi.org/10.1016/j.engstruct.2021.113163

[11] Lu X, Jin W, Zhao Y. Shear capacity of reinforced concrete beams with corroded stirrups. Struct Infrastruct Eng. 2018;14(6):765–780. https://doi.org/10.1080/15732479.2017.1357560

[12] Rossi PP, Spinella N. Influence of corrosion level on shear strength of RC beams with corroded stirrups. Comput Concr. 2022;31(1):33–52.

[13] BENTZ EC, VECCHIO FJ, COLLINS MP. SIMPLIFIED MODIFIED COMPRESSION FIELD THEORY FOR CALCULATING SHEAR STRENGTH OF REINFORCED CONCRETE ELEMENTS. ACI STRUCT J. 2006;103(4):614–624.

[14] FIB – FÉDÉRATION INTERNATIONALE DU BÉTON. FIB MODEL CODE FOR CONCRETE STRUCTURES 2020. BERLIN, GERMANY: ERNST & SOHN; 2023.

[15] DI STEFANO N. SHEAR BEHAVIOR OF REINFORCED CONCRETE BEAMS WITH CORRODED REINFORCEMENT. PHD THESIS, UNIVERSITY OF BRESCIA; 2022.

[16] ALASKAR A. RESIDUAL SHEAR STRENGTH OF CORRODED REINFORCED CONCRETE BEAMS. CONSTR BUILD MATER. 2013;38:861–871. HTTPS://DOI.ORG/10.1016/J.CONBUILDMAT.2012.09.071

[17] EL-SAYED AK, HUSSAIN RR, SHURAIM AB. SHEAR STRENGTH OF CORRODED REINFORCED CONCRETE BEAMS. CONSTR BUILD MATER. 2016;113:607–617. HTTPS://DOI.ORG/10.1016/J.CONBUILDMAT.2016.03.068

[18] HAN S, LI W, WANG Y. EXPERIMENTAL STUDY ON SHEAR PERFORMANCE OF RC BEAMS WITH CORRODED LONGITUDINAL REINFORCEMENT. MATERIALS. 2019;12:1234.

[19] LU X, JIN W, ZHAO Y. EXPERIMENTAL STUDY ON SHEAR BEHAVIOR OF RC BEAMS WITH CORRODED REINFORCEMENT. STRUCT INFRASTRUCT ENG. 2019;15(3):345–358.

[20] Rodriguez J, Ortega LM, Casal J. Load carrying capacity of concrete structures with corroded reinforcement. Constr Build Mater. 1997;11(4):239–248.

[21] Wang XH, Gao XH, Li B, Deng BR. Effect of bond and corrosion within partial length on flexural behavior of RC beams. Constr Build Mater. 2011;25(4):1812–1823. https://doi.org/10.1016/j.conbuildmat.2010.11.081

[22] Xue X, Seki H, Chen W. Shear strength of RC beams with corroded longitudinal reinforcement. Eng Struct. 2013;56:110–120.

[23] Xue X, Seki H, Song L. Shear behavior of RC beams with corroded stirrups. Eng Struct. 2014;59:417–429.

[24] Zhao YX, Jin WL. Design of shear strength of corroded reinforced concrete beams. J Zhejiang Univ Sci A. 2009;10(9):1279–1288.

[25] CEN. EN 1992-1-1:2004/A1:2004 Eurocode 2: Design of concrete structures. Brussels: European Committee for Standardization; 2004.

[26] ACI Committee 318. Building Code Requirements for Structural Concrete (ACI 318-19). Farmington Hills, MI: American Concrete Institute; 2019.

[27] CEN. EN 206:2013 Concrete – Specification, performance, production and conformity. Brussels; 2013.

[28] Cairns J, Plizzari GA, Du Y, Law DW, Franzoni C. Mechanical properties of corrosion-damaged reinforcement. ACI Struct J. 2005;102(2):256–264.

[29] Xu S, Zhang Z, Li R, Qiu B. Experimental study on shear behavior of RC beams with corroded stirrups. J Adv Concr Technol. 2017;15(4):178–189.

[30] Juarez CA, Guevara B, Fajardo G, Castro-Borges P. Ultimate and nominal shear strength of reinforced concrete beams deteriorated by corrosion. Eng Struct. 2011;33(10):3189–3196.

[31] Biondini F, Vergani M (eds.). Damage Modeling and Nonlinear Analysis of Reinforced Concrete Structures. CRC Press; 2012.

[32] Coronelli D. Shear capacity of reinforced concrete beams with corroded stirrups. Structural Concrete. 2025; Early View:1–13

[33] Lu, Z.-H., Li, H., Li, W., Zhao, Y.-G., Dong, W., 2018. An empirical model for the shear strength of corroded reinforced concrete beam. Construction and Building Materials 188, 1234–1248. https://doi.org/10.1016/j.conbuildmat.2018.08.123

2.13 LIST OF TABLES

Table 2-1: Coefficient αw employed as a function of the stirrups' diameters 20
Table 2-2: Database Characterisation. 38
Table 2-3 - Pt. (1 of 4): Application of the method to 108 samples. 41
Table 2-4 - Pt. (2 of 4): Application of the method to 108 samples. 42
Table 2-5 - Pt. (3 of 4): Application of the method to 108 samples. 43
Table 2-6 - Pt. (4 of 4): Application of the method to 108 samples. 44
Table 2-7: Maximum and minimum values of mean $VAN/VEXP$, St. Dev. and CoV. 46
Table 2-8: Comparison of the values of the proposed model and the Model Code 2020 for Corroded specimens, Control Specimens and All Specimens. 53
Table 2-9: Comparison between the proposed formulation, Model Code 2020 and Rossi&Spinella (2023) 54
Table 2-10: Comparison between the mean value, standard deviation and CoV of the V_{AN}/V_{EXP} ratio for the different formulations. 59

2.14 LIST OF FIGURES

Figure 2-1: Schematic representation of ε_x (fib MC2020) 15
Figure 2-2: Schematic plan view of concrete spalling in a beam web due to corrosion for two different stirrup spacings. Adapted from Higgins and Farrow (2010) 23
Figure 2-3: Flow chart of the proposed method. 26
Figure 2-4: Corrosion distribution along the considered section (Biondini and Vergani, 2012) 33
Figure 2-5: Analytical prediction vs. experimental shear strength. 46
Figure 2-6: Analytical predictions vs stirrups mean corrosion rate. 47
Figure 2-7: Analytical predictions vs longitudinal reinforcement mean corrosion rate. 48
Figure 2-8: Comparison between Analytical prediction and experimental shear strength of the proposed model and the MC2020 corrosion model. 53
Figure 2-9: Comparison of the analytical prediction and experimental shear strength diagram for all formulations. 57

3 EXPERIMENTAL AND NUMERICAL STUDY ON SHEAR-CRITICAL PRESTRESSED GIRDERS STRENGTHENED WITH HIGH PERFORMANCE FIBRE REINFORCED CONCRETE

ABSTRACT

This paper presents an experimental and numerical investigation on three full-scale prestressed concrete bridge girders removed from service after approximately 50 years. The beams were tested under shear-dominated loading conditions and were intentionally pre-cracked to different target crack widths in order to simulate distinct levels of structural deterioration prior to strengthening.

The adopted strengthening system consisted of two 50 mm-thick Ultra-High Performance Fibre Reinforced Concrete (UHPFRC) overlays applied to the webs. Bond with the existing substrate was ensured through mechanical surface roughening, without the use of traditional core connectors within the web. In addition, 1.4 mm-thick externally bonded FRP plates were installed at the intrados to prevent premature flexural failure and to ensure a shear-critical assessment of the strengthening technique.

Nonlinear finite element analyses were carried out using VecTor2, based on the Modified Compression Field Theory (MCFT). Numerical predictions showed good agreement with experimental results in terms of stiffness, crack development and ultimate capacity. The strengthening intervention significantly enhanced shear resistance, reduced crack widths and promoted a transition from brittle shear failure to a more ductile flexural response. The study provides rare full-scale evidence of UHPFRC overlay effectiveness on severely deteriorated prestressed bridge girders.

3.1. INTRODUCTION

In the past, reinforced and prestressed concrete structures were commonly perceived as inherently durable, and maintenance strategies were often underestimated during the design phase. However, recent collapses of major infrastructures have dramatically increased awareness of the deterioration of existing bridges (Di Prisco 2019). Several studies have since investigated the technical causes of structural failures, reflecting the growing attention devoted to infrastructure safety (Di Prisco et al. 2018). Moreover, a significant portion of existing reinforced concrete (RC) and

prestressed concrete (PC) structures has now exceeded its nominal design service life (Belletti et al. 2020), raising concerns regarding their residual structural capacity.

Among the various deterioration mechanisms, corrosion of reinforcement is widely recognized as one of the most critical issues. It is explicitly addressed in the Italian Guidelines for risk classification, safety assessment and monitoring of existing bridges (Ministero delle Infrastrutture e dei Trasporti 2020). Corrosion affects transverse reinforcement, longitudinal rebars and prestressing strands, leading not only to steel cross-section reduction but also to cracking, spalling and loss of concrete cover, as well as bond degradation between steel and concrete (Pedeferri 2005; Higgins et al. 2003). In prestressed elements, corrosion can be particularly critical, since the stress level in tendons accelerates the deterioration process and may result in significant prestress losses or even strand rupture (Rogers et al. 2012).

For these reasons, the assessment of degradation conditions and the prediction of residual structural capacity have become central topics in recent research (Belletti et al. 2020; Recupero and Spinella 2019; Savino et al. 2023; Kioumarsi et al. 2021). Despite these efforts, full-scale experimental investigations on existing, naturally deteriorated prestressed bridge girders remain relatively scarce. This lack of large-scale evidence limits the validation of assessment models and strengthening techniques under realistic boundary conditions.

When structural assessment highlights insufficient safety margins, replacement is not always a feasible option, particularly when traffic interruption is unacceptable or when sustainability considerations are taken into account. The construction sector is currently facing increasing pressure to reduce carbon emissions and extend the service life of existing infrastructures. In this context, strengthening interventions represent a viable and often preferable alternative, allowing engineers to exploit the residual capacity of deteriorated members rather than replacing them entirely (Zanotti et al. 2017; Bhutta et al. 2017).

In recent years, considerable attention has been devoted to strengthening techniques based on high-performance materials, such as Ultra-High Performance Fibre Reinforced Concrete (UHPFRC). The presence of fibres significantly enhances tensile strength and post-cracking behaviour (Soliman and Nehdi 2014; Meda, Minelli, and Plizzari 2012), while also improving durability and resistance to environmental aggression (Brandt 2008). From a structural standpoint, fibre-reinforced materials can contribute directly to shear resistance, potentially reducing or even eliminating the need for additional transverse reinforcement (Minelli and Plizzari 2008).

Within this framework, the present study investigates the effectiveness of UHPFRC overlays applied as a shear strengthening technique to existing prestressed bridge girders at the end of their service life. The experimental program involves three full-scale beams removed from a motorway bridge and characterized by severe degradation, including corrosion of strands and loss of concrete cover. Unlike most previous studies conducted on laboratory-scale specimens, this research focuses on

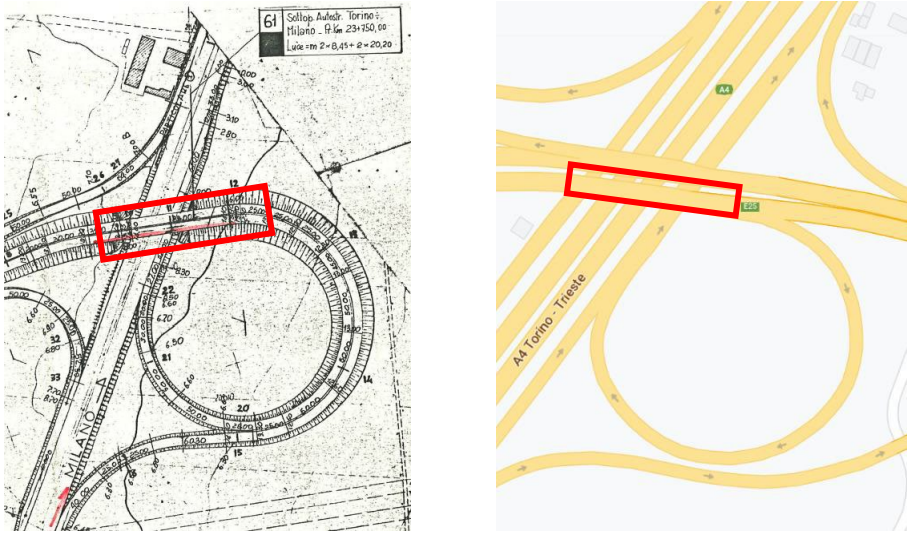
real structural elements subjected to decades of environmental exposure. Particular attention is devoted to the bond between the UHPFRC overlay and the existing substrate, exploring the possibility of optimizing or minimizing traditional core connectors.

The structural performance of the strengthened girders is evaluated through both experimental testing and nonlinear finite element analyses performed using VecTor2 (Wong, Vecchio, and Trommels 2013), based on the Modified Compression Field Theory (MCFT) (Vecchio and Collins 1986). The combined experimental–numerical approach allows not only the interpretation of observed behaviour but also the estimation of ultimate capacity beyond the limits imposed by the testing equipment.

3.2. EXPERIMENTAL PROGRAMME

3.2.1. Specimens' location and geometry

The experimental programme involved three full-scale prestressed concrete girders removed from an existing motorway bridge at the end of their service life, approximately 60 years after construction. The bridge consisted of three simply supported spans and carried the A26 (Stroppiana–Santhià branch) over the A4 Torino–Milano Highway. As shown in Figure 3-1b, the tested specimens were extracted from the Milan-bound carriageway of the deck.



(a) (b)

Figure 3-1: (a) specimens location identified on the original project drawings; (b) girders location identified on the maps on the Milan direction portion.

The experimental results discussed in this paper refer to the girders belonging to the external spans, characterized by a total length of approximately 11 m. Girders from the central spans were also tested, but their results are presented elsewhere (Lupoi, Ficociello, and Malavisi, 2022). The focus on the external spans allows a direct comparison between beams subjected to similar exposure conditions and structural configuration.

The original executive design of the bridge dates back to 1967. At the time of testing, the girders had therefore exceeded five decades of service life and exhibited severe deterioration. Extensive loss of concrete cover was observed in both flanges and web regions (Figure 3-2), accompanied by corrosion of prestressing strands, longitudinal reinforcement and transverse reinforcement.

The three specimens, hereafter referred to as Beam 1, Beam 2 and Beam 3, displayed different degrees of degradation. Beam 2 was the most severely deteriorated, with widespread loss of concrete cover in the web region and significant corrosion affecting both strands and stirrups. Beam 3 exhibited advanced corrosion of the bottom flange strands at the intrados, with some tendons locally fractured. Beam 1 showed comparatively limited corrosion; however, it suffered substantial mechanical damage to the upper flange during dismantling operations, resulting in the loss of a non-negligible portion of concrete.



(a) (b) (c)

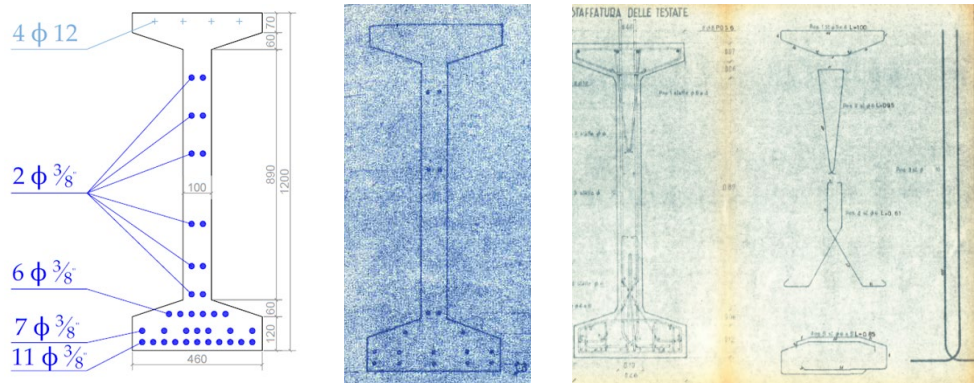
Figure 3-2: Deterioration conditions (a) Beam 1, (b) Beam 2, (c) Beam 3.

In order to reduce variability associated with localized concrete loss and to provide comparable initial geometric conditions, all girders underwent a preliminary restoration phase prior to testing. The objective of this intervention was not to eliminate the effects of long-term material degradation, but rather to reconstruct the damaged cover and partially recover the original cross-sectional geometry.

The specimens were subjected to a severe degree of corrosion; in particular, the prestressing strands were highly corroded, as shown in Figure 3-2, leading to significant losses in prestress.

Based on the original design drawings, an initial reconstruction of the reinforcement layout was performed (Figure 3-3b and Figure 3-3c). However, the detailed diagnostic investigation revealed that the as-built configuration differed from the project documentation. Specifically, the 11 m span girders were found to have the same prestressing layout as the 24 m span beams. This discrepancy highlights the importance of in-depth diagnostic assessment when evaluating existing structures.

The girders had an I-shaped cross-section (Figure 3-3a) with a total height of 1200 mm and flanges of different thicknesses. The prestressing system consisted of 24 tendons made of 3/8" seven-wire strands (equivalent diameter 9.53 mm), arranged as shown in Figure 3-3a. The transverse reinforcement (Figure 3-3c) was characterized by variable spacing: approximately 300 mm at midspan, reduced to 225 mm near the supports, and further decreasing to 100–50 mm in the prestress transfer region. The stirrups were composed of eight individual bars, but only two were continuous along the full height of the section and crossed the neutral axis, while the remaining elements primarily provided confinement. Full-height longitudinal rebars were of Rumi type with an equivalent diameter of 10 mm, whereas additional longitudinal bars had diameters in the range of 5–6 mm.



(a) (b) (c)

Figure 3-3: (a) Actual and (b) designed section; (c) particular of stirrups near the support from the original project.

3.2.2. Strengthening technique

The strengthening technique represents a heavy-target structural application of UHPFRC and HPFRC materials, both from a structural and a technical point of view. Prior to strengthening, the girders underwent a preliminary restoration phase aimed at compensating for concrete cover loss and reconstructing the damaged portions of the flanges. The restoration material was selected to exhibit mechanical properties comparable to those of the existing concrete in order to avoid introducing artificial stiffness discontinuities. Existing cracks were sealed using the same material.
This preliminary intervention was intended to ensure a reliable installation of the strengthening system and to reduce the influence of localized geometric irregularities on the structural response. It is important to emphasize that no passivation treatment of the reinforcement was carried out. While reinforcement protection would be

mandatory in a real rehabilitation scenario, it was intentionally omitted in this experimental campaign to preserve the effects of long-term corrosion and to focus the investigation on the structural contribution of the strengthening technique.
Before strengthening, pre-cracking tests were performed with different target levels for each specimen. The stopping criterion was the attainment of a predefined maximum shear crack width.
The pre-cracking phase was carried out for two main reasons: first, to obtain information on the load–deflection response of the unstrengthened configuration, allowing at least a comparison of stiffness with the subsequently strengthened tests; second, and more importantly, to apply the intervention to beams exhibiting pre-existing damage, a condition more representative of real structures, and to investigate whether different levels of prior damage could influence the effectiveness of the strengthening system.
The adopted strengthening system consisted of two 50 mm-thick UHPFRC layers cast on both web sides (Figure 3-4b). The overlays were connected to the flanges by means of Ø10 mm dowels spaced at 200 mm. With the exception of one side of Beam 1, these dowels were extended to act as additional transverse reinforcement, as illustrated in Figure 3-4a. The partial extension of dowels as additional transverse reinforcement was introduced to investigate whether their contribution could significantly influence shear capacity.
In addition to the web overlays, four 1.4 mm-thick FRP plates were bonded side by side at the intrados (Figure 3-4c). The purpose of the FRP reinforcement was to increase the flexural capacity and prevent premature flexural failure, thereby ensuring that the experimental assessment remained governed by shear behaviour.
The mechanical properties of the strengthening materials are reported in Table 3-1 and Table 3-2.

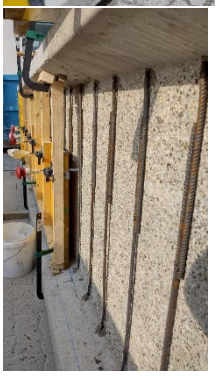




(b)



(c)



(a)

Figure 3-4: (a) connection of the overlay to the flanges, (b) detail of FRC overlay, (c) detail of FRP plates.

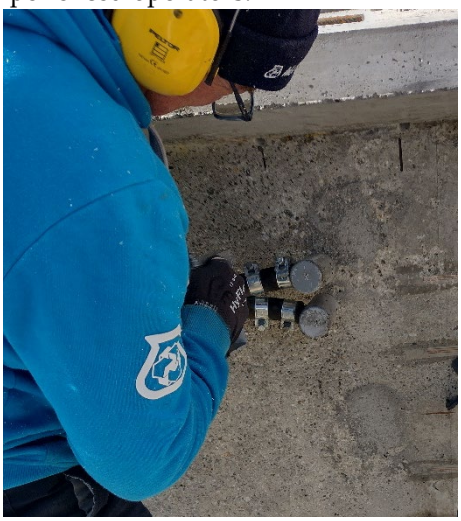
Table 3-1: UHPFRC properties.

UHPFRC "HPC floor 46"	
Cementitious Matrix	
Bulk Density [kg/m³]	1400
Maximum Size of Aggregate [mm]	6
Compressive Strength [MPa]	125
Fibres	
Shape	Hooked
Material	Steel
Volume Fraction [%]	0,96
Length [mm]	30
Diameter [mm]	0,38
Elongation at Failure [10^{-3}]	min. 7,0
Class [UNI EN 14889]	8c

Table 3-2: FRP plates properties.

FRP "CARBOPLATE E170"	
System Class	C150/2300
Thickness [mm]	1,4
Width [mm]	100
Modulus of Elasticity [GPa]	160
Tensile Strength [MPa]	2700
Elongation at Failure [10-3]	16

Given the high mechanical performance of the adopted UHPFRC, the experimental programme deliberately investigated the possibility of applying the overlay without traditional core connectors within the web. The objective was to assess whether adequate composite action could be achieved through surface preparation and limited mechanical anchorage, thereby simplifying potential practical applications.
To ensure proper bond between the existing concrete substrate and the UHPFRC overlay, the surface was mechanically roughened using a hydraulic hammer (Figure 3-5a), achieving an average roughness amplitude of approximately ±3 mm (Figure 3-5b). This treatment aimed to enhance mechanical interlock and improve shear transfer across the interface. Proper surface preparation is crucial to ensure the effectiveness of the intervention and must be executed with due care by qualified and experienced operators.



(a)



(b)

Figure 3-5: Surface treatment: (a) preparation to achieve a target roughness of ±3 mm; (b) finished surface.

Inclined holes were then drilled in the flanges to anchor the additional transverse reinforcement provided by the dowels. Stirrups were positioned accordingly before casting. The wooden formwork used for casting the UHPFRC layers was interrupted over a height of approximately 150 mm near the upper flange to allow proper placement and compaction of the strengthening material (Figure 3-6a). The uppermost portion of the overlay was subsequently completed using a thixotropic mortar compatible with the selected UHPFRC product (Figure 3-6b), ensuring continuity of the strengthening layer. Figure 3-6b shows a preliminary trial carried out to assess the feasibility of completing the final centimetres beneath the flange manually using thixotropic mortar. Subsequently, the intervention was executed by formworking the entire length of the beam.



Figure 3-6: (a) casting of the UHPFRC layers; (b) completion of the upper 15 cm with tixotropic mortar.

The strengthening intervention was primarily designed to enhance the ultimate shear capacity of the specimens. Beyond strength improvement, the application of UHPFRC overlays was also intended to improve long-term durability. By limiting crack development and reducing crack widths, the overlay contributes to improved protection of the existing reinforcement system against moisture ingress and aggressive environmental agents.

3.2.3. Experimental tests and results

Each specimen was tested in two configurations: initially in the unstrengthened condition and subsequently after strengthening, maintaining the same loading scheme to ensure comparability of results. The adopted test nomenclature is reported in Table 3-3.

In addition, each specimen was tested on both ends. After completion of the first test, the beam was rotated and tested again under the same loading configuration. The

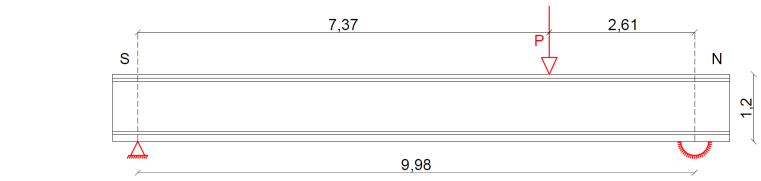
first test was designated as “Side A”, while the subsequent one was referred to as “Side B”. Consequently, each girder underwent three or four tests: one or two in the unstrengthened condition (depending on the specimen) and two in the strengthened configuration (Table 3-3).

Table 3-3: tests names.

Specimen	Strengthened / Unstrengthened	Side	Test Name
Beam1	Unstrengthened	Side A	1AU EXP
	Strengthened	Side A	1AS EXP
		Side B	1BS EXP
Beam2	Unstrengthened	Side A	2AU EXP
	Strengthened	Side A	2AS EXP
		Side B	2BS EXP
Beam3	Unstrengthened	Side A	3AU EXP
		Side B	3BU EXP
	Strengthened	Side A	3AS EXP
		Side B	3BSEXP

It should be noted that the results obtained from Side B tests must be interpreted with caution. Since these tests were performed after the beam had already sustained significant damage during the previous loading phase, they are primarily representative in terms of order of magnitude of the ultimate load rather than of the initial stiffness or cracking behaviour.

All tests were conducted under three-point bending in displacement control. The maximum capacity of the loading system differed between the pre-cracking tests and the strengthened tests, being approximately 800 kN and 1400 kN, respectively. The shear span-to-effective depth ratio (a/d) was approximately 2.22, ensuring shear-dominated behaviour in the unstrengthened configuration. The experimental setup is illustrated in Figure 3-7. Specifically, Figure 6a shows the adopted loading scheme, Figure 6b presents a specimen tested in the unstrengthened condition, and Figure 6c depicts a strengthened beam during testing.



(a)



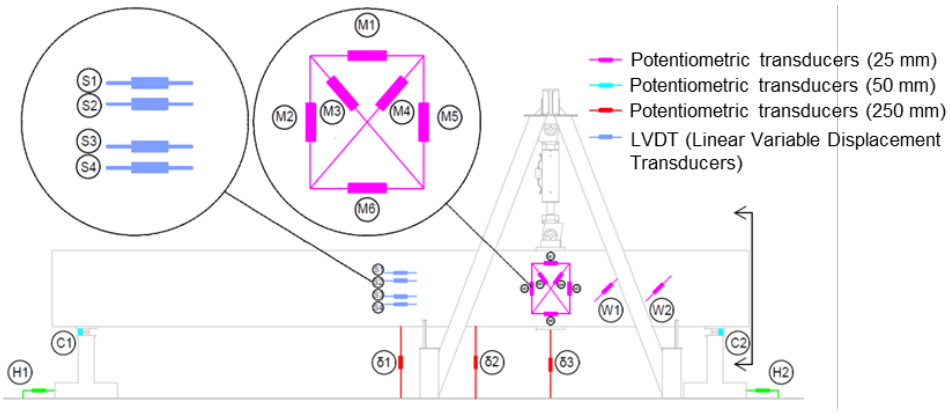
(b)



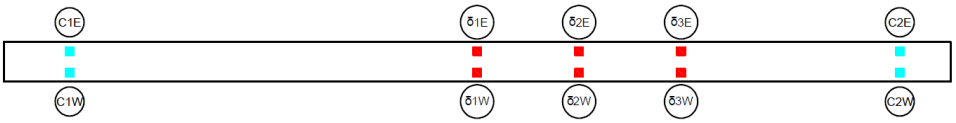
(c)

Figure 3-7: (a) Loading scheme; examples of test before (b) and after (c) the strengthening.

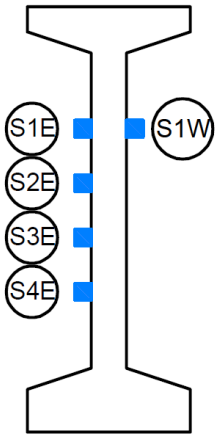
A comprehensive instrumentation system was installed to monitor global and local structural response, including displacements, strains, crack openings and applied load (Figure 3-8). Four 50 mm stroke potentiometric transducers (PTs) were positioned at the supports to measure vertical displacements. These instruments, identified as C1E, C1W, C2E and C2W in Figure 3-8, allowed accurate monitoring of support movements during testing.



(a)



(b)



(c)

Figure 3-8: tests set-up and instrumentation positions.

Six additional potentiometric transducers with a 250 mm stroke (three per side) were installed to measure vertical displacements at key locations along the span: under the

loading point, at midspan, and at an intermediate position between these two sections. These measurements were identified as δ_1, δ_2 and δ_3, respectively.
At midspan, five LVDTs were positioned to monitor flexural deformations and crack development; these instruments are indicated by the letter S in Figure 3-8c. Finally, two 50 mm stroke potentiometric transducers (W1 and W2) were installed across the principal shear crack to directly measure crack opening displacement. These measurements are particularly relevant for the present investigation, as crack width control represents one of the primary objectives of the strengthening technique.
Prior to strengthening, as mentioned before, each girder was subjected to a preliminary pre-cracking shear test. This test was intentionally interrupted once a predefined shear crack opening target was reached. Different crack width targets were selected for the three beams in order to simulate distinct levels of initial deterioration. The adopted target crack widths, together with the corresponding maximum applied load and load-point deflection, are reported in Table 3-4.
As summarized in Table 3-4, Beam 1 and Beam 2 were pre-cracked only on Side A, whereas Beam 3 underwent pre-cracking on both sides. This procedure enabled the investigation of strengthening performance under varying pre-existing damage conditions. The selected crack width targets were defined in order to represent increasing levels of structural damage, ranging from moderate cracking to more advanced deterioration conditions. Such values are consistent with crack widths typically observed in existing deteriorated prestressed concrete girders and allowed investigation of the influence of pre-existing damage on the effectiveness of the strengthening intervention. The control parameter adopted for the pre-cracking phase was the maximum shear crack opening measured by the diagonal potentiometric transducers W1 and W2, previously described. The test was interrupted once the predefined target crack width was reached by one of the instruments.

Table 3-4: Pre-crack targets tests.

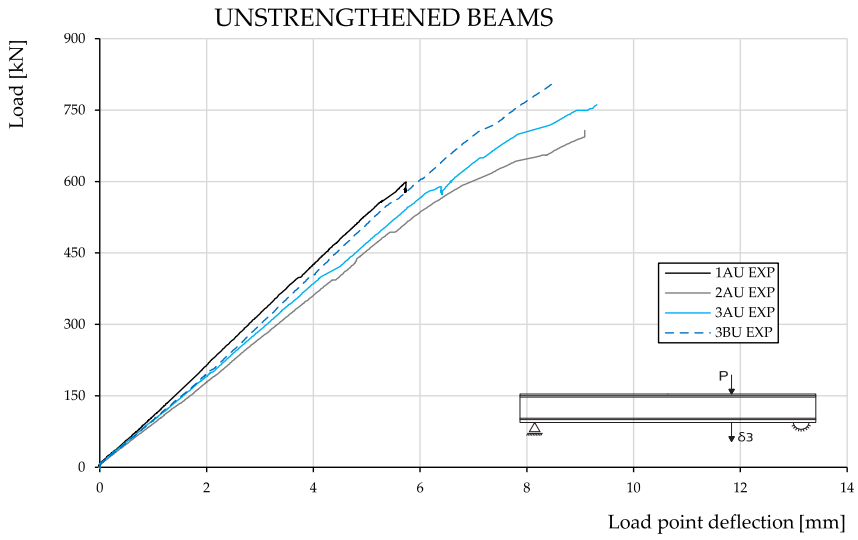
	Side	Pre-Crack Target [mm]	Max Load [kN]	Max Deflection [mm]
BEAM1	A	0.17	599	5.7
BEAM2	A	0.39	708	9.1
BEAM3	A	0.60	761	9.3
	B	0.62	805	8.4

The experimental tests were conducted at the Eucentre Laboratory in Pavia. Figure 3-9 presents the load–displacement response measured at the loading point for the unstrengthened (Figure 3-9a) and strengthened (Figure 3-9b) configurations on Side

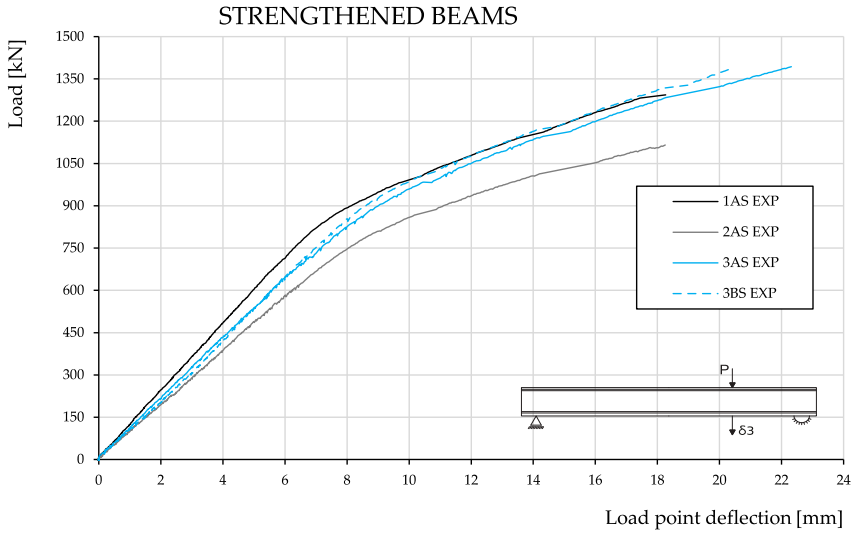
A. In the unstrengthened condition, Beam 2 exhibited the lowest initial stiffness and load-carrying capacity, reflecting its more severe degradation state. This specimen was located at the edge of the bridge deck, where exposure conditions were more aggressive, likely accelerating corrosion processes and material deterioration. The reduced stiffness observed in the grey curve is therefore consistent with the documented damage level.

A similar ranking of stiffness among specimens was observed after strengthening. Beam 1 remained the stiffest element, while Beam 2 continued to exhibit the lowest stiffness in the strengthened configuration. This consistent trend indicates that the strengthening intervention, although effective in increasing global capacity, did not fully compensate for the differences in initial degradation conditions.

These results suggest that the performance of the strengthening system is influenced by the residual mechanical integrity of the existing substrate. While the UHPFRC overlay significantly enhances shear capacity, the initial level of deterioration still affects global stiffness and deformation capacity.



(a)



(b)

Figure 3-9: comparison between unstrengthened (a) and strengthened (b) tests.

Figure 3-10 to Figure 3-12 to compare the strengthened tests performed on the same specimens on Side A (continuous lines) and Side B (dashed lines).

It should be emphasized that, with the exception of Beam 3, the Side A tests were intentionally stopped before reaching the maximum capacity of the loading system (approximately 1400 kN). This decision was made to prevent excessive damage to the specimen and to preserve structural integrity for the subsequent Side B test. Consequently, the ultimate load was not always reached during the first strengthened loading phase.

In the Side B tests, Beam 1 and Beam 3 reached the maximum load capacity of the testing setup (1400 kN). For Beam 2, however, premature debonding of one of the FRP plates at the intrados triggered a sudden load drop (Figure 3-13), leading to test interruption before reaching the actuator limit.

This behaviour highlights the sensitivity of externally bonded FRP systems to interface performance and local damage conditions, particularly in specimens exhibiting more severe initial degradation.

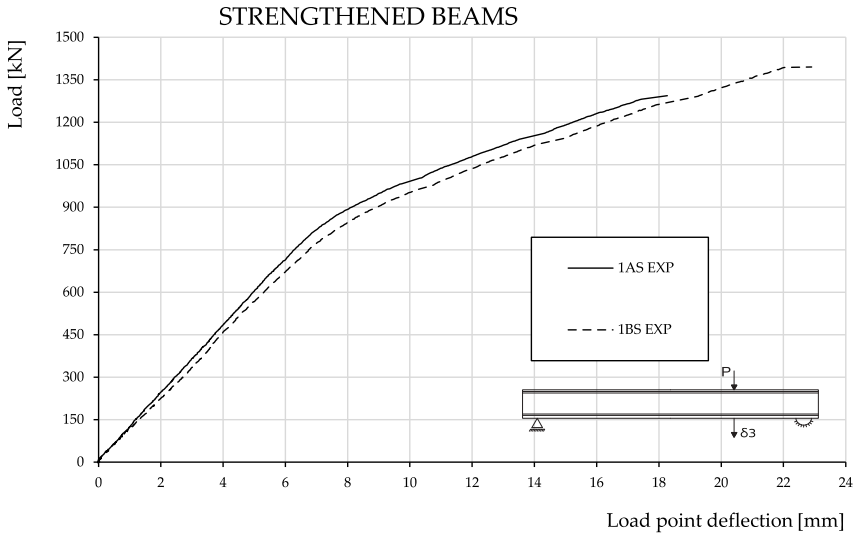


Figure 3-10: comparison between side A and side B pf the strengthened tests in Beam 1.

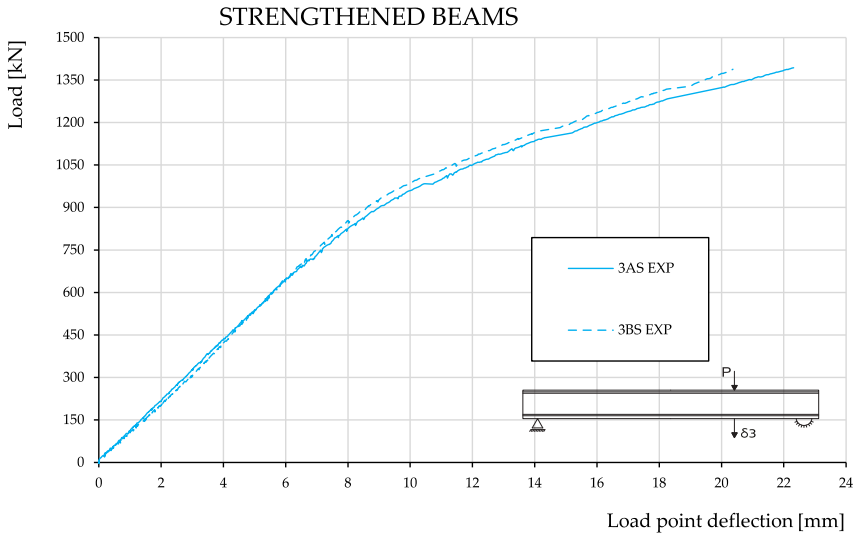


Figure 3-11: comparison between side A and side B pf the strengthened tests in Beam 3.

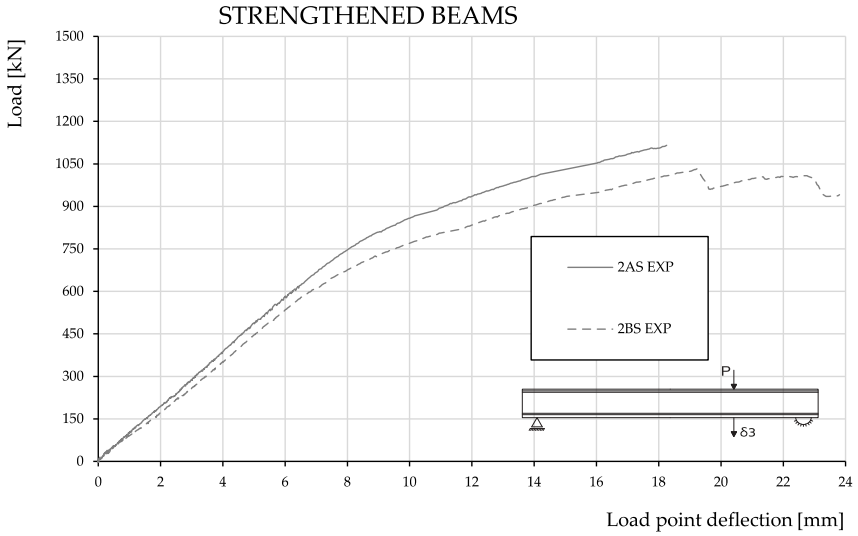


Figure 3-12: comparison between side A and side B pf the strengthened tests in Beam 2



Figure 3-13: debonding of an FRP plate at the intrados.

In Beam 1, the stiffness recorded during the Side B test was slightly lower than that observed in Side A. This reduction is consistent with the additional damage accumulated during the first loading phase which affected the global structural response in the subsequent test.

Beam 3 exhibited a nearly comparable load–displacement response in the two configurations. However, an initially unexpected trend was observed: the stiffness measured in the Side A test was lower than that recorded in Side B. Further investigation revealed that this behaviour was associated with the more severe degradation of the bottom flange on Side A, where extensive concrete cover loss and corrosion of the prestressing strands were documented (Figure 3-2c).
This observation confirms that local deterioration of critical regions, particularly in the tensile zone, can significantly influence global stiffness, even after strengthening. The reported values in Table 3-5 represent the maximum loads reached during each test. None of the specimens were tested to structural collapse.

Table 3-5: Experimentally achieved peak loads and corresponding test conditions for all beam configurations.

Beam–Side–Test	**Max P_{exp} [kN]**	**Note**	**δ_{exp} at P_{max} [mm]**
1AU EXP	599	Reached pre-crack target (0.17 mm)	5.7
1AS EXP	1294	Stopped to avoid excessive damages in side B.	18.3
1BS EXP	1395	Set-up Limit	23.0
2AU EXP	708	Reached pre-crack target (0.39 mm)	9.1
2AS EXP	1116	Stopped to avoid excessive damages in side B.	18.4
2BS EXP	1033	Debonding of FRP	23.9
3AU EXP	761	Reached pre-crack target (0.60 mm)	9.33
3BU EXP	805	Reached pre-crack target (0.62 mm)	8.4
3AS EXP	1393	Set-up Limit.	22.4
3BSEXP	1388	Set-up Limit	21.0

Unstrengthened beams were intentionally unloaded upon reaching the predefined pre-cracking targets, while strengthened beams were either stopped to preserve the opposite side for subsequent testing, interrupted due to FRP debonding, or limited by actuator capacity. Therefore, the experimental values should be interpreted as achieved peak loads rather than ultimate capacities. Therefore, direct comparison of ultimate experimental capacities between configurations is not possible, and numerical simulations were used to estimate ultimate resistance.

Following completion of the experimental campaign, a detailed post-test survey was performed to document crack patterns and damage distribution. The crack width values recorded by W1 were adopted for the crack width–shear diagrams reported in Figure 3-14 and Figure 3-15.
The figures present the relationship between shear force and crack opening for the unstrengthened and strengthened configurations, respectively. It should be noted that the curve labeled 2AS_EXP is not included in the graph due to instrumentation malfunction during the test.
The crack width values of the unstrengthened beams are governed by the predefined pre-cracking targets. Nevertheless, Beam 2 exhibits a trend very similar, in terms of crack openings, to Beam 3 – Side A. Beam 1 was subjected to the lowest pre-cracking target; accordingly, its curve (black line) terminates significantly earlier than the others.

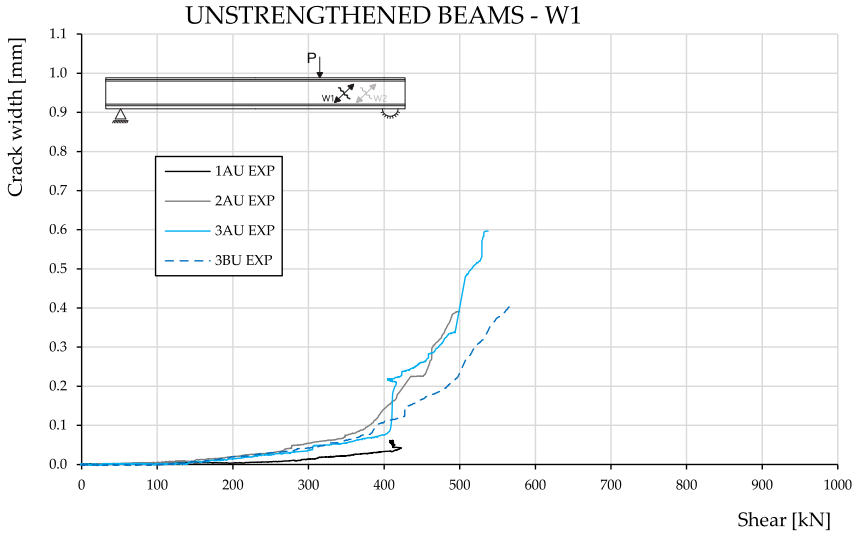


Figure 3-14: crack width diagram of the unstrengthened tests.

The strengthened response curves (Figure 3-15) indicate that, despite Beam 2 being subjected to a lower pre-cracking target than Beam 3, its behaviour is intermediate

between Beam 3 – Side A and Beam 3 – Side B. This trend may be associated with the more advanced initial damage state of Beam 2 before the strengthening intervention.

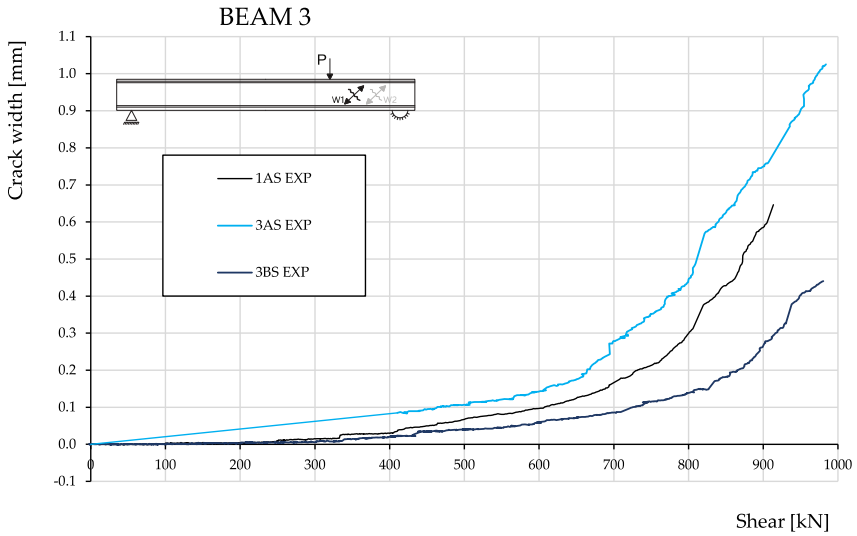


Figure 3-15: crack width diagram of the strengthened tests.

Figure 3-16 reports the crack width–shear response for Beam 3, comparing the unstrengthened (dashed lines) and strengthened (continuous lines) configurations. For a given shear level, the strengthened beam exhibits a markedly reduced crack opening. This reduction is particularly significant from a durability perspective. Limiting crack width directly decreases the potential ingress of moisture and aggressive agents, thereby improving protection of the existing reinforcement system against further corrosion.

Moreover, the strengthened configuration demonstrates a more gradual crack development, delaying the onset of large crack openings and preventing sudden crack widening. This behaviour reflects improved post-cracking performance and enhanced control of shear crack propagation, which are key advantages of the UHPFRC overlay system.

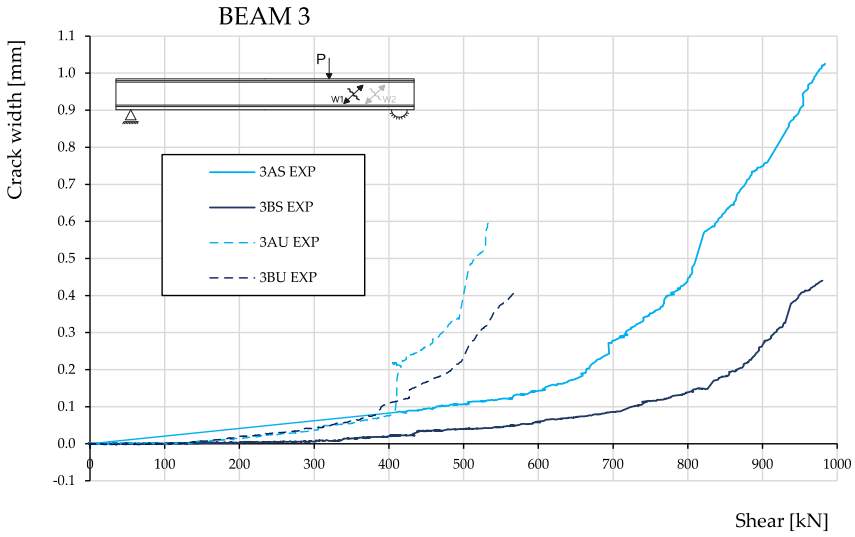


Figure 3-16: comparison of crack width between unstrengthened and strengthened tests in Beam 3

Figure 3-17 presents, as an example, the crack pattern of Beam 3. The upper portion of the figure illustrates the cracks developed during the Side A test, with different colours distinguishing the east (black) and west (grey) faces of the beam. The location of the W1 transducer is also indicated in Figure 3-17b. This instrument was installed on the east side of the girder and was used to monitor the principal shear crack opening.

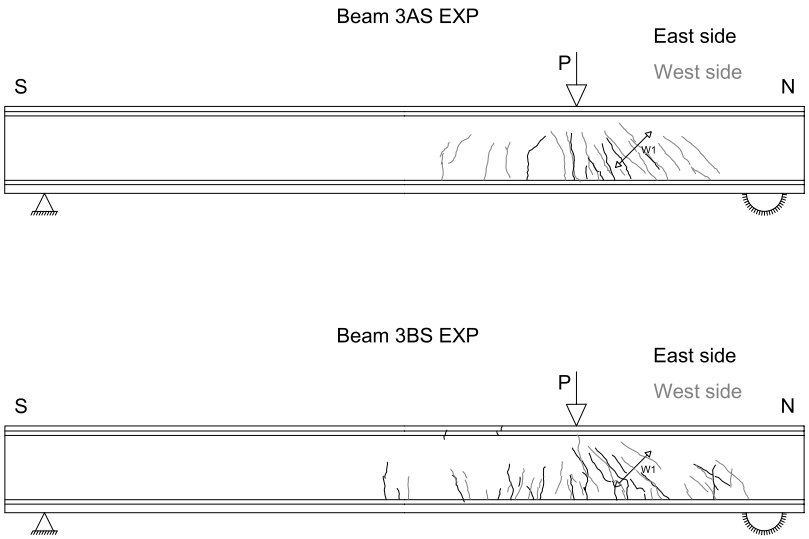


Figure 3-17: comparison of crack width between unstrenghtened and strengthened tests in Beam 3 (a); crack pattern of 3A and 3B tests (b).

To provide a quantitative comparison of the cracking behaviour before and after strengthening, crack-width values were extracted at fixed load and shear levels common to all specimens (Table 3-6). The load point displacement was evaluated at a load level of 500 kN, while crack widths were measured at shear forces of 400 kN and 500 kN by the W1 instrument.
Crack-width reduction was computed as:

$$Red[\%] = \frac{w_u - w_s}{w_u} \cdot 100$$

where w_u and w_s represent the crack width measured in the unstrengthened and strengthened configurations, respectively, at the same shear level.
Reduction values are reported only when the unstrengthened reference test reached the corresponding shear level.

Table 3-6:Midspan displacement at 500 kN and crack-width values at fixed shear levels for unstrengthened and strengthened configurations.

Beam	δ at 500 kN Load [mm]	w at 400 kN Shear [mm]	Crack Width Reduction [%]	w at 500 kN Shear [mm]	Crack Width Reduction [%]
1AU EXP	4.7	0.0325	-	-	-
1AS EXP	4.1	0.0297	8.6%	0.0674	-
1BS EXP	4.3	0.0312	4%	0.0483	-
2AU EXP	5.6	0.0142	-	0.3917	-
2AS EXP	5.1	0.0061	57%	0.0084	98%
2BS EXP	5.6	0.0223	-57%	0.0464	88%
3AU EXP	5.3	0.0747	-	0.3362	-
3BU EXP	4.9	0.108	-	0.2232	-
3AS EXP	4.6	0.0731	2%	0.107	68%
3BSEXP	4.7	0.0204	81%	0.0392	82%

Table 3-6 highlights the influence of the UHPFRC strengthening on both global deformation and crack-control performance.

At a load level of 500 kN, the midspan displacements of strengthened beams are generally comparable to or slightly lower than those of the unstrengthened configuration, indicating a moderate increase in global stiffness. The effect is more pronounced in some specimens (e.g., Beam 3A), while in others the difference remains limited, suggesting that the overall flexural stiffness is still governed primarily by the original section properties and the pre-existing damage state.

More significant differences emerge in terms of crack-width control. At a shear level of 400 kN, the reduction in crack width ranges from negligible values (2–9% for Beam 1 and Beam 3A) up to 81% for Beam 3BS. The variability reflects the different pre-damage levels and side-specific conditions. In one case (Beam 2BS at 400 kN), a negative value is observed, indicating an increase in crack width relative to the unstrengthened reference. This behaviour is likely influenced by prior damage accumulation and the local effects associated with FRP debonding.

At the higher shear level of 500 kN, the strengthening effect becomes markedly more pronounced. Crack-width reductions between 68% and 98% are recorded for the strengthened specimens, demonstrating the substantial contribution of the UHPFRC overlays to shear crack control under high demand levels. These results confirm that, although the experimental tests were not carried out to collapse, the strengthening intervention significantly enhances the post-cracking behaviour and improves durability-related performance indicators.

The crack pattern shown in Figure 3-17 further confirms the influence of the strengthening intervention on the structural behaviour. In the unstrengthened configuration, shear cracks developed more rapidly. The crack distribution appears relatively concentrated, with few dominant cracks governing the response, which is consistent with a shear-critical and potentially brittle mechanism.
After strengthening, the crack pattern becomes more distributed and controlled. Although inclined shear cracks are still present, their propagation is less abrupt and their openings remain significantly smaller. The presence of the UHPFRC overlays contributes to a more uniform stress redistribution along the web, promoting multiple cracking rather than localization into a single dominant crack.
This change in cracking morphology reflects the enhanced post-cracking tensile capacity provided by the UHPFRC layers and supports the observed reduction in crack width reported in Figure 3-16. The overall crack pattern suggests a transition toward a more stable and controlled failure mechanism, consistent with the improved structural performance recorded in the load–displacement response.

3.3. FINITE ELEMENT MODELS

Nonlinear finite element analyses (NLFEA) were performed for both the unstrengthened and strengthened configurations in order to complement the experimental investigation and to estimate the ultimate capacity of the specimens. In the experimental programme, the unstrengthened beams were intentionally pre-cracked and unloaded without being tested to collapse, due to the limited number of available specimens. Similarly, in the strengthened configuration, the tests did not reach failure because the actuator capacity was limited to 1400 kN. As a result, numerical modelling was necessary to evaluate the ultimate structural behaviour and to fully assess the effectiveness of the adopted strengthening technique.

The finite element analyses were carried out using the software VecTor2, which is based on the Modified Compression Field Theory (MCFT) (Vecchio and Collins 1986). This modelling approach is particularly suitable for reinforced and prestressed concrete elements subjected to shear-dominated loading conditions, as it accounts for cracked concrete behaviour, tension softening, compression softening and interaction between concrete and reinforcement.

3.3.1.Model Geometry and Discretization

Two-dimensional nonlinear finite element models were developed using the software VecTor2, based on the Modified Compression Field Theory (MCFT). Since VecTor2 operates under plane stress assumptions and does not account for out-of-plane stresses or torsional effects, the girders were modelled as 2D plane stress

members. This approach is appropriate for the predominantly flexural–shear behaviour investigated in this study.
Concrete was discretized using quadrilateral finite elements. A non-uniform mesh was adopted to adequately represent stress gradients and reinforcement layout: 50 × 60 mm in the prestress transfer/distribution region, 75 × 60 mm in the remaining portions of the beam, and 50 × 30 mm in the zones between adjacent tendons.
Since VecTor2 is a two-dimensional analysis program, the out-of-plane width of the section is defined as a material property rather than being geometrically discretized. As a consequence, for an I-shaped girder with tapered transitions between the web and the flanges, it is not possible to reproduce the exact three-dimensional geometry of the cross-section.
To address this limitation, three different concrete materials were defined in the model, each associated with a specific effective width corresponding to different regions of the section (web and flanges). In the zones characterized by tapered transitions between web and flanges, an area-equivalence approach was adopted (Figure 3-18). The effective widths were determined so that the two-dimensional model preserved the actual cross-sectional area of the girder.
This strategy ensures that the global stiffness and axial capacity of the section are correctly represented, despite the geometrical simplification inherent to the plane-stress modelling approach.

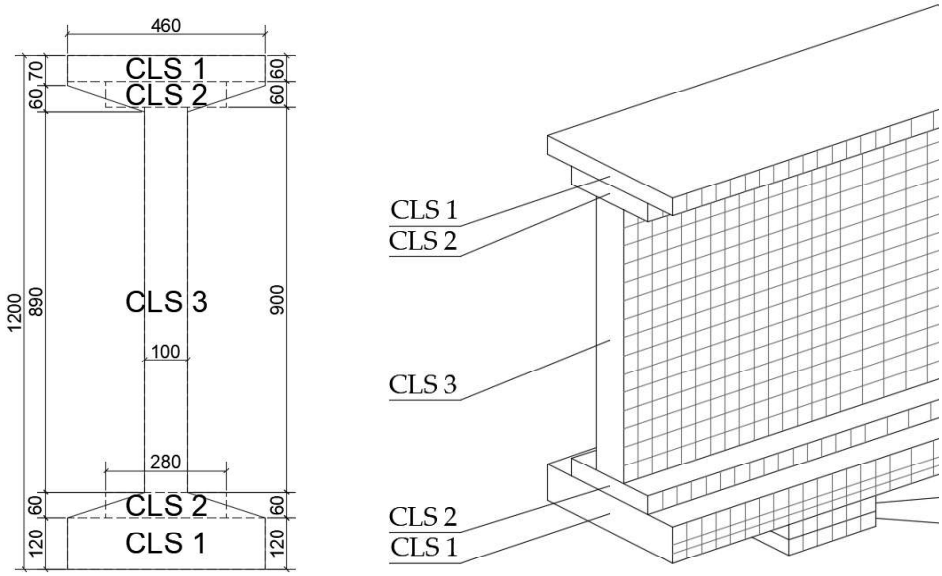


Figure 3-18: simplification of the concrete area in the numerical model in order to account for the geometrical tapering of the cross-section: (a) schematic drawing; (b) 3D view.

Prestressing tendons were modelled as discrete reinforcement elements embedded within the concrete mesh. VecTor2 does not explicitly simulate the diffusion of

prestressing force along the transfer length. To overcome this limitation, different concrete regions were assigned varying prestress levels equal to 25%, 50%, 75% and 100% of the effective prestressing force, net of long-term losses (with the exception of elastic shortening, which is directly accounted for by the software). The prestress transfer length was assumed equal to 47 cm, in accordance with the original design documentation, and was approximated to 45 cm in the numerical model. Within this length, prestress was progressively redistributed before reaching the support restraint, thereby reproducing the stress gradient associated with prestress transfer.
The prestressing force was introduced according to the values specified in the original project (Table 3-7). Since the software requires the initial strain in the steel strands rather than the prestressing force, the imposed strain was calculated by dividing the effective prestressing force by the elastic modulus of steel (185 GPa). Table 3-8 shows the employed values of prestrain.
The initial tendon strain was first determined for the reference beam and subsequently maintained constant in all degradation scenarios. In other words, the imposed prestressing deformation was kept unchanged across different modelling cases, while variations in structural response were attributed exclusively to changes in material properties. This approach ensures consistency among scenarios and prevents artificial differences in prestress level from influencing the comparative analysis.

Table 3-7:Prestress losses and effective prestress stress of the original project.

	Stress loss [MPa]
Shrinkage	50
Concrete creep	30
Concrete elastic shortening	60
Steel relaxation	162
Total prestress losses	302
Initial prestressing stress	1350
Effective prestressing stress	1050

Table 3-8:prestrain values

Prestrain [mm/m]							
25%	1,5	**50%**	3	**75%**	4.5	**100%**	6

Concerning transverse reinforcement, only the two full-height stirrups crossing the neutral axis were explicitly modelled as truss elements, while the confinement contribution of secondary stirrup branches was neglected. The stirrups were represented as discrete truss elements, positioned according to the original design layout. Longitudinal reinforcement located in compression zones was modelled as smeared reinforcement, due to its limited contribution to shear resistance and to reduce unnecessary model complexity.

Figure 3-19 illustrates the finite element model of the unstrengthened configuration, including the concrete discretization, reinforcement layout and prestressing tendons, according to the modelling assumptions described above.

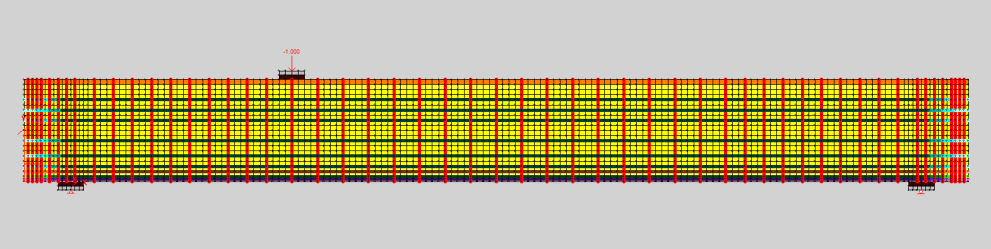


Figure 3-19: Vt2 model for the unstrengthened beams.

In the strengthened models, UHPFRC web layers and FRP plates were added to the existing substrate (Figure 3-20). The FRP plate was modelled as externally bonded linear elastic reinforcement positioned at the intrados.
Two alternative interface conditions between the existing concrete and the UHPFRC overlay were investigated:

- **Perfect bond condition**: the overlay elements were superimposed onto the existing concrete elements, sharing the same nodes and therefore enforcing full compatibility of displacements (Figure 3-21a).

- **Non-perfect bond condition**: double nodes were introduced at the interface and connected by one-dimensional link elements, allowing simulation of bond–slip behaviour between the substrate and the overlay((Figure 3-21b). The bond properties assigned to the link elements were derived from experimental shear bond tests.

It is worth noting that the integrative transverse reinforcement provided by dowels was not included in the strengthened numerical models. This assumption was adopted since numerical results indicate that, after strengthening, the governing failure mechanism shifts from shear to flexure. Furthermore, the choice is conservative.

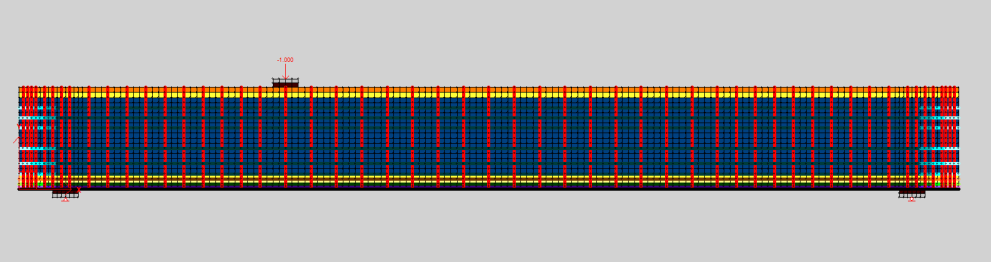
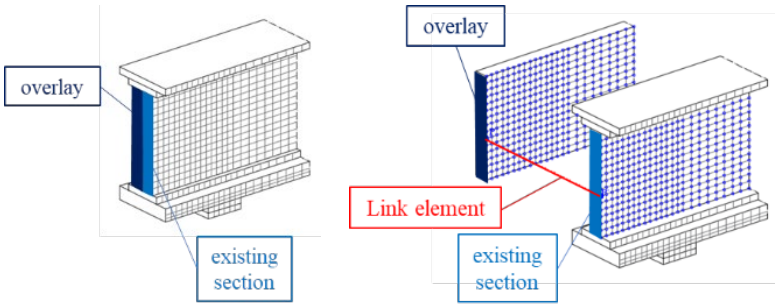


Figure 3-20: Vt2 model for the strengthened beams.



(a) (b)

Figure 3-21:bond modelling between existing section and overlay in the cases of perfect bond conditions (a) and not perfect bond conditions (b).

3.3.2. Boundary conditions and loading phases

The boundary conditions adopted in the numerical models reproduced the experimental setup. The beam was modelled as simply supported, with one support restrained in both vertical and horizontal directions and the other restrained only in the vertical direction, allowing longitudinal displacement and preventing artificial axial restraint.

The loading procedure was implemented in two sequential steps. The first step included the application of the self-weight of the beam, introduced as a uniformly distributed load and converted into equivalent nodal forces applied at each upper node. The unit weight of concrete was assumed equal to 23 kN/m³, in accordance with the results of the preliminary diagnostic and destructive tests (concrete cores). This corresponded to nodal forces ranging from approximately 0.24 kN near the supports to 0.37 kN at midspan, due to the different finite element dimensions along the beam.

In the strengthened simulations, the self-weight of the UHPFRC layer was also included, assuming a unit weight equal to 24 kN/m³. The corresponding nodal forces ranged from approximately 0.11 kN near the supports to 0.16 kN at midspan. The

self-weight of the FRP plates was neglected due to its negligible contribution compared to the concrete and UHPFRC components.
In the second loading step, the analysis was performed under displacement control. A vertical displacement was imposed at the loading point, consistently with the experimental procedure. This approach allowed a direct comparison with the experimental load–displacement curves.
In order to allow proper diffusion of the imposed displacement and of the support reactions, the real load-distribution systems used in the experimental tests were explicitly modelled. These consisted of a steel distribution plate at the loading point and neoprene pads at the supports. Their inclusion ensured a realistic transfer of stresses and prevented artificial stress concentrations in the numerical model.

3.3.3. Constitutive lows

The nonlinear material behaviour was modelled using the constitutive relationships available in VecTor2 within the framework of the Modified Compression Field Theory (MCFT).
In compression, the pre-peak response of concrete was modelled using the Hoshikuma et al. parabolic relationship, while the post-peak behaviour followed the Modified Park–Kent model. Compression softening due to transverse cracking was represented using the Vecchio 1992-A model, consistent with MCFT assumptions.
In tension, cracking was governed by a Mohr–Coulomb stress criterion, and post-cracking tensile behaviour was described using a nonlinear softening law according to Hordijk. Tension stiffening effects were incorporated using the Modified Bentz (2005) model, allowing simulation of stress transfer across cracked concrete.
Crack-slip behaviour was modelled according to the Walraven formulation, while confined concrete strength was evaluated using the Kupfer–Richart model.
For the UHPFRC overlay, tensile behaviour was modelled using the SDEM-Monotonic model, which allows representation of enhanced tensile resistance and strain-hardening behaviour typical of fibre-reinforced cementitious materials. Compressive behaviour followed the same nonlinear framework adopted for conventional concrete, with material parameters adjusted to reflect the higher strength and stiffness.
Reinforcing steel was modelled using an elastic–plastic constitutive law including strain hardening. Cyclic effects were represented using the Seckin model (Bauschinger effect), although analyses were monotonic.
Buckling of compression reinforcement was considered using the Akkaya (2012) formulation.
Prestressing tendons were assigned an initial strain corresponding to the effective prestress level, as described in the previous section.

The FRP plates were modelled as linear elastic materials up to failure, without plasticity, consistent with their brittle mechanical behaviour.

3.3.4. Diagnostic and Materials Properties

Information regarding the material properties was retrieved from the original design documentation. The girders were precast using an accelerated curing process, and the specified concrete compressive strength at 28 days was approximately 60 MPa.
The prestressing system consisted of 3/8″ strands, whose mechanical properties are summarized in Table 3-9. The transverse reinforcement (stirrups) was identified in the original project as Aq50 steel with improved bond characteristics. However, no mechanical properties were explicitly provided in the documentation. Therefore, the material parameters were defined based on values reported in the literature (Verderame et al. 2011) for steels of comparable typology (first row of Table 3-10).

Table 3-9: Strands properties in the original design.

	Original Design - Strands				
Φ **["]**	**A** **[mm^2]**	**E** **[GPa]**	**f_{yk}** **[MPa]**	**f_{uk}** **[MPa]**	**σ_{ap}** **[MPa]**
3/8	52	200	1600	1800	1048

The diagnostic investigation was conducted in multiple phases. The first campaign, hereafter referred to as Diagnostic 1, was performed on girders belonging to the original bridge structure but different from those selected for full-scale testing. In addition to visual inspections, this campaign included mechanical characterization of the principal structural materials. The experimental program comprised:

- compressive tests on concrete core samples,
- tensile tests on prestressing strands,
- tensile tests on transverse reinforcement (stirrups).

Although these tests were carried out on girders different from the specimens tested in the experimental campaign, the results were considered representative. The precast production process and accelerated curing adopted during construction reasonably ensured uniform material properties and controlled manufacturing conditions.
A total of five core samples were extracted from external-span girders (11 m) and three from central-span girders (24 m). The cores had approximately equal height and diameter (≈95 mm), leading to measured compressive strengths corresponding to cube resistance. Cylindrical compressive strength was subsequently derived through the relationship prescribed by NTC2018 (f_{ck}=0.83R_{ck}).

The compressive strength adopted for modelling was defined as the mean value of the tests, excluding two significantly lower results that were deemed non-representative compared to the remaining dataset.
Prestressing strands (nominal diameter 6.9 mm) were extracted from two external girders. Two specimens were tested, with lengths of 450 mm and 461 mm, respectively, one from an external span and one from a central span.
The measured tensile strengths were significantly lower than typical expected values for this type of strand, most likely due to the advanced corrosion state of the extracted samples. The tensile resistance used in the numerical analyses was defined as the mean stress obtained from the two tests.
Two stirrup samples were tested in tension. One test yielded a markedly low yield stress compared to the other specimen and was therefore excluded from the material characterization. As a consequence, the mechanical properties adopted for stirrups are based on a single representative tensile test.
The principal material properties derived from Diagnostic 1 are reported in Table 3-10 (second row). The differences between Table 3-9 and Table 3-10 are due to the nature of the values considered: Table 3-9 presents characteristic design values from the original documentation, whereas Table 3-10 reports mean values derived from experimental testing and adopted in the numerical analyses.

Table 3-10: material properties from the Original Project and Diagnostic Campaigns.

	Concrete	**Strands**					**Stirrups**	
	f_c [MPa]	A [mm^2]	E [GPa]	f_y [MPa]	f_u [MPa]	ε_u [%]	f_y [MPa]	f_u [MPa]
Original Design	58	52	200	1780	1945	6.3	370*	542*
Diagnostic 1	45	37,8	185	1340	1490	5.5	408	592
Diagnostic 2	36	51	165	1417	1610	3.4	465	670

Following the preliminary diagnostic campaign, a second investigation phase (hereafter referred to as Diagnostic 2) was conducted at the Eucentre Laboratory in Pavia on one of the experimental specimens, namely Beam 3.
This in-depth diagnostic phase allowed verification of the actual reinforcement layout and revealed discrepancies with respect to the original design drawings. In particular, it was observed that the strand arrangement adopted for the 11 m span girders differed from that reported in the executive project documentation. This finding confirmed the necessity of direct inspection when assessing existing structures, as original drawings may not fully reflect the as-built configuration.

Beam 3 was selected for this additional investigation because it exhibited an intermediate level of degradation in its initial condition, prior to strengthening. Unlike the most severely damaged specimen, Beam 3 did not present concrete cover loss in the web core region, which facilitated extraction of concrete core samples for material testing. However, the strands located in the bottom flange were partially exposed and affected by corrosion (Figure 3-22), providing representative evidence of deterioration in the tensile zone.



Figure 3-22: Initial degradation condition of Beam 3 (side A, side B and bottom flange intrados).

Five concrete core samples were extracted from Beam 3 for compressive testing. The cores had equal height and diameter (75 mm), ensuring consistency in specimen geometry. The cylindrical compressive strength was determined following the same procedure adopted for Diagnostic 1.

In addition to compressive tests, carbonation depth was evaluated on the extracted samples using phenolphthalein indicator. The non-coloured regions correspond to carbonated concrete, as shown in Figure 3-23. The measured carbonation penetration did not reach the level of the transverse reinforcement. This result is consistent with the observed initial degradation condition of Beam 3, which did not exhibit significant concrete cover loss in the web region.

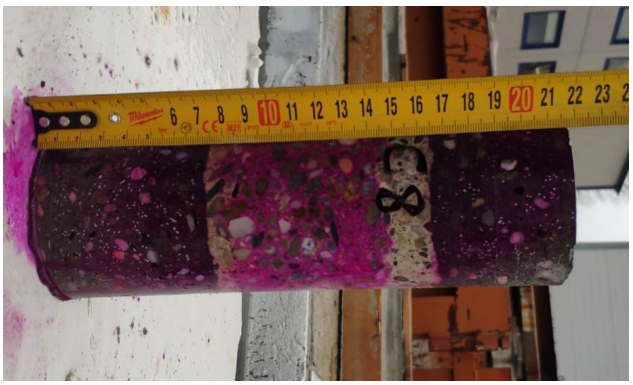


Figure 3-23: example of carbonation test on core-sample.

Seven prestressing strands were subjected to tensile testing as part of Diagnostic 2. Table 3-11 summarizes the results of the tensile tests performed on the extracted prestressing strands. The meaning of each column is specified below.

- **L_0** represents the gauge length, i.e. the length of strand between the grips during the tensile test.
- m is the mass of the specimen (in grams), while l is the total length of the strand sample.

Since the nominal diameter was not directly measured, the specimen mass and total length were used to determine an equivalent diameter. The calculation was performed assuming a steel density equal to 7.81 kg/dm³ and a circular cross-section. Based on the measured mass and length, the equivalent cross-sectional area was first obtained and subsequently used to derive the corresponding equivalent diameter. This area was then adopted for stress evaluation.

- P_u denotes the experimentally measured ultimate tensile load.
- f_u represents the ultimate tensile stress, calculated by dividing the measured load by the equivalent cross-sectional area.
- f_γ was defined as the stress corresponding to a strain level of 1%, consistently with common practice for prestressing steel characterization.
- ε_u is the ultimate strain, obtained from the measured elongation at failure divided by the gauge length L_0.

However, not all test results were included in the calculation of the mean mechanical properties.
In particular, some specimens failed prematurely within the testing clamps, indicating a non-representative failure mode. In other cases, the measured tensile resistance was significantly lower than the remaining results and was considered

inconsistent with the general trend of the dataset. These values were therefore excluded from the statistical evaluation of the mean mechanical properties.
The excluded results are indicated in grey in Table 3-11 for the sake of transparency.

Table 3-11: strands data elaboration in Diagnostic 2.

ID Test	L0 [mm]	m [g]	l [mm]	ϕ_{eq} [mm]	P_y [kN]	P_u [kN]	f_y [MPa]	f_u [MPa]	ε_u [mm/m]
T1	654	337	840	8,09	77,8	87,0	1515	1694	42
T2	664	343	860	8,06	68,8	72,3	1348	1416	13
T3	588	310	765	8,13	73,9	86,6	1424	1669	46
T4	600	271	665	8,15	79,3	86,7	1521	1662	32
T5	725	408	900	8,60	73,8	97,9	1272	1687	42
T6	600	351	870	8,11	-	61,7	-	1195	14
T7	600	384	965	8,05	-	38,3	-	751	9
mean value	**-**	**-**	**-**	**-**	**75,07**	**83,2**	**1452**	**1610**	**34**
CoV [%]							6	8	45

Figure 3-24 presents the stress–strain curves obtained from the tensile tests performed on the extracted prestressing strands. The dashed curves correspond to the specimens excluded from the calculation of the mean mechanical properties, as discussed previously.
The horizontal dashed black line represents the ultimate tensile strength adopted in the original design documentation. This reference value allows a direct comparison between the experimentally measured strand performance and the design assumptions.

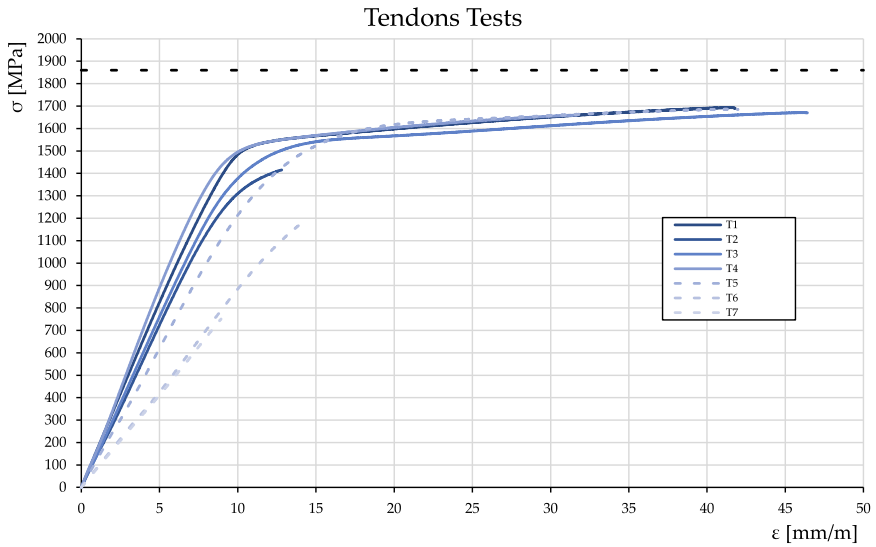


Figure 3-24:tendons tests in terms of stress and strain.

Finally, tensile tests were also performed on the extracted stirrups and longitudinal reinforcing bars. The corresponding mechanical properties are summarized in Table 3-12 and in Table 3-13, respectively.

Table 3-12: stirrups data elaboration in Diagnostic 2.

ID Test	Φ [mm]	ε_u [%]	f_y [MPa]	f_u [MPa]
1	10	13,3	453	646
2	10	12,1	465	670
3	10	9,9	478	694
4	10	9,7	-	668
mean	**10**	**11,3**	**465**	**670**
CoV [%]				**3.0**

Table 3-13: longitudinal rebars elaboration data in Diagnostic 2.

ID Test	Φ [mm]	ε_u [%]	f_y [MPa]	f_u [MPa]
1	12	12,6	428	658
2	12	12,0	434	655
3	12	12,1	433	660
4	12	15,9	453	672
mean	**12**	**13,2**	**437**	**661**
CoV [%]				**1.1**

3.3.5.Numerical Results

Two geometric configurations were considered in the finite element analyses: one representing the unstrengthened condition (U) and one representing the strengthened configuration (S). For each geometry, three different sets of material properties were assigned, derived respectively from the Original Design documentation (Reference Beam – RB), Diagnostic 1 (S1) and Diagnostic 2 (S2). As a result, six numerical analyses were performed, as summarized in Table 3-14. It should be noted that, in this modelling approach, differences in the initial degradation state among the three tested girders were not explicitly simulated. Instead, a common geometric model was adopted, and variability was introduced exclusively through material properties. This assumption allows a clearer

interpretation of the influence of material degradation on structural performance, while isolating geometric effects.

Although this simplification neglects specimen-specific damage patterns, it enables a consistent comparison among scenarios and highlights the sensitivity of structural response to variations in mechanical properties.

Table 3-14: Numerical Analyses Names

Model Name	Unstrengthened (U) or Strengthened (S)	Materials properties
U RB	U	Original Design
U S1	U	Diagnostic 1
U S2	U	Diagnostic 2
S RB	S	Original Design
S S1	S	Diagnostic 1
S S2	S	Diagnostic 2

The mechanical properties adopted in the numerical analyses are summarized in Table 3-10.

For the Reference Beam (RB) models, based on Original Design data, the yielding and ultimate stresses of stirrups were taken equal to the maximum values measured during Diagnostic 2. This choice was made because the literature-based values initially considered were found to be inconsistent with the experimentally observed mechanical capacity of the extracted specimens. Adopting lower values would have led to an unrealistic underestimation of the original structural capacity. Moreover, it is not mechanically justified to assume that transverse reinforcement, after more than 50 years of service and exposure, would exhibit an increase in strength or ductility compared to its original condition.

Longitudinal reinforcement, in the tested girders, is located predominantly in compression zones. Given its limited contribution to shear resistance, it was modelled as smeared reinforcement rather than as discrete bars. Due to the lack of alternative reliable data, the mechanical properties obtained from Diagnostic 2 (Table 3-13) were adopted consistently in all numerical scenarios.

In the strengthened models, the UHPFRC and FRP materials were added to the existing substrate, while variations among scenarios affected only the mechanical properties of the original concrete and reinforcement. The strengthening materials were kept constant in all strengthened analyses. Moreover, the integrative transverse reinforcement introduced experimentally was not included in the numerical models. As will be discussed later, the strengthened configuration exhibited a shift of the governing failure mechanism from shear to flexure. This indicates that the UHPFRC layers alone provide sufficient shear resistance; therefore, neglecting the integrative stirrups represents a conservative modelling assumption.

Figure 3-25 presents the numerical results for the unstrengthened configuration. The continuous curves represent the experimental pre-cracking phase, while the red dotted line corresponds to the flexural limit (FL), calculated using Response 2000.
The comparison between the flexural limit and the numerical curves indicates that the original design configuration was overdesigned in bending. This is consistent with the findings of the diagnostic investigation, which revealed that the tendon layout in the 11 m span girders differed from the original drawings and corresponded to the arrangement adopted for the 24 m span beams.
All unstrengthened numerical models (blue curves) reach failure governed by shear, with prestressing strands remaining below yielding. When material properties derived from the diagnostic campaigns are adopted (U S1 and U S2), the numerical responses show good agreement with the experimental results of Beam 2 and Beam 3. In particular, the U S2 model (based on Diagnostic 2 performed directly on Beam 3) shows very good correspondence with the experimental curve 3AU_EXP.
As shown in Figure 3-26, the experimental stiffness of Beam 2 is lower than that predicted numerically, whereas Beam 3 exhibits a stiffness response comparable to the numerical model. This difference is consistent with the more severe degradation observed in Beam 2, which is not fully captured by the simplified modelling approach.
The U S1 and U S2 analyses incorporate the degraded material properties obtained from the diagnostic phases, whereas the U RB model, based on original design data, represents an upper-bound condition. Interestingly, Beam 1 initially follows a response close to the U RB curve, which is coherent with its comparatively lower level of degradation.

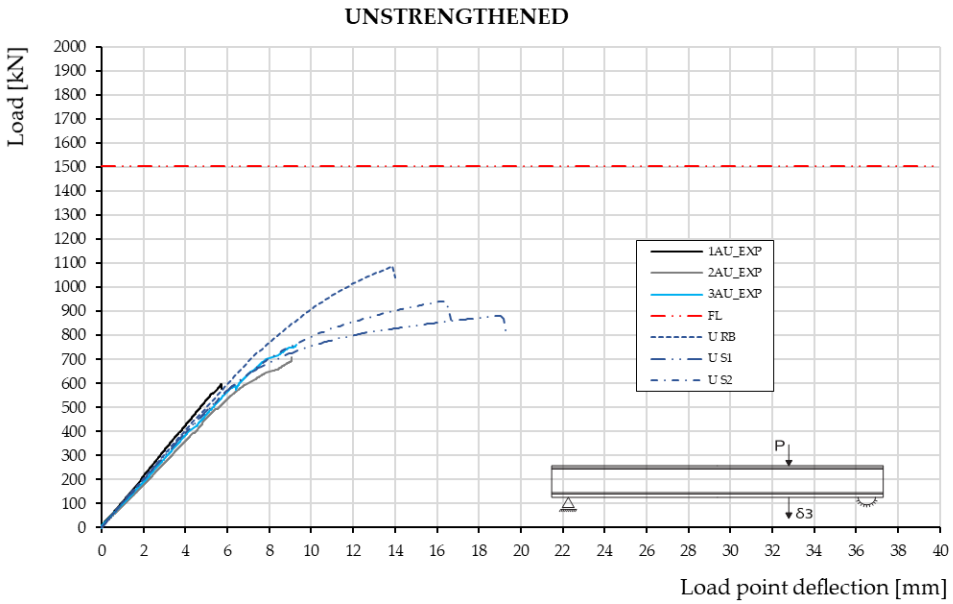


Figure 3-25: Unstrengthened tests and numerical analyses.

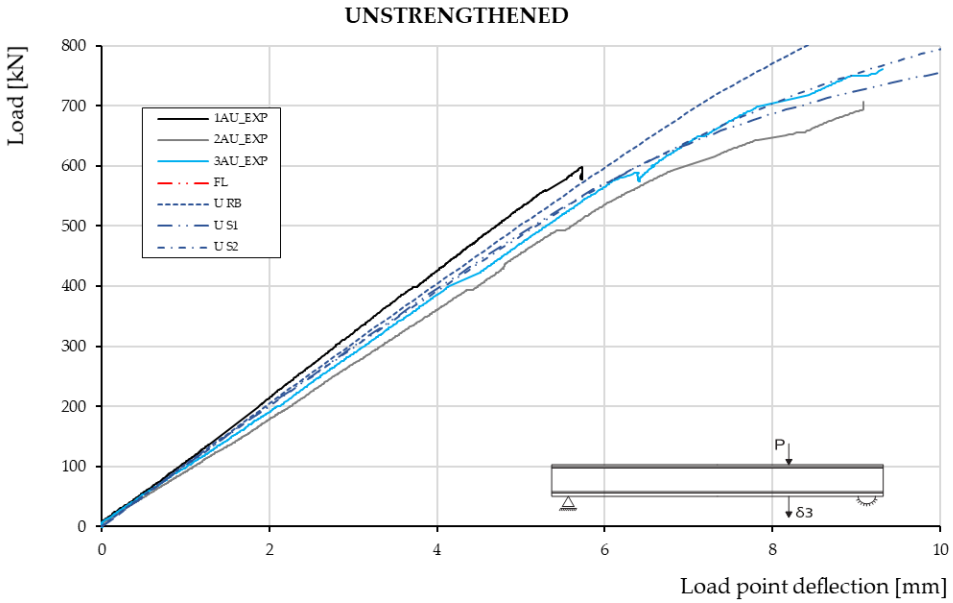


Figure 3-26: Detail of the first branch - Unstrengthened.

To quantify the predictive capability of the numerical models within the experimentally investigated load range, selected response parameters were compared between tests and NLFEA results.

For the unstrengthened configuration (Table 3-15), the load point displacement was evaluated at a load level of 500 kN, which is common to all pre-cracking tests and lies within the stable portion of the response. For the strengthened configuration (Table 3-16), the comparison was performed at 1000 kN, representing a high load level reached by all strengthened specimens while remaining below the actuator limit.

In addition to displacement, the initial stiffness K_0 was evaluated to assess the accuracy of the initial response. The stiffness K_0 was calculated as the secant slope of the load–displacement curve up to 400 kN.

The relative error of the two parameters was computed as:

$$Err[\%] = \frac{NLFEA - EXP}{EXP} \cdot 100$$

where positive values indicate overestimation by the numerical model and negative values indicate underestimation.

For each experimental test, the numerical model reported in the table corresponds to the material-property scenario considered most representative of the specific beam condition (RB, S1 or S2).

Table 3-15: Comparison between experimental results and NLFEA predictions for the unstrengthened configuration within the tested load range (δ evaluated at 500 kN).

Beam–Side–Test	Numerical Model	δ at 500 kN		Error δ [%]	K_0		Error K_0 [%]
		EXP [mm]	NLFEA [mm]		EXP [kN/mm]	NLFEA [kN/mm]	
1AU_EXP	U RB	4.7	5.0	6%	106	101	-5%
2AU_EXP	U S1	5.6	5.2	-7%	89	99	11%
3AU_EXP	U S2	5.3	5.1	-4%	96	98	1%
3BU_EXP	U S2	4.9	5.1	4%	102	98	-4%

The comparison between experimental and numerical results for the unstrengthened configuration shows a very good agreement within the tested load range.

The displacement at 500 kN is predicted with errors ranging between −7% and +6%, indicating that the global flexural stiffness and cracking response are accurately captured by the adopted material parameters.

Similarly, the initial stiffness K_0 is reproduced with deviations within +11% and -5%, with most cases showing errors below 5%. The slightly higher deviation observed for Beam 2 (11%) may be attributed to its more severe degradation state, which is only approximately represented in the numerical model through modified material properties rather than explicit local damage modelling.

Overall, these results confirm that the numerical models provide a reliable representation of the structural response of the unstrengthened beams in the tested range.

Following the analyses of the unstrengthened configuration, the strengthened beams were investigated considering the two alternative interface assumptions previously described, namely perfect bond and non-perfect bond conditions between the existing substrate and the UHPFRC overlay.

The perfect bond hypothesis was considered consistent with the experimental evidence, since no debonding phenomena were observed during testing. The alternative bond–slip model was nevertheless implemented to evaluate the potential influence of interface compliance on global structural response. In fact, during the tests, failure was not reached; therefore, it cannot be established whether, at a higher load level, slippage or material debonding might have occurred.

The comparison between these two modelling approaches allows assessment of the sensitivity of the strengthened system to interface behaviour, while keeping all other material parameters unchanged.

Perfect bond analyses were performed for the same three material scenarios adopted for the unstrengthened configuration. Figure 3-27 compares the numerical predictions with the experimental results.

Under perfect bond assumptions, all strengthened numerical models reached failure governed by flexure, characterized by crushing of the concrete in the compression flange near the loading point. This confirms that the shear capacity provided by the UHPFRC layers was sufficient to prevent shear failure, leading to a shift of the governing mechanism from brittle shear to a more ductile flexural response. The increase in ultimate deflection further supports this transition in structural behaviour.

From the comparison of the load–displacement curves (Figure 3-28), Beam 1 exhibits a response closely matching the S RB model, particularly in the initial stiffness branch. This is consistent with its comparatively lower level of degradation.

Beam 3 shows an intermediate behaviour between the S RB and S S2 numerical predictions. However, its initial stiffness is lower than the corresponding numerical curve, which can be attributed to the higher pre-crack target imposed prior to strengthening (approximately 0.6 mm). The larger initial crack width influenced the early-stage response of the strengthened configuration.

Beam 2 exhibits the lowest stiffness and ultimate load among the strengthened specimens. This behaviour reflects its more severe degradation condition, which is not entirely captured by the simplified material-based modelling approach. The fact that Beam 2 was located at the edge of the bridge deck, and therefore exposed to more aggressive environmental conditions, further explains its reduced structural

performance.

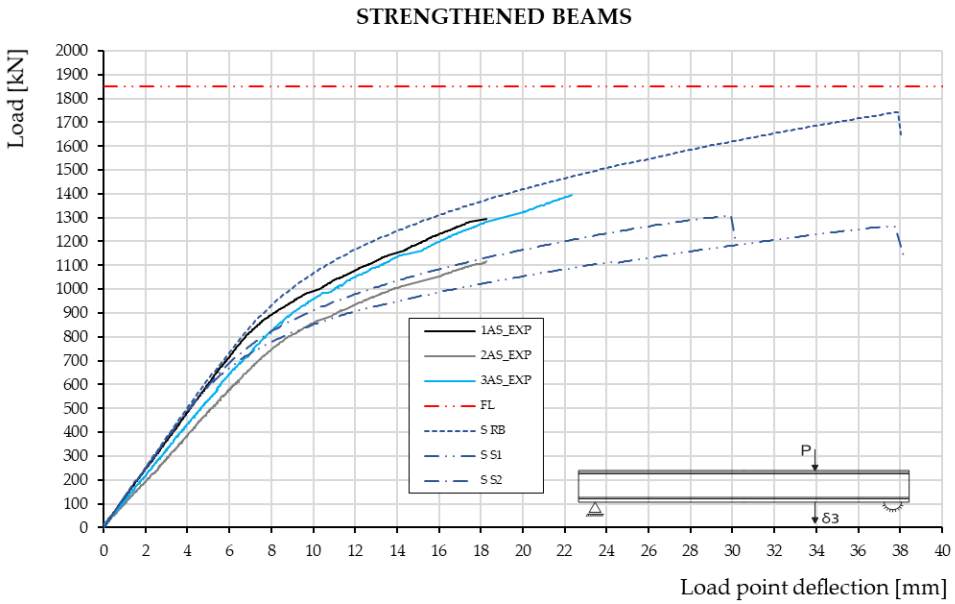


Figure 3-27: Strengthened tests and numerical analyses.

From all the analyses the results indicate that the strengthening intervention results in a more ductile structural response and a significant increase in ultimate capacity.

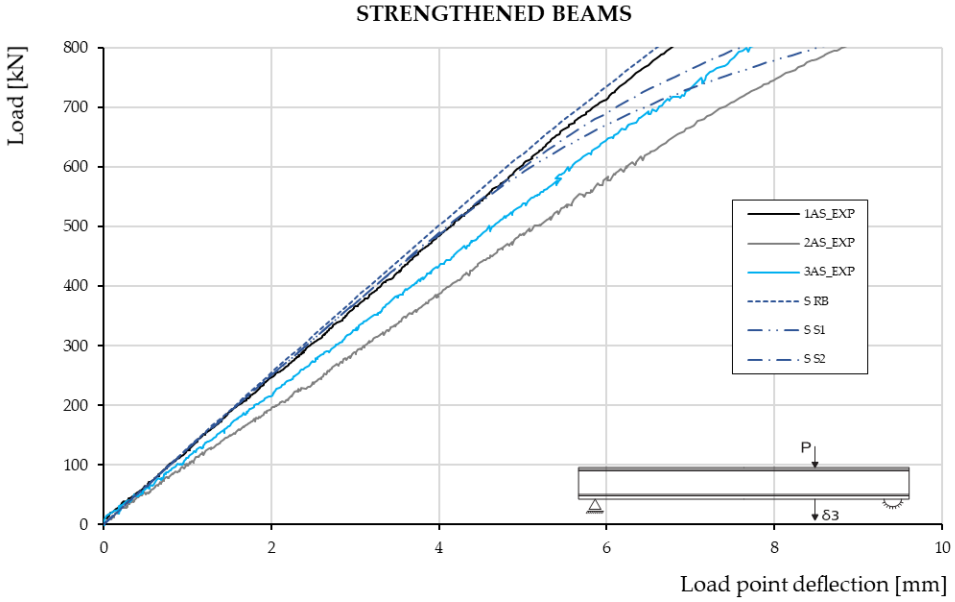


Figure 3-28: Detail of the first branch – Strengthened.

Considering Table 3-16, for the strengthened configuration, the agreement remains satisfactory, although with slightly larger discrepancies compared to the unstrengthened case.

The displacement at 1000 kN is predicted with errors between −13% and +23%. The numerical model tends to slightly overestimate deformability in most cases, particularly for Beam 2 and Beam 3. This behaviour may reflect the simplified modelling of interface conditions and the absence of explicit modelling of local FRP debonding or damage accumulation effects observed experimentally.

The initial stiffness K_0 is reproduced with errors ranging from 4% to 27%. The larger deviation observed for Beam 2 (+27%) is consistent with its higher level of initial degradation and with the experimentally observed FRP debonding, which is not explicitly simulated in the model.

Despite these discrepancies, the model correctly captures the order of magnitude of both stiffness and displacement response, providing a sufficiently accurate basis for extrapolation toward ultimate conditions.

Table 3-16:Comparison between experimental results and NLFEA predictions for the strengthened configuration within the tested load range (δ evaluated at 1000 kN).

Beam–Side–Test	Numerical Model	δ at 1000 kN		Error δ [%]	K_0		Error K_0 [%]
		EXP [mm]	NLFEA [mm]		EXP [kN/mm]	NLFEA [kN/mm]	
1AS_EXP	S RB	10.3	9.0	-13%	121	126	4%
2AS_EXP	S S1	13.8	16.7	21%	97	124	27%
3AS_EXP	S S2	11.0	12.7	15%	109	124	14%
3BS_EXP	S S2	10.3	12.7	23%	105	124	18%

In the unstrengthened case, the agreement is particularly strong, with errors generally below 10%, confirming the adequacy of the adopted material parameters and modelling assumptions.

In the strengthened configuration, although the scatter increases, the model remains within a deviation range that is acceptable for nonlinear analysis of existing, deteriorated structures. This level of agreement justifies the use of NLFEA to estimate ultimate capacity and to identify the governing failure mechanism beyond the experimental load limits imposed by the test setup.

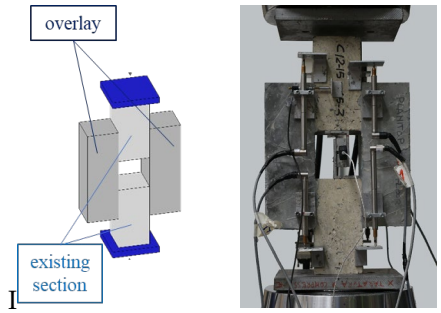
Finally, a model with non-perfect bond conditions was considered, employing only the Original Design material properties (NPB RB). The bond–slip properties assigned to the link elements were derived from experimental shear bond tests available in the literature (Iavarone et al., 2023), whose configuration is schematically represented in Figure 3-29b,c. The bond between the existing concrete substrate and the UHPFRC overlay was modelled using a bilinear bond–slip relationship implemented through link elements at the interface. The adopted τ–s law is summarized in Table 3-17. The resulting interface response is characterized by high initial stiffness and limited relative slip at peak stress, reflecting the mechanical interlock achieved through surface roughening (average amplitude ±3 mm). No post-peak softening branch was introduced, as experimental evidence did not indicate any debonding during the tests.

This assumption represents a conservative approximation, as the bond parameters were derived from shear bond tests performed with the same overlay material, but on substrates with lower mechanical properties (f_c=16/20 MPa) and without mechanical roughening of the surface.

Table 3-17:link element bond properties.

Point#	w [mm]	τ [MPa]
1	0.000	0.0
2	0.000	0.12
3	0.005	1.0

4	0.01	1.71



(a) (b)

Figure 3-29: shear bond tests set up(b) and picture (c).

Figure 3-30 compares the response obtained with perfect bond (PB) and non-perfect bond (NPB) assumptions for the same material scenario (RB).

Despite these conservative assumptions, the NPB analysis predicts a global response very close to that obtained under perfect bond conditions, with only a slightly earlier attainment of ultimate displacement. This indicates that, for the investigated configuration, the structural response is not significantly sensitive to moderate interface compliance. The numerical findings are consistent with the experimental evidence, as no debonding between the overlay and the existing substrate was observed during testing.

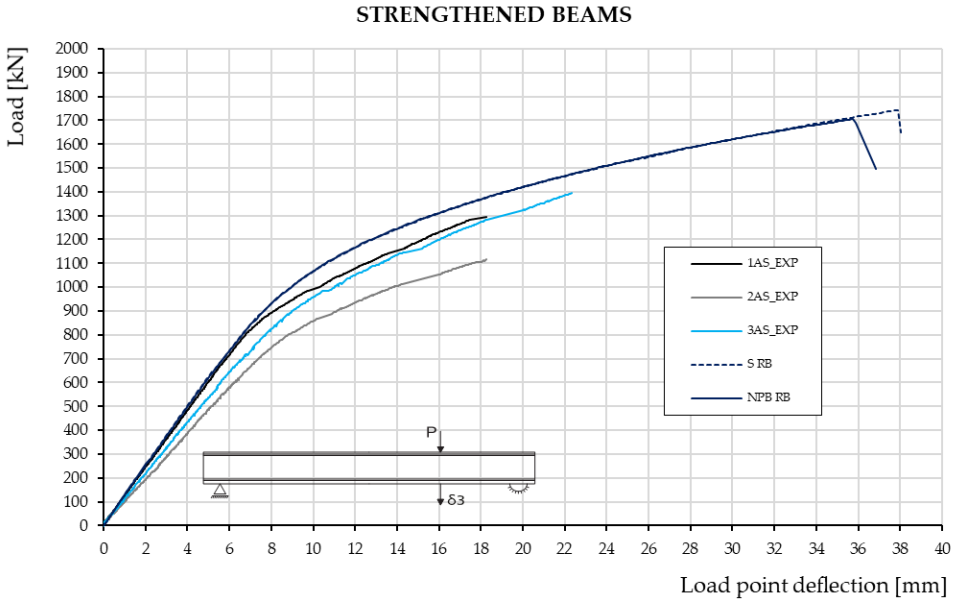


Figure 3-30: Comparison between perfect and not perfect bond conditions for RB analyses.

The crack patterns obtained from the numerical analyses further support the interpretation of the governing failure mechanisms.
In the unstrengthened configuration (Figure 3-31a), the crack pattern is characterized by the development of dominant inclined cracks within the web, extending toward the loading point and the support region. The concentration of principal tensile strains along diagonal trajectories confirms that the failure mechanism is governed by shear. The crack localization in a relatively limited region is consistent with a brittle shear-controlled response.
Conversely, in the strengthened configuration (Figure 3-31b), cracking is more uniformly distributed along the span, with flexural cracks developing in the tensile zone and propagating upward as loading increases. The numerical strain field indicates progressive compression damage in the upper flange near the loading point, leading to concrete crushing and flexural failure.
The comparison between the two crack patterns clearly illustrates the shift in structural behaviour induced by the UHPFRC strengthening, from a shear-dominated brittle mechanism to a flexure-controlled response with enhanced deformation capacity.



(a) (b)

Figure 3-31: crack pattern of the unstrengthened (a) and strengthened (b) numerical models.

The numerical analyses predict an increase in ultimate resistance of approximately 60% after strengthening.
However, the most significant outcome concerns the modification of the collapse mechanism. In the unstrengthened configuration (U RB), failure is governed by diagonal shear cracking, with prestressing strands remaining elastic (maximum stress ≈ 1387 MPa, well below yielding) and concrete compressive stresses limited to −36.7 MPa.
After strengthening, failure shifts to a flexural mechanism controlled by concrete crushing in the compression zone ($\sigma_c \approx -58$ MPa), accompanied by yielding of the existing transverse reinforcement. This transition from shear-controlled to flexure-controlled behaviour demonstrates that the UHPFRC overlay effectively enhances shear resistance, allowing full development of flexural capacity and resulting in a more ductile structural response.
Although the numerical models show satisfactory agreement with experimental results within the tested range, some limitations must be acknowledged.

First, the degradation state of the existing girders was represented through modified average material properties rather than explicit modelling of local corrosion damage, strand section loss a or spatial variability of deterioration. Pre-existing cracking and damage accumulated during the service life and during the pre-cracking phase were not explicitly introduced in the numerical mesh; instead, their effects were implicitly accounted for through adjusted material parameters. Consequently, local stiffness reductions and crack-induced stress redistributions may not be fully captured. Second, the bond between substrate and UHPFRC was simulated using a predefined bond–slip law without specific experimental tests. Finally, FRP debonding was not explicitly represented, which may partially explain the discrepancies observed in Beam 2.
Despite these simplifications, the model accurately reproduces stiffness and displacement response within the experimental range, supporting its use for estimating ultimate capacity and failure mechanisms.

3.4. CONCLUSIONS

The experimental campaign presented in this study represents a demanding large-scale structural application of UHPFRC strengthening on deteriorated prestressed bridge girders. The investigation, combining full-scale testing and nonlinear finite element analyses, allows the following conclusions to be drawn:

- the strengthening technique represents a heavy target structural application of UHPFRC and HPFRC materials, under both a structural and technical point of view;

- the UHPFRC overlay provides a significant **increase in ultimate capacity** (60% ultimate load) and effective **control of shear crack openings**. The strengthened configuration demonstrates enhanced structural performance compared to the unstrengthened condition.;

- the overlay positively influences serviceability behaviour through **improved post-cracking response**. The enhanced tensile contribution of UHPFRC leads to reduced crack widths and **improved durability**, limiting the penetration of aggressive agents. The increased sectional stiffness also results in reduced deflections under service conditions;

- experimental evidence showed **no debonding** between the substrate and the overlay, confirming the **high bond performance** achieved through adequate **surface preparation**. This suggests the possibility of optimizing or reducing mechanical connectors in practical applications;

- no significant differences were observed between the use of stirrups and dowels as transverse connections between the overlay and the flanges within the investigated configuration;

- **numerical analyses** proved essential for estimating the ultimate capacity of both unstrengthened and strengthened beams, since experimental tests were limited by loading system capacity. The models provide a **reliable estimation** of the increase in ultimate load and deformation capacity induced by the strengthening intervention;

- the strengthening technique **shifts the governing failure mode** from brittle shear to flexural crushing of the compression zone, resulting in a **more ductile global response** and significantly greater ultimate displacement capacity;

- **further investigation** is required to comprehensively **characterize the shear bond behaviour** between UHPFRC overlays and normal- or medium-strength existing concrete substrates, particularly under different surface preparation conditions.

3.5. REFERENCES

[1] Belletti, B., Rodríguez, J., Andrade, C., Franceschini, L., Sánchez Montero, J., & Vecchi, F. (2020). Experimental tests on shear capacity of naturally corroded prestressed beams. Structural Concrete, 21(5), 1777–1793. https://doi.org/10.1002/suco.202000205

[2] Bhutta, A., Borges, P. H. R., Zanotti, C., Farooq, M., & Banthia, N. (2017). Flexural behavior of geopolymer composites reinforced with steel and polypropylene macro fibers. Cement and Concrete Composites, 80, 31–40. https://doi.org/10.1016/j.cemconcomp.2016.11.014

[3] Brandt, A. M. (2008). Fibre reinforced cement-based (FRC) composites after over 40 years of development in building and civil engineering. Composite Structures, 86(1–3), 3–9. https://doi.org/10.1016/j.compstruct.2008.03.006

[4] Di Prisco, M. (2019). Critical infrastructures in Italy: State of the art, case studies, rational approaches to select the intervention priorities.

[5] Di Prisco, M., Colombo, M., Martinelli, P., & Coronelli, D. (2018). The technical causes of the collapse of Annone overpass on SS.36.

[6] Higgins, C., Farrow III, W. C., Potisuk, T., Miller, T. H., & Yim, S. C. (2003). Shear capacity assessment of corrosion damaged reinforced concrete beams. Final Report SPR 326, Oregon Department of Transportation.

[7] Iavarone, Fabiola, Frank J. Vecchio, Giovanni Plizzari, and Fausto Minelli. 2023. "Shear Bond between Existing Concrete and High-Strength Fiber Reinforced Overlay." Structural Concrete.
[8] Kioumarsi, M., Benenato, A., Ferracuti, B., & Imperatore, S. (2021). Residual flexural capacity of corroded prestressed reinforced concrete beams. Metals, 11(3), 442. https://doi.org/10.3390/met11030442
[9] Meda, A., Minelli, F., & Plizzari, G. A. (2012). Flexural behaviour of RC beams in fibre reinforced concrete. Composites Part B: Engineering, 43(8), 2930–2937. https://doi.org/10.1016/j.compositesb.2012.06.003
[10] Ministero delle Infrastrutture e dei Trasporti. (2020). Linee guida per la classificazione e gestione del rischio, la valutazione della sicurezza ed il monitoraggio dei ponti esistenti.
[11] Minelli, F., & Plizzari, G. (2008). Shear design of FRC members with little or no conventional shear reinforcement.
[12] Pedeferri, P. (2005). La corrosione nel calcestruzzo: fenomenologia, prevenzione, diagnosi, rimedi. AICAP.
[13] Recupero, A., & Spinella, N. (2019). Experimental tests on corroded prestressed concrete beams subjected to transverse load. Structural Concrete, 20(6), 2220–2229. https://doi.org/10.1002/suco.201900242
[14] Rogers, R. A., Wotherspoon, L., Scott, A., & Ingham, J. M. (2012). Residual strength assessment and destructive testing of decommissioned concrete bridge beams with corroded pretensioned reinforcement. PCI Journal, 57(3), 100–118. https://doi.org/10.15554/pcij.06012012.100.118
[15] Savino, P., Tondolo, F., Sabia, D., Quattrone, A., Biondini, F., Rosati, G., Anghileri, M., & Chiaia, B. (2023). Large-scale experimental static testing on 50-year-old prestressed concrete bridge girders. Applied Sciences, 13(2), 834. https://doi.org/10.3390/app13020834
[16] Soliman, A. M., & Nehdi, M. L. (2014). Effects of shrinkage reducing admixture and wollastonite microfiber on early-age behavior of ultra-high performance concrete. Cement and Concrete Composites, 46, 81–89. https://doi.org/10.1016/j.cemconcomp.2013.11.008
[17] Vecchio, F. J., & Collins, M. P. (1986). The Modified Compression-Field Theory for reinforced concrete elements subjected to shear. ACI Journal Proceedings, 83(2). https://doi.org/10.14359/10416
[18] Verderame, G. M., Ricci, P., Esposito, M., & Sansiviero, F. C. (2011). Le caratteristiche meccaniche degli acciai impiegati nelle strutture in c.a. realizzate dal 1950 al 1980. XXVI Convegno Nazionale AICAP
[19] Wong, P. S., Vecchio, F. J., & Trommels, H. (2013). VecTor2 & FormWorks User's Manual (2nd ed.).
[20] Zanotti, C., Borges, P. H. R., Bhutta, A., & Banthia, N. (2017). Bond strength between concrete substrate and metakaolin geopolymer

REPAIR MORTAR: EFFECT OF CURING REGIME AND PVA FIBER REINFORCEMENT. CEMENT AND CONCRETE COMPOSITES, 80, 307–316. https://doi.org/10.1016/j.cemconcomp.2016.12.014

3.6. LIST OF TABLES

Table 3-1: UHPFRC properties. 78
Table 3-2: FRP plates properties. 79
Table 3-3: tests names. 81
Table 3-4: Pre-crack targets tests. 84
Table 3-5: Experimentally achieved peak loads and corresponding test conditions for all beam configurations. 89
Table 3-6:Midspan displacement at 500 kN and crack-width values at fixed shear levels for unstrengthened and strengthened configurations. 94
Table 3-7:Prestress losses and effective prestress stress of the original project. 97
Table 3-8:prestrain values 97
Table 3-9: Strands properties in the original design. 101
Table 3-10: material properties from the Original Project and Diagnostic Campaigns. 102
Table 3-11: strands data elaboration in Diagnostic 2. 106
Table 3-12: stirrups data elaboration in Diagnostic 2. 107
Table 3-13: longitudinal rebars elaboration data in Diagnostic 2. 107
Table 3-14: Numerical Analyses Names 108
Table 3-15: Comparison between experimental results and NLFEA predictions for the unstrengthened configuration within the tested load range (δ evaluated at 500 kN). 111
Table 3-16:Comparison between experimental results and NLFEA predictions for the strengthened configuration within the tested load range (δ evaluated at 1000 kN). 115
Table 3-17:link element bond properties. 115

3.7. LIST OF FIGURES

Figure 3-1: (a) specimens location identified on the original project drawings; (b) girders location identified on the maps on the Milan direction portion. 73
Figure 3-2: Deterioration conditions (a) Beam 1, (b) Beam 2, (c) Beam 3. 75
Figure 3-3: (a) Actual and (b) designed section; (c) particular of stirrups near the support from the original project. 76
Figure 3-4: (a) connection of the overlay to the flanges, (b) detail of FRC overlay, (c) detail of FRP plates. 78

Figure 3-5: Surface treatment: (a) preparation to achieve a target roughness of ±3 mm; (b) finished surface. 80
Figure 3-6: (a) casting of the UHPFRC layers; (b) completion of the upper 15 cm with tixotropic mortar. 80
Figure 3-7: (a) Loading scheme; examples of test before (b) and after (c) the strengthening. 82
Figure 3-8: tests set-up and instrumentation positions. 83
Figure 3-9: comparison between unstrengthened (a) and strengthened (b) tests. 86
Figure 3-10: comparison between side A and side B pf the strengthened tests in Beam 1. 87
Figure 3-11: comparison between side A and side B pf the strengthened tests in Beam 3. 87
Figure 3-12: comparison between side A and side B pf the strengthened tests in Beam 2 88
Figure 3-13: debonding of an FRP plate at the intrados. 88
Figure 3-14: crack width diagram of the unstrengthened tests. 90
Figure 3-15: crack width diagram of the strengthened tests. 91
Figure 3-16: comparison of crack width between unstrengthened and strengthened tests in Beam 3 92
Figure 3-17: comparison of crack width between unstrenghtened and strengthened tests in Beam 3 (a); crack pattern of 3A and 3B tests (b). 93
Figure 3-18: simplification of the concrete area in the numerical model in order to account for the geometrical tapering of the cross-section: (a) schematic drawing; (b) 3D view. 96
Figure 3-19: Vt2 model for the unstrengthened beams. 98
Figure 3-20: Vt2 model for the strengthened beams. 99
Figure 3-21:bond modelling between existing section and overlay in the cases of perfect bond conditions (a) and not perfect bond conditions (b). 99
Figure 3-22: Initial degradation condition of Beam 3 (side A, side B and bottom flange intrados). 103
Figure 3-23: example of carbonation test on core-sample. 104
Figure 3-24:tendons tests in terms of stress and strain. 106
Figure 3-25: Unstrengthened tests and numerical analyses. 110
Figure 3-26: Detail of the first branch - Unstrengthened. 110
Figure 3-27: Strengthened tests and numerical analyses. 113
Figure 3-28: Detail of the first branch – Strengthened. 113
Figure 3-29: shear bond tests set up(b) and picture (c). 116
Figure 3-30: Comparison between perfect and not perfect bond conditions for RB analyses. 116
Figure 3-31: crack pattern of the unstrengthened (a) and strengthened (b) numerical models. 117

4. EXTENDING THE SERVICE LIFE OF HISTORICAL BRIDGES: EXPERIMENTAL EVALUATION OF A CFRP–FRM RETROFIT SYSTEM

ABSTRACT

The rehabilitation of historical bridges entails a dual challenge: preserving cultural heritage while ensuring adequate structural performance. This study investigates the strengthening of a full-scale reinforced concrete bridge girder that had been in service for nearly 90 years and exhibited severe corrosion-induced deterioration, including extensive concrete cover loss and corrosion of both longitudinal reinforcement and stirrups.

The experimental program was conducted in two phases. In the first phase, the original girder was tested under four-point bending and displacement control to assess its residual load-bearing capacity, with loading applied well beyond the yielding of the longitudinal reinforcement. In the second phase, an innovative strengthening method was applied. The retrofit combined two 12 mm carbon fibre–reinforced polymer (CFRP) bars, intended to restore and enhance flexural strength, with a 50 mm fibre-reinforced mortar (FRM) overlay containing polypropylene fibres, aimed to improve confinement and crack distribution. The strengthening procedure is described in detail, with particular attention to surface preparation, bonding mechanisms, and compatibility with the deteriorated concrete substrate.

After curing of the overlay, the girder was retested under the same loading configuration up to failure. The paper presents the experimental results and compares the structural response in the unstrengthened and strengthened conditions. The findings demonstrate that hybrid CFRP–FRM systems can provide a significant increase in load-bearing capacity while maintaining satisfactory ductility, representing a practical solution for extending the service life of deteriorated bridge elements and offering valuable insights into their application to full-scale structural components.

Keywords: Girder, Strengthening, FRM, CFRP bars, Polypropylene fibres, Innovative materials.

4.1. INTRODUCTION

A large amount of the existing reinforced concrete (RC) and prestressed concrete (PC) bridge stock worldwide was designed and constructed during the first half of the twentieth century according to design philosophies primarily focused on structural safety and serviceability, with limited consideration given to long-term durability and life-cycle performance. The progressive exposure of these structures to aggressive environmental conditions has highlighted the inadequacy of such assumptions, leading to widespread deterioration phenomena that compromise both structural performance and durability (Walraven, 2021). As a consequence, the assessment and management of aging bridge infrastructure has become a critical issue for transportation networks, particularly in Europe, where a significant number of bridges have already exceeded their nominal service life (Di Prisco, 2019).

From a bridge management perspective, corrosion-induced degradation represents one of the most severe and widespread deterioration mechanisms affecting RC and PC bridges. Reinforcement corrosion may lead to cracking and spalling of the concrete cover (Higgins et al., 2010), reduction of the reinforcement cross-section, degradation of bond conditions (Coronelli and Gambarova, 2004), and a consequent loss of strength, stiffness, and ductility (Imperatore et al., 2017; Almusallam, 2001; Zhang et al., 2009). These effects introduce significant uncertainty in the evaluation of residual structural capacity and complicate decision-making processes related to maintenance, strengthening, or replacement strategies (Lupoi et al., 2022; Adey et al., 2018). Reliable assessment tools and experimental evidence are therefore essential to support rational, risk-informed infrastructure management and to prioritize interventions based on structural condition, safety, and life-cycle considerations.

Despite the relevance of this issue, experimental data derived from real-scale structural elements affected by long-term natural corrosion remain limited. Opportunities to perform destructive testing on full-scale bridge components removed from service are rare. Some experimental studies have investigated the residual strength and structural response of naturally corroded RC and PC bridge beams, providing valuable insights into the effects of corrosion on load-bearing capacity and failure mechanisms (Rogers et al., 2012; Belletti et al., 2020; Savino et al., 2023; Lupoi et al., 2022). Nevertheless, the available literature still shows a significant lack of experimental evidence on full-scale elements subjected to decades of natural degradation, especially when compared to the vast number of aging bridges currently in service.

In this context, strengthening existing bridge structures often represents a potentially advantageous alternative to full replacement. Beyond direct construction costs, replacement interventions are frequently associated with substantial indirect costs related to traffic interruption, detours, environmental impact, and broader socioeconomic consequences, which may be particularly critical for strategic

transportation infrastructure (Frangopol and Liu, 2007). When technically feasible, strengthening solutions may therefore offer a more sustainable and economically efficient strategy to extend the service life of existing bridges while maintaining acceptable safety levels.

Among the available strengthening techniques, systems based on fibre-reinforced polymer (FRP) materials have been widely adopted due to their high strength-to-weight ratio, corrosion resistance, and ease of installation (Täljsten, 2006). However, conventional externally bonded or near-surface mounted FRP systems may present limitations when applied to deteriorated substrates, particularly in terms of bond durability, fire resistance, and long-term compatibility with existing materials (De Lorenzis and Teng, 2006). Investigations on strengthening techniques applied to real-scale bridge members are even less common. When FRP systems are adopted, applications frequently involve externally bonded laminates or plates, and the resulting increase in ultimate load may be limited, particularly when premature debonding governs the response (Aidoo et al., 2006). These findings highlight the need for strengthening solutions capable not only of increasing flexural resistance but also of ensuring reliable stress transfer and durable interaction with deteriorated substrates.

In recent years, cementitious fibre-reinforced overlays and jackets have emerged as effective solutions to strengthen existing concrete bridges by enhancing both load-bearing capacity and long-term durability. High-performance cementitious composites such as ultra-high performance fibre-reinforced concrete (UHPFRC) have been successfully applied as overlays or jackets on RC members, demonstrating improvements in structural capacity, crack control, and resistance to environmental degradation (Lampropoulos et al., 2016; Huang et al., 2022). However, a significant portion of the available literature is based on numerical or small-scale investigations, while experimental evidence on full-scale structural elements remains comparatively limited. These high-performance overlays not only contribute to mechanical performance but also enhance durability and resistance to chloride ingress, thereby addressing key aspects of service life extension in aging infrastructure. Within this context, experimental studies on real-scale, long-term deteriorated bridge elements strengthened with cementitious fibre-reinforced overlays are essential to validate their structural effectiveness and practical applicability.

The effectiveness of such overlays is strongly governed by stress transfer at the interface between the existing substrate and the overlay, where substrate surface preparation, shear bond characteristics, and roughness play a critical role in achieving composite action and exploiting the advantages of the overlay material (Mansour et al., 2017; Iavarone et al., 2024). These advancements underscore the potential of cementitious FRC overlays as viable strengthening strategies for existing bridge structures, complementing or, in some cases, substituting conventional methods based solely on polymeric composites. It should be noted, however, that

many of the referenced experimental studies focus on FRC overlays applied to concrete slabs or on small-scale bond specimens with low-strength concrete substrates rather than on full-scale bridge beams, indicating a need for further research on structural members typical of bridge applications.
Within this framework, the present study investigates the strengthening of a historic RC bridge girder that remained in service for approximately 90 years and exhibited severe corrosion-induced deterioration. The experimental program involved a full-scale T-shaped girder removed from an existing bridge and subjected to a two-phase testing procedure. In the first phase, the residual load-bearing capacity of the unstrengthened girder was assessed through a four-point bending test. In the second phase, an innovative hybrid strengthening technique was applied, consisting of two carbon fibre–reinforced polymer (CFRP) bars embedded in a sprayed fibre-reinforced mortar containing polypropylene fibres (FRM-PP) overlay. The strengthened girder was then tested up to failure under the same loading configuration.
The objectives of the study are: (i) to experimentally evaluate the residual structural capacity of a full-scale RC bridge girder affected by long-term natural corrosion; (ii) to assess the effectiveness of a hybrid CFRP–FRM strengthening system in enhancing flexural capacity and ductility; and (iii) to contribute experimental evidence supporting strengthening as a viable alternative to replacement in the context of bridge engineering and infrastructure management.

4.2. EXPERIMENTAL PROGRAM

4.2.1. Structural element and original condition

The experimental program involved a 90 years old RC bridge girder, removed during the dismantling of the Fiume Garza overpass in Brescia. The existing structure was characterized by a single-span static scheme with simply supported beams. These beams had a T-shaped cross-section. The original structure was entirely replaced with precast PRC beams, and the existing beams were demolished. However, the Municipality of Brescia donated two specimens to the university for research purposes. Only one of the beam is object of the present study, which aims to evaluate the applicability of an innovative strengthening technique that may represent, in specific cases, a cost-effective alternative to replacement while ensuring adequate structural performance.
The deterioration conditions observed in a portion of the bridge are presented in Figure 4-1a. The girder under study exhibited extensive concrete cover loss and significant corrosion affecting both the longitudinal and transverse reinforcement (Figure 4-1b).



(a) (b)

Figure 4-1: degradation conditions of the bridge in situ (a) and of the specimen considered in the experimental programme (b).

Figure 4-9a illustrates the cross-section of the specimen. It should be noted that the element is a full-scale girder with overall length of 8.8 m and an approximate total weight of 12.4 t. The girder had a T-shaped cross-section typical of historical bridge construction. The total height of the section was approximately 890 mm, while the flange width was about 1660 mm. The web width was approximately 300 mm, and the flange thickness varied, reaching about 150–160 mm near the edges.

The longitudinal tensile reinforcement consisted of a single layer of smooth (plain) steel bars, comprising three bars with a nominal diameter of 39 mm. Shear reinforcement was provided by stirrups with nominal diameters of 10 mm, characterized by six legs, arranged to confine both the web and the lower part of the flange. The spacing of the stirrups was variable along the span; in the shear critical region, the spacing was approximately 190 mm. The geometric configuration reflects early twentieth-century construction practice, characterized by large bar diameters and relatively sparse reinforcement detailing compared to modern standards.

4.2.2. Existing materials

The mechanical properties of the existing materials were derived from the extensive experimental campaign previously performed on a similar beam removed from the same bridge and previously investigated (Di Stefano, 2022). The beam was cast as part of the same original construction, although it had a different geometry. Due to the severe surface degradation and the presence of very coarse aggregates (up to approximately 50 mm), core extraction was not considered reliable. Therefore, non-destructive testing techniques were adopted. Preliminary estimates were obtained using rebound hammer tests, while the final values used in the structural assessment were derived from Windsor probe tests.

The mean compressive strength of the concrete was found to be 44 MPa. Visual inspection prior to testing revealed extensive cracking, local cover loss, and signs of advanced corrosion-induced damage, indicating a significant level of deterioration of the original material. The Young's modulus of the existing concrete was not directly measured. Therefore, it was estimated from the measured compressive strength using the ACI-based expression (Equation 1), resulting in approximately 28.9 GPa.

$$E_c = 3320\sqrt{f_c} + 6900 \qquad \textit{Equation 1}$$

The reinforcement consisted of smooth (plain) steel bars, typical of early twentieth-century construction practice. Mechanical properties were obtained from tensile tests performed on bars extraction. The main longitudinal reinforcement exhibited a mean yield strength of 287 MPa, an ultimate strength of 412 MPa, and an elastic modulus of approximately 203 GPa, with an ultimate strain of about 22%. The average mass loss due to corrosion was approximately 4%.

The stirrups, with nominal diameters of 10 mm, were found to be severely affected by corrosion. Tensile tests indicated a mean yield strength of about 268 MPa, an ultimate strength of about 344 MPa, and an elastic modulus of 185 GPa, while the average mass loss reached approximately 35%, highlighting a significant reduction in shear-resisting capacity. However, the stirrups did not play a governing role in the structural response of the tested specimen. The girder did not exhibit critical shear deficiencies and, despite the severe corrosion, the number of legs and diameter of the stirrups were originally oversized, resulting in a residual shear capacity still higher than the flexural capacity, which represents the focus of the present strengthening study. The mechanical properties of the stirrups are therefore reported for completeness.

Table 4-1 presents the main characteristics of the existing materials.

Table 4-1: existing section materials' properties.

Existing steel reinforcement	Yielding stress [MPa]	287
	Ultimate stress [MPa]	412
	Young modulus [GPa]	203
	Ultimate strain [%]	22
Existing concrete	Cylindrical compressive strength [MPa]	44
	Young Modulus [GPa]	28.9

4.2.3. Strengthening Materials

Sprayed specimens were cast to characterize the mechanical properties of the strengthening mortar under conditions representative of on-site application (Figure 4-2a,b). The values reported in the manufacturer's technical data sheet indicate higher mechanical properties, as they are obtained from specimens cast in formworks

and compacted by vibration. In the present study, the adopted procedure aimed to obtain a mechanical characterization more representative of the spray application conditions used for the overlay. Unfortunately, the adopted casting procedure was not fully suitable for some specimen types, particularly the cylinders shown in Figure 4-2c. Due to the small diameter of the moulds and the presence of fibres, difficulties were encountered in achieving uniform material deposition and proper compaction. This resulted in significant material voids and incomplete filling at the base of several cylinders. For this reason, these specimens were discarded and not used for mechanical testing, as they were not representative of the actual overlay material.



(a) (b) (c)

Figure 4-2: spraying of the specimens (a); specimens after demoulding (b); cylindrical specimens after demoulding, showing defects caused by difficulties in spray casting and compaction, leading to local heterogeneities and incomplete filling at the base (c).

Using this procedure, the following specimens were fabricated:

4.2.3.1. ***10 cubes (dimensions 150 × 150 × 150 mm)***

Uniaxial compression tests were performed on 150 × 150 × 150 mm cube specimens to evaluate the compressive strength of the strengthening mortar. The tests were carried out under monotonic loading using a hydraulic testing machine, applying load at a constant displacement rate until failure. The compressive strength was calculated as the ratio between the maximum applied load and the nominal cross-sectional area of the cube. The individual test results, together with mean value and statistical dispersion parameters, are summarized in Table 4-2. Specimens 5 and 7 (highlighted in grey) were excluded from the statistical evaluation, as they exhibited significant surface defects and incomplete material integrity, similar to those observed in the cylindrical specimens. These defects were attributed to difficulties associated with the spray casting procedure. Consequently, the measured strengths of these specimens were considered not representative of the actual material

properties and were not included in the calculation of the average compressive strength. The discarded specimens are shown in Figure 4-3.

Table 4-2: Uniaxial compressive strength results of 150 × 150 × 150 mm mortar cubes; specimens 5 and 7, affected by casting defects, were not considered in the calculation of the mean value.

Specimen	Load [kN]	Stress [MPa]
1	1196.9	53.2
2	1202.9	53.5
3	903.8	40.2
4	1232	54.8
5	799.4	35.5
6	1139.5	50.7
7	812.9	36.1
8	1023.6	45.5
9	1052.5	46.8
10	1175.9	52.3
	R_c	**49.6**
	St. Dev.	**5.0**
	CoV	**10%**



Figure 4-3: Cube specimens 5 and 7 affected by casting defects.

The average compressive cylindrical strength obtained from the tests was 41.2 MPa (f_c=0.83R_c), confirming the high mechanical performance of the sprayed mortar under the adopted curing and application conditions.

4.2.3.2. 6 notched beams (dimensions 150 × 150 × 600 mm)

The specimens were tested under three-point bending in accordance with UNI EN 14651 (Figure 4-4) to determine the residual tensile strengths of the fibre reinforced mortar (FRM) as a function of crack mouth opening displacement (CMOD). Nominal residual stresses were evaluated at the CMOD levels prescribed by the standard (0.5 mm, 1.5 mm, 2.5 mm, and 3.5 mm), yielding average values of residual tensile strength as in Table 4-3. The post-cracking performance is characterized by a residual strength ratio f_{R3}/f_{R1} equal to 1.45, indicating a pronounced strain-hardening response, with increasing load-carrying capacity as crack opening progresses. Based on the measured residual strengths and the post-cracking ratio, the investigated material was classified as class 3e FRC, denoting high ductility and significant residual load-bearing capacity at large crack openings.

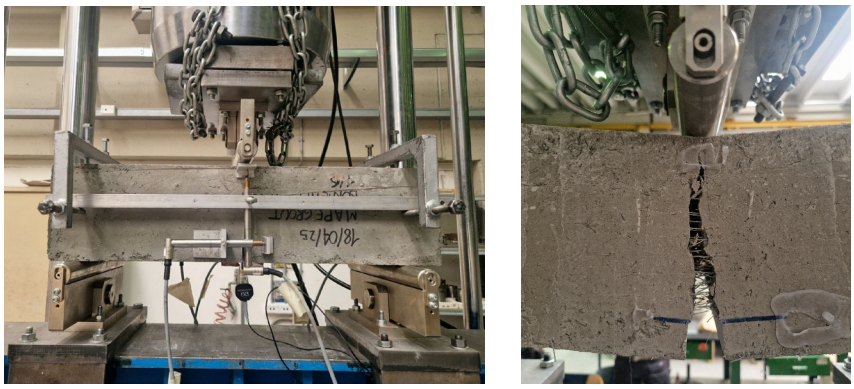


Figure 4-4: FRM-PP notched beam test setup (a) and detail of the crack-bridging mechanism (b).

Table 4-3:three point bending tests on notched FRM beams results.

	f_L	f_{R1}	f_{R2}	f_{R3}	f_{R4}
	[MPa]	[MPa]	[MPa]	[MPa]	[MPa]
#1	2.93	3.36	4.50	4.79	4.49
#2	2.99	3.67	5.07	5.30	4.85
#3	3.06	3.28	4.40	4.55	4.19
#4	1.67	3.22	4.28	4.50	4.13
#5	2.74	2.83	4.25	4.62	4.28
#6	2.43	2.31	3.08	3.34	3.30
Average [MPa]	**2.64**	**3.11**	**4.26**	**4.52**	**4.21**
St. Dev.	0.52	0.48	0.65	0.65	0.52

cov [%]	19.86	15.30	15.28	14.32	12.27

The results show good experimental repeatability, with coefficients of variation ranging between approximately 12% and 20%, which is consistent with the typical scatter reported for EN 14651 testing. A progressive increase in residual strength from f_{R1} to f_{R3} is observed, followed by a slight reduction at f_{R4}, attributable to the onset of generalized fibre pull-out mechanisms. The variability in the number of fibres intersecting the fracture plane (see Table 4-4) explains the mechanical dispersion observed across specimens. The condition $f_{R3} > f_{R1}$ confirms the hardening post-cracking behaviour of the composite material.

The nominal stress–CMOD curves (Figure 4-5) exhibit an initial post-peak drop associated with matrix cracking, followed by a stress recovery phase governed by progressive fibre engagement. A relatively stable resistance plateau is observed between approximately 1.5 and 3 mm CMOD, while a mild softening branch develops beyond 3 mm due to progressive fibre pull-out. This response confirms an efficient crack-bridging mechanism and a pseudo-ductile structural behaviour, consistent with the assigned 3e classification.

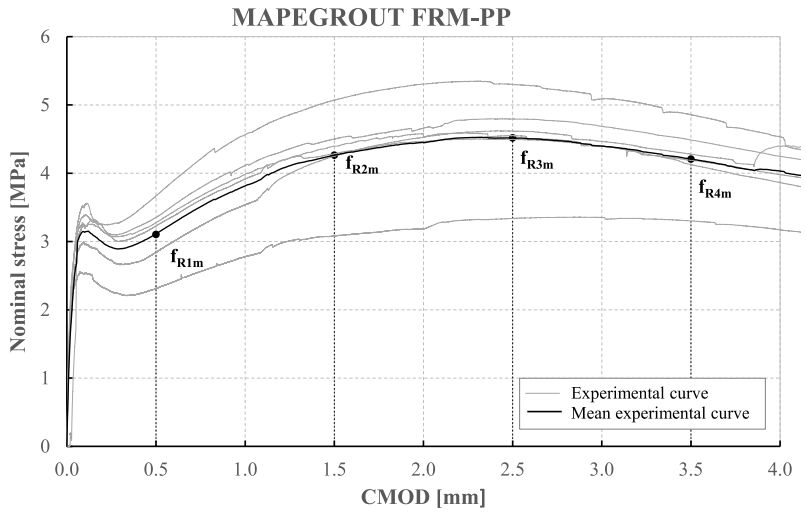


Figure 4-5: Nominal stress – CMOD curves of the mapegrout specimens.

After failure, the number of fibres exposed on the fracture surface was counted to determine the fibre content in terms of area fraction. This value was subsequently converted into an equivalent volume fraction using a correlation coefficient (Enfedaque et al., 2019), allowing an experimental estimation of the actual fibre volume fraction of the mix, which was not disclosed by the manufacturer.

In the adopted procedure, the fibre volume fraction was estimated from the number of fibres observed on the fracture surface according to:

$$V_f = \frac{n}{\theta}\frac{A_f}{A_c} \qquad \textit{Equation 2}$$

Where:

V_f is the fibre volume fraction;

n is the number of fibres counted on the fracture surface;

θ is a correlation coefficient accounting for fibre orientation and distribution (Enfedaque et al., 2019), in this case chosen equal to 0.75;

A_f is the cross-sectional area of a single fibre;

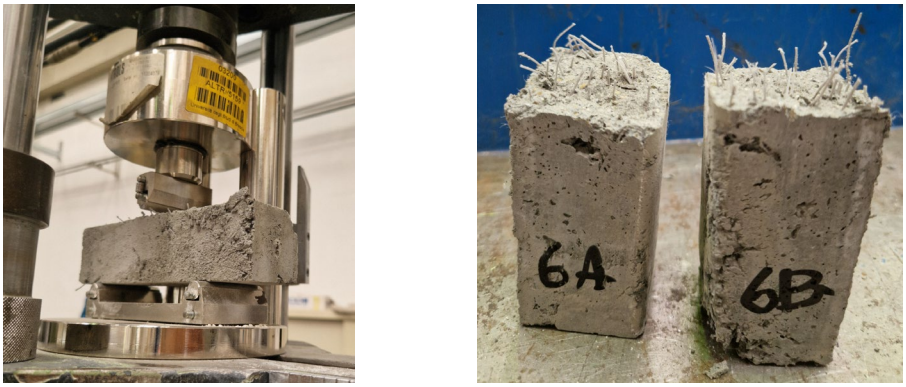
A_c is the cross-sectional area of the mortar specimen, in this case (18750 mm²).

Table 4-4: fibre content calculations. Column A_f [%] represents the previous column $n \cdot A_f$ divided for the mortar cross sectional area A_c. A and B are the two different surfaces of the fracture.

	n	$n \cdot A_f$ [mm²]	A_f [%]	$A_{f,mean}$ [%]	V_f [%]
T1A	284	62.66	0.33%	0.35%	0.47%
T1B	313	69.05	0.37%		
T2A	321	70.82	0.38%	0.37%	0.50%
T2B	316	69.72	0.37%		
T3A	261	57.58	0.31%	0.32%	0.43%
T3B	283	62.43	0.33%		
T4A	277	61.11	0.33%	0.33%	0.44%
T4B	285	62.88	0.34%		
T5A	298	65.74	0.35%	0.33%	0.44%
T5B	264	58.24	0.31%		
T6A	229	50.52	0.27%	0.29%	0.39%
T6B	264	58.24	0.31%		
			Mean	0.33%	**0.44%**
			CoV	8.6%	

4.2.3.3. 12 prismsmatic specimens (dimensions 40 × 40 × 160 mm)

Three-point bending tests were first performed to determine the flexural strength of the material (Figure 4-6a). Following flexural failure, the two portions (Figure 4-6b) generated from each broken prism were subjected to compression testing, according to the procedure specified for mortar testing in EN 196-1. Tests results are presented in *Table 4-5* and *Table 4-6*.



(a) (b)

Figure 4-6: prismatic specimens 40 x 40 x 160 mm during the three-point bending test (a) and after the rupture (b).

Table 4-5: Experimental flexural strength results for 40 × 40 × 160 mm mortar prisms.

	P [kN]	f_u [MPa]
1	3.57	12.31
2	3.84	13.71
3	4.03	14.36
4	3.36	12.14
5	3.59	13.30
6	3.95	14.85
7	3.29	11.92
8	4.86	16.82
9	4.40	15.55
10	5.32	18.87
11	3.63	13.00
12	3.38	12.55
	Mean	**14.12**
	St. Dev.	2.11
	CoV	**15%**

The difference observed between the flexural strength obtained from 40×40×160 mm prisms and 150×150×600 mm beams is attributed to scale effects and to the different stress distribution and fracture mechanisms associated with the specimen size.

Table 4-6: Compressive strength results obtained from the two halves of the fractured 40 × 40 × 160 mm prisms.

	N [kN]	σ [MPa]
1A	89.89	56.18
1B	104.00	65.00
2A	94.70	59.18
2B	76.69	47.93
3A	93.64	58.52
3B	107.53	67.20
4A	107.03	67.06
4B	102.07	63.80
5A	95.28	59.55
5B	94.52	59.07
6A	102.48	64.05
6B	88.09	55.06
7A	97.98	61.23

	N [kN]	σ [MPa]
7B	91.03	57.06
8A	114.66	71.66
8B	94.74	59.21
9A	94.73	59.20
9B	88.23	55.15
10A	101.42	63.39
10B	94.13	58.83
11A	105.75	66.10
11B	93.94	58.72
12A	92.40	57.75
12B	93.62	58.51
	Mean	**60.39**
	CoV.	**8.26%**

4.2.3.4. Elastic Modulus

The 8 cylinders (dimensions 100mm diameter x 200 mm height) were originally intended for the experimental evaluation of the elastic modulus of the mortar. However, as discussed previously (see Figure 4-2c), they were discarded due to significant defects and incomplete filling. Consequently, the elastic modulus of the strengthening mortar was estimated through a numerical approach. A finite element model was developed in Diana (Diana FEA B.V., The Netherlands) to reproduce the experimental load–displacement response of the notched beams, and the elastic modulus was calibrated iteratively by varying its value until a satisfactory agreement with the experimental curve was achieved. The calibrated value of the elastic modulus was found to be approximately 28 GPa. This value is consistent with empirical stiffness estimates derived from the measured compressive strength of the mortar (f_c=41.2 MPa). For example, according to NTC2018, the elastic modulus of normal-weight cementitious materials may be estimated as in Equation 4, resulting in this case 33.7 GPa.

Furthermore, according to ACI 318 (Equation 4) in the present case yields approximately 30.5 GPa.

$$E_C = 22000\left(\frac{f_c}{10}\right)^{0.3} \qquad \textit{Equation 3}$$

$$E_c = 4700\sqrt{f_c[MPa]} \qquad \textit{Equation 4}$$

The slightly lower calibrated value reflects the effective stiffness of the sprayed material under the adopted application conditions. The comparison between the numerical fitting curve and the average experimental response of the notched prisms is presented in Figure 4-7, showing good agreement in terms of initial stiffness and peak load. The multilinear constitutive law adopted to represent the uniaxial tensile behaviour of the material in the fitting procedure is reported in Figure 4-8.

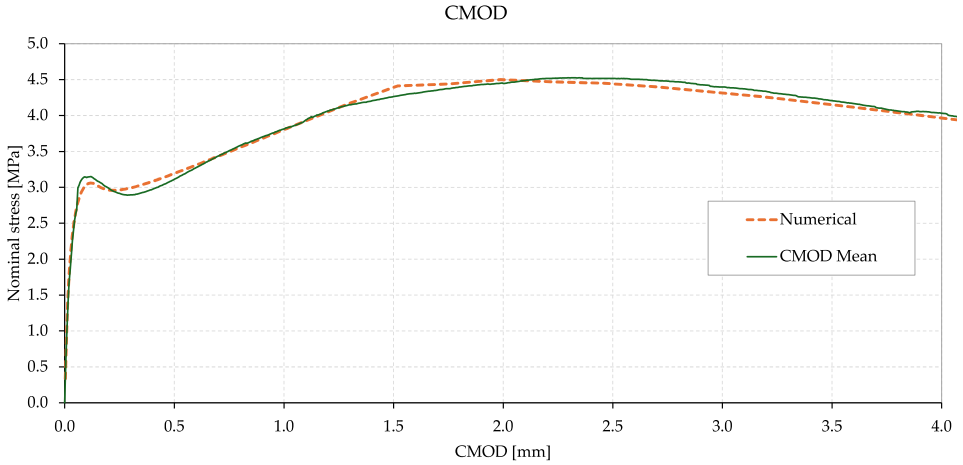


Figure 4-7: Comparison between the numerical fitting curve and the average experimental Nominal stress – CMOD curve of the notched prisms.

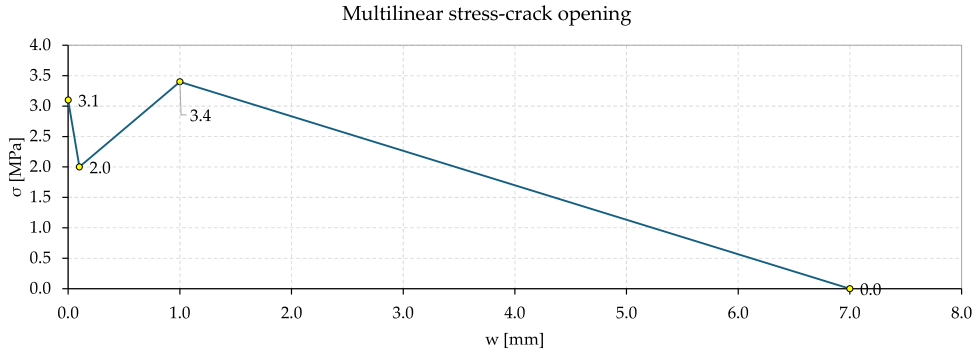


Figure 4-8: Multilinear tensile stress–crack opening law implemented in the numerical model for the strengthening mortar.

Table 4-7 summarizes the main mechanical properties of the FRM-PP.

Table 4-7: Strengthening mortar's properties.

FRM-PP	
f_c [MPa]	41.2
E_c [GPa]	28
Fibres' shape	straight
V_f [%]	0.44
Fibres' length [mm]	24
Class [UNI EN 14889]	3e

4.2.3.5. CFRP bars diameter 12 mm

The strengthening system included two CFRP bars with nominal diameter 12 mm. According to ASTM D7205/D7205M, FRP reinforcing bars exhibit a predominantly linear-elastic stress–strain response up to failure. Unlike steel reinforcement, no yielding occurs, and rupture takes place in a brittle manner once the ultimate tensile strain is reached.

The mechanical properties of the CFRP bars were not experimentally characterized within the present research program due to the inherent complexity of tensile testing procedures for composite bars. Therefore, the material parameters adopted in the experimental analysis and numerical modelling were derived from the manufacturer's technical documentation and from tensile tests performed by an external accredited laboratory on CFRP bars with nominal diameter 10 mm.

The mechanical properties declared by the manufacturer are reported in Table 4-8, under the column "Tech. Datasheet," and correspond to the mean values specified in the product documentation. However, it should be noted that the tensile strength value reported in the technical sheet is declared by the supplier without explicit reference to standardized tensile tests, and no experimental campaign directly performed by the manufacturer is documented. Independent tensile tests conducted by an external laboratory on ϕ10 specimens according to EN 2561 provided the average values (three specimens) presented in Table 4-8, under the column "Ext. Laboratory". In this case, also the St. Dev. and CoV values are presented.

Table 4-8:CFRP bars porperties based on the technical datasheet and on external laboratory tests.

CFRP properties	Tech. Datasheet	Ext. Laboratory	
Tensile strength [MPa]	2000	Mean	2539
		St. Dev.	42.7
		CoV	1.7%
Elastic modulus [GPa]	155	Mean	167.9
		St. Dev.	4.7
		CoV	2.8%
Ultimate strain [%]	1.5%	1.6%	
Diameter [mm]	10	10	

A limited dispersion was observed, indicating good repeatability of the laboratory procedure.

It is important to note that, unlike steel reinforcement, the tensile capacity of CFRP bars cannot be directly scaled based on the nominal cross-sectional area. According to ASTM D7205/D7205M, the mechanical response of FRP bars is strongly influenced by factors such as fibre volume fraction, fiber architecture, surface configuration, and manufacturing process. Consequently, bars with different nominal diameters may exhibit non-proportional variations in tensile strength and stiffness, even when produced using the same material system.

Direct tensile testing of CFRP bars presents significant experimental challenges. ASTM D7205/D7205M highlights that premature failures may occur due to grip-induced stress concentrations or inadequate force transfer at the specimen ends. To avoid such issues, the standard recommends the use of specialized anchorage systems and sufficiently long specimens to ensure that failure occurs within the free gauge length rather than at the grips. In particular, the required free length of the specimen should not be less than 40 times the effective bar diameter, leading to total specimen lengths on the order of 1.5-2 m for typical CFRP reinforcing bars. The need for long specimens, specialized anchors, strict alignment control, and testing machines with sufficient stroke and capacity makes tensile testing of CFRP bars experimentally demanding. For these reasons, and in the absence of direct testing on φ12 bars within the present study, the adopted mechanical properties were conservatively selected based on a combination of manufacturer-provided characteristic values and independent laboratory test results on φ10 bars, in accordance with the principles outlined in ASTM D7205/D7205M.

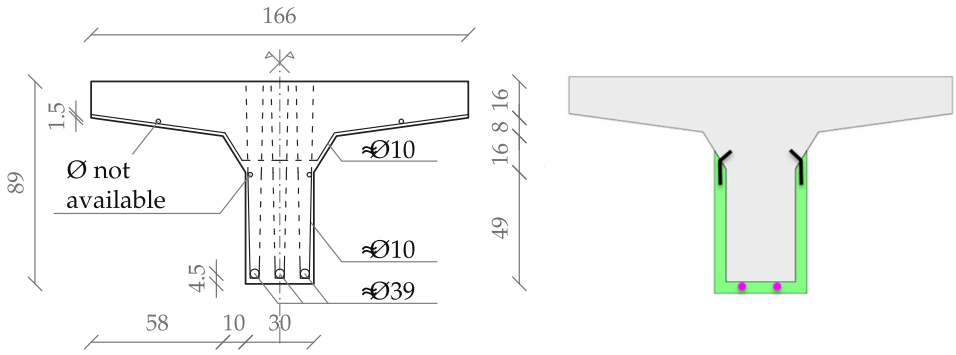
Table 4-9 shows the properties adopted in the present study for the CFRP strengthening bars.

Table 4-9: CFRP bars properties.

CFRP bars	
Φ [mm]	12
fu [MPa]	2540
E [GPa]	168
Ultimate strain [%]	1.5%

4.2.4. Strengthening procedure

The beam considered in the experimental program was at first tested under four-point loading in its unstrengthened condition. The test was stopped after yielding of the longitudinal reinforcement to avoid excessive damage while still allowing evaluation of the residual load-bearing capacity. Subsequently, the beam was unloaded and the strengthening technique was applied, consisting of the installation of two carbon fibre–reinforced polymer (CFRP) bars diameter 12 mm at the intrados of the beam, jacketed with a fibre-reinforced mortar containing polypropylene fibres (FRM-PP). The overlay was 50 mm thick (Figure 4-9b).



(a) (b)

Figure 4-9: cross-section of the unstrengthened (a) and strengthened girder (b).

It should be noted that the strengthening system was not designed according to conventional design loads associated with service conditions. Since the objective of the experimental program was to investigate the ultimate response of the strengthened girder, the intervention was dimensioned to achieve failure within the maximum capacity of the available test setup, corresponding to a total applied load of 1500 kN. The CFRP reinforcement, which primarily governs the increase in flexural resistance, was therefore selected through preliminary moment-curvature and sectional analyses in order to maximize the strengthening effectiveness while ensuring that the expected ultimate load remained slightly below this limit.

The thickness of the FRM-PP overlay was mainly governed by geometrical and construction requirements rather than by strength considerations. In particular, the overlay thickness was selected to provide adequate embedment of the CFRP bars and a reasonable protective cover. The bars were positioned at a clear distance of 15 mm from the existing concrete surface; considering the 12 mm bar diameter and an additional clear cover of approximately 23 mm, a total overlay thickness of 50 mm was adopted.
Furthermore, it should be noted that the choice of strengthening materials was primarily driven by durability considerations, as the bridge environment was classified as aggressive with respect to corrosion exposure. Indeed, the environment in which the beam was located was aggressive with respect to exposure conditions. The use of polymer-based materials, which are inherently resistant to corrosion, can enhance the durability of the structural element. Furthermore, the mortar is designed to be applied using a spray technique, without the need for formwork, in fact, casting would have been difficult to implement in the environment where the beams were located. Figure 4-10 shows the location of the specimens in 1927, during the casting phase, and in 2021, during the dismantling process.



(a) (b)

Figure 4-10: pictures of the bridge location at the moment of casting (a) and during the dismantling process (b).

The strengthening intervention was carried out through a sequence of preparatory and executive phases aimed at ensuring adequate adhesion and structural effectiveness of the retrofit system. Initially, the exposed concrete surface was cleaned by high-pressure water jetting in order to remove delaminated concrete and surface dust, thereby promoting proper bond with the strengthening layer. Although reinforcement passivation is typically required in real strengthening interventions to ensure long-term durability under aggressive environmental exposure, it was not performed in the present experimental program because the girder was tested under

laboratory conditions and was not intended for further service. In practical applications, where the strengthened structure would remain in service in an aggressive environment, appropriate corrosion protection measures would be necessary. Holes were then drilled for the installation of connectors (dowels, see Figure 4-11a) for transferring the stresses from the overlay to the existing flange; they were bonded using epoxy resin. Subsequently, local repairs of the concrete cross-section were performed using a thixotropic repair mortar (cylindrical compressive strength 62 MPa) to restore damaged cover concrete and seal pre-existing cracks resulting from the previous loading test (Figure 4-11b). Before the repair of existing cracks and concrete cover loss, the longitudinal reinforcement was instrumented with strain gauges. The beam surface was mechanically roughened, with a demolition hammer, to achieve adequate interface roughness for stress transfer between the existing concrete and the strengthening overlay. The target surface roughness was approximately ±5 mm.



(a) (b)

Figure 4-11:position of dowels to connect the overlay to the flange (a) and restored cracks and concrete cover loss (b).

The CFRP bars were then positioned and instrumented with strain gauges (Figure 4-12a). Temporary wooden reference guides were installed at 1.5 m intervals to control the thickness of the sprayed mortar layer (Figure 4-12b). Prior to casting, the substrate was pre-wetted to a saturated-surface-dry condition. As mentioned before, the strengthening mortar was applied mainly by spraying, with local manual application in the areas where the temporary formwork guides were removed, after the target thickness had been achieved, to ensure continuity of the strengthening layer (Figure 4-12c).



(a) (b) (c)

Figure 4-12: CFRP strengthening bars (a); wood temporary reference guide for the thickness of the overlay (b), detail of the overlay application at a location where the wooden formwork guides were removed (c).

As shown in Figure 4-13, the strengthening overlay extended 250 mm beyond the support position of the load test configuration.



Figure 4-13: Close-up view of the support region in the load test configuration.

Furthermore, Figure 4-14 illustrates the types of reinforcement employed in the strengthening intervention. Type "A" corresponds to the CFRP strengthening bars, while Type "C" refers to the dowels used to connect the overlay to the existing flange. Type "B" consists of four inclined B450C steel bars (diameter 16 mm) placed in the support region. The inclined B450C steel bars were installed in the region of maximum shear demand in order to intercept potential diagonal cracking and to ensure stress transfer to the strengthening reinforcement through an overlap length of 1150 mm. Nevertheless, as steel components, they are not consistent with the durability-driven strategy based on non-metallic materials. For practical applications, the use of non-metallic solutions for these elements as well should be considered.

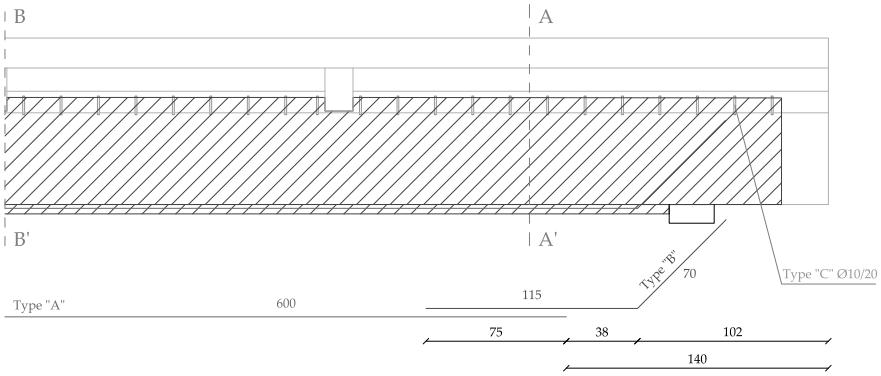


Figure 4-14: Technical drawing of the strengthening intervention, indicating the adopted reinforcement lengths.

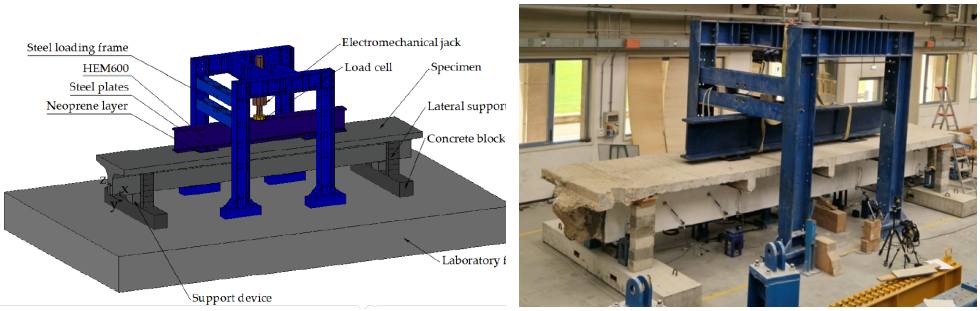
After completion of the strengthening intervention, the mortar was allowed to cure for 28 days before the girder was moved and positioned in the test setup.

4.2.5. Test setup and instrumentation

After curing of the mortar, the girder was positioned in the test setup, which was reproduced as closely as possible to the configuration adopted for the unstrengthened test, particularly with regard to loading distances and instrumentation positioning. The tests were conducted under displacement control. The vertical load was applied using a 1500 kN electromechanical jack installed within a steel loading frame. The frame consisted of four HEB400 columns and two HEB450 transverse beams at the top, further stiffened by lateral cross beams (Figure 4-15a and Figure 4-15b). The frame was anchored to a reinforced laboratory floor slab, approximately 1 m thick, through Dywidag bars; the slab was designed to withstand concentrated loads of up to 1000 kN over 0.5 m × 0.5 m areas, providing adequate reaction to the applied load.

A 2000 kN load cell was placed beneath the jack to monitor the applied force. The load was transferred to the specimen through a 5 m long HEM600 steel distribution beam (S355), enabling a four-point loading configuration. Steel bearing plates with welded solid steel cylinders were positioned between the distribution beam and the specimen to ensure proper load transfer. Two neoprene pads (18 mm thick) were placed beneath the plates to prevent local concrete crushing.

The beam was supported on two custom-made supports reproducing idealized hinge and roller boundary conditions, thus preventing horizontal restraint forces due to friction.



(a) (b)

Figure 4-15:test setup under four-point loading: schematic view (a) and photograph (b).

In addition to the load cell, 28 measuring devices were installed, as summarized in Figure 4-16.

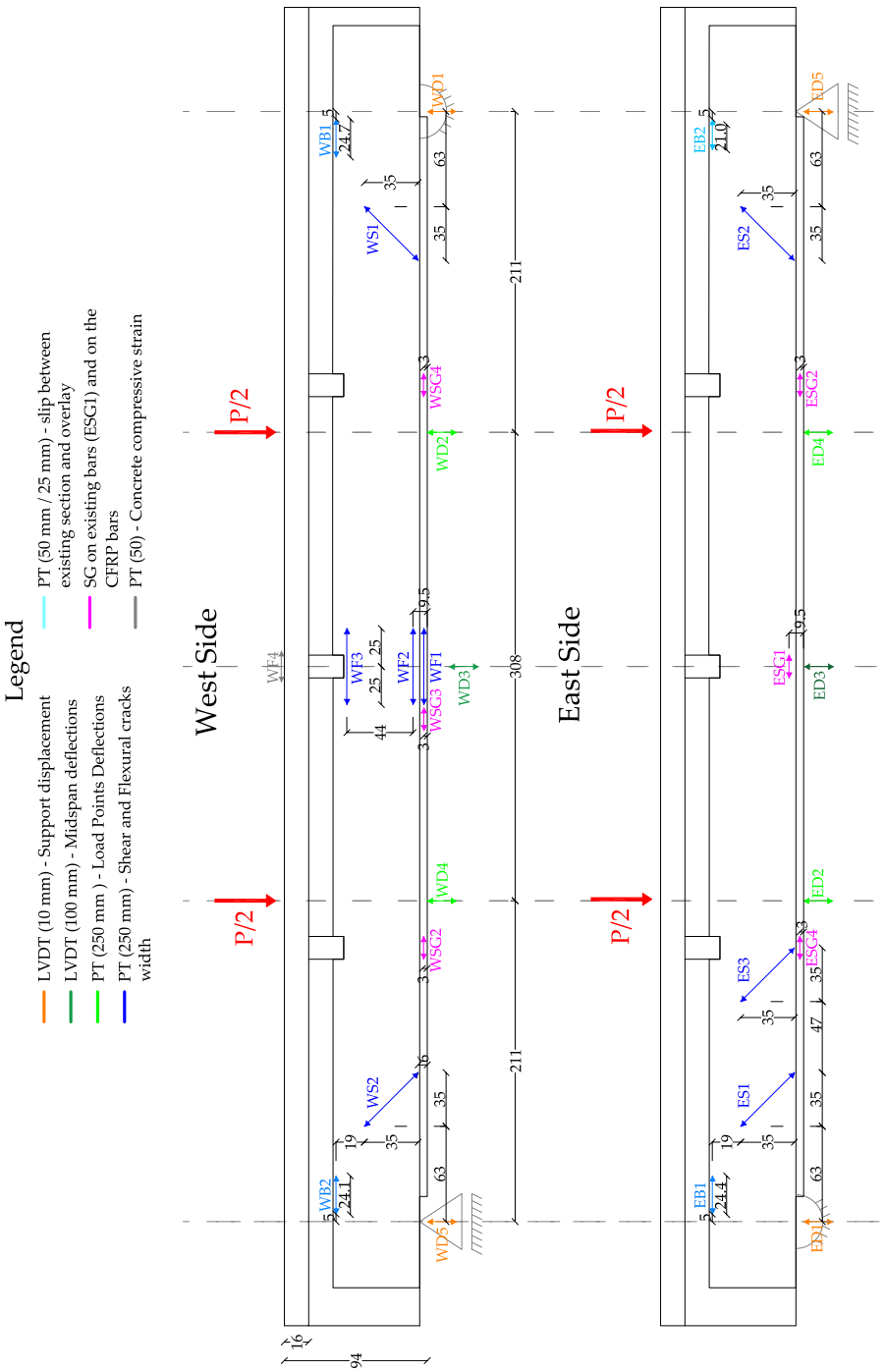


Figure 4-16: instrumentation layout and loading scheme.

Support displacement were monitored using four LVDTs (Linear Variable Differential Transformers) with a capacity of 20 mm, while two LVDTs with a capacity of 100 mm were used to measure midspan deflections. Deflections at the load points were measured by four potentiometric transducers with a capacity of 250 mm. Additional wire-type potentiometers (six in total) were installed at the loading points and at midspan to provide redundant measurements of vertical displacements; these instruments are not shown in the figure.
Strains in the strengthening reinforcement were measured using five strain gauges bonded to the CFRP bars: two at each loading point (Figure 4-17a) and one at midspan. An additional strain gauge was installed on the existing longitudinal steel reinforcement at midspan (Figure 4-17b).



(a) (b)

Figure 4-17:photographs of strain gauges on the CFRP strengthening bars (a) and on the existing steel reinforcement (b).

To monitor flexural crack width, three 250 mm potentiometric transducers were placed horizontally at midspan, aligned respectively with the strengthening reinforcement, the existing longitudinal reinforcement, and below the original transverse beam (Figure 4-18a). Crack openings in the shear-critical region were monitored using five potentiometric transducers positioned across the expected shear crack paths (Figure 4-18b).



(a) (b)

Figure 4-18: potentiometric transducers at midspan, aligned respectively with the strengthening reinforcement, the existing longitudinal reinforcement, and below the original transverse beam (a); potentiometric transducer positioned for measuring shear crack widths (b).

In addition, one 20 mm potentiometric transducer was installed at the top fibre of the beam in the compression zone along the same section (Figure 4-19a).
Finally, the slip between the existing concrete and the mortar overlay was monitored using four displacement transducers, positioned, as shown in Figure 4-19b, near the supports. The beam was tested under four-point loading (Figure 4-16) up to failure, which occurred due to tensile rupture of the CFRP bars.



(a) (b)

Figure 4-19: potentiometric transducers for the measurement of the compression strain of the concrete (a); potentiometric transducer for the measurement of the slip between the existing section and the overlay (b).

4.3. EXPERIMENTAL RESULTS

Figure 4-20 shows the load–midspan deflection curves of the unstrengthened test (black), conducted over the yielding of the existing longitudinal reinforcement, and of the strengthened specimen (light blue). In the graph, the experimentally recorded loads include the self-weight of the beam and of the loading system. Specifically, a value of 124 kN was added for the self-weight of the unstrengthened beam, 12 kN for the strengthening overlay, and 14 kN for the HEM steel beam used to distribute the load at the two loading points.

A significant increase, of about 33%, in ultimate load is observed. The response of the strengthened beam exhibits the typical initial uncracked branch followed by the cracked stage. After reaching the load corresponding to yielding of the existing steel reinforcement, no load plateau is observed; instead, the final portion of the curve remains approximately linear, with a residual stiffness. This behaviour results from the yielding of the existing steel reinforcement combined with the elastic response of the CFRP bars, which remain in the linear range up to failure. Despite the elastic–brittle behaviour of CFRP, its combination with steel reinforcement provides an overall ductile response of the structural element, resulting in a ductility of approximately 6 in terms of displacement. The global ductility of the strengthened member remained satisfactory because the response was still governed by the yielding of the existing steel reinforcement. The CFRP bars primarily increased the flexural capacity, while plastic deformations developed in the steel reinforcement, allowing significant displacement prior to failure.

Finally, two load drops leading to collapse can be observed, one associated with the rupture of each CFRP bar. After failure of the first bar, a limited load increase was recorded before the rupture of the second bar. The load–deflection diagram shows that, following rupture of both strengthening bars, the applied load returns to the value corresponding to the plateau observed in the unstrengthened test. This indicates that the CFRP bars are primarily responsible for the entire increase in load-bearing capacity. In this case, the mortar application was mainly required to protect the cross-section against the progression of corrosion and to enhance the durability of the structural element. In actual cases, the overlay could also make a significant contribution to shear strength; however, this potential was not exploited here because the specimen's shear demand was not critical.

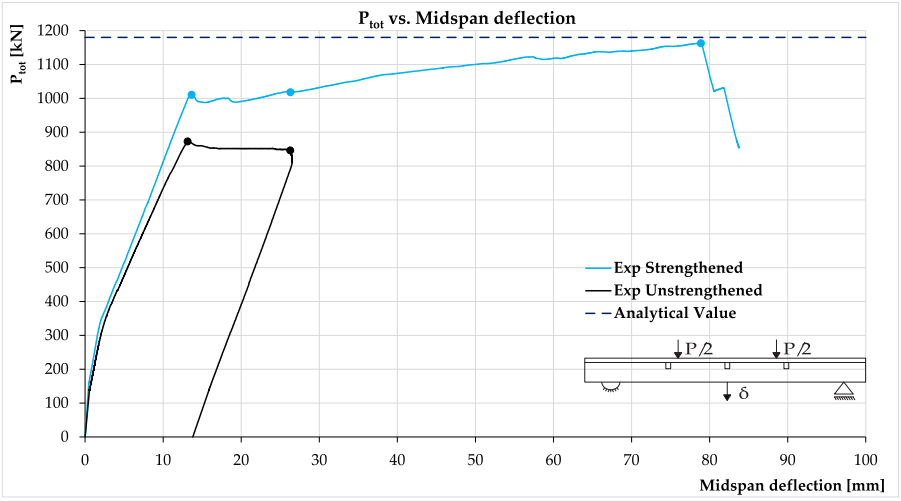


Figure 4-20: Load - Midspan deflection Curve of the unstrengthened and strengthened (black and light blue) tests.

Table 4-10 summarizes the load levels recorded during the strengthened and unstrengthened tests at key response stages, namely at the yielding of the longitudinal reinforcement and at the unloading stage of the unstrengthened specimen. The points are indicated in the diagram by solid circular markers. The last row reports the maximum load attained in each test. In the strengthened configuration, the peak load corresponds to the rupture of the first CFRP bar, whereas in the unstrengthened specimen it coincides with the peak associated with longitudinal reinforcement yielding.

Table 4-10: Load levels reached in the strengthened and unstrengthened tests at significant response stages, including longitudinal reinforcement yielding, unloading (unstrengthened specimen), and maximum load.

	P_s [kN]	δ_s [mm]	P_{un} [kN]
Yielding	**1011**	**13.6**	**873**
Unloading	**1018**	**26.3**	**846**
Max Load	**1163**	**78.9**	**873**

The crack pattern is shown in Figure 4-21. The critical crack developed in the proximity of loading point 4, reaching a width of approximately 15 mm. Another significant crack also formed near loading point 2; however, rupture of the CFRP bars

occurred at the location of the former. Consistently, the load-point displacement diagram (Figure 4-22) indicates that loading point 4 exhibited higher deflections.

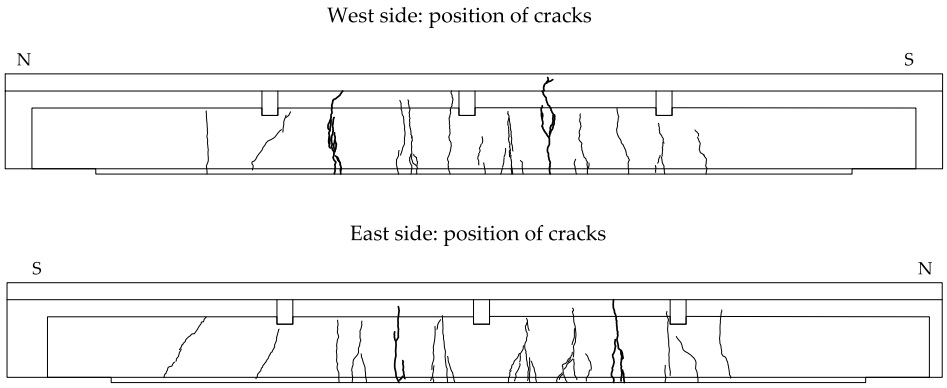


Figure 4-21: crack pattern of the strengthened test.

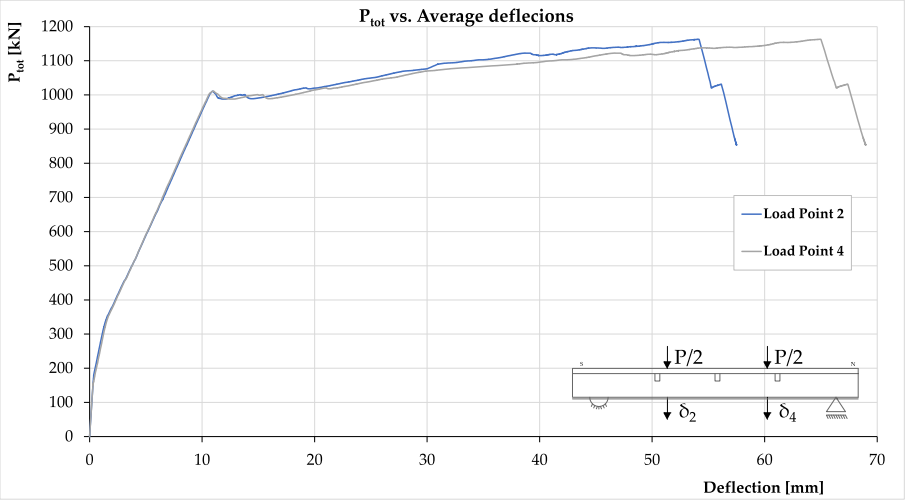


Figure 4-22: Load – deflection curves of the two load points (2 blue and 4 gray).

As mentioned in "Test setup and instrumentation" paragraph, four potentiometric transducers were installed near the support, where the highest slip was expected, to measure possible slip between the existing section and the overlay. At the flange side, the transducer was anchored to the existing section by means of an L-shaped steel profile fixed with a mechanical anchor screwed in the concrete. The L-shaped profile was perforated, and one of the holes was used to connect the transducer through a threaded screw. At the opposite end, the transducer was connected by a screw to a

small steel block, which was bonded to the surface of the overlay using hot-melt adhesive (Figure 4-19b). It should be noted that stress transfer between the two materials, with regard to the web connections, is mainly provided by mechanical interlock due to the high surface roughness, as no mechanical connectors were employed in the strengthening intervention. In fact, the dowels are employed just to connect the overlay to the existing flange. In light of this, the instrumentation results indicate that the maximum measured slip was approximately $1{,}0 \cdot 10^{-2}$ mm. When referred to the gauge length between the fixed points, this corresponds to a maximum strain of about $4{,}3 \cdot 10^{-5}$. The measured maximum slip of approximately 0.01 mm indicates an almost perfect composite action between the existing section and the overlay, thereby experimentally supporting the assumption of full bond adopted in the analytical model. Figure 4-23 presents the recorded slip values corresponding to the different load levels.

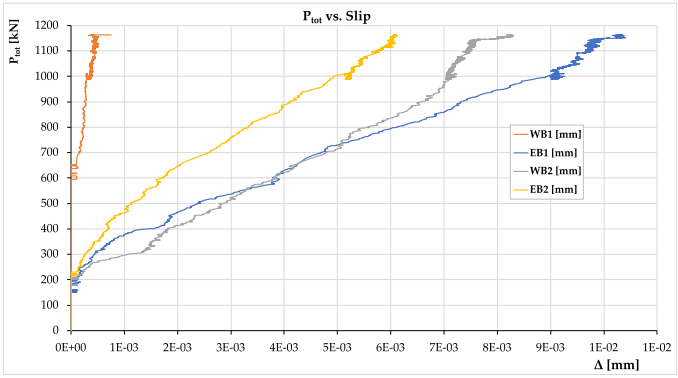


Figure 4-23:Total load-Slip diagrams of the four instruments.

The strain gauges bonded to the CFRP bars were located at midspan and at the two loading sections (three gauges per bar). Since the girder was tested under four-point bending, the region between the two loading points was subjected to a constant bending moment and negligible shear. Accordingly, the measured CFRP strains within this constant-moment region were generally comparable, with differences mainly attributable to local effects (e.g., crack pattern, local bond conditions, and slight eccentricities in gauge positioning) rather than to variations in bending demand.

Some strain gauges failed prematurely during the test due to instrumentation damage, resulting in loss of signal before the end of the loading history. In Figure 4-24, the "x" marker at the end of a curve denotes the premature failure of the strain gauge rather than a structural event. Figure 4-25 reports the specific stage of the test at which the gauge failure occurred and the corresponding strain value recorded immediately before signal loss.

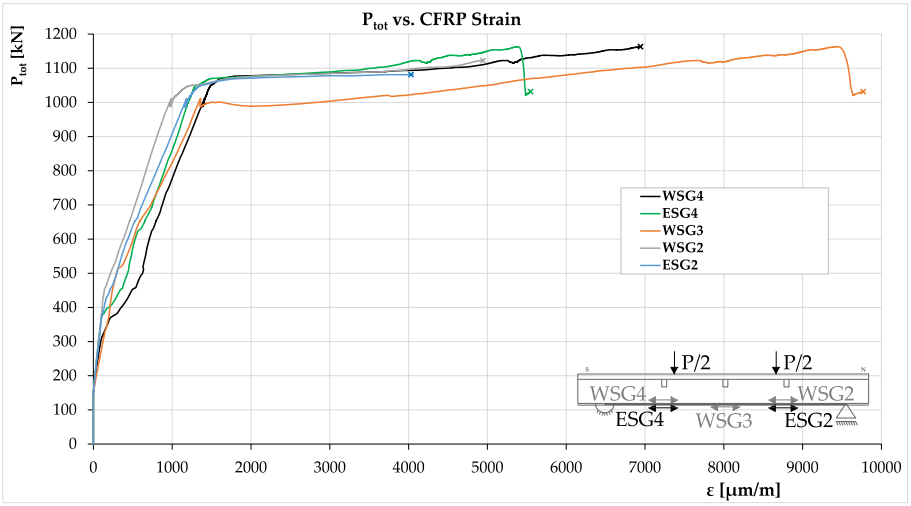


Figure 4-24: Strain gauge measurements on CFRP bars

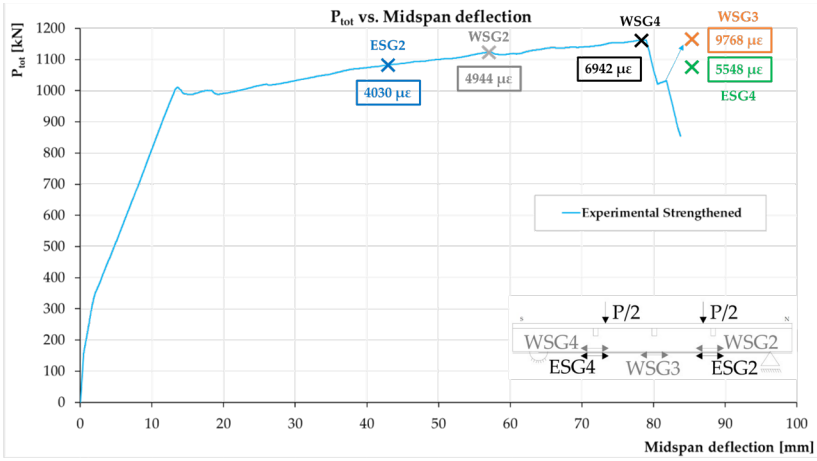


Figure 4-25: Test stage corresponding to the premature failure of the CFRP strain gauge, with indication of the strain value recorded immediately before signal loss (expressed in μm/m, here reported as με).

The strain values recorded immediately before strain-gauge malfunction (approximately 0.40–0.98%) are lower than the ultimate tensile strain reported for the CFRP bars (≈1.5–1.6%). Nevertheless, both CFRP bars eventually ruptured during the test. This apparent discrepancy suggests that the rupture occurred at a cross-section that was not instrumented (or was no longer instrumented due to premature sensor failure), where the local strain demand likely reached the ultimate value. In other words, the recorded strains should be interpreted as representative of the instrumented sections only, while the critical section leading to CFRP rupture may

have experienced higher localized strains due to crack localization and strain concentration. In this case, CFRP rupture was governed by the most critical cracked section, where strain localization occurred.

An alternative interpretation may involve lower actual tensile strength or ultimate strain values of the specific CFRP bars used in this experimental campaign. This hypothesis cannot be excluded at this stage, as the mechanical properties of the ϕ12 bars employed in the test have not yet been directly characterized. Confirmation of this aspect would require dedicated tensile testing of the installed reinforcement.

Figure 4-26 shows the strain measured by the gauge installed on the existing longitudinal steel reinforcement at midspan as a function of the total applied load. Based on the measured mechanical properties of the longitudinal bars, yield strength of approximately 287 MPa and an elastic modulus of 203 GPa, the corresponding yield strain is about 0.141% (≈1410 με). The maximum recorded strain reached about 5071 με, i.e., approximately 3.6 times the yielding strain, confirming that the existing longitudinal reinforcement underwent significant plastic deformation during the test.

This evidence supports the observed ductile global response of the strengthened girder, despite the elastic–brittle behaviour of the CFRP reinforcement.

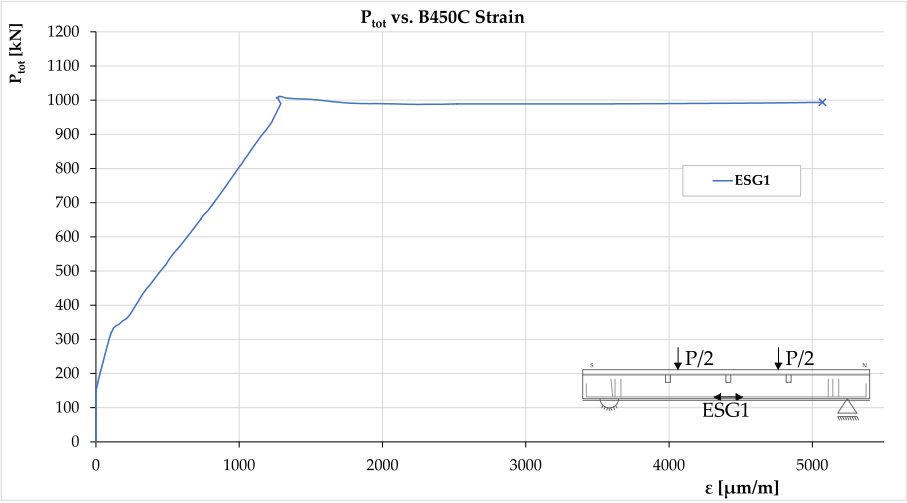


Figure 4-26: Strain gauge measurement on the existing steel bar.

The shear crack openings monitored in the critical shear region remained comparatively limited throughout most of the loading history. Although inclined cracks were observed, their opening remained moderate and did not exhibit unstable growth prior to failure, as shown in Figure 4-27.

The measured shear crack widths increased progressively with load but did not show abrupt changes indicative of shear-controlled failure. All recorded shear crack openings remained below 0.6 mm, even at high load levels. This observation, combined with the strain measurements and the observed failure mode, confirms that the strengthened girder maintained a flexural-dominated response, with shear capacity remaining higher than the corresponding flexural demand.

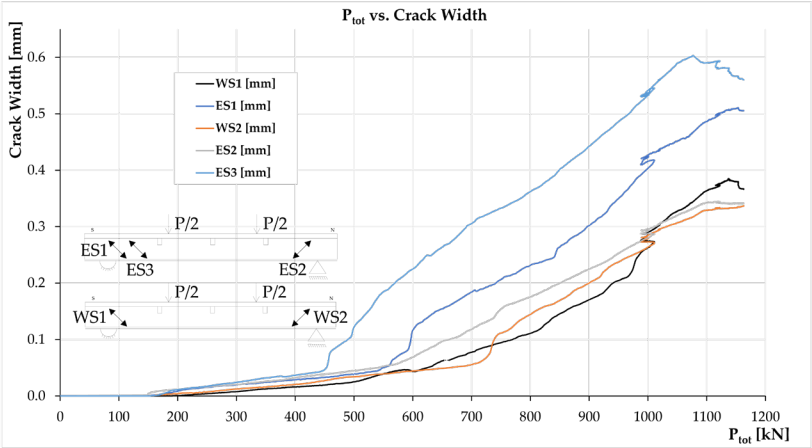


Figure 4-27: Shear crack openings versus applied load.

The flexural crack openings measured at midspan exhibited a progressive and stable increase with increasing applied load (Figure 4-28). Cracking initiated within the constant-moment region between the loading points and subsequently developed in a distributed pattern, consistent with a flexure-dominated response.
The crack opening evolution remained gradual over a wide load range (till a total load of approximately 1000 kN), indicating an adequate interaction between the existing concrete section and the strengthening system. The presence of the FRM overlay contributed to crack control, promoting a more uniform crack distribution and limiting localized crack widening during intermediate load stages. At a total load of 994 kN, marking the initiation of the final branch of the response after yielding of the longitudinal reinforcement, a pronounced increase in crack opening occurred at the level of the CFRP bars. This behaviour is consistent with the redistribution of tensile stresses following steel yielding. Once the existing longitudinal reinforcement reached the plastic regime, additional tensile demand was progressively transferred to the CFRP bars, which remained in the linear-elastic range. As a consequence, higher tensile stresses developed at the level of the strengthening reinforcement,

leading to localized crack widening in that region. This phenomenon reflects the transition from a steel-governed response to a composite action in which the CFRP bars played a dominant role in sustaining the increasing bending demand up to failure.

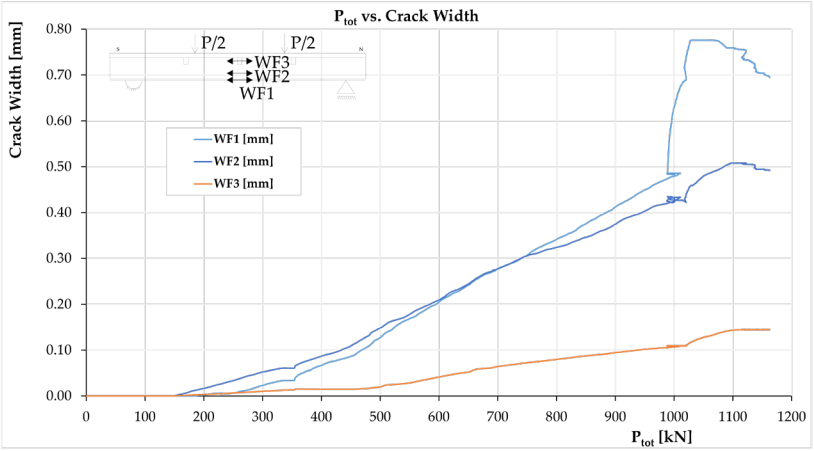


Figure 4-28: Flexural crack openings versus applied load.

Finally, the experimental moment–curvature diagram was derived. At midspan, a potentiometric transducer was installed at the top of the flange to measure the compressive strain of the concrete (Figure 4-19a). In addition, two strain gauges were placed at the same cross-section, one on an existing steel reinforcement bar and one on a CFRP strengthening bar. By combining the strain distribution across the section at different load stages, the curvature χ was determined. The bending moment was then computed from the applied load and the loading scheme.
The initial curvature χ_0 was introduced to account for the self-weight of the girder prior to the application of the external test load. Assuming simply supported boundary conditions and linear-elastic uncracked behaviour, the self-weight W (=150 kN) was modelled as a uniformly distributed load q equal to W/L over the span L. The corresponding midspan bending moment is

$$M_g = \frac{qL^2}{8} = \frac{WL}{8}$$

The initial curvature at midspan was then computed as

$$\chi_0 = \frac{M_g}{E_c J}$$

where:
E_c is the concrete elastic modulus (28 GPa);
J is the moment of inertia of the T-shaped uncracked section ($3.4 \cdot 10^{10}$ mm^4).
The obtained value χ_0=$1.4 \cdot 10^{-7}$ mm^{-1} was added to the experimentally measured curvature values to account for the initial curvature induced by the self-weight of the girder. The blue curve in Figure 4-31 represents the experimental moment–curvature response of the midspan section.

4.4. ANALYTICAL MOMENT-CURVATURE DIAGRAM

The experimental moment–curvature (M–χ) diagram was then compared with the corresponding analytical curve. The analytical evaluation was performed by developing a MATLAB script that computes, for successive increments of curvature χ, the corresponding resisting bending moment M_R by enforcing strain compatibility and internal axial force equilibrium.
The input data consist of the geometric characteristics of the cross-section, which in this case is T-shaped (flange thickness and width, overall section depth, effective depths of the existing and strengthening reinforcements, and web width), as well as the main material properties of both the existing section and the strengthening materials (yield stress, ultimate stress, yield and ultimate strains, and elastic modulus).
The formulation assumes Bernoulli's hypothesis (plane sections remain plane after bending), implying a linear longitudinal strain distribution over the cross-section depth. From this linear distribution (Figure 4-29), the extreme concrete compressive strain and the reinforcement strains follow directly as in Equation 5a,b,c.

Equation 5: strain calculations

$$\varepsilon_c = \chi x_c \quad \text{(a)}$$
$$\varepsilon_s = \chi(d_s - x_c) \quad \text{(b)}$$
$$\varepsilon_{cfrp} = \chi(d_{cfrp} - x_c) \quad \text{(c)}$$

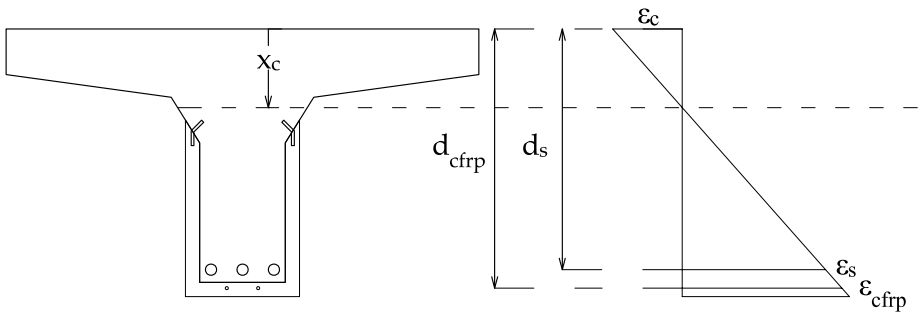


Figure 4-29: Strain profile

Given the strain field, stresses are computed via the adopted constitutive relationships. Concrete in compression is described by a nonlinear stress–strain law (*Equation 6*), adopting the generalized formulation of the expressions originally proposed by Popovics (1970), as reported by Collins (1991). Concrete in tension is considered up to cracking and no tension stiffening is included. The behaviour in tension is considered as in *Equation 7*, where $\varepsilon_{ct} = \frac{f_{ct}}{E_c}$.

Steel reinforcement is modelled with an elastic–perfectly plastic law (*Equation 8* and *Equation 9*). Finally, the strengthening CFRP bars were modelled as linearly elastic up to rupture (*Equation 10*).

$$\sigma_c = f_{cm}\frac{n(\varepsilon_c/\varepsilon_{cm})}{n-1+(\varepsilon_c/\varepsilon_{cm})^{nk}} \quad \text{se } \varepsilon_c < 0 \quad \textit{Equation 6}$$

$$\sigma_c = E_c\varepsilon_c \quad \text{se } 0 < \varepsilon_c < \varepsilon_{ct} \quad \textit{Equation 7}$$

$$\sigma_s = E_s\varepsilon_s \quad \text{se } \varepsilon_s < \varepsilon_{sy} \quad \textit{Equation 8}$$

$$\sigma_s = f_y \quad \text{se } \varepsilon_{sy} \le \varepsilon_s \le \varepsilon_u \quad \textit{Equation 9}$$

$$\sigma_{CFRP} = E_{CFRP}\varepsilon_{CFRP} \quad \text{se } \varepsilon_{FRP} \le \varepsilon_{FRPu} \quad \textit{Equation 10}$$

Concrete stress resultants are evaluated through a fibre-based integration of the section. In particular, the compressed concrete depth x_c, is subdivided into a finite number of layers (6 in the present implementation), within which the stress is taken as constant and equal to the stress computed from the strain at the representative point of the layer (Figure 4-30); analogously, the uncracked tensile region is subdivided into a smaller number of layers (3).

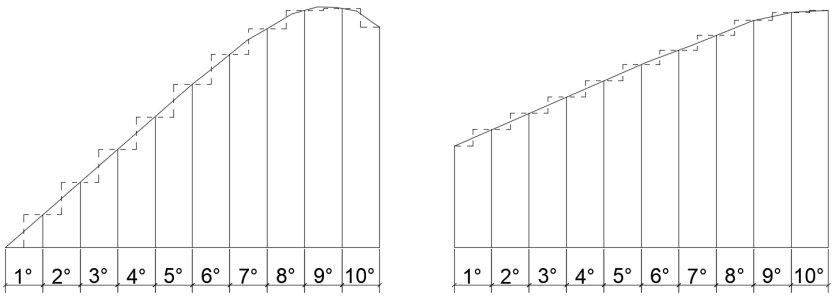


Figure 4-30:examples of the concrete stress approximation in the implemented method

The concrete compressive and tensile resultants are obtained as in Equation 11.

Equation 11

$$C = \sum_{k=1}^{n} \sigma_{ck} b_k \Delta y_k$$

Where b_k denoting the effective width of each layer (accounting for flange/web geometry) and Δy_k its thickness.

The internal forces of the steel layer and of the strengthening bars are obtained as in *Equation 12* and *Equation 13*.

$$T_s = A_s \sigma_s \qquad \textit{Equation 12}$$

$$T_{CFRP} = A_{CRFP} \sigma_{CFRP} \qquad \textit{Equation 13}$$

For each curvature level, axial force equilibrium is enforced by summing all tensile and compressive contributions (existing steel, CFRP bars, concrete in compression and concrete in tension), obtaining the sectional axial force N (Equation 14), which is then imposed equal to zero changing the value of x_c. The sequence compatibility → constitutive laws → stress resultants → equilibrium is repeated until convergence.

Equation 14

$$N = \sum_i T_i - \sum_i C_i = 0$$

Once equilibrium is satisfied, the bending moment corresponding to χ is computed by summing the moments of all internal resultants about the chosen reference axis (in the present work, distances are taken from the upper edge under zero axial force conditions).

Repeating the iterative equilibrium procedure for increasing curvature levels yields the complete nonlinear M-χ relationship of the analysed strengthened section. The analytical M–χ diagram is presented in Figure 4-31b with the grey line.

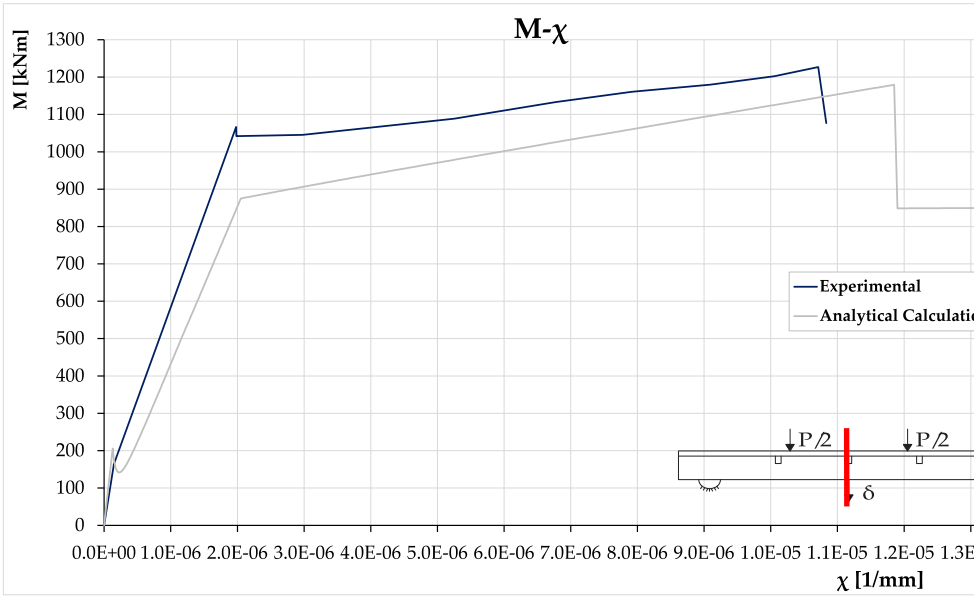


Figure 4-31: Comparison between experimental and analytical curves of moment-curvature.

The two curves (Figure 4-31b) exhibit a reasonably similar trend, with nearly the same slope in the cracked stage. The experimental curve shows a little steeper initial response and reaches higher moments at low curvature, indicating greater early stiffness/strength than predicted. Overall, the analytical model is more gradual and tends to underestimate the moment for a given curvature over most of the loading path. Near the ultimate range, both curves capture a peak followed by degradation, but the analytical prediction exhibits a more abrupt post-peak drop. The resisting bending moment obtained from the analytical calculation is also in good agreement with the experimental result, with values of 1178 kNm and 1227 kNm, respectively.

4.5. CONCLUDING REMARKS

The main conclusions of the experimental investigation can be summarized as follows:

• The proposed strengthening system demonstrated satisfactory structural performance, resulting in an increase in ultimate load of approximately 33% compared to the unstrengthened beam.

• Despite the elastic–brittle behaviour of CFRP, the strengthened member exhibited a satisfactory level of global ductility, with a displacement-based ductility ratio of about 6, due to the combined contribution of the existing steel reinforcement and the CFRP bars.

• The study provides rare experimental evidence on the strengthening of a full-scale RC beam subjected to more than 90 years of natural degradation, contributing to the limited database available for real, long-term deteriorated bridge elements.
• The strengthening intervention can be executed without total interruption of traffic, representing a significant practical advantage compared to full structural replacement.
• The strengthening materials employed are inherently resistant to corrosion and contribute to enhancing the durability of the existing cross-section, which had been significantly compromised by deterioration.
• The analytical moment–curvature model was able to reproduce with good accuracy the ultimate moment and curvature observed experimentally, indicating that the adopted analytical approach can be effectively used as a predictive tool for the structural behaviour of similarly strengthened beams.
These findings support the feasibility of hybrid CFRP–FRM systems as a viable strengthening strategy within bridge management frameworks aimed at extending the service life of aging infrastructure.

4.6. NOTATION

Latin symbols

$\mathbf{A_c}$ – Effective cross-sectional area of the mortar specimen, accounting for the notch.

$\mathbf{A_{cfrp}}$ – Cross-sectional area of the CFRP strengthening bars.

$\mathbf{A_f}$ – Cross-sectional area of a single fibre.

$\mathbf{A_s}$ – Cross-sectional area of the existing reinforcing steel bars.

$\boldsymbol{b_k}$ – effective width of each concrete layer.

C – Resultant compressive force in concrete obtained by sectional integration.

$\mathbf{d_{cfrp}}$ – Effective depth of the strengthening CFRP bars.

$\mathbf{d_s}$ – Effective depth of the existing reinforcing bars.

$\mathbf{E_c}$ – Elastic modulus of concrete or mortar (depending on the equation).

$\mathbf{E_{cfrp}}$ – Elastic modulus of the CFRP bars.

$\mathbf{f_c}$ – Cylindrical compressive strength.

$\mathbf{f_{cm}}$ – Concrete stress at the mid-depth of the considered interval.

$\mathbf{f_{ct}}$ – Concrete tensile strength.

$\mathbf{f_y}$ – Yielding stress of the existing steel bars.

$\mathbf{f_u}$ – Ultimate tensile strength.

J – Second moment of area (moment of inertia) of the section.

k – post-peak shape parameter in the generalized Popovics stress–strain law, governing the descending branch of the concrete compressive response.

L – Span length.

$\mathbf{M_R}$ – Resisting bending moment.

$\mathbf{M_g}$ – Bending moment due to self-weight prior to external loading.

N – Section axial force resultant (imposed equal to zero).

n – (Equation 6) shape parameter of the Popovics stress–strain law, defined as $\frac{E_c \varepsilon_{cm}}{f_{cm}}$.

$\mathbf{T_{CFRP}}$ – Internal axial force in traction of the CFRP strengthening bars.

$\mathbf{T_S}$ – Internal axial force in traction of the existing steel layer.

$\mathbf{V_f}$ – Fibre volume fraction [%].

W – Self-weight of the girder [kN].

$\mathbf{x_c}$ – Compressed concrete depth / neutral axis depth.

Greek symbols

$\Delta \boldsymbol{y_k}$ – thickness of the concrete layer.

$\boldsymbol{\varepsilon_c}$ –Concrete strain at the top of the section.

$\boldsymbol{\varepsilon_{cfrp}}$ – Strengthening CFRP bars strain.

$\boldsymbol{\varepsilon_{cm}}$ – Concrete strain at the mid-depth of the considered interval.

$\boldsymbol{\varepsilon_{ct}}$ – Concrete strain corresponding to the tensile strength.

$\boldsymbol{\varepsilon_s}$ – Existing reinforcing bars strain.

$\boldsymbol{\varepsilon_s}$ – Strain at the level of existing reinforcing bars.

$\boldsymbol{\varepsilon_{sy}}$ – Yielding strain of existing reinforcing bars.

$\boldsymbol{\theta}$ – correlation coefficient accounting for fibre orientation and distribution (Enfedaque et al., 2019), in this case chosen equal to 0.75.

$\boldsymbol{\sigma_c}$ – Concrete stress.

$\boldsymbol{\sigma_{cfrp}}$ – Strengthening CFPR bars stress.

σ_{ck} – Concrete stress at mid-depth of the considered layer.

σ_s – Existing reinforcing bars stress.

ϕ – Bar diameter.

χ – Generic curvature associated to the strain distribution.

χ_0 – Initial curvature due to self-weight prior to external loading.

4.7. REFERENCES

[1] ADEY, B.T. (2019). A ROAD INFRASTRUCTURE ASSET MANAGEMENT PROCESS: GAINS IN EFFICIENCY AND EFFECTIVENESS. INFRASTRUCTURE ASSET MANAGEMENT, 6(1), 2–14. https://doi.org/10.1680/jinam.17.00018

[2] AIDOO, J., HARRIES, K.A., & PETROU, M.F. (2006). FULL-SCALE EXPERIMENTAL INVESTIGATION OF REPAIR OF REINFORCED CONCRETE INTERSTATE BRIDGE USING CFRP MATERIALS. JOURNAL OF BRIDGE ENGINEERING, 11(3), 350–358.

[3] ALMUSALLAM, A.A. (2001). EFFECT OF DEGREE OF CORROSION ON THE PROPERTIES OF REINFORCING STEEL BARS. CONSTRUCTION AND BUILDING MATERIALS, 15(8), 361–368.

[4] BELLETTI, B., RODRÍGUEZ, J., ANDRADE, C., FRANCESCHINI, L., SÁNCHEZ MONTERO, J., & VECCHI, F. (2020). EXPERIMENTAL TESTS ON SHEAR CAPACITY OF NATURALLY CORRODED PRESTRESSED BEAMS. STRUCTURAL CONCRETE, 21(5), 1777–1793.

[5] CORONELLI, D., & GAMBAROVA, P. (2004). STRUCTURAL ASSESSMENT OF CORRODED REINFORCED CONCRETE BEAMS:

Modeling guidelines. Journal of Structural Engineering (ASCE), 130(8), 1214–1224.

[6] De Lorenzis, L., & Teng, J.G. (2006). Near-surface mounted FRP reinforcement: An emerging technique for strengthening structures. Composites Part B: Engineering, 37(2–3), 119–143.

[7]

[8] Di Prisco, M. (2019). Critical infrastructures in Italy: State of the art, case studies, rational approaches to select intervention priorities. In: fib Symposium Proceedings.

[9] Di Stefano, N. (2022). Assessment of existing bridges with special emphasis on corrosion. PhD Thesis, University of Brescia, Curriculum "Rehabilitation of Historical and Modern Buildings".

[10] DIANA FEA B.V. (2022). DIANA Finite Element Analysis (Release 10.6). Delft, The Netherlands.

[11] Frangopol, D.M., & Liu, M. (2007). Maintenance and management of civil infrastructure based on condition, safety, optimization, and life-cycle cost. Structure and Infrastructure Engineering, 3(1), 29–41.

[12] Higgins, C., et al. (2010). Influence of corrosion on cracking and spalling of reinforced concrete. ACI Materials Journal, 107(2), 179–187.

[13] HUANG, Y., GRÜNEWALD, S., SCHLANGEN, E., & LUKOVIĆ, M. (2022). STRENGTHENING OF CONCRETE STRUCTURES WITH ULTRA-HIGH PERFORMANCE FIBER REINFORCED CONCRETE (UHPFRC): A CRITICAL REVIEW. CONSTRUCTION AND BUILDING MATERIALS, 336, 127398.

[14] IMPERATORE, S., RINALDI, Z., & COCCIA, S. (2017). INFLUENCE OF CORROSION ON THE DUCTILITY OF REINFORCED CONCRETE BEAMS. ENGINEERING STRUCTURES, 146, 28–37.

[15] IAVARONE, F., DI LUDOVICO, M., PROTA, A., ET AL. (2024). SHEAR BOND BETWEEN EXISTING CONCRETE AND HIGH-STRENGTH FIBER-REINFORCED OVERLAY: INFLUENCE OF SUBSTRATE STRENGTH AND INTERFACE ROUGHNESS. STRUCTURAL CONCRETE, 25, 526–536.

[16] LAMPROPOULOS, A.P., TSIOULOU, O., & DRITSOS, S.E. (2016). STRENGTHENING OF REINFORCED CONCRETE BEAMS USING UHPFRC LAYERS OR JACKETS. CONSTRUCTION AND BUILDING MATERIALS, 106, 103–112.

[17] LUPOI, A., BELLETTI, B., VECCHI, F., ET AL. (2022). EXPERIMENTAL ASSESSMENT OF NATURALLY CORRODED REINFORCED CONCRETE BRIDGE ELEMENTS. STRUCTURAL CONCRETE, 23(4), 2501–2516.

[18] MANSOUR, M., BAKHOUM, M.M., & EL-SALAKAWY, E. (2017). EFFECT OF SUBSTRATE SURFACE ROUGHNESS ON THE FLEXURAL PERFORMANCE OF CONCRETE SLABS STRENGTHENED WITH AN SFRC OVERLAY. PCI JOURNAL, 62(1), 44–61.

[19] ROGERS, R.A., WOTHERSPOON, L., SCOTT, A., & INGHAM, J.M. (2012). RESIDUAL STRENGTH ASSESSMENT AND DESTRUCTIVE TESTING OF DECOMMISSIONED CONCRETE BRIDGE BEAMS WITH CORRODED PRETENSIONED REINFORCEMENT. PCI JOURNAL, 57(3), 100–118.

[20] SAVINO, P., TONDOLO, F., SABIA, D., ET AL. (2023). LARGE-SCALE EXPERIMENTAL STATIC TESTING ON 50-YEAR-OLD PRESTRESSED CONCRETE BRIDGE GIRDERS. APPLIED SCIENCES, 13(2), 834.

[21] TÄLJSTEN, B. (2006). STRENGTHENING OF CONCRETE STRUCTURES WITH FRP COMPOSITES. JOURNAL OF COMPOSITES FOR CONSTRUCTION (ASCE), 10(3), 187–194.

[22] WALRAVEN, J. (2021). ASSESSMENT OF CONCRETE STRUCTURES WITH CORRODED REINFORCEMENT: DEVELOPMENT OF RECOMMENDATIONS. IN: PROCEEDINGS OF THE 3RD CACRCS WORKSHOP – CAPACITY ASSESSMENT OF CORRODED REINFORCED CONCRETE STRUCTURES, DELFT UNIVERSITY OF TECHNOLOGY.

[23] ZHANG, R., CASTEL, A., & FRANÇOIS, R. (2009). CONCRETE COVER CRACKING WITH REINFORCEMENT CORROSION OF RC BEAMS. CEMENT AND CONCRETE RESEARCH, **39(5), 371–382.**

4.8. LIST OF TABLES

Table 4-1: existing section materials' properties. 128

Table 4-2: Uniaxial compressive strength results of 150 × 150 × 150 mm mortar cubes; specimens 5 and 7, affected by casting defects, were not considered in the calculation of the mean value. 130
Table 4-3:three point bending tests on notched FRM beams results. 131
Table 4-4: fibre content calculations. Column A_f [%] represents the previous column $n \cdot A_f$ divided for the mortar cross sectional area A_c. A and B are the two different surfaces of the fracture. 133
Table 4-5: Experimental flexural strength results for 40 × 40 × 160 mm mortar prisms. 134
Table 4-6: Compressive strength results obtained from the two halves of the fractured 40 × 40 × 160 mm prisms. 135
Table 4-7: Strengthening mortar's properties. 138
Table 4-8:CFRP bars porperties based on the technical datasheet and on external laboratory tests. 139
Table 4-9: CFRP bars properties. 140
Table 4-10: Load levels reached in the strengthened and unstrengthened tests at significant response stages, including longitudinal reinforcement yielding, unloading (unstrengthened specimen), and maximum load. 150

4.9. LIST OF FIGURES

Figure 4-1: degradation conditions of the bridge in situ (a) and of the specimen considered in the experimental programme (b). 127
Figure 4-2: spraying of the specimens (a); specimens after demoulding (b); cylindrical specimens after demoulding, showing defects caused by difficulties in spray casting and compaction, leading to local heterogeneities and incomplete filling at the base (c). 129
Figure 4-3: Cube specimens 5 and 7 affected by casting defects. 130
Figure 4-4: FRM-PP notched beam test setup (a) and detail of the crack-bridging mechanism (b). 131
Figure 4-5: Nominal stress – CMOD curves of the mapegrout specimens. 132
Figure 4-6: prismatic specimens 40 x 40 x 160 mm during the three-point bending test (a) and after the rupture (b). 134
Figure 4-7: Comparison between the numerical fitting curve and the average experimental Nominal stress – CMOD curve of the notched prisms. 137
Figure 4-8: Multilinear tensile stress–crack opening law implemented in the numerical model for the strengthening mortar. 137
Figure 4-9: cross-section of the unstrengthened (a) and strengthened girder (b). 140
Figure 4-10: pictures of the bridge location at the moment of casting (a) and during the dismantling process (b). 141

Figure 4-11:position of dowels to connect the overlay to the flange (a) and restored cracks and concrete cover loss (b). 142
Figure 4-12: CFRP strengthening bars (a); wood temporary reference guide for the thickness of the overlay (b), detail of the overlay application at a location where the wooden formwork guides were removed (c). 143
Figure 4-13: Close-up view of the support region in the load test configuration. 143
Figure 4-14: Technical drawing of the strengthening intervention, indicating the adopted reinforcement lengths. 144
Figure 4-15:test setup under four-point loading: schematic view (a) and photograph (b). 145
Figure 4-16: instrumentation layout and loading scheme. 146
Figure 4-17:photographs of strain gauges on the CFRP strengthening bars (a) and on the existing steel reinforcement (b) 147
Figure 4-18: potentiometric transducers at midspan, aligned respectively with the strengthening reinforcement, the existing longitudinal reinforcement, and below the original transverse beam (a); potentiometric transducer positioned for measuring shear crack widths (b). 148
Figure 4-19: potentiometric transducers for the measurement of the compression strain of the concrete (a); potentiometric transducer for the measurement of the slip between the existing section and the overlay (b). 148
Figure 4-20: Load - Midspan deflection Curve of the unstrengthened and strengthened (black and light blue) tests. 150
Figure 4-21: crack pattern of the strengthened test. 151
Figure 4-22: Load – deflection curves of the two load points (2 blue and 4 gray). 151
Figure 4-23:Total load-Slip diagrams of the four instruments. 152
Figure 4-24: Strain gauge measurements on CFRP bars 153
Figure 4-25: Test stage corresponding to the premature failure of the CFRP strain gauge, with indication of the strain value recorded immediately before signal loss (expressed in μm/m, here reported as με). 153
Figure 4-26: Strain gauge measurement on the existing steel bar. 154
Figure 4-27: Shear crack openings versus applied load. 155
Figure 4-28: Flexural crack openings versus applied load. 156
Figure 4-29: Strain profile 158
Figure 4-30:examples of the concrete stress approximation in the implemented method 159
Figure 4-31: Comparison between experimental and analytical curves of moment-curvature. 160

5. STOCHASTIC MODELLING OF ADVANCED STRENGTHENING STRATEGIES ON EXISTING DETERIORATED GIRDERS

ABSTRACT

This study proposes a stochastic nonlinear finite element framework for assessing the structural response of existing deteriorated reinforced concrete (RC) and prestressed reinforced concrete (PRC) girders strengthened with advanced retrofit systems. The investigated case studies include a 90-year-old RC T-girder strengthened with a CFRP–FRM overlay system and 60-year-old PRC I-girders strengthened with UHPFRC web enlargement and externally bonded FRP plates.

Nonlinear analyses were performed using the Disturbed Stress Field Model implemented in VecTor2, incorporating detailed constitutive relationships for concrete, reinforcement, bond-slip, prestressing, and fibre-reinforced materials. Uncertainty was introduced through a Monte Carlo simulation framework considering three stochastic scenarios: corrosion-only variability, material-property variability and combined corrosion and material uncertainty. Corrosion was modelled as a lognormal random variable governing steel cross-section loss, bond degradation, and cover cracking, while material variability was represented through statistically correlated models for concrete and steel properties.

Results indicate that, for moderate levels of natural corrosion, variability in mechanical properties governs the dispersion of ultimate load capacity, whereas corrosion-rate uncertainty produces negligible response variability. In all cases, deterministic nonlinear analyses underestimate the stochastic mean capacity by approximately 9–18%, confirming that deterministic predictions do not represent the expected value of nonlinear stochastic systems. The coefficient of variation of ultimate load remained moderate (≈3–3.5%) for both RC and PRC girders, despite the presence of deterioration and strengthening systems.

The proposed framework provides a rational basis for probabilistic assessment of strengthened deteriorated girders and highlights the importance of accounting for material uncertainty when evaluating the structural reliability and expected performance of existing infrastructure.

Keywords: Stochastic Modelling; Monte Carlo Simulation; Reinforced Concrete; Prestressed Concrete; Corrosion; Strengthening; UHPFRC; CFRP; Nonlinear Finite Element Analysis.

5.1. INTRODUCTION

A significant portion of the existing reinforced concrete (RC) infrastructure worldwide has reached or exceeded its nominal service life, often exhibiting varying degrees of deterioration due to environmental exposure and corrosion of reinforcement. Corrosion-induced damage remains one of the primary causes of structural degradation, leading to steel cross-section loss, cracking of the concrete cover, bond deterioration, and ultimately reduction of structural capacity (Tuutti, 1982; Andrade et al., 1993; fib Bulletin 34, 2006).

In addition to deterioration, uncertainty in material properties plays a crucial role in the assessment of existing structures. Concrete compressive strength, tensile strength, and elastic modulus may significantly differ from specified values due to construction practices, aging, and environmental effects. Similarly, steel mechanical properties exhibit statistical variability related to production processes (Mirza et al., 1979; Nowak & Szerszen, 2003). For existing structures, particularly historical girders with limited documentation, these uncertainties can be substantial.

Traditional deterministic nonlinear finite element analyses provide a single prediction based on nominal or measured mean properties. However, nonlinear structural response is highly sensitive to variations in material parameters, especially when damage localization and bond degradation mechanisms govern failure. As demonstrated in stochastic finite element studies (e.g., Ma, 2018), deterministic analyses do not necessarily represent the mean structural response and may correspond to lower-bound capacity estimates due to nonlinear interaction among random inputs and skewed capacity distributions.

To address these limitations, stochastic finite element methods (SFEM) have been increasingly adopted in structural engineering to quantify uncertainty propagation and evaluate probabilistic structural performance (Liu et al., 1986; Sudret, 2007). In the context of reinforced concrete, stochastic approaches have been applied to material variability, spatial random fields, and deterioration processes, highlighting the importance of accounting for both mechanical and environmental uncertainties (Hunter, 2016; Ma, 2018).

At the same time, advanced strengthening techniques such as externally bonded CFRP systems and ultra-high-performance fibre-reinforced concrete (UHP-FRC) overlays have demonstrated significant potential in restoring or enhancing the capacity of deteriorated girders. Nevertheless, the effectiveness of such interventions under uncertainty conditions remains insufficiently investigated, particularly when corrosion damage and material variability coexist.

This study proposes a structured stochastic nonlinear finite element modelling framework for existing deteriorated RC and PRC girders strengthened with innovative retrofit systems. Nonlinear finite element analyses are performed using the Modified Compression Field Theory (MCFT) implemented in VecTor2 software

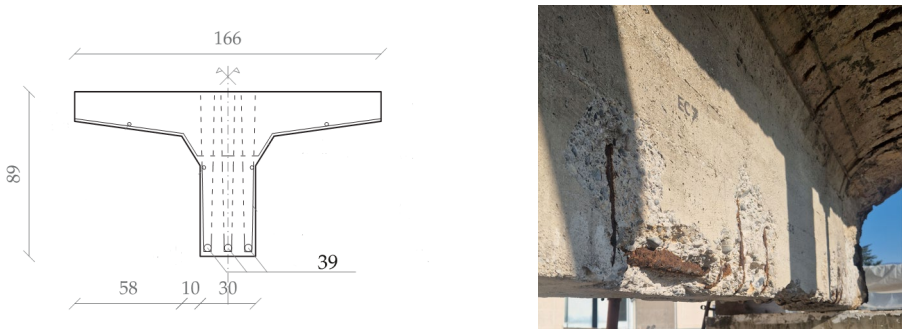
(Vecchio, 2001), coupled with Monte Carlo simulations to propagate uncertainties associated with corrosion parameters and material properties. Two stochastic approaches are considered: (i) corrosion-only variability, (ii) materials-only variability and (iii) combined material and corrosion variability. The objective is to quantify the influence of uncertainty on structural response and to assess the reliability of advanced strengthening strategies under realistic deterioration scenarios.

In addition to the naturally deteriorated girders described previously, an additional set of analyses was conducted on beams subjected to accelerated corrosion. These simulations were introduced in order to better investigate the sensitivity of the structural response to corrosion-related parameters under conditions where corrosion effects are more pronounced. The results obtained for all case studies are presented and critically discussed in the following sections.

5.2. EXPERIMENTAL PROGRAMS AND RESULTS

5.2.1. Historical girder strengthened with a CFRP–FRM retrofit system

The first experimental campaign involved a reinforced concrete (RC) T-beam extracted from an existing structure that had been in service for more than 90 years. The geometry of the cross-section is shown in Figure 5-1a. Given its prolonged exposure to environmental actions, the beam exhibited typical signs of aging and deterioration, including surface cracking and localized degradation of the concrete cover (Figure 5-1b). The longitudinal tensile reinforcement consisted of three diameter 39 mm steel bars located at the intrados, while transverse reinforcement nominal diameter was about 10 mm, characterized by six legs. These measured diameters were used as reference values in the deterministic model and as mean values in the stochastic simulations.



(a) (b)

Figure 5-1: existing section (a) and degradation conditions (b) of the historical RC girder.

To restore and enhance its flexural capacity, the beam was strengthened using an externally applied hybrid retrofit system. The intervention consisted of two

pultruded CFRP bars with a nominal diameter of 12 mm, installed at the intrados of the beam along the longitudinal axis. The CFRP reinforcement was embedded within a 50 mm thick overlay made of fibre-reinforced mortar incorporating polypropylene fibres. The overlay served both as a protective jacket and as a mechanical anchorage system for the CFRP bars, ensuring composite action between the existing concrete substrate and the strengthening layer. The geometric properties of the CFRP bars (area, nominal tensile strength, elastic modulus) and of the overlay material (thickness and mechanical properties) were experimentally characterized and subsequently adopted as input parameters in the numerical model.

Surface preparation was performed using an electromechanical hammer prior to the application of the overlay, achieving a surface roughness of approximately ±5 mm to ensure adequate bond between the existing concrete substrate and the new mortar layer.

The beam was tested under a symmetric four-point bending configuration with a total span of 7.30 m and a shear span of about 2.11 m. The test was conducted under displacement control using. Midspan deflection was recorded continuously throughout the test. The corresponding load–displacement curve is reported in Figure 5-2.

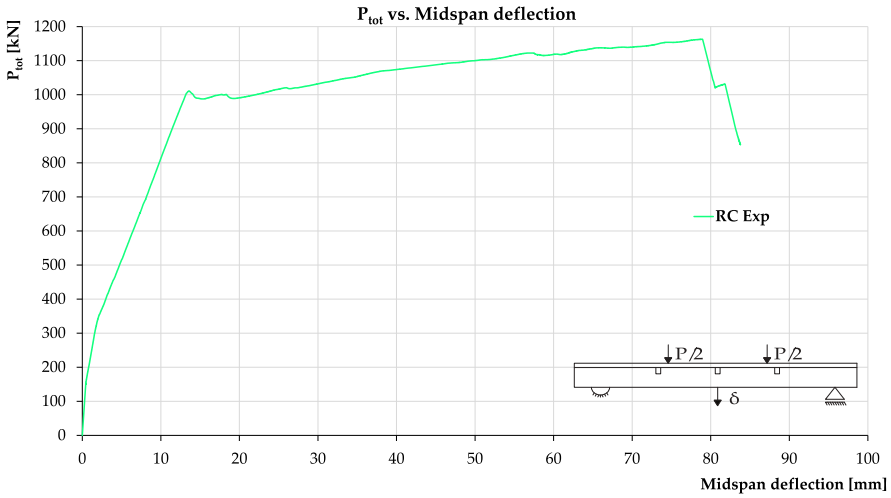


Figure 5-2:Total Load versus Midspan deflection of the strengthened RC beam

The load–displacement response exhibited an initial approximately linear phase up to first cracking, followed by progressive stiffness reduction associated with crack development and reinforcement yielding. The beam reached a maximum total applied load of 1163 kN, corresponding to a midspan deflection of approximately 79 mm. These values were used as reference targets for validation of the deterministic and stochastic numerical models.

Ultimate collapse was governed by rupture of the externally added CFRP bars at the intrados. Prior to CFRP rupture, yielding of the existing tensile steel reinforcement

occurred, allowing the development of plastic deformations. This sequence of events defined the governing failure mechanism adopted in the numerical simulations.
The observed crack pattern was predominantly flexural, with multiple cracks forming within the constant moment region between the loading points. Crack distribution and spacing were documented during testing and used as qualitative reference for assessing the ability of the numerical model to reproduce crack localization and stiffness degradation.

5.2.2. 60 years PRC girders strengthened with UHPFRC

The second experimental campaign involved three prestressed reinforced concrete girders with I-shaped cross-sections, extracted from an existing structure that had been in service for approximately 60 years. The geometric characteristics of the cross-section and the observed deterioration conditions are reported in Figure 5-3.

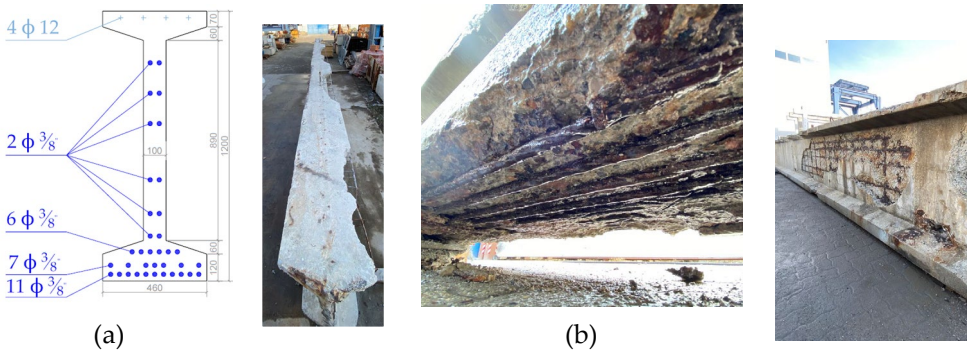
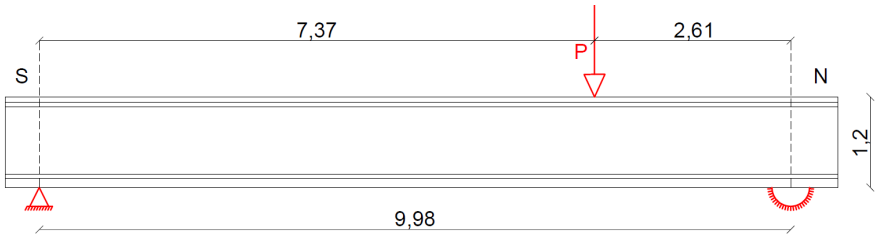


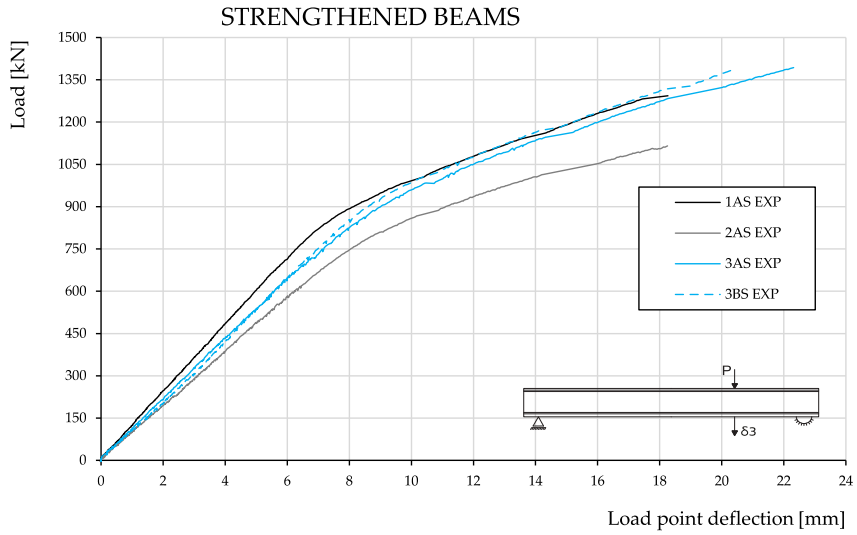
Figure 5-3:existing section (a) and degradation conditions (b) of the PRC girders.

The original prestressing system was defined according to the available design documentation. The initial prestressing stress was 1350 MPa. Estimated prestress losses due to shrinkage (50 MPa), concrete creep (30 MPa), elastic shortening of concrete (60 MPa), and steel relaxation (162 MPa) resulted in total losses of 302 MPa. The corresponding effective prestressing stress adopted for numerical modelling was therefore about 1050 MPa. Further details regarding the implementation of prestress in the finite element model are provided in Paragraph 3.
Transverse reinforcement consisted of two-legged stirrups with a diameter of 10 mm. The strengthening intervention included a web overlay of 50 mm per side realized using ultra-high-performance fibre-reinforced concrete (UHPFRC) with a measured compressive strength of 125 MPa. In addition, four externally bonded FRP plates with a nominal thickness of 1.4 mm were installed at the intrados to enhance flexural capacity.
The web enlargement modified the cross-sectional geometry and shear-resistant area, while the externally bonded FRP plates provided additional tensile reinforcement at the bottom fibre. The geometric and mechanical properties of the strengthening materials were used as input parameters in the numerical simulations.

The beams were tested under displacement control using a non-symmetric three-point bending configuration, as illustrated in Figure 5-4a. The maximum applied load reached 1400 kN, corresponding to the capacity limit of the jack. Structural collapse was not achieved during testing. The recorded total load–load point displacement response, shown in Figure 5-4b, was used for calibration and validation of the deterministic finite element model and for comparison with the stochastic simulations.



(a)



(b)

Figure 5-4: experimental set-up of the PRC girders (a) and experimental results in terms of total load versus load point deflection (b).

5.3. DETERMINISTIC ANALYSES

5.3.1. Constitutive Models

The nonlinear analyses were performed using the VecTor2 formulation based on the Disturbed Stress Field Model (DSFM), an extension of the Modified Compression Field Theory (MCFT) for reinforced concrete membrane elements (Vecchio, 2001).

The material response at the element level is obtained through iterative enforcement of compatibility, equilibrium and constitutive relationships.
The constitutive relationships adopted for each material are described below.
The pre-peak compressive response of concrete was modelled using the parabolic stress–strain relationship proposed by Hognestad (1951). The ascending branch up to the peak compressive strength f'_c is defined as:

$$\sigma_c = f'_c \left[2\left(\frac{\varepsilon_c}{\varepsilon_0}\right) - \left(\frac{\varepsilon_c}{\varepsilon_0}\right)^2 \right]$$

where ε_0 is the strain corresponding to peak stress.
The post-peak descending branch was defined according to the Modified Park–Kent model (Scott et al., 1982), allowing representation of strain softening and confinement effects.
Confinement was modelled using the Kupfer–Richart criterion (Kupfer et al., 1969), accounting for biaxial stress interaction. Compression softening due to transverse cracking was introduced following the formulation by Vecchio (1992a), in which the effective compressive stress is reduced as a function of principal tensile strain:

$$\sigma_c = \beta_c f'_c$$

where β_c is a softening coefficient dependent on the transverse tensile strain.
Concrete tensile behaviour was represented by a linear elastic response up to the tensile strength f_t, followed by a nonlinear tension softening law according to Hordijk (1991). The post-cracking stress–strain relationship is governed by a fracture-energy-based formulation:

$$\sigma_t = f_t \cdot g(\varepsilon_t)$$

where $g(\varepsilon_t)$ follows the exponential softening function proposed by Hordijk.
Tension stiffening effects were modelled using the Modified Bentz formulation (Bentz, 2005), which accounts for interaction between cracked concrete and embedded reinforcement within the MCFT framework.
Crack orientation was determined according to the Mohr–Coulomb stress criterion, while crack slip behaviour followed the Walraven aggregate interlock model (Walraven, 1981). Crack spacing was defined according to CEB-FIP Model Code (1978).
Reinforcing steel was modelled using a nonlinear cyclic constitutive law incorporating the Bauschinger effect according to Seckin (1981). Dowel action across cracks was represented following Tassios (1980), and bar buckling under compression was modelled using the formulation proposed by Akkaya et al. (2012).
Bond-slip behaviour between reinforcement and concrete was described using the model proposed by Eligehausen et al. (1983), enabling simulation of bond deterioration and tension stiffening mechanisms.
Prestressing tendons were modelled as discrete truss-bar elements supporting axial tension. In VecTor2, no dedicated constitutive model specific to prestressing steel

(including time-dependent losses or relaxation laws) is implemented. Instead, prestress is introduced through an initial strain condition applied to the tendon elements, while their mechanical behaviour follows the standard steel constitutive formulation available for truss reinforcement.
The CFRP bars and externally bonded FRP plates were modelled as linear elastic brittle materials, characterized by elastic modulus and ultimate tensile strength. Failure was assumed to occur upon reaching the ultimate tensile strain, with no post-peak behaviour.
The UHPFRC web enlargement and the fibre-reinforced mortar overlay were modelled using the constitutive framework available in VecTor2 for fibre-reinforced concrete (FRC). The compressive response was defined using the same nonlinear compressive law adopted for the other concrete materials. The tensile behaviour was defined according to the fib Model Code 2010 formulation for fibre-reinforced concrete. This model distinguishes between pre-cracking behaviour and post-cracking residual strength levels, typically characterized by residual tensile strengths at specified crack mouth opening displacements (CMOD). In VecTor2, the fib 2010 implementation corresponds to a tension softening law that accounts for fibre bridging effects through residual tensile stress parameters. The tensile response is characterized by an initial linear elastic behaviour up to the cracking strength (f_{R1}), followed by a post-cracking phase with residual tensile stresses governed by fibre contribution (f_{R3}), according to fib Model Code 2010.

5.3.2. Historical RC Girder

The deterministic numerical model of the historical reinforced concrete T-girder was developed using VecTor2 within a two-dimensional plane stress formulation. The modelling strategy aimed to reproduce the actual geometry, material properties, reinforcement layout, and boundary conditions of the tested specimen while ensuring numerical stability and computational efficiency.
The original cross-section exhibits a T-shaped geometry with variable flange width and tapered transitions between flange and web. Since VecTor2 is a two-dimensional program, the three-dimensional geometry was reproduced by assigning different out-of-plane thicknesses to concrete regions within the 2D mesh.
Multiple concrete material regions were defined to approximate the variable cross-sectional width. The adopted equivalent thicknesses ranged between 300 mm (web region) and 1660 mm (maximum flange width), allowing a piecewise representation of the real section geometry (Figure 5-5a). The inclined transition between flange and web was discretized using stepped regions; this geometric simplification had negligible influence on the global structural response.
The thickness values adopted for each material region are summarized in Table 5-1.

Table 5-1: Out-of-plane thickness assigned to concrete regions (Historical RC Girder).

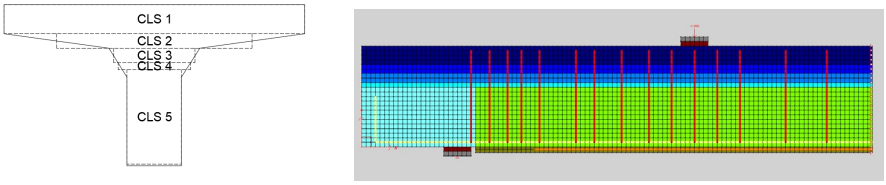
Material ID	Structural Region	Assigned Thickness [mm]
CLS1	Flange – maximum width	1660
CLS2	Transition region	1080
CLS3	Transition region	450
CLS4	Transition region	400
CLS5	Web	300
FRM	Bottom overlay	300

Figure 5-5b shows the numerical model. The element size was 40 × 40 mm throughout the main body of the beam, while a refined mesh of 40 × 30 mm was adopted in the bottom FRM overlay. The strengthened configuration was modelled under the assumption of perfect bond between the existing concrete substrate and the FRM overlay. In VecTor2, this condition was implemented by superimposing the plane stress elements of the overlay onto those of the existing concrete and assigning identical nodal coordinates to the corresponding vertices. This approach enforces full displacement compatibility between the two materials without introducing interface elements. The existing longitudinal reinforcement and stirrups, as well as the strengthening reinforcement, were modelled as discrete truss elements embedded within the concrete mesh. Since VecTor2 requires the reinforcement area to be defined per transverse section, the total equivalent areas of longitudinal bars, stirrups, and strengthening reinforcement were calculated and assigned accordingly. The reinforcement areas adopted in the deterministic model are reported in Table 5-2.

Table 5-2: Reinforcement areas adopted in the deterministic model (Historical RC Girder).

Reinforcement Type	Bar Diameter [mm]	Number of Bars	Total Area [mm²]
Longitudinal steel	39	3	3448
Stirrups (6 legs)	8	6	300
CFRP bars	12	2	226

Owing to geometric and loading symmetry, only half of the beam was modelled.



(a) (b)

Figure 5-5: discretization of the section (a) and finite element model (b) of the historical RC girder.

The experimental support conditions were reproduced by modelling steel bearing plates and elastomeric layers at the support regions. Boundary conditions were defined as follows:

- support node: horizontal and vertical displacements restrained;
- symmetry axis at midspan: horizontal displacement restrained.

The analysis was performed in two loading stages:

In the first stage, self-weight, was applied as distributed nodal loads based on:

- concrete density (25 kN/m³). In the finite element implementation, this resulted in equivalent nodal loads of approximately 0.56 kN per node;
- the additional weight of the FRM overlay was included by assigning a unit weight of 24 kN/m³ to the strengthening layer, corresponding to an additional equivalent nodal load of approximately 0.04 kN per node in the overlay region;
- the self-weight of half of the steel spreader beam used in the experimental setup was applied as a concentrated load of 7 kN at the central node of the loading plate, consistent with the half-beam symmetry assumption adopted in the numerical model.

In the second stage, a displacement-controlled loading was applied at the loading node, with incremental vertical displacement of 0.1 mm per step.

Geometric nonlinearity was activated throughout the analysis.

Table 5-3 shows the material properties assigned in the deterministic finite element model correspond to experimentally measured mean values. These values constitute the reference configuration for subsequent stochastic analyses.

Table 5-3:Material Properties Adopted in the Deterministic Model (Historical RC Girder).

Material	Parameter	Symbol	Value	Unit
Existing Concrete	Compressive strength	f'_c	44	MPa
	Elastic modulus	E_c	28.9	GPa
	Tensile strength	f_t	2.19	MPa
	Unit weight	γ_c	25	kN/m³
Longitudinal Steel Reinforcement	Yield strength	f_y	287	MPa
	Ultimate strength	f_u	412	MPa
	Elastic modulus	E_s	203	GPa
	Ultimate strain	ε_u	21.8	%
Stirrups	Yield strength	f_y	268	MPa
	Ultimate strength	f_u	344	MPa
	Elastic modulus	E_s	185	GPa
	Ultimate strain	ε_u	6.4	%
FRM Overlay	Compressive strength	f'_c	41.2	MPa
	Elastic modulus	E_c	28	GPa

Material	Parameter	Symbol	Value	Unit
	Tensile strength	f_t	2.12	MPa
	Unit weight	γ_c	24	kN/m³
Fibre Smeared Reinforcement	Fibre type	-	Polypropylene-Straigth	-
	Volume fraction	V_f	0.44	%
	Fibre length	L_f	24	mm
	Fibre Diameter	D_f	0.53	mm
	Residual flexural strength	f_{R1}	3.11	MPa
	Residual flexural strength	f_{R3}	4.52	MPa
CFRP Bars	Elastic modulus	E_{cfrp}	168	GPa
	Ultimate strength	f_u	2540	MPa
	Ultimate strain	ε_u	1.5	%

5.3.3. 60 Years PRC Girders

Since VecTor2 is a 2D program, the out-of-plane width of the I-section was introduced through material thickness properties rather than geometric modelling. To account for the tapered transition between web and flanges, three concrete materials were defined, each assigned an effective width corresponding to a specific cross-sectional region (Figure 5-6a). In the transition zones, an area-equivalence approach was adopted so that the two-dimensional model preserved the actual cross-sectional area of the girder. The thickness values adopted for each material region are summarized in Table 5-4.

Table 5-4: Out-of-plane thickness assigned to concrete regions (PRC Girders).

Material ID	Structural Region	Assigned Thickness [mm]
CLS1	Flange – maximum width	460
CLS2	Transition region	280
CLS3	Web	100
FRC	Web overlay	100

Figure 5-6b shows the numerical model. Concrete was discretized using four-node quadrilateral elements. A non-uniform mesh was adopted in order to capture stress gradients in critical regions. Element dimensions were:

- 50 × 60 mm in the prestress transfer region,
- 75 × 60 mm in the remaining span,
- 50 × 30 mm in the zones between adjacent strands.

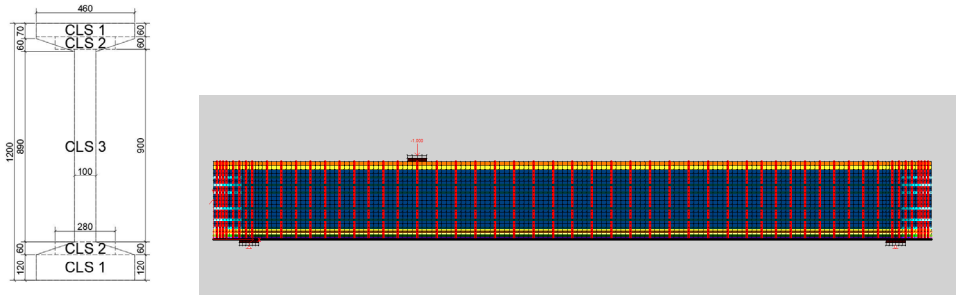


Figure 5-6: discretization of the section (a) and finite element model (b) of the historical PRC girders.

Prestressing strands were modelled as discrete truss elements embedded within the concrete mesh.

VecTor2 does not explicitly simulate the stress diffusion along the transfer length. Therefore, the prestress force was introduced through imposed initial strains in the tendons. The imposed strain was calculated as:

$$\varepsilon_{p0} = \frac{\sigma_{p,eff}}{E_p}$$

Where $\sigma_{p,eff}$=1050 MPa represents the effective prestressing stress after long-term losses (net of shrinkage, creep and relaxation), and E_p=185 GPa.

To approximate the prestress transfer length (assumed equal to 45 cm), the effective prestress was progressively distributed in four regions corresponding to 25%, 50%, 75% and 100% of the effective strain before reaching the support.

The initial strands strain was kept constant across all numerical scenarios; variations in structural response were introduced exclusively through material properties.

Only the two full-height stirrup branches crossing the neutral axis were explicitly modelled as discrete truss elements. Longitudinal reinforcement located in compression zones was modelled as smeared reinforcement to reduce model complexity, given its limited influence on shear response. Note that the prestressing strands are distributed in nine layers along the cross-section, as shown in Figure 5-7.

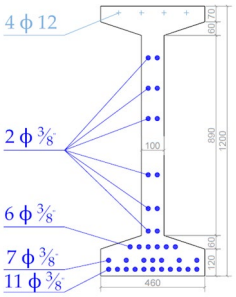


Figure 5-7: strands and reinforcement layout in PRC Girders.

The strands and reinforcement areas adopted in the deterministic model are summarized in Table 5-5. The strand layers are numbered from bottom to top, with Layer 1 corresponding to the lowest layer and Layer 9 to the uppermost layer.

Table 5-5: Reinforcement areas adopted in the deterministic model (PRC Girder).

Reinforcement Type	Bar Diameter [mm]	Number of Bars	Total Area [mm²]
Stirrups	9.91	2	154
Strands – Layer 1	9.3	11	572
Strands – Layer 2	9.3	7	364
Strands – Layer 3	9.3	6	312
Strands – Layer 4/9	9.3	2	364
External Bonded FRP	1.4x100	4	560

The UHPFRC web enlargement was modelled using plane stress elements assigned to the side regions of the web. A perfect bond condition between the existing concrete and the UHPFRC overlay was assumed. In VecTor2, this was implemented by superimposing the overlay elements onto the existing concrete elements and assigning identical nodes along the interface, thereby enforcing full displacement compatibility without introducing interface elements.

FRP plates were modelled as externally bonded linear elastic truss elements placed at the intrados, whose failure was governed by attainment of the ultimate strain.

The girders were modelled as simply supported beams: one support restrained in both horizontal and vertical directions and the other restrained only vertically.

The loading procedure consisted of two sequential phases:

1. Self-weight application, introduced as nodal loads based on a unit weight of 23 kN/m³ for concrete and 24 kN/m³ for UHPFRC. The self-weight of FRP plates was neglected;
2. Displacement-controlled loading, applied at the loading point in accordance with the experimental three-point bending setup.

Steel distribution plates and neoprene pads were explicitly modelled to ensure realistic stress transfer and prevent artificial stress concentrations.

In Table 5-6, the presented values correspond to original design configuration. Strengthening material properties (UHPFRC and FRP plates) were kept constant in all strengthened analyses. These values constitute the reference configuration for subsequent stochastic analyses.

Table 5-6:Material Properties Adopted in the Deterministic Model (PRC Girder).

Material	Parameter	Symbol	Value	Unit
Existing Concrete	Compressive strength	f'_c	58	MPa
	Elastic modulus	E_c		GPa
	Unit weight	γ_c	23	kN/m³
Prestressing Steel (Strands)	Elastic modulus	E_p	200	GPa

Material	Parameter	Symbol	Value	Unit
	Initial prestrain	ε_{p0}	0.6	%
	Yield strength	f_{py}	1780	MPa
	Ultimate strength	f_{pu}	1945	MPa
Stirrups	Yield strength	f_y	465	MPa
	Elastic modulus	E_s	200	GPa
UHPFRC Overlay	Compressive strength	f'_c	125	MPa
	Elastic modulus	E_c	38	GPa
	Unit weight	γ_c	24	kN/m³
Fibre Smeared Reinforcement	Fibre type	-	-	
	Volume fraction	V_f	-	%
	Fibre length	L_f	30	mm
	Fibre Diameter	D_f	0.38	mm
	Residual flexural strength	f_{R1}	11.9	MPa
	Residual flexural strength	f_{R3}	12	MPa
FRP Plates	Elastic modulus	E_{frp}	160	GPa
	Ultimate strength	f_u	2900	MPa
	Ultimate strain	ε_u	1.8	%

5.4. STOCHASTIC ANALYSES

Two different stochastic modelling approaches were adopted in this study in order to isolate and then combine the effects of deterioration and material uncertainty on the structural response of the investigated beams: corrosion-only stochastic analysis and full stochastic material + corrosion analysis.

5.4.1. Stochastic Modelling Strategy

The stochastic analyses were performed using a Monte Carlo Simulation (MCS) framework implemented in VecTor2. In this approach, selected input parameters are treated as random variables characterized by prescribed probability distributions, while all remaining model parameters are kept deterministic.

Let the vector of random variables be defined as:

$$\boldsymbol{X} = [X_1, X_2, \dots, X_n]$$

where the components of $\boldsymbol{X}$ represent either corrosion-related parameters or mechanical properties of materials, depending on the adopted stochastic scenario. For each realization **j,** a sampled vector $\mathbf{X^{(j)}}$ is generated and introduced into the nonlinear finite element model, resulting in a structural response:

$$Y^{(j)} = g(\boldsymbol{X}^{(\mathbf{j})})$$

where $g(\cdot)$ represents the nonlinear finite element model implemented in VecTor2, including geometry, constitutive laws, boundary conditions and loading. By repeating the analysis for a sufficiently large number of simulations, a statistical distribution of the response quantities of interest (e.g., ultimate load, displacement at peak load, failure mode indicators) is obtained. The mean value, standard deviation, and coefficient of variation are then evaluated from the simulated ensemble.

5.4.2. Corrosion-Only Stochastic analysis

In the corrosion-only stochastic scenario, uncertainty is introduced exclusively through parameters governing the corrosion process, while all mechanical properties of concrete, steel, and strengthening materials are kept deterministic. The corrosion rate $i_{corr}^{(j)}$ is treated as a random variable and assumed to follow a lognormal probability distribution. The lognormal assumption is consistent with the strictly positive nature of corrosion rate and with experimental evidence reported in the literature for corrosion processes in reinforced concrete structures. For each Monte Carlo realization j, a corrosion rate $i_{corr}^{(j)}$ is sampled and used to compute the corresponding:

- steel cross-section loss;
- corrosion-induced cover cracking;
- bond degradation.

This approach allows the structural variability to be attributed solely to the deterioration process.

5.4.2.1. Random variable: Corrosion rate

In the corrosion-only stochastic analyses, the uncertainty is introduced at the level of the corrosion rate. For each Monte Carlo simulation, a corrosion rate i_{corr}^{j} [mm/year] is sampled from a lognormal distribution, consistent with commonly adopted probabilistic representations of corrosion kinetics. Experimental evidence shows that corrosion rates exhibit significant scatter due to variability in environmental exposure, chloride concentration, moisture, and microclimatic conditions. For this reason, $i_{corr}^{(j)}$ is modelled as a lognormal random variable, which ensures strictly positive values and reflects the right-skewed nature of measured corrosion data.

The definition of the lognormal distribution requires the specification of a mean value and a standard deviation. In the subsequent formulations, the corrosion rate, together with time, serves as the governing input variable for all corrosion laws. The exposure time t is taken as deterministic and corresponds to the duration of the corrosion phase in days. Since the corrosion initiation time was unknown, an equivalent constant corrosion rate was back-calculated from the measured corrosion penetration and the service life of the structure. This approach assumes that the entire service period corresponds to the propagation phase of corrosion. In the adopted formulation, steel penetration depends solely on the product of corrosion rate and

exposure time. This assumption preserves the correct mechanical level of deterioration while avoiding explicit modelling of the initiation phase. Accordingly, the variability of corrosion rate reflects uncertainty in the corrosion history, measurement dispersion, and the assumption of uniform corrosion, rather than instantaneous electrochemical fluctuations. This approach ensures that the mean level of deterioration matches the observed steel loss while allowing its mechanical consequences to be probabilistically propagated.

The statistical parameters adopted for the corrosion rate in the analysed beams are summarized in Table 5-7. The lognormal distribution was defined in terms of physical mean value and standard deviation. The corresponding logarithmic parameters were internally derived by the software.

In order to properly capture the stochastic influence of corrosion while avoiding numerical truncation of very small corrosion-rate values in the solver input files, three equivalent corrosion scenarios were considered. In all cases, the same target physical damage level (expressed in terms of corrosion penetration and corresponding steel cross-section loss) was preserved.

The different scenarios were obtained by rescaling the corrosion rate and the corresponding exposure duration while keeping the product $x = i_{corr}^{(j)} t$ invariant. Since the structural deterioration mechanisms (steel area reduction, bond degradation, and cover cracking) depend on the corrosion penetration rather than on corrosion rate or time individually, this rescaling does not alter the mechanical damage level but only the numerical representation of the stochastic parameter.

Accordingly, the three corrosion-only scenarios differ in terms of corrosion-rate magnitude and statistical dispersion, while representing the same underlying physical deterioration state.

Table 5-7: Statistical parameters adopted for corrosion rate.

Beam	N	Mean corrosion rate [mm/year]	St.Dev. [mm/year]	Corrosion duration [days]
Historical RC Girder	1	0.0038	0.0011	33215
	2	0.3458	0.1037	365
	3	4.5070	1.3500	28
PRC Girders	1	0.0423	0.01269	20440
	2	2.3688	0.71064	365
	3	30.879	9.2637	28

5.4.2.2. Resulting steel cross-section loss

Once the corrosion rate $i_{corr}^{(j)}$ is sampled, it is converted into corrosion penetration, representing the radial thickness of steel lost due to oxidation. Assuming uniform

corrosion along the bar perimeter, Faraday's law provides the link between electrochemical current and metal loss:

$$x^{(j)}(t) = \frac{i_{corr}^{(j)}\ t\ M}{z\ F\ \rho}$$

where $x^{(j)}(t)$ is the radial penetration of corrosion, M is the molar mass of iron, z the valence of the iron ions, F the Faraday constant, equal to and ρ the density of steel. This equation states that the amount of dissolved iron is proportional to the total electrical charge transferred through the system. Under the assumption of uniform corrosion, the penetration occurs evenly around the bar perimeter, so the bar diameter reduces symmetrically. For an initial nominal bar diameter d_{b0}, the corroded diameter for realization j becomes:

$$d_b^{(j)}(t) = d_{b0} - 2x^{(j)}(t)$$

This reduction directly affects the steel cross-sectional area, which is updated as:

$$A_s^{(j)}(t) = \frac{\pi}{4}\left(d_b^{(j)}(t)\right)^2$$

Hence, corrosion translates the stochastic variability of the corrosion rate into variability of the reinforcement area.

5.4.2.3. Bond strength degradation due to corrosion (Feng et al., 2016)

The deterioration of bond strength induced by corrosion is accounted for through a reduction factor, R, which represents the loss of mechanical interlock and confinement between the reinforcing steel and the surrounding concrete. The formulation was developed through the application of the model to 377 documented case studies.

$$R = \frac{\tau_b}{\tau_{b,0}}$$

where τ_b is the bond strength of a corroded bar and $\tau_{b,0}$ the original value.

The model proposed by Feng et al. (2016) describes three distinct stages of bond evolution:

- Pre-cracking stage, characterized by a slight increase in the bond due to radial pressure induced by corrosion products;
- Cracking stage, during which progressive degradation of bond capacity occurs;
- Severe corrosion stage, characterized by residual bond strength.

The reduction factor R is defined separately for each stage.

$$R = \begin{cases} \left(-0.0320\frac{c}{d_b} + 0.576\right)C(t) + 1 & if\ C(t) \le C_{pk} \\ \left(0.0137\frac{c}{d_b} - 0.247\right)C(t) + 1.42 + 0.0475\frac{c}{d_b} & if\ C_{pk} < C(t) \le C_{2-3} \\ -0.0016C(t) + 0.224 & if\ C(t) > C_{2-3} \end{cases}$$

Where:

c is the clear concrete cover in mm;

$d_b$is the nominal diameter of the reinforcing bar;
$C(t)$ is the percentage of mass loss as a function of the age of the structural element, calculated as:

$$C(t)^{(j)} = 1 - \frac{A_s^{(j)}(t)}{A_{s0}}$$

where A_{s0} is the original reinforcement bar area;
C_{pk} is the threshold percentage of mass loss corresponding to the transition from the pre-cracking stage to the cracking stage, calculated as:

$$C_{pk} = 0.0864\frac{c}{d_b} + 0.516$$

C_{2-3} is the threshold value of the mass loss parameter corresponding to the transition between the cracking stage and the severe corrosion stage, calculated as:

$$C_{2-3} = \frac{-1.2 - 0.0475\left(c/d_b\right) + 0.003094\left(c/d_b\right)^2}{0.0137\left(c/d_b\right) - 0.245}$$

5.4.2.4. Cover cracking due to corrosion (Pantazopoulou & Papoulia, 2001)

Pantazopoulou and Papoulia (2001) analyzed cover concrete cracking using a finite difference formulation in which the concrete cover is divided into *N* radial segments (Figure 5-8). The differential equilibrium equation of a hollow cylinder under uniform internal pressure is solved at discrete points across the cover thickness using a cell-centered grid.

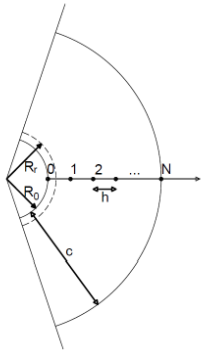


Figure 5-8:Discretization of the concrete cover (Habibi, 2017)

Radial and tangential stresses are expressed in terms of strains (Eq. 1 and Eq. 2), and the corresponding strains in terms of radial displacements (Eq. 3 and Eq. 4), allowing the governing equation to be rewritten solely as a function of displacement.

$$\sigma_r = \frac{1}{1 - \nu_{r\theta}\nu_{\theta r}}(E_r\varepsilon_r + \nu_{r\theta}E_\theta\varepsilon_\theta) \qquad \text{Eq. 1}$$

$$\sigma_\theta = \frac{1}{1 - \nu_{r\theta}\nu_{\theta r}}(E_\theta\varepsilon_\theta + \nu_{\theta r}E_r\varepsilon_r) \qquad \text{Eq. 2}$$

$$\varepsilon_r = \frac{du_r}{dr} \quad \text{Eq. 3}$$

$$\varepsilon_\theta = \frac{u_r}{r} \quad \text{Eq. 4}$$

By substituting these relationships into the equilibrium equation (Eq. 5) and approximating spatial derivatives using central difference schemes (Eq. 6 and Eq. 7), the continuous problem is converted into a system of finite difference equations (Eq. 8).

$$\sigma_r + \frac{d\sigma_r}{dr} r - \sigma_\theta = 0 \quad \text{Eq. 5}$$

$$\frac{du_r}{dr} = \frac{u_{r,i+1} - u_{r,i-1}}{2h} \quad \text{Eq. 6}$$

$$\frac{d^2u_r}{dr^2} = \frac{u_{r,i+1} - 2u_{r,i} + u_{r,i-1}}{h^2} \quad \text{Eq. 7}$$

$$u_{r,i-1}\left(\frac{1}{h^2} - \frac{1}{2r_i h}\right) - u_{r,i}\left(\frac{2}{h^2} + \frac{1}{r_i{}^2} \cdot \frac{E_{\theta,i}}{E_{r,i}}\right) + u_{r,i+1}\left(\frac{1}{h^2} - \frac{1}{2r_i h}\right) = 0 \quad \text{Eq. 8}$$

Eq. 8 can also be expressed in matrix form (Eq. 9). Where K is the stiffness matrix, u_r the displacements of the discretized points, B is the boundary conditions array, with all terms equal to zero, except for the B_1, equal to $(R_r - R_0)\left(\frac{1}{h^2} - \frac{1}{2r_i h}\right)$. Substantially, $R_r - R_0$ is the equivalent width of the corrosion product, estimated from the attack penetration $x^{(j)}(t)$ [mm] multiplied by a volumetric expansion factor of corrosion products η. The adopted expansion ratio in the present study is equal to 3.75, consistent with commonly reported values for iron oxidation products.

$$[K]\{u_r\}^T = \{B\} \quad \text{Eq. 9}$$

Furthermore, the concrete cover is modelled as an orthotropic material. In the radial direction, the modulus E_r is assumed to remain approximately equal to the elastic modulus of concrete, since stresses in this direction are predominantly compressive. In the tangential direction, which is subjected to circumferential tensile stresses, the modulus E_θ, is initially taken equal to the elastic modulus of concrete up to the onset of cracking. Beyond first cracking, E_θ is updated iteratively as a secant stiffness derived from the tensile softening law. This procedure enables the progressive reduction of tangential stiffness to be captured, thereby representing the degradation associated with circumferential cracking of the cover concrete.

The tensile softening behaviour adopted for concrete follows a fracture-mechanics-based formulation in which post-peak stress transfer is governed by the fracture energy. After the tensile strength f_t is reached at the cracking strain ε_{ct}, the stress decreases according to a bilinear softening law (Eq. 10).

$$\sigma_t = \begin{cases} E_c \varepsilon_t & if\ \varepsilon_t \le \varepsilon_{ct} \\ f_t\left(1 - 0.85\dfrac{\varepsilon_t - \varepsilon_{ct}}{\varepsilon_1 - \varepsilon_{ct}}\right) & if\ \varepsilon_{ct} < \varepsilon_t \le \varepsilon_1 \\ 0.15 f_t \dfrac{\varepsilon_u - \varepsilon_t}{\varepsilon_u - \varepsilon_1} & \end{cases} \quad \text{Eq. 10}$$

where ε_1 and ε_u define the transition and ultimate softening strains, respectively. The parameters of the descending branch are calibrated such that the area under the stress–strain curve equals the fracture energy, ensuring mesh-objectivity of the cracking response. This softening law derives from the smeared crack approach and fracture energy concepts originally formalized in nonlinear fracture mechanics for concrete and subsequently adopted in rotating smeared crack formulations. The secant tangential modulus is therefore evaluated as:

$$E_\theta = \frac{\sigma_t}{\varepsilon_t}$$

and updated iteratively during the solution process. The tensile softening law is based on fracture mechanics concepts and commonly adopted in smeared crack formulations (Vecchio, 2001).

This formulation ensures that the stochastic description of corrosion rate is translated into variability of reinforcement area and interaction mechanisms, thereby enabling the Monte Carlo simulation to quantify the structural response uncertainty associated with corrosion.
Specifically, the stochastic corrosion rate affects the structural model through the following mechanisms:

- The reduced steel area $A_s(t)$ is calculated as a function of the corrosion penetration $x(t)$;
- The corrosion level $C(t)$ is used in the bond degradation model to determine the reduction factor R;
- The penetration $x(t)$ governs the radial expansion demand responsible for corrosion-induced cover cracking.

5.4.3. Materials-Only Stochastic analysis

In addition to the corrosion-driven stochastic simulations, a materials-only stochastic scenario was considered in order to isolate the influence of intrinsic variability of existing materials from deterioration-induced effects.
In this configuration, the corrosion rate was set equal to zero, thereby suppressing any corrosion-induced steel cross-section loss, bond degradation, or cover cracking mechanisms. Uncertainty was introduced exclusively through the internal statistical material models implemented in VecTor2.
Concrete compressive strength was modelled according to Bartlett and MacGregor (1996), while the associated tensile strength and elastic modulus were statistically linked to the compressive strength following Mirza et al. (1979).

$$f_t = \alpha\sqrt{f'_c}$$
$$E_c = \beta(f'_c)^n$$

where α, β and n are empirical coefficients consistent with the adopted material model. This formulation ensures mechanical coherence between stiffness and strength parameters.

Reinforcing steel yield strength was modelled based on Nowak and Szerszen (2003), and ultimate strength and elastic modulus followed the statistical characterization proposed by Mirza et al. (1979).

The correlation coefficients among material properties were kept equal to the default values implemented in the internal statistical models. Strengthening materials were defined within the stochastic module but explicitly set as "Not a random variable," ensuring deterministic behaviour of the strengthening system.

This scenario allows assessment of the dispersion in structural capacity solely attributable to material property variability, providing a reference case for comparison with corrosion-only and combined stochastic analyses.

5.4.4. Full Stochastic material + corrosion analysis

In the combined stochastic scenario, uncertainty is simultaneously introduced in both the corrosion process and the mechanical properties of the existing materials. This configuration integrates the corrosion-only and materials-only formulations previously described, allowing interaction between deterioration-induced damage and intrinsic material variability.

The statistical characterization of concrete and reinforcing steel follows the internal probabilistic material models implemented in VecTor2, as detailed in the materials-only scenario. Strengthening materials remain deterministic and are explicitly defined as "Not a random variable."

The corrosion rate is modelled as an independent lognormal random variable. For each Monte Carlo realization, both corrosion parameters and material properties are sampled and introduced into the nonlinear finite element model:

$$Y^{(j)} = g(i_{corr}{}^{(j)}, f'^{(j)}_c, f_y^{(j)}, \dots)$$

In this scenario, the structural response reflects the combined effect of section loss, bond degradation, cover cracking, and material strength dispersion. The interaction between these sources of uncertainty may influence not only the magnitude of the ultimate load but also the governing failure mechanism.

5.4.5. Monte Carlo Implementation and Convergence

The stochastic simulations were performed using direct Monte Carlo sampling. For each stochastic scenario, N = 50 realizations were executed. This sample size represents a compromise between statistical resolution and computational cost, given the high nonlinearity and the relatively large number of finite elements adopted in the numerical models. In the present study, a set of 50 simulations required approximately two days of computation.

Convergence was evaluated by tracking the evolution of the sample mean and standard deviation of the ultimate load as the number of realizations increased up to N. Although a larger number of simulations would be desirable, especially for accurate characterization of distribution tails, the adopted sample size was deemed sufficient to provide a stable estimate of the first two statistical moments of the response within the available computational resources.

The mean and standard deviation were computed as:

$$\mu_Y = \frac{1}{N}\sum_{j=1}^{N} Y^{(j)}$$

$$\sigma_Y = \sqrt{\frac{1}{N-1}\sum_{j=1}^{N}(Y^{(j)} - \mu_Y)^2}$$

where $Y^{(j)}$ represents the ultimate load of the j-th realization (e.g., ultimate load).

5.5. NUMERICAL RESULTS AND DISCUSSION

The stochastic results are discussed primarily in terms of ultimate load capacity rather than ultimate displacement. While both quantities can be extracted from the nonlinear analyses, the ultimate displacement is more sensitive to numerical instability and post-peak response truncation, particularly in Monte Carlo simulations where individual realizations may exhibit different softening slopes and convergence characteristics.

In order to ensure consistent identification of the ultimate load across all realizations, a post-processing procedure was implemented in MATLAB. For each load–displacement curve obtained from the 50 stochastic simulations, the response was truncated at the point corresponding to a load drop exceeding 15% from the peak value. This criterion was adopted to avoid including extended softening branches or numerical artifacts that may arise after significant loss of load-carrying capacity. The ultimate load was therefore defined as the maximum load reached prior to this 15% post-peak reduction.

This procedure guarantees a consistent and objective extraction of the ultimate capacity across all stochastic realizations, while minimizing the influence of post-peak numerical variability. Consequently, the statistical comparisons among deterministic, corrosion-only, materials-only, and combined scenarios are performed based on ultimate load values.

The deterministic nonlinear analysis of the historical RC girder (black line in Figure 5-9-Figure 5-12) predicted an ultimate load of 1323 kN, corresponding to a midspan deflection of about 89 mm.

Table 5-8 summarizes the comparison between the experimental response (green dashed line in Figure 5-9-Figure 5-12) and the corresponding numerical results.

Table 5-8: comparison between numerical and experimental response.

Parameter	Deterministic analysis	Experimental test	Relative Error (%)
Ultimate load $\mathbf{P_u}$ [kN]	1323	1163	14
Midspan deflection at P_u $\boldsymbol{\delta_u}$ [mm]	89	79	13

The numerical model overestimates the structural response, as the girder had been previously subjected to a load test aimed at assessing its residual capacity prior to strengthening. Although the cracks induced during the earlier test were repaired, a certain level of pre-existing damage remained. This prior damage was not explicitly accounted for in the numerical analyses.

The corrosion-only stochastic simulations (Figure 5-9), performed using the equivalent corrosion rate calibrated over 28 days, resulted in a mean value of the ultimate load of 1444.18 kN with a coefficient of variation of 0.03%. The extremely

small dispersion indicates that, for the adopted natural corrosion level, uncertainty in corrosion rate produces negligible variability in global structural capacity.

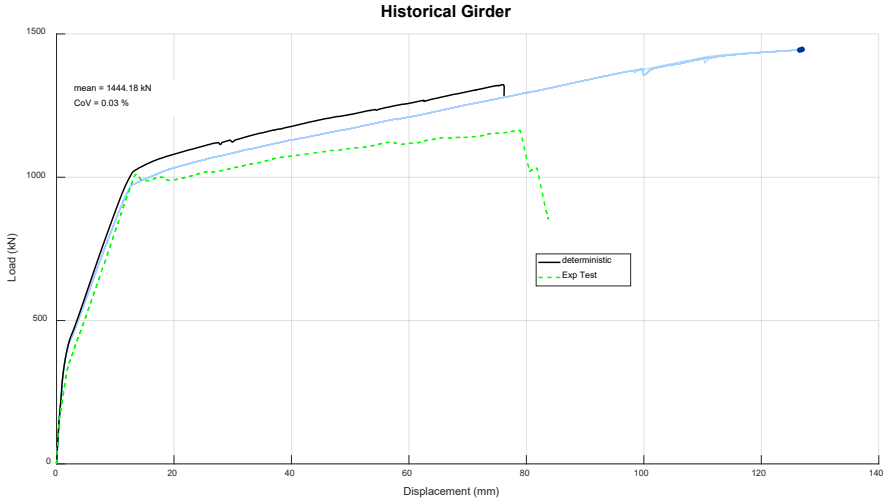


Figure 5-9: stochastic analysis corrosion-only considering corrosion for 28 days with a corresponding equivalent corrosion rate.

Additional simulations were conducted using equivalent corrosion rates calibrated over 365 days and over the full-service life of the girder (approximately 90 years), while maintaining the same physical level of steel penetration. In both cases, the coefficient of variation of the ultimate load was practically zero (Figure 5-10).

This behaviour can be explained by the fact that the structural response is governed by the resulting corrosion penetration and associated section loss, rather than by the specific time–rate combination used to represent it. Since the penetration depth was kept constant among the alternative time calibrations, the variability of the corrosion rate translated into extremely small variations of effective steel area. Due to the nonlinear but weak sensitivity of global capacity to small changes in reinforcement area at the investigated damage level, the dispersion of the structural response remained negligible. In fact, the penetration value measured was about 0.35 mm.

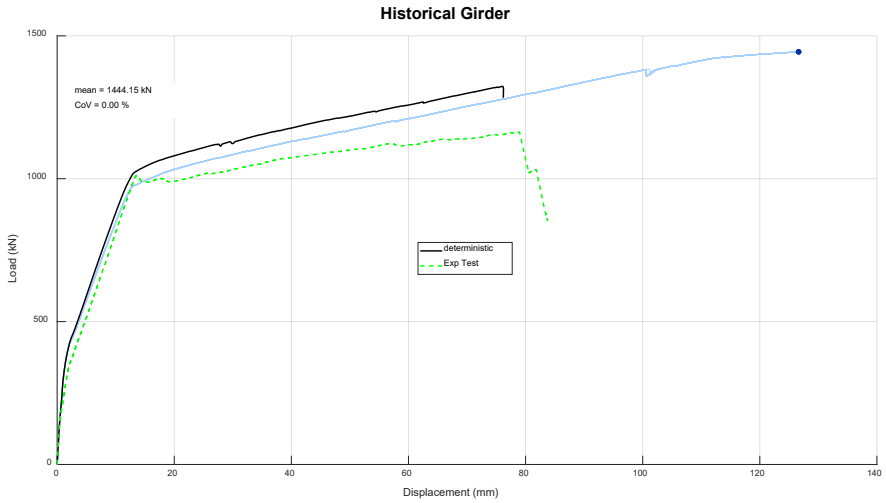


Figure 5-10: stochastic analysis corrosion-only considering corrosion for 365 days with a corresponding equivalent corrosion rate.

When only material-property uncertainties were considered (Figure 5-11), the mean ultimate load increased to 1567 kN, with a coefficient of variation equal to 2.99%. This demonstrates that variability in concrete and steel mechanical properties governs the dispersion of the global response. The increase in mean capacity relative to the deterministic value reflects the nonlinear dependence of structural resistance on material parameters.

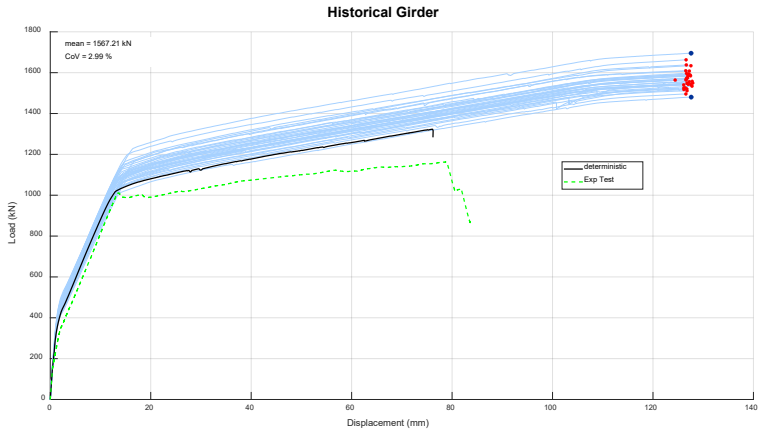


Figure 5-11: stochastic analysis materials-only.

The combined stochastic scenario (Figure 5-12) yielded a mean ultimate load of 1551.15 kN with CoV = 3.39%. The dispersion is only slightly larger than in the materials-only case, confirming that response variability is primarily controlled by

material uncertainty. Corrosion, in this case, mainly shifts the mean capacity rather than contributing significantly to variance.

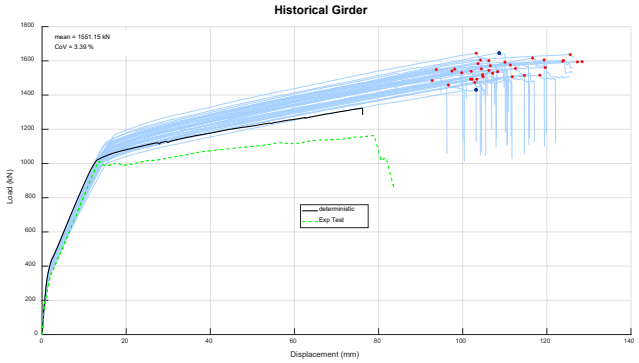


Figure 5-12: stochastic analysis full stochastic considering corrosion for 28 days with a corresponding equivalent corrosion rate.

A notable outcome of the simulations is that the deterministic ultimate load (1323 kN) is consistently lower than the mean capacity obtained from all stochastic scenarios. The deterministic solution underestimates the stochastic mean by approximately:

- 9% in the corrosion-only case;
- 18% in the materials-only case;
- 17% in the combined case.

This behaviour is consistent with nonlinear stochastic structural mechanics. As seen in paragraph 4, the structural capacity can be expressed as:

$$P_u = g(f'_c, f_y, E_c, A_s, \dots.)$$

Where $g(\cdot)$ represents a strongly nonlinear finite element operator.

Due to the asymmetric nature of the adopted lognormal distributions and the nonlinear relationship between material strength and global capacity, the expected structural response tends to exceed the response evaluated at mean input parameters. This behaviour reflects the nonlinear relationship between material properties and structural capacity. Due to this nonlinearity, the expected structural response does not coincide with the response evaluated at mean input parameters, and the stochastic mean capacity may exceed the deterministic prediction.

Consequently, the deterministic analysis does not represent the statistical mean response of the system and may act as a lower-bound estimate of the mean structural capacity in nonlinear stochastic simulations.

The comparative analysis of stochastic scenarios provides important insight into the relative contribution of different uncertainty sources.

For the historical girder subjected to natural corrosion:

- Corrosion-rate uncertainty produces negligible response dispersion;

- Material-property uncertainty produces moderate dispersion (CoV ≈ 3%);
- The combined scenario is governed by material variability.

This behaviour can be explained by the limited sensitivity of the global capacity to small variations in corrosion penetration at the investigated damage level. Although corrosion reduces the effective steel area and modifies bond conditions, the variability of the corrosion rate over the considered time span results in minor fluctuations in cross-sectional properties. In contrast, variability in concrete compressive strength and steel yield strength directly affects sectional resistance and plastic redistribution mechanisms, leading to a more pronounced dispersion of ultimate load.

These results indicate that, for existing girders characterized by moderate natural corrosion, uncertainty in mechanical properties may dominate over corrosion-rate uncertainty in governing structural response variability.

For the prestressed deteriorated girders, the stochastic assessment was performed considering the combined uncertainty scenario, accounting simultaneously for corrosion effects and variability in material properties of concrete, prestressing strands, and reinforcement. Results are presented in Figure 5-13.

The deterministic nonlinear analysis (black line) predicted an ultimate load of 1614 kN. The combined stochastic simulations yielded a mean ultimate load of 1826 kN with a coefficient of variation equal to 3.53%. The stochastic mean capacity is therefore approximately 13% higher than the deterministic prediction. It should be noted that, in this case, the experimental results (dashed lines in Figure 5-13) were not conducted up to failure of the structural element due to set-up load limitation (1400 kN). Consequently, a direct comparison between deterministic ultimate capacity and experimental failure load, as performed for the historical RC girder, is not possible for the prestressed specimens.

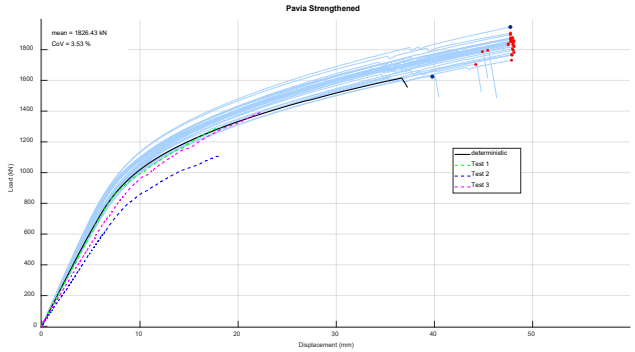


Figure 5-13: stochastic analysis full stochastic of the PRC girders.

Consistent with the results obtained for the historical RC girder, the deterministic solution does not represent the statistical mean response of the nonlinear system. The observed shift reflects the nonlinear relationship between structural capacity and

mechanical parameters, combined with the asymmetric nature of the adopted probability distributions.
The dispersion level (CoV ≈ 3.5%) is comparable to that obtained for the RC girder in the combined scenario, suggesting that variability in material properties governs response uncertainty in both structural systems. Despite the additional mechanical complexity associated with prestressing and strengthening systems, the overall sensitivity of ultimate load to input variability remains moderate.

5.6. LABORATORY BEAMS WITH ACCELERATED CORROSION

The stochastic analyses presented in the previous sections were performed on existing reinforced and prestressed concrete girders characterized by natural corrosion and subsequently strengthened with advanced retrofit systems. The results consistently indicated that, for the investigated damage levels, uncertainty in mechanical material properties governed the dispersion of ultimate load capacity, while variability in the corrosion rate produced negligible influence on the global structural response. In particular, the coefficient of variation of the ultimate load remained limited (≈3–3.5%) and was primarily controlled by the statistical variability of concrete and steel properties rather than by corrosion-rate uncertainty.

The negligible contribution of corrosion-rate variability to the dispersion of ultimate capacity observed in the previous analyses is strictly related to the magnitude of the corrosion penetration characterizing the examined girders. As such, the relative hierarchy between corrosion-induced and material-induced uncertainties must be evaluated under different deterioration regimes before broader conclusions can be drawn.
To address this issue, an additional set of reinforced concrete beams subjected to accelerated corrosion under laboratory conditions is introduced in the present chapter. These specimens were not extracted from existing structures and were not strengthened. Instead, corrosion damage was artificially induced through controlled accelerated processes, leading to higher reinforcement mass loss compared to the naturally deteriorated girders previously examined.
The inclusion of these laboratory beams serves a specific methodological purpose. By analyzing structural members characterized by more severe corrosion levels and controlled deterioration states, it becomes possible to investigate whether the stochastic influence of corrosion becomes dominant when section loss, bond degradation, and cracking reach more pronounced levels. In this deterioration regime, corrosion-induced mechanisms may significantly affect not only the mean structural capacity but also its statistical dispersion.

Although the experimental specimens were produced in laboratory conditions and material properties are therefore characterized by reduced uncertainty compared to historical structures, stochastic analyses were nevertheless performed considering both corrosion-only variability and combined corrosion–material variability scenarios. The inclusion of material uncertainty in this context is primarily intended to ensure methodological consistency with the previously analysed cases and to enable direct comparison between natural and accelerated corrosion regimes within the same probabilistic framework.
The numerical modelling strategy, Monte Carlo procedure, and statistical material formulations remain consistent with those previously described. Consequently, differences in response variability can be directly attributed to the severity and nature of corrosion damage rather than to changes in modelling assumptions.
The objective of this extension is therefore not to replicate the analysis of strengthened existing girders, but rather to clarify the sensitivity of structural capacity to corrosion-induced uncertainty as a function of deterioration severity.
This comparative approach provides a broader and more comprehensive understanding of the stochastic behaviour of corroded reinforced concrete members and strengthens the overall interpretation of the results obtained for existing strengthened infrastructure.

5.6.1. Experimental Program

An experimental campaign was carried out on reinforced concrete beams subjected to accelerated corrosion under controlled laboratory conditions (Di Stefano, 2022). Five beams were cast at the Pietro Pisa Laboratory of the University of Brescia: one control specimen without corrosion and four beams in which reinforcement corrosion was artificially induced prior to structural testing. The primary objective of the program was to investigate the shear response of beams with deteriorated stirrups and to quantify the mechanical effects of different corrosion levels.
All specimens had identical geometry, consisting of rectangular cross-sections 500 mm in height and 200 mm in width, with a total length of 4550 mm (Figure 5-14). The beams were intentionally designed to exhibit shear-critical behaviour. The shear reinforcement ratio was approximately 0.085%, slightly lower than the minimum value prescribed by fib Model Code 2010 for members with transverse reinforcement, in order to reproduce typical detailing deficiencies observed in older reinforced concrete structures.

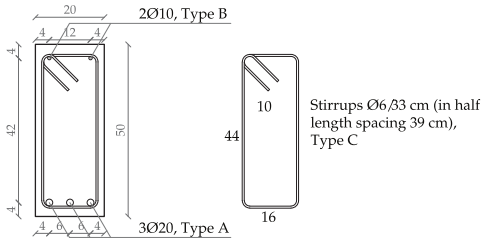


Figure 5-14: cross-section of the artificially corroded bems.

The mean cubic compressive strength measured at casting was approximately 42 MPa, corresponding to a mean cylindrical strength of about 35 MPa. The mean elastic modulus obtained from cylinder tests was approximately 27.7 GPa, with moderate coefficients of variation. A relatively low-strength and relatively porous concrete was deliberately selected to facilitate the accelerated corrosion process and to simulate the mechanical characteristics of dated structures.

Reinforcement consisted of ribbed B450C steel. The longitudinal tensile reinforcement at the bottom was composed of three 20 mm diameter bars, corresponding to a reinforcement ratio of approximately 1.04%. Two 10 mm diameter bars were placed at the top. The transverse reinforcement consisted of two-legged 6 mm diameter stirrups spaced at 330 mm, except in the central region where the spacing increased to 390 mm. The clear concrete cover was 40 mm for the longitudinal reinforcement and 24 mm for the stirrups. Mechanical characterization of the uncorroded bars showed limited variability, with mean yield strengths of approximately 524 MPa for the 6 mm stirrups and 516 MPa for the 20 mm longitudinal bars.

The beams were tested under a four-point bending configuration designed to activate a shear-critical region near one support.

The beams were simply supported over a span of 4.55 m. The load was applied through a 2.45 m long steel spreader beam, resulting in a shear span a equal to 1.05 m on each side.

Each specimen was subjected to two shear tests, one for each side. After the first failure, the damaged end was locally strengthened, and the loading configuration was reversed to test the opposite shear span.

Corrosion was induced using an impressed current technique. The two stirrups closest to each support were connected as anodes to a potentiostat, while stainless steel sheets immersed in a 5% NaCl electrolyte solution acted as cathodes. In one specimen, corrosion was also imposed on a 500 mm long segment of the lower longitudinal reinforcement. The duration of current application was determined using Faraday's law, adopting a correction coefficient α = 2 to account for the protective effect of concrete.

The actual corrosion levels (Table 5-9) were determined after structural testing through extraction, cleaning and weighing of the reinforcement.

Table 5-9: Experimental corrosion parameters of laboratory beams subjected to accelerated corrosion.

Beam	Side	Corroded reinforcement	Diameter [mm]	Effective mass loss [%]	Mean corrosion rate [mm/year]	Std. dev. [mm/year]	CoV [%]	Connection time [days]
1	A	Stirrups	6	24.4	3.237	0.109	3.39	44
1	B	Stirrups	6	18.4	2.598	1.082	39.27	41
2	A	Stirrups	6	16.6	2.281	0.382	16.96	42
2	B	Stirrups	6	16.6	2.211	0.603	27.35	43
3	A	Stirrups	6	39.1	4.555	1.644	37.27	53
3	B	Stirrups	6	32.5	3.718	0.715	18.47	53
4	A	Stirrups	6	24.1	3.257	0.202	6.17	43
4	B	Stirrups	6	17.1	2.271	0.385	16.97	43
4	–	Bottom longitudinal bars	20	4.7	2.019	0.372	18.40	43

5.6.2. Deterministic Modelling

The deterministic numerical analyses were performed using VecTor2. Due to geometric and loading symmetry, only half of each beam was modelled, as shown in Figure 5-15. The concrete was discretized using four-node rectangular plane stress elements with a mesh size of approximately 20 mm in both longitudinal and vertical directions, allowing an adequate representation of cracking and shear stress redistribution.

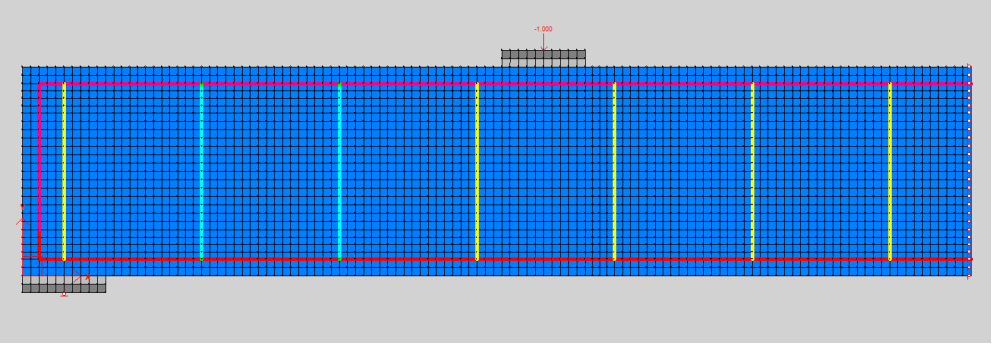


Figure 5-15: Finite Element Model of the artificially corroded beams.

The support node was restrained in vertical direction, while symmetry conditions were imposed at the midspan section by preventing horizontal displacement. The loading procedure consisted of three sequential steps: (i) application of self-weight of the beam and half of the steel distribution beam and (ii) displacement-controlled loading applied at the load point with increments of 0.5 mm.
Concrete was defined using the average material properties measured experimentally, with a cylindrical compressive strength of 35 MPa and an elastic modulus of 27.7 GPa. Default VecTor2 constitutive relationships were adopted for concrete. Reinforcement was modelled using discrete truss elements positioned according to the actual layout of longitudinal bars and stirrups. The experimentally measured steel properties were assigned, including yield strength and ultimate strain. Material properties are shown in Table 5-10.

Table 5-10:Material properties of the artificially corroded beams.

Material	Parameter	Value	Unit
Concrete (C25/30)	Cylindrical compressive strength	35	MPa
	Elastic modulus	27.7	GPa
	Unit weight	25	kN/m³
Reinforcing steel (B450C)	Yield strength (Ø20)	516	MPa
	Yield strength (Ø6)	524	MPa
	Elastic modulus	210	GPa

The load transfer at supports and loading points was modelled through steel plates and interposed rubber bearings in order to avoid artificial stress concentrations and local crushing.
The modelling strategy was therefore consistent with the experimental configuration and aimed at reproducing the global shear response and crack development up to failure using experimentally calibrated material parameters.

5.6.3. Stochastic Scenarios

The stochastic assessment of the laboratory beams subjected to accelerated corrosion was performed within the same Monte Carlo framework previously adopted for the existing girders. Two probabilistic configurations were considered in order to isolate and then combine the effects of corrosion-induced deterioration and intrinsic material variability.
In the first scenario, uncertainty was introduced exclusively through the corrosion rate expressed in mm/year. The corrosion rate was modelled as a lognormal random variable, consistently with its strictly positive nature and with the right-skewed distribution typically associated with corrosion processes. The statistical parameters of the corrosion rate adopted in the stochastic simulations, including mean value,

standard deviation, and corresponding duration of electrical connection for each beam, are reported in Table 5-11.

Table 5-11: Statistical parameters of the corrosion rate adopted in the stochastic analyses of laboratory beams 1–4, including mean corrosion rate (mm/year), corresponding standard deviation and duration of electrical connection used to reproduce the experimentally observed corrosion levels.

Beam	Mean corrosion rate [mm/year]	St.Dev. [mm/year]	Corrosion duration [days]
1	3.2	0.96	44
2	2.3	0.69	42
3	4.6	1.38	53
4	3.3	0.99	43

Although experimental measurements provided specimen-specific estimates of corrosion rate dispersion, the number of available measurements per beam was limited and strongly influenced by local electrochemical fluctuations associated with the accelerated corrosion process. In order to ensure methodological consistency and enable a meaningful comparison among the different specimens, a uniform coefficient of variation equal to 30% was adopted for the corrosion rate in all stochastic simulations.

This value is representative of the significant variability typically associated with corrosion processes, particularly under accelerated and non-stationary laboratory conditions. By prescribing a consistent CoV across all beams, the stochastic analyses focus on the structural sensitivity to a realistically high level of corrosion uncertainty, rather than on specimen-specific statistical scatter.

For each Monte Carlo realization, a value of corrosion rate was sampled and used to update the corrosion penetration, the corresponding reduction of reinforcement cross-sectional area, and the associated mechanical degradation. This configuration allows the structural response dispersion to be attributed solely to variability in the corrosion process.

In the second scenario, uncertainty was simultaneously introduced in both the corrosion rate and the mechanical properties of materials. In addition to the stochastic representation of corrosion rate, concrete compressive strength and reinforcing steel yield strength were treated as random variables according to the statistical models previously described for the existing girders. This combined configuration enables direct comparison with the natural corrosion cases and allows assessment of the relative contribution of corrosion-induced variability and intrinsic material variability to the global structural response.

The modelling strategy ensures consistency between accelerated and natural corrosion regimes, allowing differences in response dispersion to be interpreted as a function of corrosion severity rather than changes in probabilistic assumptions.

5.6.4. *Results and Discussion*

This section presents the results of the stochastic analyses in terms of shear ultimate capacity versus midspan deflection response obtained from the Monte Carlo simulations with corrosion rate as the only stochastic variable. In each figure, the deterministic finite element response is shown as a black continuous curve, while the experimental results from tests A and B are represented by dashed lines. The dispersion of the stochastic response is quantified through the coefficient of variation (CoV) of the ultimate shear force.

As shown in Figure 5-16 to Figure 5-19, when the corrosion rate is considered as the only stochastic variable, the dispersion of ultimate shear capacity remains limited for all specimens, with coefficients of variation ranging between 3.3% and 5.3%. This indicates that, within the adopted probabilistic framework, the uncertainty associated with corrosion rate alone does not induce substantial variability in global shear resistance.

For Beam 1 (Figure 5-16), the deterministic shear capacity is equal to 148.2 kN, while the mean stochastic value is 146.6 kN (CoV 3.6%). The deterministic curve therefore practically coincides with the mean stochastic response, showing that the deterministic solution can be interpreted as a central estimate of structural behaviour in the only-corroded configuration. The experimental capacities (135.6 kN and 109.5 kN) are both lower than the numerical predictions, suggesting that factors not explicitly modelled, such as local damage concentration, may contribute to the experimentally observed reduction in shear resistance.

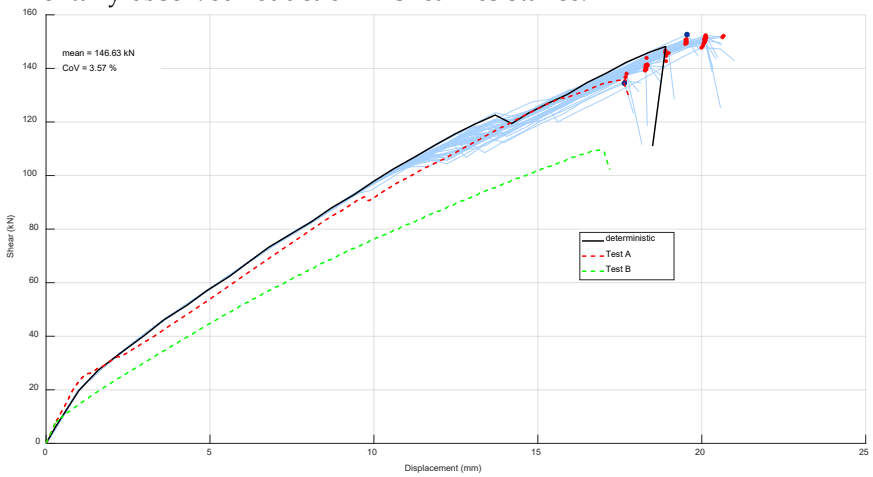


Figure 5-16: Stochastic analysis with corrosion rate as the only random variable for Beam 1.

A similar trend is observed for Beam 2 (Figure 5-17), where the deterministic prediction (142.9 kN) and the stochastic mean (141.5 kN, CoV 5.3%) are nearly coincident. The experimental scatter, however, is pronounced (117.9 kN in test A and 180.6 kN in test B), exceeding the dispersion induced numerically by corrosion-rate

variability. This suggests that experimental variability is influenced by additional mechanisms beyond the stochastic representation of corrosion penetration alone.

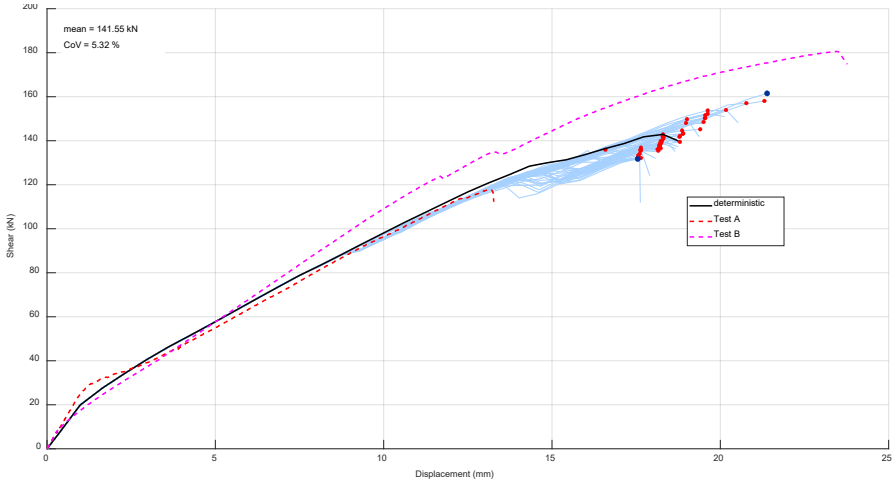


Figure 5-17: Stochastic analysis with corrosion rate as the only random variable for Beam 2.

In Beam 3 (Figure 5-18), despite the higher corrosion level, the dispersion remains limited (CoV 3.3%). The stochastic mean (140.7 kN) exceeds the deterministic prediction (126.7 kN), indicating a nonlinear sensitivity of shear capacity to corrosion penetration. The experimental results (160.7 kN and 170.5 kN) are higher than both numerical estimates, implying that the numerical model may conservatively estimate the shear resistance for this specimen.

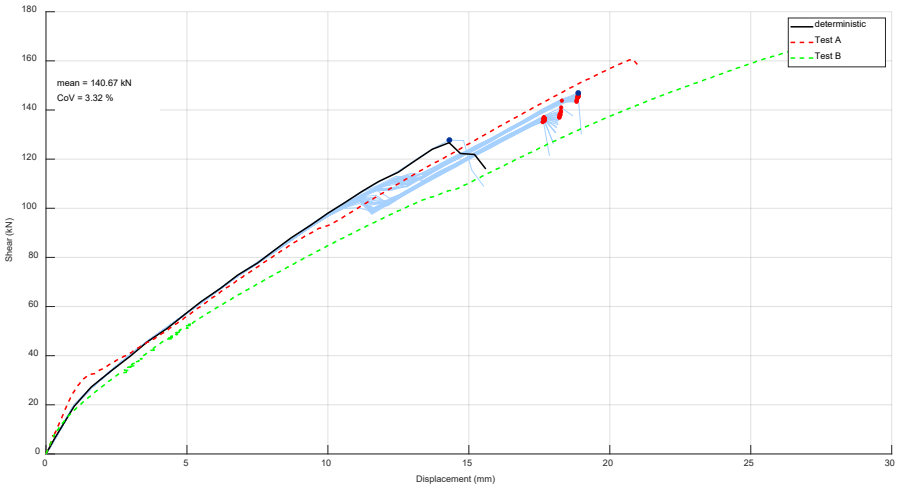


Figure 5-18: Stochastic analysis with corrosion rate as the only random variable for Beam 3.

Beam 4 (Figure 5-19) exhibits a mean stochastic capacity of 89.6 kN (CoV 3.9%), which is significantly lower than the deterministic prediction (113.5 kN). In this case, the introduction of corrosion-rate variability results in a downward shift of the mean shear capacity. The experimental value from test A (99.9 kN) aligns closely with the stochastic mean, whereas test B (129.5 kN) remains substantially higher.

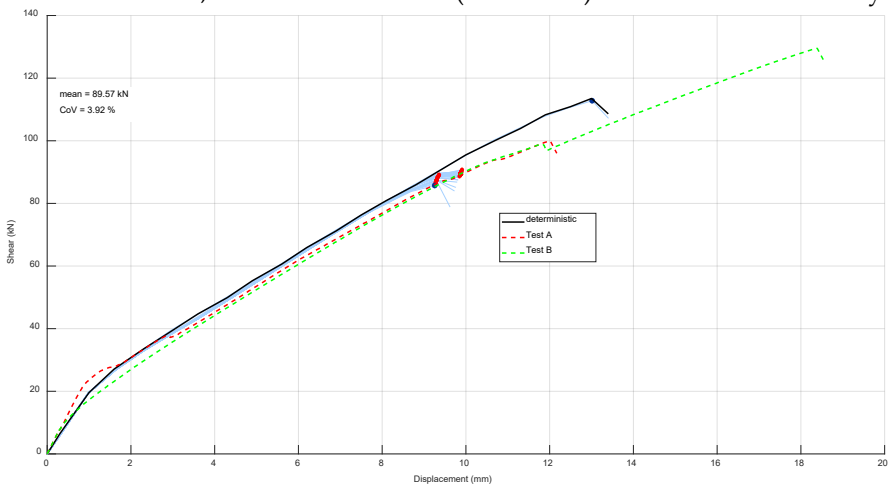


Figure 5-19: Stochastic analysis with corrosion rate as the only random variable for Beam 4.

Overall, the corrosion-only scenario demonstrates that variability in corrosion rate, even when modelled probabilistically, does not generate large dispersion in ultimate shear capacity. The deterministic solution generally approximates the mean stochastic response, and deviations are primarily associated with nonlinear interactions between section loss and shear mechanisms rather than with amplified statistical scatter.

Furthermore, in this configuration, the deterministic analysis tends to approximate the central tendency of the stochastic response, and discrepancies arise mainly from nonlinear effects related to corrosion-induced section loss rather than from significant probabilistic amplification.

Table 5-12 summarizes the ultimate shear capacity obtained from the corrosion-only stochastic analyses for all four beams. The deterministic ultimate shear strength, the mean stochastic prediction with its coefficient of variation, and the experimental shear capacities measured in tests A and B are reported for direct comparison.

Table 5-12: Summary of ultimate shear capacity for corrosion-only stochastic analyses.

Beam	Deterministic [kN]	Stochastic Mean [kN]	Stochastic CoV [%]	Experimental Side A [kN]	Experimental Side B [kN]
1	148.2	146.6	3.6	135.6	109.5
2	142.9	141.5	5.3	117.9	180.6

Beam	Deterministic [kN]	Stochastic Mean [kN]	Stochastic CoV [%]	Experimental Side A [kN]	Experimental Side B [kN]
3	126.7	140.7	3.3	160.7	170.5
4	113.5	89.6	3.9	99.9	129.5

The results reported confirm that, when corrosion rate is treated as the only stochastic variable, the dispersion of ultimate shear capacity remains limited, with CoV values not exceeding 5.3%. In this configuration, the deterministic prediction generally approximates the mean stochastic response, particularly for Beams 1 and 2. The deviations observed in Beams 3 and 4 are mainly attributable to nonlinear sensitivity of shear resistance to corrosion penetration rather than to a significant amplification of statistical variability. Overall, corrosion-rate uncertainty alone does not induce substantial dispersion in global shear capacity within the investigated range.

The combined stochastic analyses, in which both corrosion rate and material properties are treated as random variables, lead to a significantly larger dispersion of ultimate shear capacity, as shown in Figure 5-20 to Figure 5-23. CoV values range from 8.3% to 14.8%, indicating that the simultaneous variability of deterioration and mechanical properties amplifies the uncertainty in global structural response.
In Beam 1 (Figure 5-20), the mean stochastic shear capacity increases to 165.5 kN with a CoV of 10.1%, compared to the deterministic value of 148.2 kN. The stochastic envelope is therefore both wider and shifted upward relative to the deterministic baseline. The experimental values (135.6 kN and 109.5 kN) remain below the numerical mean, highlighting a persistent overestimation of shear resistance by the model in this specimen.

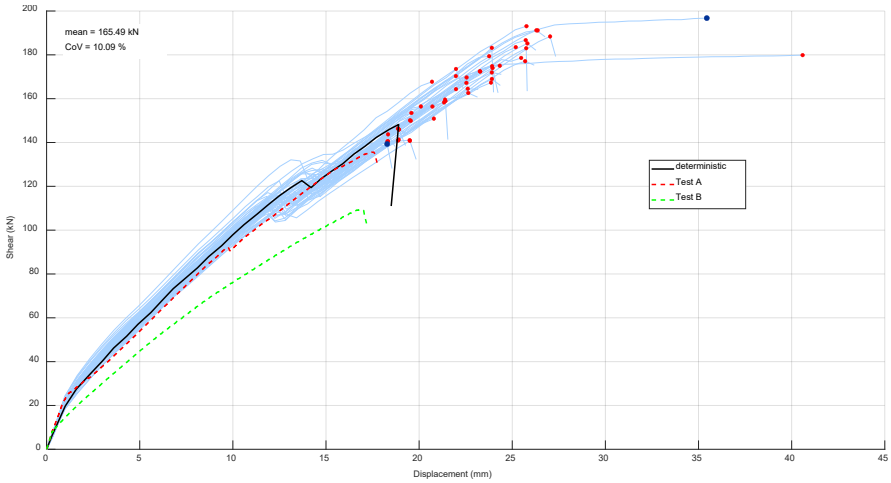


Figure 5-20: Stochastic analysis with corrosion rate and material properties as random variables for Beam 1.

Beam 2 (Figure 5-21) shows a similar increase in dispersion, with a mean stochastic capacity of 165.1 kN (CoV 8.3%), exceeding the deterministic prediction (142.9 kN). The experimental results again exhibit substantial scatter, with test B (180.6 kN) surpassing even the stochastic mean. The numerical dispersion remains smaller than the experimental spread but significantly larger than in the corrosion-only scenario.

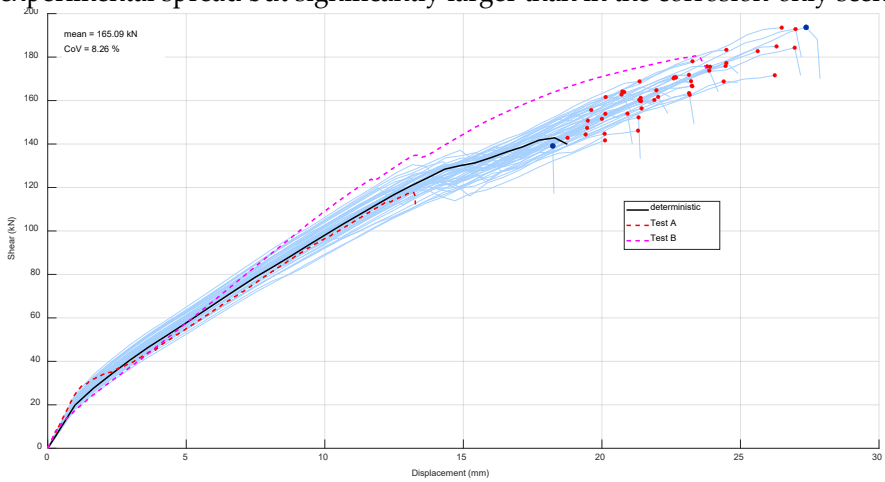


Figure 5-21: Stochastic analysis with corrosion rate and material properties as random variables for Beam 2.

The most pronounced variability is observed in Beam 3 (Figure 5-22), where the mean stochastic shear capacity reaches 158.2 kN and the CoV rises to 14.8%. The deterministic value (126.7 kN) appears markedly conservative relative to the stochastic mean. The experimental capacities (160.7 kN and 170.5 kN) align well with the numerical mean, indicating that the combined stochastic modelling better captures the observed response level for this highly corroded specimen.

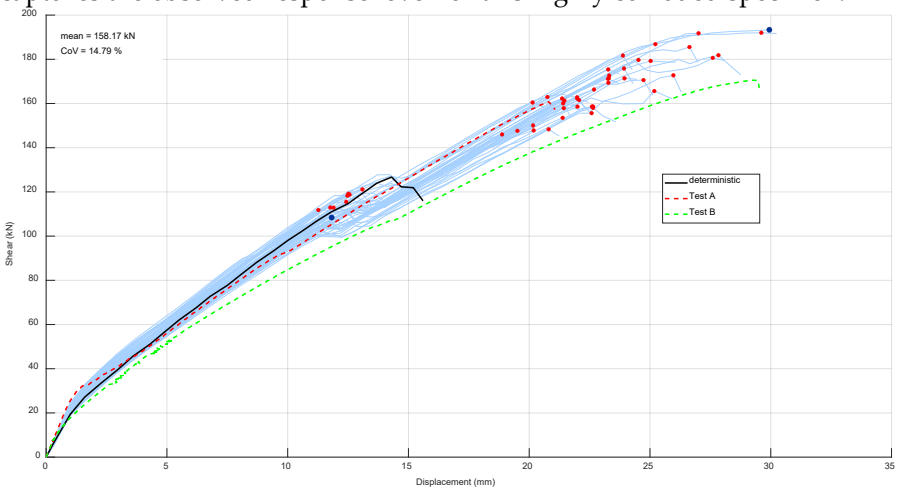


Figure 5-22: Stochastic analysis with corrosion rate and material properties as random variables for Beam 3.

In Beam 4 (Figure 5-23), the mean stochastic capacity is 98.7 kN (CoV 9.1%), which remains lower than the deterministic prediction (113.5 kN). As in the corrosion-only case, the stochastic mean is closer to the lower experimental value (99.9 kN), while test B (129.5 kN) exceeds both numerical predictions.

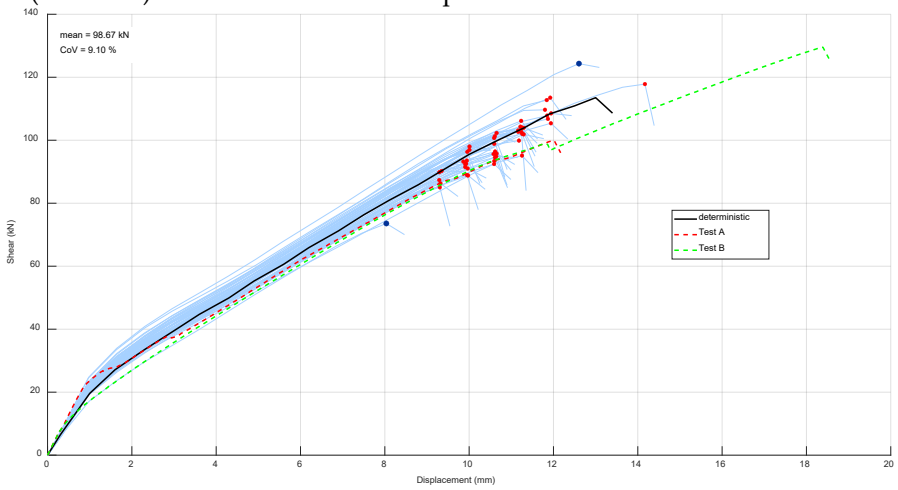


Figure 5-23: Stochastic analysis with corrosion rate and material properties as random variables for Beam 4.

Overall, the combined scenario clearly increases the dispersion of ultimate shear capacity compared to the corrosion-only configuration. The deterministic solution no longer consistently represents the mean stochastic response, as the interaction between corrosion penetration and material variability produces both upward and downward shifts of the mean shear resistance depending on the specimen. This behaviour confirms that the structural response becomes significantly more sensitive to uncertainty when both deterioration and material properties are simultaneously considered.

Table 5-13 summarizes the ultimate shear capacity obtained from the combined stochastic analyses, in which both corrosion rate and material properties are treated as random variables. The deterministic shear capacity, the mean stochastic prediction with its corresponding coefficient of variation, and the experimental results from tests A and B are reported for comparison.

Table 5-13: Summary of ultimate shear capacity for combined stochastic analyses.

Beam	Deterministic [kN]	Stochastic Mean [kN]	Stochastic CoV [%]	Experimental Side A [kN]	Experimental Side B [kN]
1	148.2	165.5	10.1	135.6	109.5
2	142.9	165.1	8.3	117.9	180.6
3	126.7	158.2	14.8	160.7	170.5
4	113.5	98.7	9.1	99.9	129.5

A comparison between deterministic and stochastic results highlights a non-uniform trend across the specimens. For Beams 1, 2 and 3, the mean stochastic shear capacity

exceeds the deterministic prediction. In particular, Beam 1 shows an increase from 148.2 kN (deterministic) to 165.5 kN (mean stochastic), while Beam 3 exhibits a substantial difference, with the deterministic prediction equal to 126.7 kN compared to a stochastic mean of 158.2 kN. This behaviour indicates that, when materials variability is introduced, the deterministic analysis does not necessarily coincide with the mean structural response, especially at higher corrosion levels.
Conversely, for Beam 4, the deterministic prediction (113.5 kN) is higher than the stochastic mean value (98.7 kN). This inversion suggests that, for this specimen, the nonlinear interaction produces a downward shift of the mean response when variability is introduced.
Compared to the corrosion-only scenario, the uncertainty amplification is evident for all specimens, particularly for Beam 3, characterized by the highest corrosion level. In this configuration, the deterministic solution no longer consistently represents the central tendency of the stochastic response, as the mean shear capacity may shift significantly depending on the interaction between deterioration and material variability. These results highlight the increased structural sensitivity to combined uncertainty sources.

5.7. GLOBAL DISCUSSION

The analyses performed on the laboratory beams subjected to accelerated corrosion allow certain observations derived from the naturally deteriorated girders to be both confirmed and clarified. In particular, they help to better interpret the role of the deterministic prediction with respect to the stochastic response and to distinguish the influence of corrosion-rate variability from that associated with material uncertainty.
For the naturally deteriorated girders, the stochastic analyses with corrosion rate as the only random variable resulted in negligible dispersion of ultimate capacity. When material variability was introduced in addition to corrosion uncertainty, the dispersion increased, although it remained limited in absolute terms; in this configuration, the deterministic ultimate capacity tended to lie toward the lower bound of the stochastic distribution.
A similar two-level behaviour is observed in the laboratory beams subjected to accelerated corrosion. In the corrosion-only configuration, the dispersion of ultimate shear capacity remains moderate, and the deterministic prediction is very close to the mean stochastic response. Conversely, when both corrosion rate and material properties are treated as stochastic variables, the dispersion increases significantly, and the deterministic ultimate shear capacity again tends to represent one of the lowest values within the probabilistic distribution rather than its central tendency.
From a comparison with regard to the corrosion-only configuration, the analyses performed on the laboratory beams subjected to accelerated corrosion clearly show that, when corrosion rate is treated as the sole stochastic variable, the mean stochastic

response is very close to the deterministic prediction. Despite the presence of more severe deterioration levels, the introduction of corrosion-rate variability alone does not significantly shift the central tendency of the ultimate shear capacity.
This aspect could not be distinctly identified in the naturally deteriorated girders, not because the behaviour was different, but because the dispersion of the stochastic results was extremely small. In that case, the near coincidence between deterministic and stochastic responses was masked by the almost negligible statistical spread. The accelerated corrosion regime therefore allows this trend to be explicitly observed and confirmed under conditions of higher variability.
Conversely, when material variability is introduced in addition to corrosion uncertainty, the behaviour changes significantly. The combined stochastic analyses performed on the laboratory beams show a marked increase in dispersion and, more importantly, confirm that the deterministic ultimate shear capacity tends to lie toward the lower tail of the stochastic distribution rather than near its mean. The same trend was already observed in the naturally deteriorated girders, where the deterministic prediction systematically appeared as one of the lowest values within the probabilistic response. The accelerated corrosion regime therefore does not introduce a new behavioural pattern, but rather confirms, under higher variability levels, that the deterministic solution should be interpreted as a conservative estimate when combined uncertainty sources are considered.

5.8. CONCLUDING REMARKS

This study developed and applied a stochastic nonlinear finite element framework for the assessment of existing deteriorated RC and PRC girders strengthened with advanced retrofit systems. Based on the numerical and stochastic results presented, the following conclusions can be drawn:

- In all investigated cases, the deterministic nonlinear solution evaluated at mean material properties resulted in an ultimate load lower than the mean value obtained from Monte Carlo combined simulations. The deterministic prediction underestimated the stochastic mean capacity by approximately 9–18%, depending on the adopted stochastic scenario. This confirms that, in nonlinear structural systems with asymmetric input distributions, the response evaluated at mean parameters does not coincide with the expected structural capacity. In the combined stochastic configurations, the deterministic ultimate capacity systematically tended to lie toward the lower bound of the stochastic distribution rather than at its central value, both for naturally deteriorated girders and for laboratory beams subjected to accelerated corrosion.

- For both the historical RC girder and the PRC girders, variability in concrete and steel mechanical properties produced a coefficient of variation of ultimate load of approximately 3–3.5%. This dispersion level remained consistent even when corrosion effects were included, indicating that intrinsic material variability is the dominant source of global response uncertainty for the investigated natural deterioration levels. The analyses on laboratory beams confirmed this trend and showed that, when material variability is combined with corrosion uncertainty under more severe deterioration conditions, the overall dispersion increases significantly, revealing a stronger structural sensitivity to interacting uncertainty sources.

- When uncertainty was introduced exclusively through the corrosion rate while maintaining the same physical corrosion penetration, the resulting variability of ultimate load was practically negligible in the naturally deteriorated girders. The analyses on the accelerated corrosion specimens clarified this aspect: even under higher corrosion levels, when corrosion rate is treated as the sole stochastic variable, the mean stochastic response remains very close to the deterministic prediction and the dispersion remains limited. This confirms that, in isolation, statistical fluctuations of the corrosion rate parameter have a minor influence on global structural capacity compared to the effect of the actual section loss.

- Despite the complexity introduced by CFRP bars, FRM overlays, UHPFRC web enlargement, and externally bonded FRP plates, the overall dispersion of ultimate load remained moderate. This indicates that advanced strengthening systems can provide robust structural performance even in the presence of combined deterioration and material uncertainty.

- The results highlight that deterministic nonlinear analysis may provide conservative estimates of mean structural capacity but does not capture the statistical nature of performance. The distinction between corrosion-only and combined stochastic scenarios further demonstrates that the deterministic solution approximates the mean response when corrosion rate is the only uncertainty source, whereas it tends to represent a lower-bound estimate when material variability is also included. For reliability-oriented assessment of deteriorated and strengthened girders, stochastic modelling enables quantification of response dispersion and identification of dominant uncertainty sources.

- Although Monte Carlo simulation is computationally demanding in highly nonlinear finite element models, the adopted sample size (N = 50) provided

stable estimates of the first statistical moments within acceptable computational time.

Overall, the proposed stochastic modelling strategy represents a consistent and physically grounded approach for evaluating deteriorated existing girders and for quantifying the reliability of innovative strengthening interventions. The methodology is directly applicable to life-cycle assessment and reliability-based decision-making for aging reinforced and prestressed concrete infrastructure.

5.9. REFERENCES

[1] AKKAYA, Y., DHAKAL, R. P., & MAEKAWA, K. (2012). BUCKLING MODEL FOR REINFORCING BARS IN CONCRETE. JOURNAL OF STRUCTURAL ENGINEERING.

[2] ANDRADE, C., ALONSO, C., & MOLINA, F. J. (1993). COVER CRACKING AS A FUNCTION OF BAR CORROSION: PART I – EXPERIMENTAL TEST. MATERIALS AND STRUCTURES, 26, 453–464.

[3] BENTZ, E. C. (2005). MODIFIED TENSION STIFFENING MODEL FOR CRACKED REINFORCED CONCRETE. UNIVERSITY OF TORONTO.

[4] CEB-FIP (1978). MODEL CODE FOR CONCRETE STRUCTURES.

[5] DI STEFANO, N. (2022). ASSESSMENT OF EXISTING BRIDGES WITH SPECIAL EMPHASIS ON CORROSION. PHD THESIS, UNIVERSITY OF BRESCIA, CURRICULUM "REHABILITATION OF HISTORICAL AND MODERN BUILDINGS".

[6] ELIGEHAUSEN, R., POPOV, E. P., & BERTERO, V. V. (1983). LOCAL BOND STRESS–SLIP RELATIONSHIPS OF DEFORMED BARS UNDER GENERALIZED EXCITATIONS. UCB/EERC REPORT.

[7] FIB BULLETIN 34 (2006). MODEL CODE FOR SERVICE LIFE DESIGN. FÉDÉRATION INTERNATIONALE DU BÉTON.

[8] FIB (2010). MODEL CODE 2010. FÉDÉRATION INTERNATIONALE DU BÉTON.

[9] HOGNESTAD, E. (1951). STUDY OF COMBINED BENDING AND AXIAL LOAD IN REINFORCED CONCRETE MEMBERS. UNIVERSITY OF ILLINOIS BULLETIN.

[10] HORDIJK, D. A. (1991). LOCAL APPROACH TO FATIGUE OF CONCRETE. PHD THESIS, DELFT UNIVERSITY.

[11] HUNTER, M. D. (2016). STOCHASTIC FINITE ELEMENT MODELING OF REINFORCED CONCRETE STRUCTURES. MAS THESIS, UNIVERSITY OF TORONTO.

[12] KUPFER, H., HILSDORF, H. K., & RUSCH, H. (1969). BEHAVIOR OF CONCRETE UNDER BIAXIAL STRESSES. ACI JOURNAL.

[13] LIU, P. L., & DER KIUREGHIAN, A. (1986). FINITE ELEMENT RELIABILITY OF GEOMETRICALLY NONLINEAR STRUCTURES. JOURNAL OF ENGINEERING MECHANICS, ASCE.

[14] MA, J. (2018). A TOOL FOR STOCHASTIC FEM ANALYSIS AND FIELD ASSESSMENT OF CONCRETE STRUCTURES. MAS THESIS, UNIVERSITY OF TORONTO.

[15] MIRZA, S. A., HATZINIKOLAS, M., & MACGREGOR, J. G. (1979). STATISTICAL DESCRIPTIONS OF STRENGTH OF CONCRETE. JOURNAL OF THE STRUCTURAL DIVISION, ASCE.

[16] NOWAK, A. S., & SZERSZEN, M. M. (2003). CALIBRATION OF DESIGN CODE FOR BUILDINGS (STEEL STATISTICS). JOURNAL OF STRUCTURAL ENGINEERING, ASCE.

[17] SCOTT, B. D., PARK, R., & PRIESTLEY, M. J. N. (1982). STRESS–STRAIN BEHAVIOR OF CONCRETE CONFINED BY OVERLAPPING HOOPS. ACI JOURNAL.

[18] SECKIN, M. (1981). HYSTERETIC BEHAVIOR OF REINFORCING STEEL. JOURNAL OF STRUCTURAL ENGINEERING.

[19] SUDRET, B. (2007). UNCERTAINTY PROPAGATION AND SENSITIVITY ANALYSIS IN MECHANICAL MODELS. RELIABILITY ENGINEERING & SYSTEM SAFETY.

[20] TASSIOS, T. P. (1980). DOWEL ACTION IN REINFORCED CONCRETE MEMBERS. ACI JOURNAL.

[21] TUUTTI, K. (1982). CORROSION OF STEEL IN CONCRETE. SWEDISH CEMENT AND CONCRETE RESEARCH INSTITUTE.

[22] VECCHIO, F. J. (1992A). COMPRESSION SOFTENING OF CONCRETE: A REVIEW AND FORMULATION. ACI STRUCTURAL JOURNAL.

[23] VECCHIO, F. J. (2001). DISTURBED STRESS FIELD MODEL FOR REINFORCED CONCRETE: IMPLEMENTATION. JOURNAL OF STRUCTURAL ENGINEERING, ASCE, 127(1), 12–20.

[24] WALRAVEN, J. C. (1981). FUNDAMENTAL ANALYSIS OF AGGREGATE INTERLOCK. JOURNAL OF STRUCTURAL ENGINEERING.

[25] WONG, P. S., VECCHIO, F. J., & TROMMELS, H. (2013). VECTOR2 & FORMWORKS USER'S MANUAL (2ND ED.).

5.10. LIST OF TABLES

Table 5-1: Out-of-plane thickness assigned to concrete regions (Historical RC Girder). 176
Table 5-2: Reinforcement areas adopted in the deterministic model (Historical RC Girder). 176
Table 5-3:Material Properties Adopted in the Deterministic Model (Historical RC Girder). 177
Table 5-4: Out-of-plane thickness assigned to concrete regions (PRC Girders). 178
Table 5-5: Reinforcement areas adopted in the deterministic model (PRC Girder). 180
Table 5-6:Material Properties Adopted in the Deterministic Model (PRC Girder). 180
Table 5-7: Statistical parameters adopted for corrosion rate. 183
Table 5-8: comparison between numerical and experimental response. 190
Table 5-9: Experimental corrosion parameters of laboratory beams subjected to accelerated corrosion. 198
Table 5-10:Material properties of the artificially corroded beams. 199
Table 5-11: Statistical parameters of the corrosion rate adopted in the stochastic analyses of laboratory beams 1–4, including mean corrosion rate (mm/year), corresponding standard deviation and duration of electrical connection used to reproduce the experimentally observed corrosion levels. 200
Table 5-12: Summary of ultimate shear capacity for corrosion-only stochastic analyses. 203
Table 5-13: Summary of ultimate shear capacity for combined stochastic analyses. 206

5.11. LIST OF FIGURES

Figure 5-1: existing section (a) and degradation conditions (b) of the historical RC girder. 170
Figure 5-2:Total Load versus Midspan deflection of the strengthened RC beam ... 171
Figure 5-3:existing section (a) and degradation conditions (b) of the PRC girders. 172
Figure 5-4: experimental set-up of the PRC girders (a) and experimental results in terms of total load versus load point deflection (b). 173
Figure 5-5: discretization of the section (a) and finite element model (b) of the historical RC girder. 176
Figure 5-6: discretization of the section (a) and finite element model (b) of the historical PRC girders. 179
Figure 5-7: strands and reinforcement layout in PRC Girders. 179
Figure 5-8:Discretization of the concrete cover (Habibi, 2017) 185

Figure 5-9: stochastic analysis corrosion-only considering corrosion for 28 days with a corresponding equivalent corrosion rate. 191
Figure 5-10: stochastic analysis corrosion-only considering corrosion for 365 days with a corresponding equivalent corrosion rate. 192
Figure 5-11: stochastic analysis materials-only. 192
Figure 5-12: stochastic analysis full stochastic considering corrosion for 28 days with a corresponding equivalent corrosion rate. 193
Figure 5-13: stochastic analysis full stochastic of the PRC girders. 194
Figure 5-14: cross-section of the artificially corroded bems. 197
Figure 5-15: Finite Element Model of the artificially corroded beams. 198
Figure 5-16: Stochastic analysis with corrosion rate as the only random variable for Beam 1. 201
Figure 5-17: Stochastic analysis with corrosion rate as the only random variable for Beam 2. 202
Figure 5-18: Stochastic analysis with corrosion rate as the only random variable for Beam 3. 202
Figure 5-19: Stochastic analysis with corrosion rate as the only random variable for Beam 4. 203
Figure 5-20: Stochastic analysis with corrosion rate and material properties as random variables for Beam 1. 204
Figure 5-21: Stochastic analysis with corrosion rate and material properties as random variables for Beam 2. 205
Figure 5-22: Stochastic analysis with corrosion rate and material properties as random variables for Beam 3. 205
Figure 5-23: Stochastic analysis with corrosion rate and material properties as random variables for Beam 4. 206

6 CONCLUSIONS AND RECOMMENDATIONS FOR FUTURE WORK

6.1 Conclusions

The primary objective of this doctoral research was to contribute to the assessment and strengthening of deteriorated reinforced and prestressed concrete bridge girders, with particular emphasis on full-scale structural members affected by long-term natural corrosion and tested at the end of their service life.
A central motivation of the work lies in the recognition that many existing bridges are approaching or exceeding their nominal design life. In this context, reliable quantification of residual structural capacity becomes essential to support rational decisions regarding maintenance, strengthening, or replacement. The research therefore focused on mechanically grounded formulations, full-scale experimentation, and supportive numerical interpretation.
The main conclusions of the thesis are summarized below, organized according to the core themes addressed in each chapter.

With regard to the analytical assessment of corroded members, a formulation for predicting the shear strength of reinforced concrete beams affected by corrosion was developed within the framework of *fib* Model Code 2020. The method explicitly incorporates corrosion-induced degradation mechanisms, including reduction of longitudinal reinforcement area, deterioration of transverse reinforcement mechanical properties, and reduction of effective concrete width due to cracking and cover damage. The formulation provides a rational tool for estimating the residual shear capacity of degraded beams during the assessment phase. Its validation against available experimental results indicates satisfactory agreement and confirms its potential applicability in practical engineering.

Concerning full-scale experimental investigation, the tests performed on naturally deteriorated bridge girders provide valuable evidence on structural behaviour at the end of service life. The results confirm that long-term natural corrosion may significantly affect structural performance, but that the governing failure mechanisms depend on the interaction between geometry, reinforcement layout, and degradation pattern.

Two strengthening interventions were investigated: an heavy-target application of UHPFRC overlay for shear strengthening, and a CFRP–FRM system providing combined flexural and shear strengthening.
With respect to the research theme, the application of these strengthening systems to full-scale degraded members demonstrated that service-life extension through targeted reinforcement is technically feasible. The strengthened configurations exhibited increased load-bearing capacity and controlled crack development, while preserving global structural behaviour compatible with the original system. The results highlight the importance of proper interface preparation and mechanical compatibility between new materials and aged substrates. The strengthening techniques investigated appear suitable for practical application in cases where replacement would otherwise be required.

Regarding numerical interpretation, nonlinear finite element analyses were employed to reproduce and interpret the observed structural behaviour under degradation and strengthening scenarios. The numerical models provided useful insight into stress redistribution, crack development, and sectional response. However, they were adopted as interpretative and supportive tools rather than as primary sources of evidence. The study confirms that advanced mechanical models can effectively complement full-scale experimentation when used with appropriate calibration and engineering judgment. In particular, the complementary stochastic investigation highlighted the influence of material and corrosion variability on structural response. Although deterministic nonlinear analyses remain central to practical assessment, the results indicate that variability in mechanical properties may significantly affect predicted capacity. The integration of probabilistic considerations, even in a simplified form, contributes to a more comprehensive understanding of structural performance under uncertainty.

Overall, the research demonstrates that a mechanics-based and experimentally validated approach to the assessment of naturally deteriorated full-scale bridge girders can support rational decisions for strengthening and service-life extension, contributing to a more sustainable management of aging infrastructure.

6.2 Recommendations for future research

The present research addresses several aspects of bridge assessment and strengthening, yet it also highlights directions for further investigation.
First, additional experimental campaigns on naturally deteriorated full-scale members are strongly recommended. The limited availability of such specimens represents one of the main constraints in advancing knowledge on real long-term

corrosion effects. Future studies should aim to test elements with well-documented construction details and degradation histories in order to refine residual capacity models.

Second, further refinement and validation of the proposed analytical shear formulation would benefit from comparison with a broader experimental database, including both reinforced and prestressed concrete members. Extension of the approach to prestressed girders, with explicit consideration of prestress loss due to corrosion, represents a natural development.

Third, additional research on the long-term performance of strengthening systems applied to degraded substrates is needed. In particular, investigation of interface durability, bond evolution under cyclic loading, and environmental exposure effects would enhance confidence in service-life extension strategies.

Fourth, improvements in nonlinear numerical modelling could focus on more detailed representation of corrosion-induced bond deterioration and localized cross-section loss. Although the current numerical analyses provided satisfactory interpretation of experimental results, further developments could increase predictive robustness.

Finally, the integration of probabilistic approaches into practical assessment procedures deserves continued attention. Simplified reliability-oriented tools, calibrated on mechanically consistent models and experimental evidence, could support bridge management strategies by linking residual capacity estimates with safety margins and intervention thresholds.

In conclusion, this doctoral research provides a structured contribution to the assessment and strengthening of deteriorated bridge girders, while also outlining several avenues for continued scientific and engineering development in the field of aging infrastructure.